The University Of Sheffield.

The Development of Instrumentation to Increase the Accessibility and Throughput of Single-Molecule FRET

Dylan George

A thesis submitted in partial fulfilment of the requirements for the degree of Doctor of Philosophy

The University of Sheffield
Faculty of Science
Department of Chemistry

Submission Date: 12th May 2022

Declaration

I, the author, confirm that the Thesis is my own work. I am aware of the University's Guidance on the Use of Unfair Means (www.sheffield.ac.uk/ssid/unfair-means). This work has not been previously been presented for an award at this, or any other, university.

Signature: Dylan George
Date: 12/05/2022

Publications arising from this work:

- Chapter 2 has been submitted to bioRxiv and has been accepted for publication, after being reviewed, at Advanced Biology.

  George, D. R., Ambrose, B., Cadby, A. J. & Craggs, T. D. An Open-source, Cost-Efficient Excitation Module for Single-molecule Microscopy. *bioRxiv* 2022.02.28.482236 (2022). doi:10.1101/2022.02.28.482236

Acknowledgements

I would like to thank and recognize EPSRC for the funding for this project. I am also very grateful to my two academic supervisors: Dr. Timothy Craggs and Professor Ashley Cadby. Both have continually supported me throughout my PhD journey. Elliot Steele for his help in the early stages of my project using his expertise and code to the control digital micromirror device and assistance with software. Ben Ambrose for useful discussions, ideas and constructive feedback on research. Mahmoud Abdelhamid, in the later stages of my PhD for providing DNA oligo solutions in suitable buffers and for help with imaging on the smfBox. Finally, my family and Devanshi for always supporting me.

Abstract

Current drug discovery approaches use high-throughput ensemble methods combined with large libraries of small molecules to measure and quantify the drug-ligand interactions. These methods currently suffer from ensemble averaging, meaning only the average conformational state is measured. Diffusion-based single-molecule Förster resonance energy transfer (FRET) can measure tightly bound drug candidates with high affinity and has the potential to overcome the limitations of these methods by identifying multiple conformational states and, in the process, minimises sample consumption. However, this technique suffers from high acquisition times which limits the throughput of this method. Furthermore, high instrument costs and a lack of open-source hardware have limited the use of single-molecule FRET to specialists. We aim to extend this method by making it affordable, easy to use and applicable for high-throughput drug discovery.

Here we present a commercially available, affordable, single-spot, single-molecule microscope that allows flexibility for single-molecule researchers. In addition, an open-source, compact and cost-effective excitation module for single-molecule imaging and spectroscopy is presented. By comparing this module to commercially available lasers, this excitation module reported a similar degree in accuracy of single-molecule FRET measurements for three well studied oligonucleotides. By combining common confocal microscopy principles with single-molecule methods we also studied the performance of a multi-spot setup for high-throughput single-molecule FRET. Here we observed single-molecules at high frame rates (1000 frames per second) and observed FRET in a multi-spot setup using a transmission electron microscopy (TEM) grid.

We envisage that this research will make this powerful single-molecule technique more widely available for users in academia and industry and more applicable to the drug discovery process.

Contents

	Abbreviations	1
	List of Figures	3
	List Tables	10
Chapter 1. Introduction		11
1.	Introduction	12
1.1	FRET Theory, Applications and Limitations	14
1.1.1	Förster Resonance Energy Transfer (FRET)	14
1.1.2	The Theory of FRET	16
1.1.3	Ensemble and Single-molecule methods	19
1.1.4	Applications of Single-Molecule FRET	20
1.1.4.1	Conformational states and dynamics	20
1.1.4.2	Structure Determination	21
1.1.5	Limitations of smFRET	22
1.2	Single-Molecule FRET – System Selection	24
1.2.1	Achieving FRET measurements	25
1.2.2	Experimental design and hardware	26
1.3	The road to high-throughput single-molecule FRET	30
1.3.1	Generating a multi-spot pattern	31
1.3.2	Optimizing signal to noise ratio and increasing temporal resolution	33
1.3.2.1	Sensitive Detectors	33
1.4	Summary	36
1.5	References	37
Chapter 2. An Affordable, Easy to use, Confocal Single-Molecule FRET Instrument		43
2.1	Introduction	45
2.1.1	Home-made and commercial single-molecule instrumentation	45
2.2	Design and Methods	47
2.3	Results and Discussion	49
2.3.1	Excitation Module	49
2.3.2	The Pinhole Module	57
2.3.3	Emission Module	61
2.3.4	Sample stage and Lid	65
2.3.5	Configurations	67
2.4	Conclusions & Further Design Suggestions	69
2.5	References	69
Chapter 3. An Open-source, Cost-Efficient Excitation Module for Single-molecule Microscopy		71
3.	Abstract	73
3.1	Introduction	73
3.2	Hardware/ Methods	78
3.3	Results and Discussion	79
3.3.1	Power and power stability	79
3.3.2	Alternation rise and fall times for ALEX	81

3.3.3 Applications 82
3.3.3.1 smFRET 82
3.3.3.2 FCS 85
3.4 Discussion 86
3.5 Methods 88
3.5.1 Characterisation of the Laser diodes 88
3.5.2 Accurate smFRET Measurements 89
3.5.3 FCS measurements 90
3.6 References 90
3.7 Supplementary Material 93

Chapter 4. Performance of Modern Cameras for Single-Molecule Detection 99

4.1 Introduction 101
4.1.1 Types of noise in modern cameras 102
4.1.2 The signal-to-noise ratio 105
4.1.3 Photon Transfer Curve 106
4.2 Methods 108
4.3 Results 109
4.3.1 Photon Transfer Curves Comparison 109
4.3.2 SNR of Fluorescent Molecules 112
4.3.3 DNA Paint Comparison 113
4.4 Conclusion 118
4.5 References 119

Chapter 5. Identifying Single-Molecules with a Camera at High Speeds using a Digital Micromirror Device 120

5.1 Introduction 122
5.1.1 Developing a multi-spot confocal microscope 122
5.1.2 Integrating single-molecule analysis for multi-point detection 128
5.2 Methods 131
5.3 Results and Discussion 131
5.3.1 Preliminary Fluorescent Time Traces 131
5.3.2 Identifying Individual Spots containing Fluorescence Emission 133
5.3.3 Changing the spot size 138
5.3.4 Measuring the Diffusion Coefficient of Fluorescent Beads 139
5.3.5 An APD detector in combination with the digital micromirror device 145
5.4 Conclusion 149
5.5 References 150

Chapter 6. Developing a Single-Molecule Multipoint Detection System using Multiple Static Pinholes 153

6.1 Introduction 155
6.2 Methods 156
6.2.1 Optical Setup 156
6.3 Results and Discussion 158
6.3.1 Performance Measurements 158
6.3.2 Single-molecule (dye) measurements 164

6.3.3 Improve In-Focus Molecular Detection 166
6.3.4 Simultaneous imaging of single-molecules with an APD and an sCMOS camera 168
6.3.5 Using a TEM Grid as a multiple pinhole array 171
6.3.6 Characterizing the TEM Grid 174
6.3.7 Z-drift Measurements 179
6.3.8 Concentration Measurements 180
6.3.9 Dual Colour Measurements 182
6.3.10 Analysis of FRET Efficiencies using an image splitter 184
6.4 Future work analysing single-molecule bursts 190
6.4.1 Identifying single-molecule bursts 190
6.4.2 Location of single-molecule bursts 191
6.5. Conclusion 197
6.6 References 198

Chapter 7. Conclusion and Future work 200
7.1 Summary and Future work 202
7.2 Impact of this work 205
7.3 References 206

Abbreviations

A	**Adenine**
ADC	**Analogue-Digital Converter**
ALEX	**Alternating-Laser Excitation**
AU	**Airy Unit**
BNC	**Bayonet Neill-Concelman**
BSA	**Bovine Serum Albumin**
C	**Cytosine**
CAD	**Computer-Aided Design**
CARS	**Coherent Anti-Stokes Raman Scattering**
CCD	**Charge-Coupled Device**
CMOS	**Complementary Metal-Oxide Semiconductor**
CNC	**Computer Numerical Control**
CW	**Continuous Wave**
DAQ	**Data Acquisition**
DMD	**Digital Micromirror Device**
DNA	**Deoxyribonucleic Acid**
EM-CCD	**Electron-Multiplying Charge-Coupled Device**
FCCS	**Fluorescence Cross-Correlation Spectroscopy**
FCS	**Fluorescence Correlation Spectroscopy**
FPN	**Fixed Pattern Noise**
FRET	**Förster Resonance Energy Transfer**
FWHM	**Full Width Half Maximum**
G	**Guanine**
ISM	**Image Scanning Microscopy**
ISMS	**Interactive Single-Molecule Software**
LCOS	**Liquid Crystal On Silicon**
LED	**Light-emitting Diode**
LSM	**Light-Sheet Microscopy**
M	**Magnification**
MINFLUX	**Minimal Photon Fluxes**
MM	**Multi-Mode**
MPPC	**Multi-Pixel Photon Counters**
MSD	**Mean Squared Displacement**
NA	**Numerical Aperture**
NDR	**Non-Destructive Readout**
NHS	**N-Hydroxysuccinimide**
NMR	**Nuclear Magnetic Resonance**
NI	**National Instruments**
ONI	**Oxford Nanoimaging**
PALM	**Photoactivated Localization Microscopy**
PAM	**Pulsed Interleaved Excitation Analysis with Matlab**
PCA	**Principal Component Analysis**
PEG	**Polyethylene Glycol**
PM	**Polarisation-Maintaining**
PSF	**Point Spread Function**
PSNR	**Peak Signal-to-Noise Ratio**
QTY	**Quantity**

RNA	**Ribonucleic Acid**
SD	**Standard Deviation**
SIM	**Structured Illumination Microscopy**
SMFRET	**Single-Molecule Förster Resonance Energy Transfer**
SMLM	**Single-Molecule Localization Microscopy**
SNR	**Signal-to-Noise Ratio**
SPAD	**Single-Photon Avalanche Diode**
SPIM	**Selective Plane Illumination Microscopy**
STED	**Stimulated Emission Depletion Microscopy**
STORM	**Stochastic Optical Reconstruction Microscopy**
T	**Thymine**
TEM	**Transmission Electron Microscopy**
THL	**Thorlabs**
TIRF	**Total Internal Reflection Microscopy**
TL	**Tube Lens**

List of Figures

Figure 1.1. A schematic showing the occurrence of FRET with two fluorophores; the donor and acceptor. In the first instance, the donor absorbs and emits the emission because the acceptor is not close enough. In the second instance, the donor and acceptor are close enough for FRET to occur.
Figure 1.2. A Jablonski diagram showing the energy levels of the acceptor and donor molecules when FRET occurs.
Figure 1.3. A schematic of the FRET efficiency against the frequency observed in an example smFRET experiment showing the resultant weighted (ensemble) average that would be obtained from a FRET experiment. An smFRET experiment would be able to distinguish between these two conformations.
Figure 1.4. A schematic showing the Holliday Junction and the dyes attached for smFRET measurements. The yellow rectangles represent homologous regions capable of branch migration. The diagram shows that after magnesium or calcium presence, migration occurs and high FRET is detected.
Figure 1.5. An illustration of the stoichiometry against the transfer efficiency (FRET efficiency) distinguishing between the donor only molecule and the low FRET molecule.
Figure 1.6. Illustration two microscopy techniques at the sample that improve the SNR by rejecting out of focus fluorophores. A) TIRF Microscopy illuminates the first 100 nm above the coverslip and does not illuminate fluorophores above this B) Confocal Microscopy illuminates a small spot at the sample and the observation volume is only at the focal plane, disallowing the detection of fluorophores above and below the focal plane.
Figure 1.7. The laser beam excitation path in objective TIRF.
Figure 1.8. The smfBox and the optical setup pathway.
Figure 1.9. A) A photograph of the digital micromirror chip used in this project B) An illustration of the different ways the digital micromirror device can reflect incident rays.
Figure 1.10. A) A binary program uploaded by the computer, implemented onto the DMD, and imaged on an sCMOS camera. The intensity that is reflected by the DMD is from a laser source. B) A multi-spot pattern uploaded from MATLAB onto the DMD and shown on an sCMOS camera.
Figure 1.11. A schematic to show each component of a photodiode.
Figure 2.1. A Venn diagram showing the main reasons for the lack of uptake in single-molecule FRET instruments.
Figure 2.2. The openFrame by Cairn Research. This inverted microscope design is composed of five sections. The bottom of the microscope has a base section capable of being attached to optical tables. Above this is the camera section which is a thicker section to allow cameras to be attached. Above this are two further thinner sections allowing for excitation light to enter and customizable optics to be placed as inputs. The final section is the stage which accommodates the sample.
Figure 2.3. A simplistic schematic of the openFrame modules designed and the laser beam (yellow) and emission (orange) pathways.
Figure 2.4. A diagram of the excitation module for the openFrame with all the optical components aligned inside the module labelled. The green arrow represents the laser beam path towards the openFrame and the sample.
Figure 2.5. A) A simplistic schematic of the alignment tool in the perfect alignment on the openFrame. M1 and M2 represent mirrors. I1, I2 and I3 represent irises. D1 represents the dichroic mirror. The laser beam is represented by a yellow line. B) A photograph of the alignment tool. C) A picture of the alignment tool on the openFrame with the excitation module attached.

Figure 2.6. Alignment of the openFrame excitation pathway by taking out the dichroic mirror (D1). The laser beam travels directly through the openFrame and out the other end.
Figure 2.7. The openFrame by Cairn Research with an early draft excitation module on the top layer. The excitation module was designed to input and easily align laser light into the microscope.
Figure 2.8. The openFrame by Cairn Research with an early draft excitation module on the top layer. The excitation module was designed to input and easily align laser light into the microscope.
Figure 2.9. A photograph of the excitation module for the openFrame with all the optical components aligned inside the module.
Figure 2.10. A diagram showing the intensity profile of the diffraction limit and the Airy Disc.
Figure 2.11. A diagram showing the pinhole module of the microscope. A tube lens (TL) focuses the light rays through the pinhole and the lens after directs the light rays parallel to the optical axis.
Figure 2.12. A) A schematic of the middle section of the microscope with the parts labelled. B) A photograph of the manufactured pinhole module with a collimator and power meter attached. This setup was used to align the pinhole module.
Figure 2.13. A draft version of two emission modules shown attached to the bottom two openFrame layers.
Figure 2.14. A diagram of the emission module for the openFrame with all the parts inside the module labelled.
Figure 2.15. A diagram of the final two emission modules for the openFrame. This configuration can be used for polarisation studies.
Figure 2.16. A schematic of the emission module showing the incoming emission from the openFrame, the two avalanche photodiodes, the dichroic mirror, and the achromatic lenses.
Figure 2.17. The sample stage (left) of the openFrame was replaced with a customised, light-tight lid (right).
Figure 2.18. A) The fully designed openFrame with both detection and excitation modules attached B) A photograph of the CNC machined microscope with all the parts inside and modules attached.
Figure 2.19. The openFrame design with a camera attachment used for super-resolution imaging and widefield microscopy.
Figure 3.1. A) A schematic showing the excitation pathway of the module. Red and green line shows the path of the laser beams travelling towards the coupler. The mirrors (M1-M5) are used to align the laser beam. A dichroic beamsplitter (B1) reflects the red laser beam and allows the green laser beam to travel through. Both laser beams are then coupled into a fibre via a coupler. Further details (including part numbers) are found in supplementary information 1.1) B) A photograph of the finished excitation module showing the excitation in the same orientation as the schematic.
Figure 3.2. A-C) The power stability of the lasers with different heat dissipation mountings: posts alone (A), breadboard (B) and heatsinks (C) D) Relative power stability for both lasers under continuous wave mode E) Relative power stability for both lasers under 20 kHz alternation F) The wavelength spectrum of the 520 nm 100 mW and the 638 nm 700 mW lasers.
Figure 3.3. A) Time-resolved measurements of the laser power measured by a photodiode B) The rise and fall times of the green laser of both the commercially available laser (omicron laser system) and the excitation module. C) The rise and fall times of the red laser of both the commercially available laser and the excitation module. An exponential curve was fitted to the multiple tests conducted.

Figure 3.4. A graph showing the FRET efficiencies using the excitation module compared to the benchmark study. The samples 1a, 1b and 1c represent low, medium and high FRET samples, respectively. The results from the excitation layer and the FRET histogram of the excitation module are also shown at the top of the figure. These data points have error bars calculated from the standard deviation of the repeats. The 1c sample has error bars that are too small to be seen in this graph. Compared with this is the data from different labs represented by the colours in the legend. The dashed line shows the mean FRET efficiency of the labs in the benchmark study.
Figure 3.5. Fluorescence correlation spectroscopy measurements taken on Rhodamine 6G (orange) and a concentrated sample of ATTO 550 labelled DNA (blue) showing an autocorrelation curve.
Figure 3.6. E-S histograms for the samples 1a, 1b and 1c. A-C) 1a-1c E-S histograms D-F) 1a-1c repeat experiment E-S histograms.
Figure 3.7. Alternation cycle of the laser diodes.
Figure 3.8. Uncorrected E-S histogram for sample 1a, used to determine bursts in the donor only and acceptor only region.
Figure 3.9. Uncorrected E-S histogram for sample 1a, highlighting the donor only region ($S > 0.95$).
Figure 3.10. Uncorrected E-S histogram for sample 1a, showing the acceptor only region ($S < 0.2$).
Figure 3.11. A graph showing the extracted E and S positions of all three duplex DNA standards.
Figure 4.1. A general schematic of how digital values are obtained in detectors, including the factors; quantum efficiency, gain, dark noise and quantization noise.
Figure 4.2. A schematic of the process of converting the charge generated by electrons to obtaining a digital value.
Figure 4.3. A typical Photon Transfer Curve indicating three parts of the curve; the read noise, the photon shot noise and the fixed pattern noise (FPN). The green line shows the sum of the contributions.
Figure 4.4. The method taken for generating photon transfer curves on the Photometrics Prime 95B.
Figure 4.5. A graph showing the standard deviation in grey values against the mean signal in grey values for the Photometrics Prime 95B.
Figure 4.6. A) A cross section of the illumination pattern of pixels on the detector B) The grey values across this cross-section of the illumination pattern.
Figure 4.7. A photon transfer curves for the Hamamatsu Flash v4.0, Hamamatsu Fusion and Photometrics Prime 95B.
Figure 4.8. The signal on an sCMOS camera (Photometrics 95B) at a range of camera speeds. A background count of 120 grey counts was recognized as the main contribution to not observing fluorescent beads (0.1 μm) at high frame rates.
Figure 4.9. A maximum intensity projection of DNA paint detected on an EMCCD camera (Andor iXon) at A) 17 frames per second B) 100 frames per second.
Figure 4.10: A maximum intensity projection of DNA paint detected on an sCMOS camera (Photometrics Prime 95B) at A) 17 frames per second B) 100 frames per second.
Figure 4.11. A maximum intensity projection of DNA paint detected on an sCMOS camera (Hamamatsu Flash 4.0) at 17 frames per second.
Figure 4.12. A graph representing the Peak SNR (PSNR) of DNA Paint against the frame rates for the EM-CCD camera (Andor iXon). The PSNR was calculated by taking the maximum value of an averaged 4 pixel x 4 pixel area and dividing this value by the standard deviation of the same 4 pixel x 4 pixel area.

Figure 4.13. A graph representing the Peak SNR (PSNR) and the SNR of DNA Paint against the frame rates for the Photometrics Prime 95B. The PSNR was calculated by taking the maximum value of an averaged 4 pixel x 4 pixel area and dividing this value by the standard deviation of the same averaged 4 pixel x 4 pixel area of a background sample of water. The SNR was taken by the same method but by taking the mean of the 4 pixel x 4 pixel area instead of the maximum.

Figure 5.1. An example of a multi-spot pattern formed by the DMD and projected on a sCMOS camera where each spot is measured by a number of 'x' pixels in the x direction and a number of 'y' pixels in the y direction. The micromirrors are small enough to act as pinholes. A sample of fluorescent beads was used.

Figure 5.2. A schematic showing the setup of the Cairnfocal. The digital micromirror device reflects both in the 'on' and 'off' direction. If a multi-spot pattern is generated on the DMD the resultant multifocal structured illumination is produced.

Figure 5.3. A) A photograph showing the emission path of the Cairnfocal. The emission is directed towards detector 1. The micromirrors angle can be changed so that detector 2 observes emission too. The orange circle shows where the laser enters via an optical fibre. The laser follows the same path as the emission path to the sample.

Figure 5.4. A) Three-dimensional point spread function observed by both the illumination and emission of the Cairnfocal B) The 'tube effect' created by placing the pinhole in the emission path. Simulated 3-D Point Spread Function generated by PSFGenerator.

Figure 5.5. The lobes highlighted in white that contain most of the background signal to be rejected. Simulated 3-D Point Spread Function generated by PSFGenerator.

Figure 5.6. A schematic showing the illumination from a multi-spot pattern of the microscope and the observation (confocal) volumes. Fluorophores that are illuminated are shown in yellow and fluorophores that are not illuminated are shown in orange.

Figure 5.7. An image of the resultant z-stack showing the maximum signal of each pixel for all 255 frames at an exposure of 100 ms. A highly concentrated sample of fluorescent beads (4 μm) were imaged. The spots in this image are 10 pixels x 10 pixels in size. The spots which show fluorescent activity (a fluorescent bead has passed through them) result in white squares.

Figure 5.8. Multiple graphs showing the mean fluorescent signal of 4 μm fluorescent beads inside a 2 x 2 pixel area within 10 pixel x 10 pixel spots. This pattern was projected onto the DMD and recorded by a camera at an exposure time of 100 ms.

Figure 5.9. A simulated time trace showing centroids plotted on burst greater than a SNR of 5.

Figure 5.10. Time traces of 0.1 μm fluorescent beads in a 10 x 10 pixel spot. A) Inside the spot. The background was taken between the red dashed lines where no burst was visually observed. B) Outside the spot the background was taken of all this data.

Figure 5.11. A figure generated from MATLAB code showing the maximum z-stack signal of the image on the detector with centroids marked on areas of intensity greater than 3 pixels^2. The intensity below a grey count of 130 is coloured in purple.

Figure 5.12. This graph shows the SNR and background standard deviation with different size spots (in pixels) and a sample of 0.1 μm fluorescent beads. The SNR was calculated from the signal of the fluorescent emission inside and the background inside the spot without fluorescence emission.

Figure 5.13. A graph showing the spot size against the number of consecutive frames the fluorescent beads stayed in the spot. The exposure time of the camera was 100 ms. A linear dotted line was fit to the average number of frames and a second order polynomial was fit to the maximum number of frames.

Figure 5.14. A graph displaying the region of a 100 pixel x 100 pixel multi-spot pattern on the camera. The tracking of 0.1 μm fluorescent beads is shown in multicolour lines by TrackMate a 10 ms exposure time using the Photometrics 95B.
Figure 5.15. A mean squared displacement graph using a; A) 100 pixel x 100 pixel spot pattern B) 10 pixel x 10 pixel spot pattern C) 5 pixel x 5 pixel spot pattern. [17] A line of best fit (red) was added to the first 25% of data points.
Figure 5.16. A graph showing the maximum number of frames fluorescent beads were inside the spot against the size of the spot. Simulated time frames are based upon the Stokes-Einstein equation.
Figure 5.17. A) A picture of the red emission of dsDNA attached with ATTO 647N and ATTO 550 at an exposure of 100 ms. B) A time trace of the dsDNA with two-fold binning of pixels at an exposure of 2 ms.
Figure 5.18. A graph showing the signal from an avalanche photodiode at various concentrations of dsDNA with ATTO 550 and ATTO 647N attached.
Figure 5.19. The counts/10 ms of the whole DMD turned 'on' in sequence. Data was acquired by switching a 5 pixels^2 area on and off sequentially until the whole DMD had been on once.
Figure 6.1. A copper, round hole TEM grid. The diameter of the grid is 3.05 mm and the diameter of each hole is 35 μm.
Figure 6.2. A reflective, confocal microscope design for single-molecule fluorescence measurements. The illumination light (red) from a 647 nm laser travels through an excitation filter and the pinhole to the sample via an inverted microscope (Nikon Eclipse Ti2). The fluorescent emission (orange) travels back through the same pinhole to the detectors. A 50:50 beam splitter (BS) is placed in the emission path to direct half the emission towards an avalanche photodiode and half to the camera (Hamamatsu Flash 4.0).
Figure 6.3. A preliminary test of a bright chroma slide (Orange) against a non-fluorescent imaging buffer (Blue) on the avalanche photodiode. The avalanche photodiode binned the signal every millisecond.
Figure 6.4. A background experiment showing the signal on an avalanche photodiode with the red laser on at different power percentages. The dsDNA sample with shutter open is represented with circle symbols. The Milli-Q water sample with shutter open is represented with square symbols. Below this are both the dsDNA sample and the Milli-Q water with the shutter closed sharing the same values. Both are visible beyond 50 % compared with the shutter open experiments.
Figure 6.5. Filters in the microscope, values retrieved from the suppliers. FF02-628/40 is the excitation filter, FF02-685/40 is the emission filter and FF662-FDi01 is the dichroic mirror.
Figure 6.6. Experimental values of the filters in the microscope. FF02-628/40 is the excitation filter, FF02-685/40 is the emission filter and FF662-FDi01 is the dichroic mirror. Values measured by illuminating with a white laser. The resultant intensity after passing through the filters was recorded with a spectrometer (Ocean Optics).
Figure 6.7. A) The 647 nm laser wavelength, measured by a spectrometer (Ocean Optics) B) The 647 nm laser wavelength, with an excitation filter in front. C) The 647 nm laser wavelength with an excitation and dichroic mirror in front.
Figure 6.8. Signal on the APD with Milli-Q water in dark conditions with varying laser power. The laser was off in the dark measurement.
Figure 6.9. Signal on the APD with ATTO 647N dye in dark conditions with varying laser power.
Figure 6.10. A time trace from an ATTO 647N sample at a concentration of hundreds of picomolar measured on the avalanche photodiode over a 100 second period (right) and a zoomed in time trace of a 10 second period at the start of the experiment.

Figure 6.11. The schematic of the optical pathway of the single-molecule fluorescence microscope having removed the Nikon Eclipse Ti2 and added a z-stage piezo scanner (PS). The tube lens (L3) was changed to a focal length of 150 mm.
Figure 6.12. The signal from a picomolar concentration of dye (ATTO 647N) sample inside the pinhole spot on the Hamamatsu Flash 4.0 camera with an exposure time of 10ms and binned over 4 x 4 pixels.
Figure 6.13. The signal from a picomolar concentration of dye (ATTO 647N) sample outside the pinhole spot on the Hamamatsu Flash 4.0 camera with an exposure time of 10ms and binned over 4 x 4 pixels.
Figure 6.14. The SNR of a dilute sample of Atto647N (10pM) detected at an exposure time of 100 ms with; A) Avalanche Photodiode B) sCMOS Camera (Hamamatsu Flash 4.0).
Figure 6.15. A dilute sample of ATTO 647N (10pM) detected at an exposure time of 1 ms (without the 50:50 beam splitter in place) with; A) Avalanche Photodiode B) sCMOS Camera (Hamamatsu Flash 4.0)**.**
Figure 6.16. A repeat of a 1000 frames per second. A dilute sample of ATTO 647N (10pM) detected at an exposure time of 1 ms (without the 50:50 beam splitter in place) withan sCMOS Camera (Hamamatsu Flash 4.0)**.**
Figure 6.17. The schematic of the multi-confocal setup with the multiple pinholes (TEM grid) and the image splitter before the camera. The focal lengths of the lenses: L1- collimator, L2- 45 mm, L3- 150 mm, L4- 75 mm, L5 & L6 – inside image splitter.
Figure 6.18. Filters in the single-molecule microscope. Excitation filter – Chroma HQ525/50m, green emission filter – Omega 600BP40, red emission filter – Semrock FF01-685/40, dichroic mirror (D1) – Semrock FF545/650. Values from FPBase.
Figure 6.19. The absorption and emission spectrum of the dyes ATTO 550 and ATTO 647N. Values from FPBase.
Figure 6.20. A) The surface of the coverslip showing static bright molecules B) The surface of the coverslip observed with the TEM grid placed at the focal length of the tube lens.
Figure 6.21. Time traces of a sample of 0.1 μm TetraSpeck Microspheres (ThermoFisher) recorded with the Hamamatsu Flash 4.0 at an exposure time of 10 ms A) Max z-stack images of fluorescent beads without the TEM grid (left) with the TEM grid (right) B) An image at a peak signal at 5000 ms into the image without the TEM grid (left) and with the TEM grid (right) C) Time traces of an average of 5 x 5 pixels shown in the yellow boxes without the TEM grid (left) and with the TEM grid (right).
Figure 6.22. A) An image of the mask (TEM Grid) in the green channel of the camera B) A max z-stack of the acquisition of a low FRET dsDNA sample (10 pM) taken with the Hamamatsu Flash 4.0 and the TEM grid in place at an exposure time of 1ms C) Three time traces of the corresponding colour coded boxes (3 x 3 pixels average) at a camera exposure time of 1 ms.
Figure 6.23. A maximum intensity projection (z-stack) of the fluorescent emission in the green (left) and red (right) emission channel at different stages of the acquisition. During the acquisition the axial position of the objective was increased to focus on the red emission and then the green emission. The fluorescence emission in the green channel is from the dye ATTO 550 and the fluorescence emission on the right from the ATTO 647N dye (FRET). A) the axial position of the objective focusing on the red emission at the start of the acquisition. B) the axial position of the objective focusing on the green emission at the end of the acquisition.
Figure 6.24. The optimized image splitter showing an additional achromatic lens (focal length 10,000 mm) added.
Figure 6.25. A graph representing the z-drift of the microscope in the green channel. The maximum signal of the whole image was recorded and left untouched. The dashed line shows

the time at which the microscope was refocused. A z-stack image above the graph shows the molecules that were observed consistent with the time of the graph.
Figure 6.26. Multiple time traces of fluorescent emission in the green channel at 50pM (blue) and at 5000 pM (beige). A 3 x 3 pixel average was selected for single-molecules present in both acquisitions and conditions were the same except for the concentration.
Figure 6.27. A) An average z-stack of the TEM grids in both the green emission channel (left) and red emission channel (right) used to subtract as the background. B) The area of the TEM grid imaged for the following acquisitions so that low exposure times could be taken. C-E) Acquisitions were taken at 30 ms with the Hamamatsu Flash 4.0 and a high FRET dsDNA sample concentration of 50 pM. The background of the TEM grid was subtracted so cannot be seen. C) Combined green and red emission channel showing green single-molecules observed. D) Combined green and red emission channel showing red (FRET) single-molecules observed. E) Combined green and red emission channel showing FRET signal (yellow) observed when there is an overlap of red and green emission.
Figure 6.28. A time trace of both the green and red molecules in a single 'spot' at an exposure time of 30 ms.
Figure 6.29. A picture of the multi-spot pattern out of alignment using the iSMS software. These spots were put into alignment by matching the two regions of interest (left). The combined fluorescent emission was combined, and the spots were matched (right). Here we show the spots unmatched for demonstration.
Figure 6.30. A time trace of one of the spots in the multi-spot pattern using the iSMS software at a camera exposure time of 30 ms.
Figure 6.31. A FRET Histogram showing the FRET efficiency when a high FRET sample of ds DNA was placed on the microscope and analysed with iSMS. This was recorded at an exposure time of 30 ms for a time of 2.5 minutes on 25 spots. In comparison to the excitation module on the smfBox with the same sample recording for 1 hour.
Figure 6.32. Time traces for the low FRET sample inside four spots at an exposure time of 1 ms in the green emission channel (green, top) and the red emission channel (red, bottom). B) A FRET Efficiency histogram of the low FRET sample recorded at an exposure time of 1 ms and measured for 10 seconds inside 25 spots C) A FRET Efficiency histogram of the high FRET sample recorded at an exposure time of 1 ms and measured for 20 seconds inside 25 spots.
Figure 6.33. Images of TetraSpeck™ Microspheres (0.1 μm) taken separately without the TEM grid in place. In the green box, an image of this sample in the green emission channel with green laser illumination. In the red box an image of this sample in the red emission channel with red laser illumination.
Figure 6.34. The FRET efficiency histograms of dsDNA samples used in this chapter recorded on the smfBox. A) Low FRET dsDNA sample B) Medium FRET dsDNA sample C) High FRET dsDNA sample.
Figure 6.35. Initial change point analysis performed on a single-molecule dataset. The blue areas show detected events, and the red area shows areas where the analysis revealed no significant changes. This time trace was recorded with the Hamamtsu Flash 4.0 at an exposure time of 1 ms with a 100 μm pinhole in place.
Figure 6.36. The change point analysis performed after increasing the penalty on a single-molecule dataset. The blue area shows detected events, and the red area shows areas where the analysis revealed no significant changes. This time trace was recorded with the Hamamatsu Flash 4.0 at an exposure time of 1 ms with a 100 μm pinhole in place.
Figure 6.37. A) A simulation of single-molecule trajectories. Each track represents the location of the molecule in time from a starting point at the centre. The circle represents the detection volume, showing that in this acquisition no molecules entered. B) Simulation of

time traces of four single-molecules that entered the 3D array in the central circle of the 3D array.
Figure 6.38. Principal Component Analysis of a simulation of four molecules diffusing in a 3D array (blue) compared to four background only datasets (red).
Figure 6.39. Simulation of time traces of single-molecules with a decreased detection area and a read noise and photon shot noise based on an sCMOS camera (Hamamatsu Flash 4.0).
Figure 6.40. A PCA plot on multiple images of simulated single-molecule data based off the optical system in this chapter. Time traces containing single-molecule events (blue) and time traces containing only background (red) are shown.
Figure 6.41. Experimental time traces of single-molecule data and principal component analysis plots A) time traces of two background measurements B) Time traces of one background measurement and one measurement containing single-molecule events. The sample was a low FRET dsDNA sample (10 pM) recorded at an exposure time of 1 ms with the Hamamatsu Flash 4.0.
Figure 6.42. Timeline of the experiments (dark blue), problems (green) and components (light blue) added to the setup.

List of Tables

Table 1.1. A list of common smFRET dyes their excitation, emission, brightness and photostability displayed. The brightness shows the intensity of the donor dyes compared with Cy3 and the acceptor dyes compared with Cy5. Reprinted by permission from Nature Methods : Springer Nature, A practical guide to single-molecule FRET by Rahul Roy et al, Copyright Clearance Center (2008).
Table 1.2. A table showing detectors used for fluorescence and additionally the advantages and disadvantages of them.
Table 2.1. A table comprising of all the parts used inside of the excitation module.
Table 2.2. The parts contained in the middle section of the microscope.
Tables 2.3. The parts contained in one APD box in the emission module of the microscope.
Tables 2.4. The parts contained in the full emission module of the microscope.
Table 3.1. Common fluorescent applications, their excitation system requirements and primary expense.
Table 3.2. A list of current open-source laser excitation modules; their properties and their primary application.
Table 3.3. Comparison of the excitation module to literature values.
Table 3.4. Accurate FRET standards used in the previous studies. Highlighted base pairs in red (acceptor) are labelled with ATTO 647N and the base pairs in green are labelled with ATTO 550. Biotin was also labelled for surface immobilisation for TIRF experiments, which were not used in this study.
Table 3.5. List of all the parts (all from Thorlabs unless stated otherwise).
Table 3.6. A table showing the mean half-life and R squared values of the commercially available (Omicron laser system) rise and fall times for both the green and red laser. These values were determined by using the mean of multiple test runs.
Table 3.7. A table showing the mean half-life and R squared values of the excitation module rise and fall times for both the green and red laser. These values were determined by using the mean of multiple test runs.
Table 3.8. FRET Efficiency values for the samples; 1a, 1b and 1c.
Table 3.9. FCS data acquired from the MATLAB package PAM.

Chapter 1. Introduction

1. Introduction

High-throughput screening has revolutionized the early drug discovery process in the last few decades. This practice consists of scanning large databases of compounds on target molecules with the hope of detecting a desired interaction. Samples that are above a 'hit threshold' are transferred into the next phase of the drug discovery pipeline, to be examined in closer detail. Screening began in the late 1980's, primarily due to the emergence of large chemical libraries and new synthetic techniques such as combinatorial chemistry and automated synthesis. [1] Driven by a desire to identify drugs with specific targets more efficiently, pharmaceutical companies have advanced screening capability to allow 100,000 samples a day to be investigated. [2],[3]

One method used in screening is Förster Resonance Energy Transfer (FRET), a non-radiative mechanism that describes the energy transfer between two fluorescent molecules in proximity. This technique has been used in high-throughput screening for over 20 years. [1] Assays based on energy transfer can measure distance changes when ligands bind to target macromolecules and induce a conformational change – an important benefit over other techniques. FRET can measure distances between biological molecules as low as 1 nm and as high as 10 nm with precision. [4] Moreover, FRET can measure a range of dynamics and can identify fast conformational changes in biomolecules.

However, conventional FRET measures an 'ensemble population' of molecules. This means only the average FRET arising from all the different conformations of the molecules present is measured. This removes the possibility of observing rare populations in a heterogeneous sample, those molecules that differ from the observed average conformation. Single-molecule FRET (smFRET) overcomes this problem by measuring one molecule at any given time. As a

result, visualization of a spread of conformations of the molecules is observed and the dynamics of individual molecules can be determined. While measuring single-molecules provides much more information about the sample, sampling at low concentrations to achieve this impedes the collection of a large dataset of smFRET events, commonly called ‘bursts’, required for statistical analysis. [5] To add to this problem, smFRET measurements require expensive instruments, and the area has lacked in open-source hardware and software making it difficult for researchers to carry out these experiments.

This research intends to increase the uptake of single-molecule fluorescent methods by designing affordable open-source and commercial instrumentation, bypassing the challenges researchers face when building their own systems. We also aim to deliver a high-throughput single-molecule system capable of identifying tightly-bound drugs. A successful high-throughput smFRET system would be capable of detecting rare populations and single-molecule events, identifying conformational changes in target proteins, possibly revealing cryptic binding sites for drugs, and observing fluctuations due to changes in environmental conditions (e.g., pH and concentration). The system would also tackle the challenge of measuring a statistically significant number of events in short time periods. Furthermore, the system would be able to determine target-ligand interactions with high affinity, advancing the field of drug discovery.

To achieve an affordable single-molecule microscope we need to first assess if the current components and optics available could make an optical system that is sufficiently affordable. In addition, whether these affordable parts compromise the performance of the system. We also aim to address the question of whether a high-throughput smFRET microscope is possible and if single-molecules can be imaged at high speeds to capture their biomolecular dynamics. In

this regard, one of our goals is to measure the performance of the latest modern cameras and use data analysis techniques to locate and simultaneously measure multiple single-molecules.

1.1 Förster Resonance Energy Transfer (FRET) Theory, Applications and Limitations

1.1.1 Förster Resonance Energy Transfer (FRET)

Förster Resonance Energy Transfer (FRET) provides information about the dynamics, conformations, and structure of biological molecules. This energy transfer occurs between a donor fluorophore and an acceptor chromophore that have permanent dipoles. This technique has been used to unravel new molecular mechanisms in a broad area of research including; protein folding, RNA folding, DNA maintenance, repair, replication, transcription and translation, enzymatic function, nucleic acids and membrane transport. [6]–[16] Acting as a "spectroscopic ruler", FRET can measure distances between fluorophores as low as 1nm and as high as 10nm. [4] Alternatives such as X-ray Crystallography, Nuclear Magnetic Resonance (NMR) spectroscopy and cryo-Electron Microscopy (cryo-EM) also offer a understanding of biomolecular interactions. [16] However, these techniques often provide only a static "snapshot" of single molecules, whereas, FRET provides dynamic measurements. [16] Fluorescence occurs from the absorption of photons that promote an electron from the singlet ground state to the singlet excited state. [17] As the excited molecule returns to the ground state, a photon of a longer wavelength than the absorbed photon, is emitted. FRET occurs when an excited fluorophore, commonly known as the donor, is in proximity of an 'acceptor' fluorophore as shown in Figure 1.1.

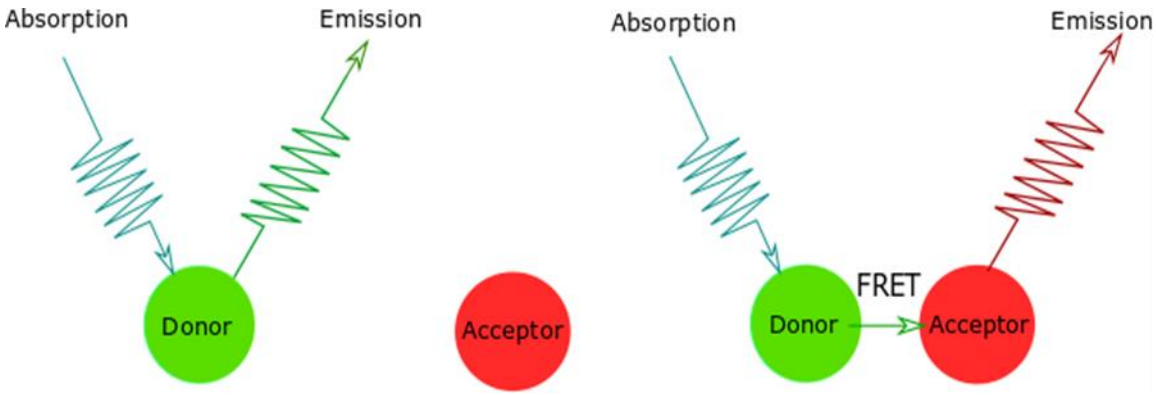

Figure 1.1. A schematic showing the occurrence of FRET with two fluorophores; the donor and acceptor. In the first instance, the donor absorbs and emits the emission because the acceptor is not close enough. In the second instance, the donor and acceptor are close enough for FRET to occur.

For FRET to occur the absorption band of the acceptor must overlap with the emission band of the donor. A light source, commonly a laser, illuminates the sample and excites the donor into a higher electronic state (Figure 1.2). If the oscillation of the excited donor coherence is resonant with the ground state electronic energy gap of the acceptor, energy will be transferred to the acceptor. Subsequently, this leads to the vibrational relaxation of the acceptor and fluorescence that is spectrally shifted from the donor fluorescence. [18]

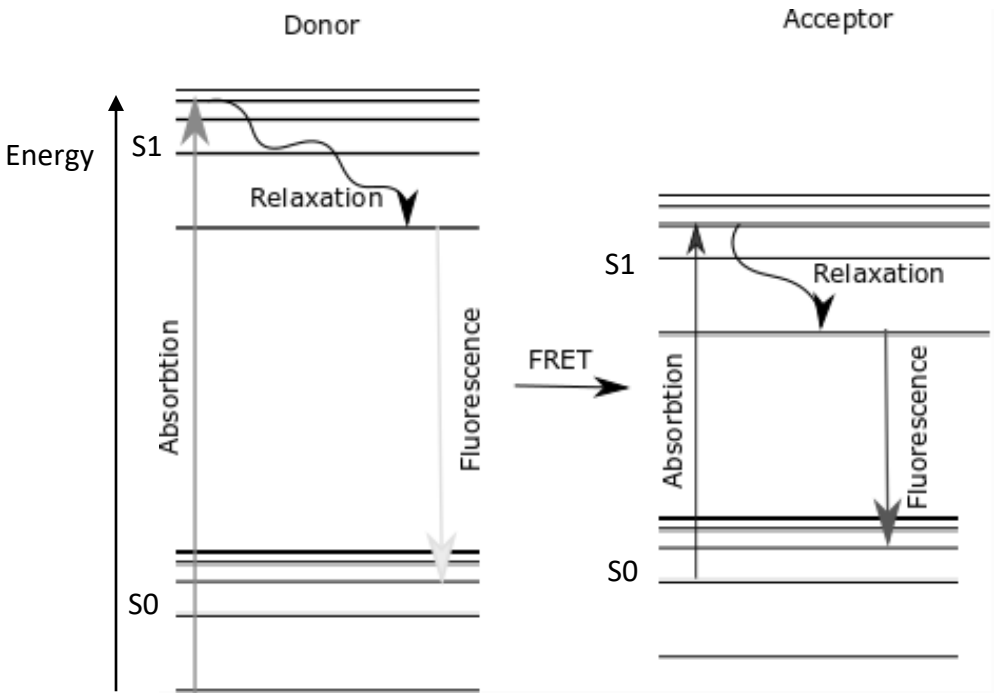

Figure 1.2. A Jablonski diagram showing the energy levels of the acceptor and donor molecules when FRET occurs.

1.1.2 The Theory of FRET

When two fluorophores are in proximity to each other, there is a possibility that FRET can occur. As a result, the excited donor fluorophore transfers energy to the acceptor fluorophore via a non-radiative dipole-dipole interaction. However, this only arises when the emission spectrum of the donor and the absorption spectrum of the acceptor fluorophores overlap. The efficiency of FRET (E_{FRET}) is strongly dependent on the distance between both fluorophores and is shown in Equation 1.1: [19]

$$E_{FRET} = \frac{1}{1+(r/R_0)^6} . \qquad (1.1)$$

The distance between donor and acceptor fluorophore is stated as r and the Förster distance, R_0 (the distance at which the energy transfer efficiency is 50%), which is dependent on the fluorophores chosen, is given in Equation 1.2: [20]

$$\mathrm{R_0} = \frac{9000(\ln 10)\mathrm{Q_D}\kappa^2\mathrm{J}(\lambda)}{128\pi^5\mathrm{N}n^4}. \qquad (1.2)$$

To obtain the Förster distance, the quantum yield of the donor in the absence of the acceptor (Q_D) is required. The orientation factor (κ^2) conveys the orientation of the fluorophores relative to each other. This is generally difficult to determine. However, it has been shown for dyes labelled using linkers, κ^2 is approximated to the value of 2/3, assuming random orientation of the acceptor and donor dipoles. [21] The overlap integral ($J(\lambda)$) signifies the degree of overlap between the absorption spectrum of the acceptor and the emission spectrum of the donor. Additionally, Avogadro's number (N) and the refractive index (n) in the medium are required. Equation 1.1 shows the strong dependence of distance between the fluorophores ($(r/R_0)^6$) on FRET efficiency and that a high spectral overlap, high quantum yield and a low refractive index is key to achieving a high Förster distance. The efficiency of FRET measured by the microscope, commonly called the apparent FRET efficiency ($\mathrm{E_{app}}$), is obtained from the measured intensities of the fluorophores shown in Equation 1.3:

$$\mathrm{E_{app}} = \frac{\mathrm{I_A}}{\mathrm{I_A} + \mathrm{I_D}}. \qquad (1.3)$$

Here, I_A and I_D are the measurable intensities of the acceptor and donor, respectively. In practice, the apparent FRET efficiency obtained by this approach usually differs from the FRET efficiency achieved in Equation 1.1. This is primarily due to experimental limitations of

the instrument and photophysical effects. [22] Two of the main sources contributing to this disagreement are compensated for in Equation 1.4:

$$E_{FRET} = \frac{I_A - \beta I_D}{I_A + (\gamma - \beta) I_D}. \quad (1.4)$$

In this equation, the parameter β corrects for the fluorescent leakage of donor emission in the acceptor channel. This occurs due to the broad emission of the donor, meaning that a fraction of the emission occurs at wavelengths that pass through the dichroic mirror rather than being reflected. Additionally, the parameter γ corrects for the different detection efficiency of the two dyes. Both parameters can be obtained experimentally and can be used to measure the corrected FRET efficiency.

Fluorescent lifetimes of fluorophores can provide an alternative way of measuring the FRET efficiency. In this case, a pulsed laser is used to find the lag time between the absorption of excited light of the fluorophore and its respective emission. A decay constant from the exponential fit can then be calculated. The FRET efficiency is then calculated using Equation 1.5: [23]

$$E_{FRET} = 1 - \frac{\tau_{DA}}{\tau_D}. \quad (1.5)$$

Here, τ_{DA} and τ_D are the decay constants of the donor in the presence of the acceptor, and the donor only, respectively. One advantage of this approach over detecting changes in the intensity of donor and acceptor emission is that it provides a way of distinguishing between free and bound donor molecules. [24]

1.1.3 Ensemble and Single-molecule methods

Ensemble methods measure all of the molecules in the sample volume at once. Ensemble methods include; FRET, nuclear magnetic resonance (NMR), and fluorescence anisotropy. These methods can still offer a great deal of insight into the dynamics of molecules. [16] In fact, measuring FRET at the ensemble level with fast-mixing devices can measure rates of conformational changes and binding (or dissociation) events under pre-equilibrium conditions. [6] However, the conformational changes in molecules in an ensemble occur asynchronously. This means different conformations are present at any given time in the bulk volume leading to a weighted average signal of the bulk sample shown in Figure 1.3. [16]

Single-molecule FRET (smFRET) is one of the most notable advances in the history of FRET. As described above, this technique allows the measurement of individual molecules, providing key information about different biomolecular conformations and the distribution of these. An example of using smFRET is the study of the enzyme adenylate kinase by Henzler-Wildman *et al.* [25] Before this study, adenylate kinase was thought to have a single conformational state. This was due to a broad distance distribution in the absence of its substrates. [16] Single-molecule FRET studies found that two conformations existed, and significantly, only one of them actively catalysed the substrates.

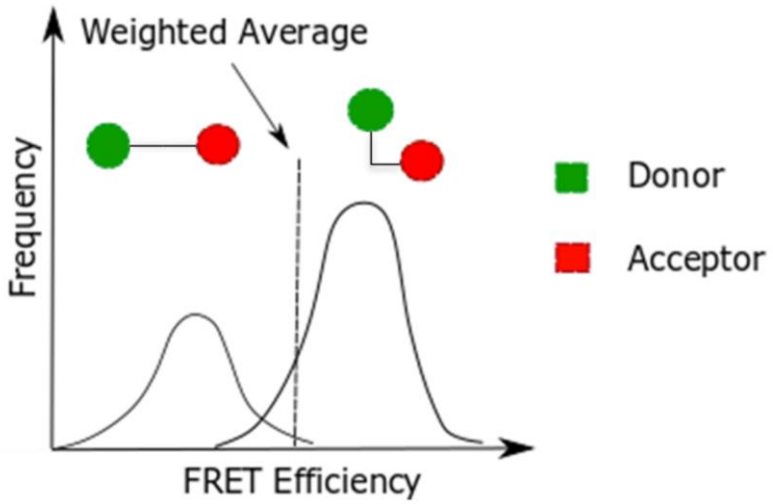

Figure 1.3. A schematic of the FRET efficiency against the frequency observed in an example smFRET experiment showing the resultant weighted (ensemble) average that would be obtained from a FRET experiment. An smFRET experiment would be able to distinguish between these two conformations.

Single-molecule methods can provide information on the heterogeneity and identification of multiple molecular populations. [26] Single-molecules are studied at very low concentrations, as only one molecule in the confocal volume is required. More concentrated solutions risk having more than one molecule in the confocal volume resulting in the measurement of an average conformational state. Since smFRET experiments only measure one molecule at a time, to reach a statistically relevant dataset, more single-molecule events need to be collected. Consequently, smFRET experiments are typically long, time-consuming processes that require careful preparation. Therefore, there is a strong demand to combine single-molecule techniques such as smFRET with a high-throughput system to increase the speed at which measurements are taken and so increase the precision of the overall measurements.

1.1.4 Applications of Single-Molecule FRET

1.1.4.1 Conformational states and dynamics

Generally, there are two formats of dynamic single molecule FRET experiments. One capable of interrogating slow conformational dynamics and the other more suited to fast conformational

dynamics. For molecules that exhibit slow conformational transitions (on the order 0.1 – 10 s), longer observation times are required. [27] In such cases, immobilized molecules are commonly used as they can be observed for an extended period of time. [16] Both the dynamics and the different FRET states can be extracted by Total Internal Reflection Fluorescence (TIRF) microscopy experiments described later in this chapter.

On the other hand, fast conformational dynamics (occurring on the order of 10 μs to 0.1 s) are usually measured using diffusion-based smFRET. [16] Studying the fluctuations in the FRET efficiency of single molecule events enables the dynamics of these molecules to be extracted. Problems arise if the molecule changes conformation within the observational volume. This can lead to a time-averaged FRET efficiency and suggests that the molecule may be exhibiting faster conformational dynamics than the timeline defined by the experimental setup. [28]-[29] In these circumstances, photon statistics of FRET efficiencies within each burst (single-molecule event) are required. [16]

1.1.4.2 Structure Determination

An important feature of smFRET is the ability to determine structures of biomolecules. One of the first applications was the study of a four- stranded DNA complex called the 'Holliday Junction'. [30] The Holliday junction is an intermediate in homologous recombination, a DNA repair mechanism commonly associated with double strand breaks. In the absence of magnesium, the four DNA strands adopt a structure whereby each strand points to four corners of a square shown in Figure 1.4.

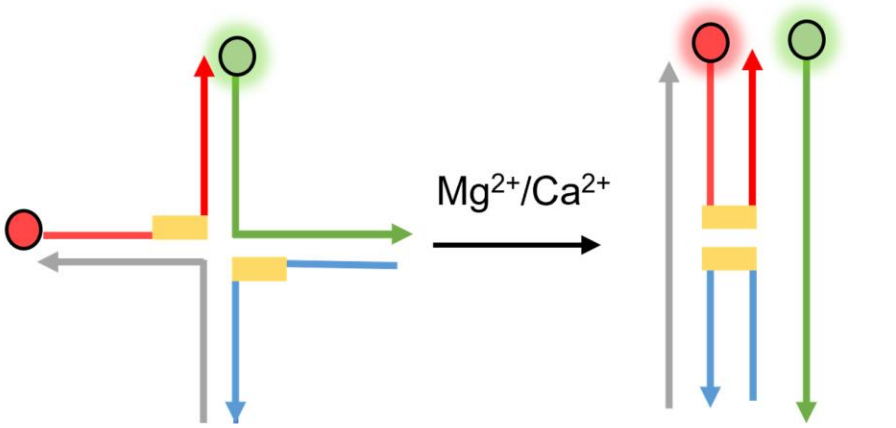

Figure 1.4. A schematic showing the Holliday Junction and the dyes attached for smFRET measurements. The yellow rectangles represent homologous regions capable of branch migration. The diagram shows that after magnesium or calcium presence, migration occurs and high FRET is detected. [30]

In the presence of magnesium, the structure adopted a compact stacked 'X' shaped structure. [30] In this study, three-colour smFRET confirmed this hypothesis of the changed conformation when magnesium was present.

1.1.5 Limitations of smFRET

Although approximately 10^5 - 10^6 photons are emitted by a fluorophore per second, due to limitations in microscopy, only a maximum of 10-15% of these are detected. [23],[31] Since smFRET relies heavily on sensitive fluctuations of the acceptor and donor signals, the signal-to-noise ratio (SNR) is paramount in obtaining accurate smFRET data. A high SNR gives confidence that the signal measured is significant. Additionally, to accurately measure distances within biological molecules, it is very important to attach the fluorophore to a precise target site. This is challenging, particularly in biological molecules such as proteins due to the sheer number of potential labelling sites. The photobleaching of dyes amplifies this problem. Photobleaching occurs when the covalent bonds or non-specific reactions between the fluorophore and the surrounding molecule are cleaved during illumination, lowering the SNR.

Although improvements have been made in developing more robust organic dyes, photobleaching remains a constraining factor on the maximal observation time and temporal resolution. [32]

Previously, a limitation of smFRET was that it could not distinguish between donor-only molecules and a low FRET species within the same sample. [33] Introduction of the Microsecond Alternated Laser Excitation (usALEX) resolved this issue. Alternating two lasers of different wavelengths on and off every 45 microseconds can help distinguish between donor-only and low FRET species. Since the same molecule will be subjected to both lasers in quick succession, a biomolecule with only a donor can be identified: If the donor laser excites the molecule and we detect donor emission, we know that the molecule must have a donor dye attached. However, if we then excite the molecule with the acceptor laser and do not detect acceptor emission, we can deduce that there is only a donor dye present. A stoichiometry ratio (S) can be calculated and is shown in Equation 1.6:

$$S = \frac{\Lambda}{\Lambda + F_{A_{ex}A_{Em}}}. \qquad (1.6)$$

Here *S* represents the stoichiometry ratio, Λ is the total signal and $F_{A_{ex}A_{Em}}$ is the fluorescence of the emitted intensity of the acceptor when the laser excites the acceptor. For a donor only molecule, $F_{A_{ex}A_{Em}} = 0$, therefore $S = 1$. Whereas, for a low FRET species $F_{A_{ex}A_{Em}} > 0$, therefore $S < 1$. In this case, the stoichiometry ratio is usually situated around 0.5. Figure 1.5 illustrates this separation as a graph of Stoichiometry against FRET efficiency. Acceptor only molecules will exhibit a stoichiometry close to zero.

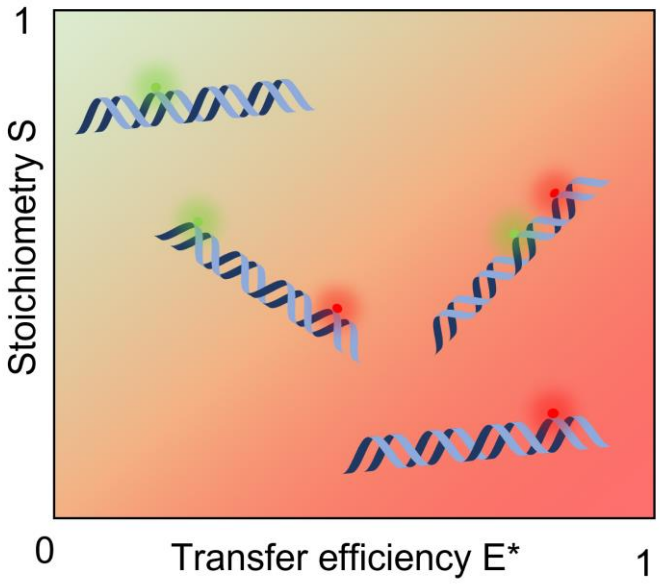

Figure 1.5. An illustration of the stoichiometry against the transfer efficiency (FRET efficiency) distinguishing between the donor only molecule and the low FRET molecule. [34]

1.2 Single-Molecule FRET – System Selection

1.2.1 Achieving FRET measurements

Single-molecule FRET experiments are very sensitive, requiring well-thought-out methodology. A very good starting point is presented in 'A Practical Guide to Single molecule FRET' review from Ha *et al.* [35] This review states that the ideal fluorophore should:

- be bright (extinction coefficient, ε > 50,000 $M^{-1}cm^{-1}$ and a quantum yield > 0.1)
- be photostable
- have minimum photophysical, chemical and aggregation effects
- be small
- be water soluble
- have an associated multitude of bioconjugation chemistry

Additionally, the ideal smFRET pair should:

- have a large spectral overlap between donor and acceptor emissions
- have similar quantum yields and detection efficiencies between the donor and acceptor

In the past, fluorescent proteins have been used for smFRET experiments. [36] However, they lack photostability and are prone to photo induced blinking. This occurs when the fluorescent molecule jumps between “dark” and “bright” states upon laser excitation. Alternatively, quantum dots combined with a suppression of their chemical blinking (random fluctuations of emission) have also been used. [37]–[39] However, the use of photostable, quantum dots is challenging due to their large size (>20 nm in diameter) and lack the monovalent conjugation needed to bind to biomolecules. [35] The yield of the NHS reaction, used for attaching the quantum dots, is low due to steric hindrance from surface bound polyethylene glycol (PEG) groups and off-target effects. This makes it difficult to deliver quantum dots on the amines needed for bioimaging. [40] As a result, organic dyes have been favoured for single-molecule studies due to their small size (smaller than one hundredth the size of fluorescent proteins and quantum dots). [41] The most common FRET pairs in the range of 500-700 nm are Cyanine, Alexa- and Atto-dyes, which are from the Cyanine, Oxazine and Rhodamine family of dyes, respectively. [35],[42] These are listed below in Table 1.1. [35] As shown, the dyes ATTO 647N and ATTO 550 are the brightest and were selected for this project. Although these dyes do not achieve the highest photostability in the table, since the detection and illumination volumes are small in confocal smFRET experiments (described later), there are always molecules present in the solution to detect. Also, since all molecules in the sample exhibit the same range of conformations, there are no issues involved with the absence of molecules that have photobleached.

Dye	Excitation λ_{max} (nm)	Emission λ_{max} (nm)	Brightness	Photostability (s) (in Trolox/βME)
Donors				
Cy3	550	565	1.0	91/50
ATTO550	554	577	1.9	72/27
Alexa555	555	567	0.8	65/35
Acceptors				
Cy5	655	667	1.0	82/25
ATTO647N	644	664	1.3	62/31
Alexa647	650	667	1.2	58/20

Table 1.1. A list of common smFRET dyes their excitation, emission, brightness and photostability displayed. The brightness shows the intensity of the donor dyes compared with Cy3 and the acceptor dyes compared with Cy5. Reprinted by permission from *Nature Methods : Springer Nature*, A practical guide to single-molecule FRET by Rahul Roy et al, Copyright Clearance Center (2008). [35]

1.2.2 Experimental design and hardware

At present, there are two common types of experimental setups that measure smFRET. The first spectroscopy technique is confocal microscopy. Confocal microscopy uses a pinhole to collect light from a defined volume in the sample. This ultimately blocks out of focus light above and below the observation volume and allows the formation of an image only at one, narrow depth in the sample. The second technique is Total Internal Reflection Fluorescence microscopy (TIRF). TIRF illuminates the surface of the glass slide with an evanescent wave creating an image of a thin region (~100 nm) where the sample is in contact with the glass slide. [23] Both of these techniques are shown in Figure 1.6.

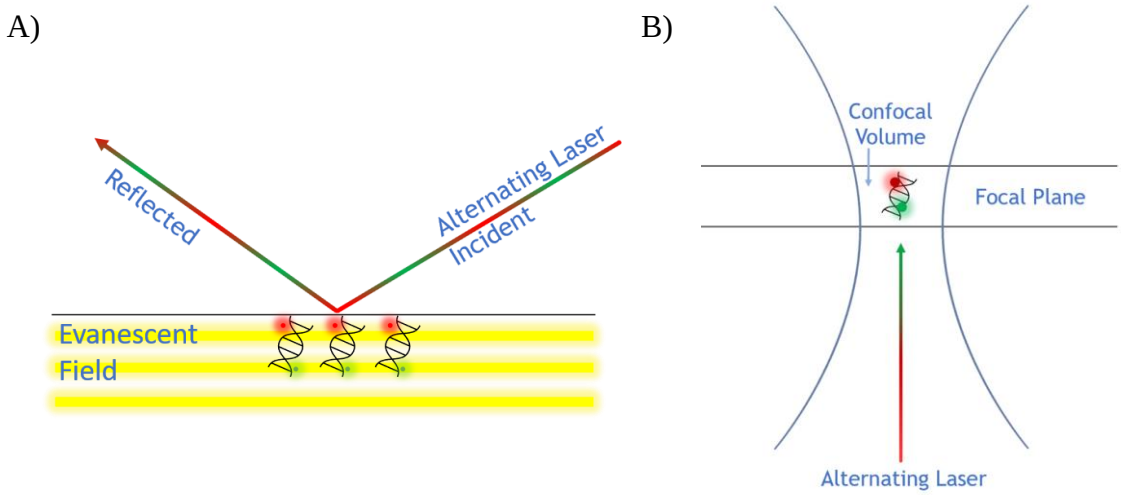

Figure 1.6. Illustration two microscopy techniques at the sample that improve the SNR by rejecting out of focus fluorophores. A) TIRF Microscopy illuminates the first 100 nm above the coverslip and does not illuminate fluorophores above this B) Confocal Microscopy illuminates a small spot at the sample and the observation volume is only at the focal plane, rejecting out of focus fluorophores.

The benefits of using confocal microscopy include being able to image beyond 100 nm between the coverslip and glass slide, the ability to create image slices (z-stacks) of the sample and achieving a high SNR due to the rejection of out of focus light. However, confocal microscopy commonly suffers from high power laser irradiation, which can damage the sample. In contrast, TIRF provides a high SNR by reducing background fluorescence above the illumination area at the surface. [23] One advantage of TIRF is that immobilized molecules on the surface of the glass slide can be analysed and can be imaged in combination with a camera.

For both techniques, to measure the fluorescence signal from the sample, the laser beam must travel through the objective lens to illuminate the sample. In confocal microscopy this laser beam travels through the centre of the objective lens. In TIRF microscopy, the laser beam travels through one side of the objective lens shown in Figure 1.7.

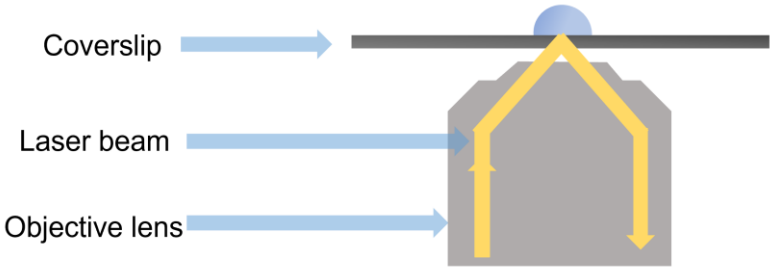

Figure 1.7. The laser beam excitation path in objective TIRF.

The fluorescent signal from the sample then travels back through the objective and is separated from the excitation laser beam by a dichroic mirror. Another dichroic mirror is commonly used to split the acceptor and donor signals and image them on one or two Avalanche Photodiodes (APDs) or cameras. A three-colour smFRET setup splits the acceptor signal with an additional dichroic mirror into two further signals, which are then detected. [35] A recent technique called 'Light sheet fluorescence microscopy', which provides a reduced background signal, similar to TIRF microscopy, is also of interest. This technique illuminates a thin slice of the sample perpendicular to the direction of observation. This reduces photobleaching of the sample, unlike confocal microscopy, which illuminates the whole sample but rejects the light that does not pass through the pinhole. However, due to the requirement of multiple objective lenses and the past implementation of a well understood and working confocal setup, this approach will not be used. Since single-molecule TIRF measurements do not provide a significant gain in SNR compared with confocal microscopy and require increased sample manipulation to optimise surface immobilization, in this project confocal microscopy was chosen. In addition, since low laser powers are commonly used for confocal smFRET, photobleaching would not be an issue.

Much of this study has been inspired by the smfBox shown in Figure 1.8. [43] The smfBox is a confocal microscope based around one pinhole in the emission pathway. In this setup the excitation source is a laser beam that is directed by two mirrors (M1 and M2) through a beamsplitter (BS1) onto the back aperture of the objective lens (O1). An iris cuts this beam size down to a 5 mm diameter to achieve a larger excitation spot.

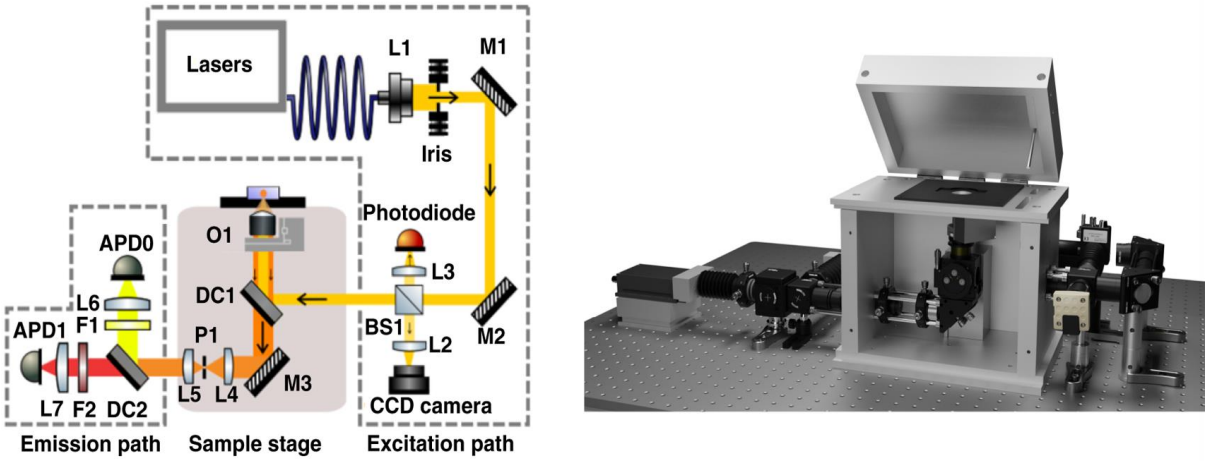

Figure 1.8. The smfBox and the optical setup pathway. Figure reproduced from Ambrose et al. [43]

The pinhole (P1) lies in the emission path of the microscope after the fluorescence emission passes through the dichroic mirror (DC1). A lens (L4) focusses the emission through the pinhole and a lens after (L5) collimates the light. A dichroic mirror (DC2) then splits the emission light which is focused by two lenses (L6 and L7) into green and red light onto two avalanche photodiodes (APD0 and APD1) after passing through emission filters (F1 and F2). These detectors are capable of counting photons on the nanosecond timescale, which makes this system optimal for detecting biomolecules with fast conformational dynamics.

The high-throughput smFRET system will need to use the principles of confocal microscopy to maximize the SNR and to measure freely diffusing biomolecules at high speeds. For this reason, combined with the smfBox availability to calibrate samples before experiments, a

confocal-based setup will be used. However, the approach we took differs slightly by placing the pinhole in both the illumination and emission pathways, similar to structured illumination and spinning disk microscopy. [44] Here, we will benefit from multiple illumination and observation volumes to the conformations of molecules simultaneously.

1.3 The road to high-throughput smFRET

At present, drug discovery proceeds by measuring the affinity of drug-ligand interactions. For screening large libraries of small molecules at a fast rate, high-throughput ensemble techniques are employed. [16] Many of these techniques screen over 10,000 samples a day, either quantifying drug-ligand affinity on the bulk sample, or on immobilized molecules using surface plasmon resonance (SPR). [16],[45] Previously, diffusion-based smFRET has been well documented as a low throughput method with long acquisition times. [45] However, advances in the development of high-throughput single-molecule systems have made improvements in the rate of measurements down to hundreds of milliseconds per molecule feasible. [46] Furthermore, as a result of shorter acquisition times, a reduction in sample degradation and setup drift can be achieved. [5] Recently, Kim *et al* used automated titration and a microfluidic mixing device to measure smFRET in different conditions. [47] Ingargiola *et al* used a multi-colour and multi-spot method. Here they were able to measure smFRET of doubly labelled double-stranded DNA oligonucleotides simultaneously in 48 spots. [33] In this study, they used a liquid crystal on silicon (LCOS) spatial light modulator to reflect the light in a pattern and align it onto SPAD arrays. This would reduce these experiments to 2-5 minutes per sample.

These advances have progressed the smFRET field. Yet, increasing the speed of acquisition by 48-fold remains far from ideal to facilitate fast rates of high-throughput screening in drug discovery. This thesis lays out methods of generating a larger multi-spot pattern which we expect will further increase the rate of measurements. Our aim is then to explore whether we

can increase the throughput of smFRET experiments by using more multiple observation volumes (spots).

1.3.1 Generating a multi-spot pattern

The first method to generate a multi-spot pattern is by using a Digital Micromirror Device (DMD). This device is a type of spatial light modulator (SLM) that reflects light via a multitude of micromirrors. This enables the segregation of the image by size and allows a multi-spot pattern to be generated by a program. These switchable micromirrors are set at angles of either -12 degrees or +12 degrees and are situated on a complementary metal oxide-semiconductor (CMOS) board shown in Figure 1.9. [48]

A)

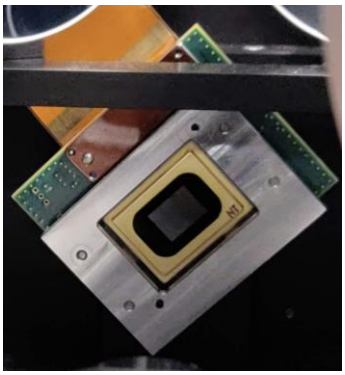

B)

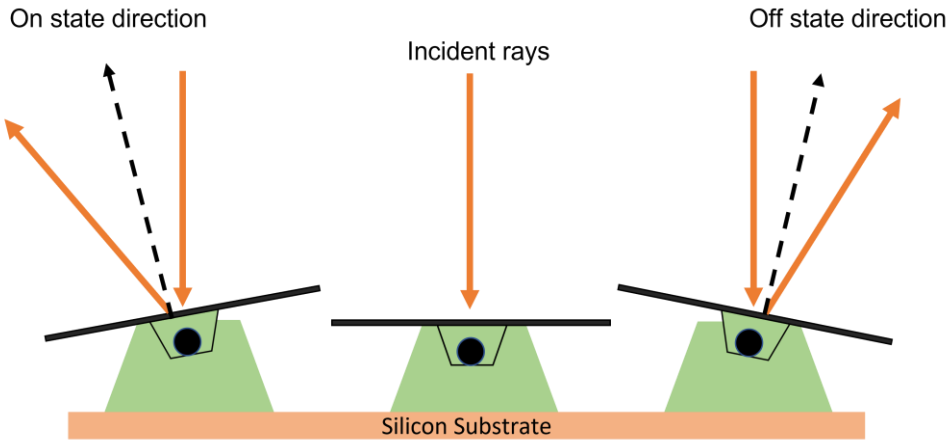

Figure 1.9. A) A photograph of the digital micromirror chip used in this project. B) An illustration of the different ways the digital micromirror device can reflect incident rays.

A Binary program, uploaded onto the DMD via a computer, can switch each micromirror on the DMD to an ‘on’ or ‘off’ state. Therefore, each of these micromirrors can reflect an illumination in the form of a pattern, controlled by a computer, towards the detector. Widely studied applications of the DMD include laser beam shaping, wavefront distortion and high-resolution microscopy. They have also been used in televisions and digital light processing projectors. Digital micromirrors were chosen for this project because they offer a fast way to pattern light from an illumination source onto the sample and improve the SNR. [49] They have been used in this field as a method for structured illumination microscopy (SIM) as it reduces out of focus light and improves the resolution. SIM is based on a known excitation pattern combined with the generation of interference patterns known as the Moiré effect. [50] In this technique different images are acquired and after deconvolving an interference signal, a super-resolution image is created. However, in this project, the resolution does not affect the result of smFRET efficiencies and so we will use the principles of SIM only for its improved SNR capability.

Importantly, these DMDs can generate a 1000+ multi-spot pattern shown in Figure 1.10. Each spot corresponds to a discrete size in the x and y axis in pixels. Since each spot generates a confocal volume as mentioned previously, it rejects out-of-focus light. A high-powered laser beam is reflected by each of the spots containing micromirrors in the ‘on’ direction. This allows only small, multiple spots of illumination to be formed on the sample. Additionally, only the emission from these spots can be reflected towards the detector. Over 1000+ smFRET measurements can, therefore, be taken simultaneously at any given time, with a reduced background signal.

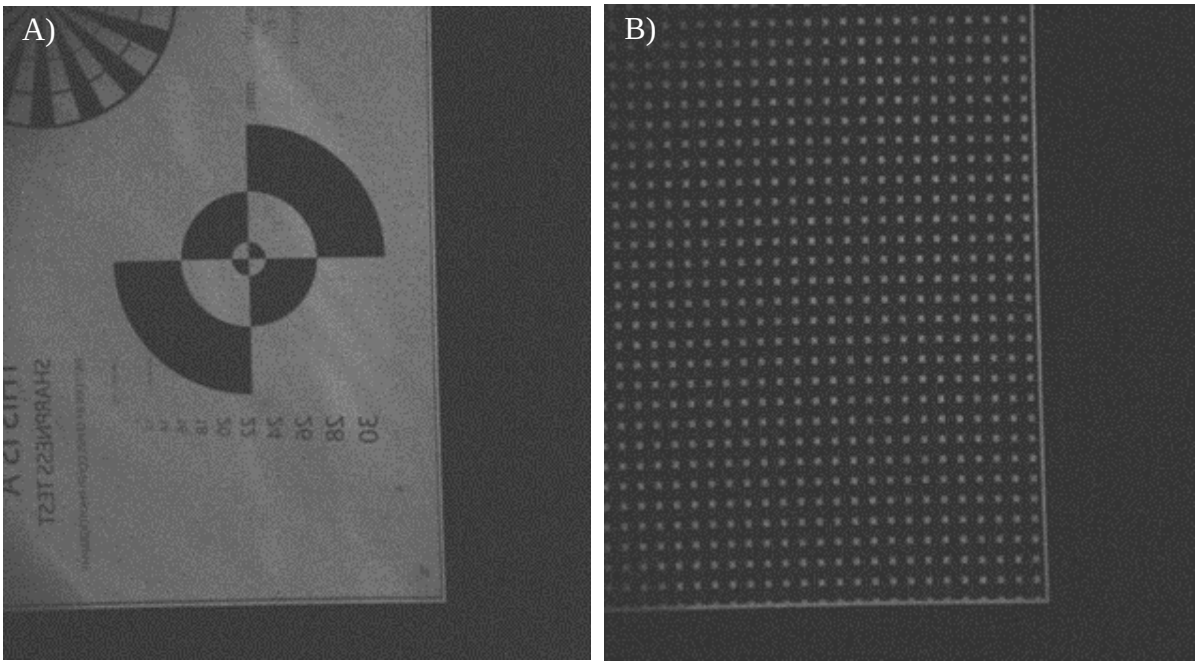

Figure 1.10. A) A binary program uploaded by the computer, implemented onto the DMD, and imaged on an sCMOS camera. The intensity that is reflected by the DMD is from a laser source. B) A multi-spot pattern uploaded from MATLAB onto the DMD and shown on an sCMOS camera.

3.2. Optimizing the SNR and increasing temporal resolution

3.21 Sensitive Detectors

To capture fast biomolecular dynamics, highly performing detectors capable of fast imaging speeds and a large field of view to observe multiple spots are required. In this regard, cameras offer a good balance between fast imaging (on the order of milliseconds) and a large field of view. The two main types of camera sensors widely used for general fluorescent imaging are the Charge-Coupled Devices (CCD) and the scientific Complementary Metal Oxide Semiconductors (sCMOS) cameras. The main differences are depicted in Table 1.2. More recently developed cameras such as the non-destructive readout camera (NDR) have also been developed. The NDR camera collects photons over a longer period of time before the 'readout' occurs. In effect this reduces the 'read noise', introduced later in Chapter 4. Reducing this noise greatly improves the SNR single-molecule imaging experiments. [51] As discussed above,

avalanche photodiodes are commonly used in traditional, confocal, smFRET experiments. These detectors have high speeds (on the order of nanoseconds), low dark current and typically provide higher SNR values. However, their lack of field of view means these detectors can only detect one single-molecule at a time.

Detector	**Advantages**	**Disadvantages**
sCMOS camera	Fast (millisecond exposure times) Low read noise (as low as 0.8e-) Large field of view	Not as sensitive as EM-CCD. Not as fast as Avalanche Photodiodes
EM-CCD camera	More sensitive than current sCMOS cameras Commonly used for low-light applications Large field of view	Not as fast as sCMOS cameras An EM multiplier is added to the read noise
Non-destructive readout (NDR) camera	Very fast (sub-millisecond exposure times) Improved SNR for single-molecule imaging	Difficult to analyse data Expensive Early experimental camera that has only recently been studied
Avalanche Photodiode (APD), Single Pixels Avalanche Diode (SPAD) Arrays, Multi pixel photo counter (MPPC)	Counts events (photons) in the range of tens of picoseconds. Most sensitive for fluorescent applications	Small field of view (limited to counting photons) Arrays that improve field of view are not large enough, have high dark counts and a low quantum efficiency and fill-factor.

Table 1.2. A table showing detectors used for fluorescence and additionally the advantages and disadvantages of them.

For all cameras, photons are collected within each pixel of the sensor. These photons hit the silicon substrate and photoelectrons are generated. These electrons are then stored in the electron storage well and after the exposure time is completed, are transferred to an amplifier, which ultimately generates a voltage. The analogue-digital converter measures this voltage and converts this into a digital signal. The whole system is displayed in Figure 1.11.

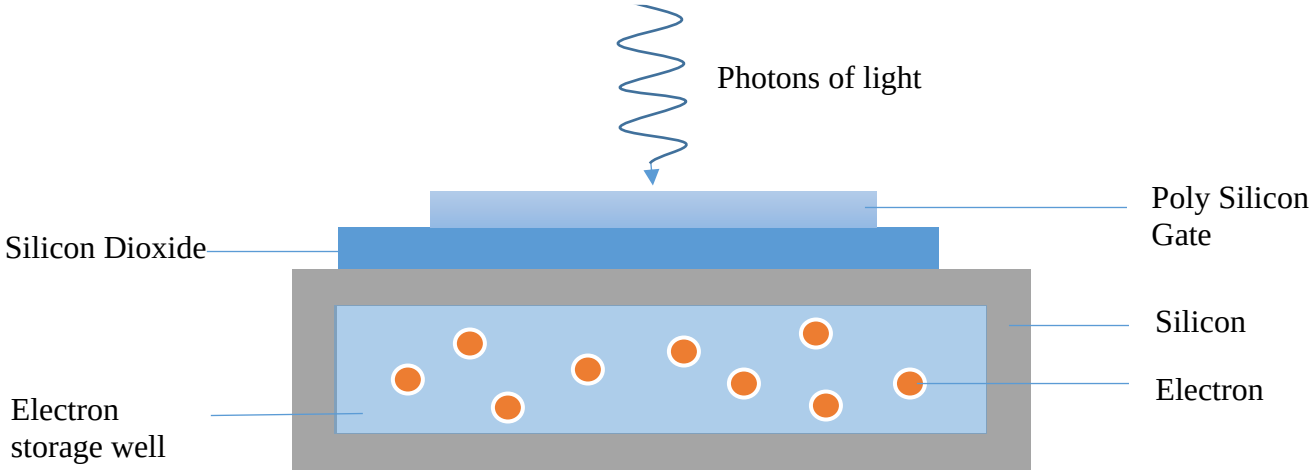

Figure 1.11. A schematic to show each component of a photodiode. [52]

In CMOS detectors, rows of pixels can be readout in parallel to achieve higher frame rates. To achieve this, each pixel or column of pixels has its own associated amplifier. Therefore, each pixel contains its own gain, linearity and noise performance variation. [52] The EMCCD has the same structure to a normal CCD but with one additional feature. Instead of the stored charge being transferred to one parallel register of the CCD camera, the stored charge is transferred to an additional register in which the charge is amplified. The signal is then amplified above the readout noise of the amplifier. This process lowers the speed capability of the camera but can attain greater sensitivity.

1.4 Summary

In this project I will use the latest advances in optical microscopy combined with single-molecule fluorescence methods. My goal is to improve the accessibility and throughput of smFRET measurements.

Chapters 2 and 3 report efforts to improve the accessibility of smFRET by designing cheaper and more robust instrumentation based upon the traditional single-spot confocal microscope. Chapters 4, 5 and 6, present work on improving the throughput of smFRET by identifying the most optimal setup and using novel multi-spot confocal techniques.

In Chapter 2, I present work towards the first affordable, benchtop, accurate smFRET instrument that provides researchers with customisable options to conduct many single-molecule methods.

In Chapter 3, my goal is to further the access of single-molecule fluorescence methods to researchers by designing an affordable excitation module capable of conducting accurate smFRET measurements and fluorescence correlation spectroscopy (FCS).

In Chapter 4, I present characterisations of the latest sCMOS and EMCCD cameras. These results will indicate which cameras are the best to use for single-molecule imaging, and if this can be done at a high enough speed to detect molecules freely diffusing in solution.

In Chapter 5, I present work towards improving the throughput of smFRET by using a digital micromirror device. While this technique is commonly used in structured illumination

microscopy, here I explore its use and limitations for measuring single-molecule FRET efficiencies in multiple excitation spots.

In Chapter 6, I will investigate the throughput of smFRET further by using a novel technique to address some of the limitations of the DMD approach. Here, I aim to explore whether high-throughput smFRET is possible by using an affordable array of pinholes by using a transmission electron microscopy grid. I develop the analysis needed for this high-throughput single-molecule microscope to calculate FRET efficiencies in multiple spots.

Finally, in Chapter 7, I provide a view of the status of the technology and suggest a way forward for realising high-throughput smFRET in a working environment.

1.5 References

[1] J. J. Burbaum, N. H. Sigal, and H. E. Specialisee, "New technologies for high-throughput screening.," *Curr. Opin. Chem. Biol.*, vol. 1, no. 1, pp. 72–8, 2015

[2] W. P. Janzen, "High throughput screening as a discovery tool in the pharmaceutical industry," *Lab. Robot. Autom.*, vol. 8, no. 5, pp. 261–265, 1996

[3] G. S. Sittampalam, S. D. Kahl, and W. P. Janzen, "High-throughput screening: Advances in assay technologies," *Curr. Opin. Chem. Biol.*, vol. 1, no. 3, pp. 384–391, 1997

[4] F. Ritort, "Single-molecule experiments in biological physics: Methods and applications," *J. Phys. Condens. Matter*, vol. 18, no. 32, 2006

[5] M. Segal *et al.*, "High-throughput smFRET analysis of freely diffusing nucleic acid molecules and associated proteins,"

[6] B. Schuler and W. A. Eaton, "Protein folding studied by single-molecule FRET," *Current*

Opinion in Structural Biology, vol. 18, no. 1. pp. 16–26, 2008

[7] Y. Gambin and A. A. Deniz, "Multicolor single-molecule FRET to explore protein folding and binding," *Molecular BioSystems*, vol. 6, no. 9. pp. 1540–1547, 2010

[8] R. Zhao and D. Rueda, "RNA folding dynamics by single-molecule fluorescence resonance energy transfer," *Methods*, vol. 49, no. 2. pp. 112–117, 2009

[9] X. Zhuang, "Single-Molecule RNA Science," *Annu. Rev. Biophys. Biomol. Struct.*, vol. 34, no. 1, pp. 399–414, 2005

[10] M. Helm, A. Y. Kobitski, and G. U. Nienhaus, "Single-molecule Förster resonance energy transfer studies of RNA structure, dynamics and function," *Biophysical Reviews*, vol. 1, no. 4. pp. 161–176, 2009

[11] M. Stracy, S. Uphoff, F. Garza De Leon, and A. N. Kapanidis, "In vivo single-molecule imaging of bacterial DNA replication, transcription, and repair," *FEBS Letters*, vol. 588, no. 19. pp. 3585–3594, 2014

[12] A. Robinson and A. M. Van Oijen, "Bacterial replication, transcription and translation: Mechanistic insights from single-molecule biochemical studies," *Nature Reviews Microbiology*, vol. 11, no. 5. pp. 303–315, 2013

[13] Y. Alhadid, S. Y. Chung, E. Lerner, D. J. Taatjes, S. Borukhov, and S. Weiss, "Studying transcription initiation by RNA polymerase with diffusion-based single-molecule fluorescence," *Protein Science*, vol. 26, no. 7. pp. 1278–1290, 2017

[14] H. P. Lu, "Revealing time bunching effect in single-molecule enzyme conformational dynamics," *Physical Chemistry Chemical Physics*, vol. 13, no. 15. pp. 6734–6749, 2011

[15] G. Haran, "Single-molecule fluorescence spectroscopy of biomolecular folding," *Journal of Physics Condensed Matter*, vol. 15, no. 32. 2003

[16] E. Lerner *et al.*, "Toward dynamic structural biology: Two decades of single-molecule

förster resonance energy transfer," *Science*, vol. 359, no. 6373. 2018

[17] "Fluorescence - Chemistry LibreTexts." https://chem.libretexts.org/Bookshelves/Physical_and_Theoretical_Chemistry_Textbook_Maps/Supplemental_Modules_(Physical_and_Theoretical_Chemistry)/Spectroscopy/Electronic_Spectroscopy/Radiative_Decay/Fluorescence (accessed Jun. 12, 2019).

[18] A. Tokmakoff, "Zwischenmoleculare Energiewanderung und Fluoreszenz," 1949. Accessed: Jun. 12, 2019

[19] M. C. Chirio-Lebrun and M. Prats, "Fluorescence resonance energy transfer (FRET): Theory and experiments," *Biochem. Educ.*, vol. 26, no. 4, pp. 320–323, 1998

[20] F. Schaufele, I. Demarco, and R. N. Day, "FRET Imaging in the Wide-Field Microscope," in *Molecular Imaging*, 2005, pp. 72–94.

[21] B. W. Van Der Meer, "Kappa-squared: From nuisance to new sense," *Rev. Mol. Biotechnol.*, vol. 82, no. 3, pp. 181–196, 2002

[22] J. J. McCann, U. B. Choi, L. Zheng, K. Weninger, and M. E. Bowen, "Optimizing methods to recover absolute FRET efficiency from immobilized single molecules," *Biophys. J.*, vol. 99, no. 3, pp. 961–970, 2010

[23] D. K. Sasmal, L. E. Pulido, S. Kasal, and J. Huang, "Single-molecule fluorescence resonance energy transfer in molecular biology," *Nanoscale*, vol. 8, no. 48. pp. 19928–19944, 2016

[24] C. Biskup *et al.*, "Multi-dimensional fluorescence lifetime and FRET measurements," in *Microscopy Research and Technique*, 2007, vol. 70, no. 5, pp. 442–451

[25] K. A. Henzler-Wildman *et al.*, "Intrinsic motions along an enzymatic reaction trajectory," *Nature*, vol. 450, no. 7171, pp. 838–844, 2007

[26] M. Kastantin and D. K. Schwartz, “Identifying multiple populations from single-molecule lifetime distributions,” *ChemPhysChem*, vol. 14, no. 2, pp. 374–380, 2013

[27] J. G. Yodh, M. Schlierf, and T. Ha, “Insight into helicase mechanism and function revealed through single-molecule approaches,” *Q. Rev. Biophys.*, vol. 43, no. 2, pp. 185–217, 2010

[28] E. Nir *et al.*, “Shot-noise limited single-molecule FRET histograms: Comparison between theory and experiments,” *J. Phys. Chem. B*, vol. 110, no. 44, pp. 22103–22124, 2006

[29] S. Kalinin, E. Sisamakis, S. W. Magennis, S. Felekyan, and C. A. M. Seidel, “On the origin of broadening of single-molecule FRET efficiency distributions beyond shot noise limits,” *J. Phys. Chem. B*, vol. 114, no. 18, pp. 6197–6206, 2010

[30] M. Karymov, D. Daniel, O. F. Sankey, and Y. L. Lyubchenko, “Holliday junction dynamics and branch migration: Single-molecule analysis,” *Proc. Natl. Acad. Sci. U. S. A.*, vol. 102, no. 23, pp. 8186–8191, 2005

[31] E. E. Weatherill and M. I. Wallace, “Combining single-molecule imaging and single-channel electrophysiology,” *Journal of Molecular Biology*, vol. 427, no. 1. pp. 146–157, 2015

[32] T. Ha and P. Tinnefeld, “Photophysics of fluorescent probes for single-molecule biophysics and super-resolution imaging.,” *Annu. Rev. Phys. Chem.*, vol. 63, pp. 595–617, 2012

[33] A. Ingargiola *et al.*, “48-spot single-molecule FRET setup with periodic acceptor excitation,” *J. Chem. Phys.*, vol. 148, no. 12, 2018

[34] J. Hohlbein, T. D. Craggs, and T. Cordes, “Alternating-laser excitation: Single-molecule FRET and beyond,” *Chemical Society Reviews*, vol. 43, no. 4. pp. 1156–1171, 2014

[35] R. Roy, S. Hohng, and T. Ha, “A practical guide to single-molecule FRET.,” *Nat. Methods*, vol. 5, no. 6, pp. 507–16, 2008

[36] B. D. Slaughter, M. W. Allen, J. R. Unruh, R. J. Bieber Urbauer, and C. K. Johnson, “Single-molecule resonance energy transfer and fluorescence correlation spectroscopy of calmodulin in solution,” *J. Phys. Chem. B*, vol. 108, no. 29, pp. 10388–10397, 2004

[37] G. Yuan, D. E. Gómez, N. Kirkwood, K. Boldt, and P. Mulvaney, “Two Mechanisms Determine Quantum Dot Blinking,” *ACS Nano*, vol. 12, no. 4, pp. 3397–3405, 2018

[38] S. Hohng and T. Ha, “Single-molecule quantum-dot fluorescence resonance energy transfer,” *ChemPhysChem*, vol. 6, no. 5, pp. 956–960, 2005

[39] S. Hohng and T. Ha, “Near-Complete Suppression of Quantum Dot Blinking in Ambient Conditions,” *J. Am. Chem. Soc.*, vol. 126, no. 5, pp. 1324–1325, 2004

[40] J. Farlow, D. Seo, K. E. Broaders, M. J. Taylor, Z. J. Gartner, and Y.-W. Jun, “Formation of targeted monovalent quantum dots by steric exclusion.,” *Nat. Methods*, vol. 10, no. 12, pp. 1203–5, 2013

[41] Q. Zheng *et al.*, “Ultra-stable organic fluorophores for single-molecule research,” *Chemical Society Reviews*, vol. 43, no. 4. pp. 1044–1056, 2014

[42] A. E. Miller *et al.*, “Single-molecule dynamics of phytochrome-bound fluorophores probed by fluorescence correlation spectroscopy,” *Proc. Natl. Acad. Sci.*, vol. 103, no. 30, pp. 11136–11141, 2006

[43] B. Ambrose *et al.*, “The smfBox is an open-source platform for single-molecule FRET,” *Nat. Commun.*, vol. 11, no. 1, p. 5641, 2020

[44] A. Nakano, “Spinning-disk confocal microscopy - A cutting-edge tool for imaging of membrane traffic,” *Cell Structure and Function*, vol. 27, no. 5. pp. 349–355, 2002

[45] J. P. Renaud *et al.*, “Biophysics in drug discovery: Impact, challenges and opportunities,” *Nature Reviews Drug Discovery*, vol. 15, no. 10. pp. 679–698, 2016

[46] A. Ingargiola *et al.*, “16-Ch time-resolved single-molecule spectroscopy using line excitation,” in *Single Molecule Spectroscopy and Superresolution Imaging X*, 2017, vol. 10071, p. 100710Q

[47] S. Kim, A. M. Streets, R. R. Lin, S. R. Quake, S. Weiss, and D. S. Majumdar, “High-throughput single-molecule optofluidic analysis,” *Nat. Methods*, vol. 8, no. 3, pp. 242–245, 2011

[48] Z. Xiong *et al.*, “Diffraction analysis of digital micromirror device in maskless photolithography system,” *J. Micro/Nanolithography, MEMS, MOEMS*, vol. 13, no. 4, p. 43016, 2014

[49] M. Lachetta, H. Sandmeyer, A. Sandmeyer, J. S. A. Esch, T. Huser, and M. MÃller, “Simulating digital micromirror devices for patterning coherent excitation light in structured illumination microscopy,” *Philos. Trans. R. Soc. A Math. Phys. Eng. Sci.*, vol. 379, no. 2199, 2021

[50] N. Feiner-Gracia, S. Pujals, P. Delcanale, and L. Albertazzi, “Advanced Optical Microscopy Techniques for the Investigation of Cell-Nanoparticle Interactions,” in *Smart Nanoparticles for Biomedicine*, 2018, pp. 219–236.

[51] S. F. H. Barnett, M. Snape, C. N. Hunter, M. A. Juárez, and A. J. Cadby, “A Novel Application of Non-Destructive Readout Technology to Localisation Microscopy,” *Sci. Rep.*, vol. 7, 2017

Chapter 2. An Affordable, Easy to Use, Confocal Single-Molecule FRET Instrument

This commercial equipment was created in collaboration with Cairn Research. The draft modules of the pinhole, excitation and emission path were designed by Dylan George. The final versions that were manufactured were created by Cairn Research with direction from both Timothy Craggs and Dylan George. All renders and models were completed by Dylan George. Mahmoud Abdelhamid provided data and pictures on the openFrame with the modules attached.

Contents

2.1	Introduction	45
2.1.1	Home-made and commercial single-molecule instrumentation	45
2.2	Design and Methods	47
2.3	Results and Discussion	49
2.3.1	Excitation Module	49
2.3.2	The Pinhole Module	57
2.3.3	Emission Module	61
2.3.4	Sample stage and Lid	65
2.3.5	Configurations	67
2.4	Conclusions & Further Design Suggestions	69
2.5	References	69

2.1. Introduction

In single-molecule fluorescence microscopy, commercial microscopes are designed for only a handful of applications, primarily due to the complex arrangement and precision of optical components. As a result, these expensive instruments restrict research and require researchers to travel to centres that have purchased the desired instrument with usually delicate samples. Here we present an alternative that encompasses many single-molecule fluorescence techniques within a modular microscopy instrument. By using the Cairn openFrame as a foundation, three modules were designed for confocal single-molecule FRET and Fluorescence Correlation Spectroscopy (FCS). We anticipate by using this approach we can add more modules for TIRF single-molecule FRET and super-resolution applications.

2.1.1 Home-made and commercial single-molecule instrumentation

Single-molecule FRET is a commonly used technique in fluorescence microscopy for measuring the conformations of biological molecules at the angstrom level. [1,2] In the past, instruments that have offered this technique have been expensive, difficult to use and have required optical equipment and expertise to maintain and set up. Recently, a new commercial instrument, the Nanoimager by ONI, offering benchtop TIRF single-molecule FRET measurements has entered the market (https://oni.bio/nanoimager/). This has provided researchers a gateway into the technique. This instrument, however, remains highly expensive for researchers and lacks the flexibility for a wide range of applications. Recently, the availability of open-source hardware and software has enabled researchers access to affordable single-molecule techniques. [3–7] In particular, the smfBox, which offers confocal single-molecule FRET and FCS measurements at a fraction of the price (~£40,000). [8] This kit can be assembled using all the parts displayed online and the software is freely available to download. However, with these projects, optical expertise and an optical table is still required.

As such, with current commercial and open-source single-molecule instruments, access to single-molecule FRET measurements remains limited.

The main academic research groups that use single-molecule FRET are biologists, biophysicists, and single-molecule experts. Figure 2.1 collates the main problems, regarding the access to the technique, based on market research carried out as part of the project.

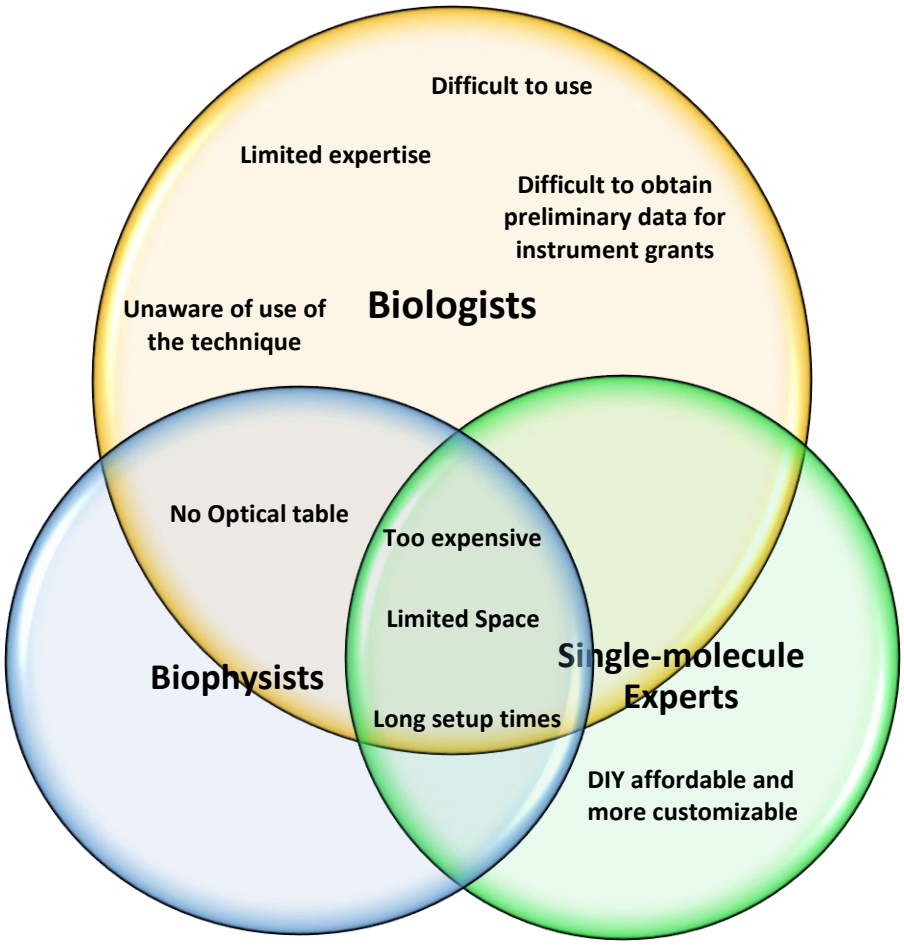

Figure 2.1. A Venn diagram showing the main reasons for the lack of uptake in single-molecule FRET instruments.

Here we can see that while there are obvious advantages to single-molecule FRET, there are also many challenges that prevent researchers using it; - primarily, the long set up times and expertise needed in the area. In this chapter, we present a single-molecule instrument designed

to address these problems and provide non-experts access to this technique. We aim to make the technique affordable, customizable, and easy to use. Furthermore, to make single-molecule measurements accessible outside the lab, on any benchtop.

2.2 Design and Methods

The openFrame by Cairn Research allows users to customize their optical setup for different applications. By adding modules onto the openFrame, a range of different optical components and detectors can be utilized. Using the openFrame as a foundation, three compatible modules were designed to provide confocal single-molecule FRET and FCS measurements.

To counter the cost of traditional single-molecule setups, all the parts were either custom-made or sourced based on their affordability. The design was based on the smfBox, a single-molecule microscope that measures accurate, confocal single-molecule FRET and fluorescence correlation spectroscopy (FCS). By using AutoCAD Fusion 360 software, optical components were downloaded from Thorlabs, and modules were then designed to provide a light-tight optical system.

The openFrame by Cairn Research is composed of five main sections. At the bottom of the openFrame is the base. The base of the unit provides stable support and can be mounted onto an optical table. Importantly, the optical table significantly reduces the vibrations of the instrument. Above the base is the emission layer. Multiple cameras can be inserted into this layer. A dichroic filter or mirror can also be inserted to direct light towards these detectors. Above this layer is a thinner compartment for any additional cameras or unique optics required. The layer above this is the excitation layer which can direct the illumination source to the sample via a dichroic mirror. Lastly, the objective and sample stage at the top of the openFrame, allows the sample to be placed on the microscope easily. Figure 2.2 shows the openFrame

before any modifications were added to make it suitable for single-molecule experiments. Figure 2.3 also shows a simple model of the modules as a reference.

Figure 2.2. The openFrame by Cairn Research. This inverted microscope design is composed of five sections. The bottom of the microscope has a base section capable of being attached to optical tables. Above this is the camera section which is a thicker section to allow cameras to be attached. Above this are two further thinner sections allowing for excitation light to enter and customizable optics to be placed as inputs. The final section is the stage which accommodates the sample.

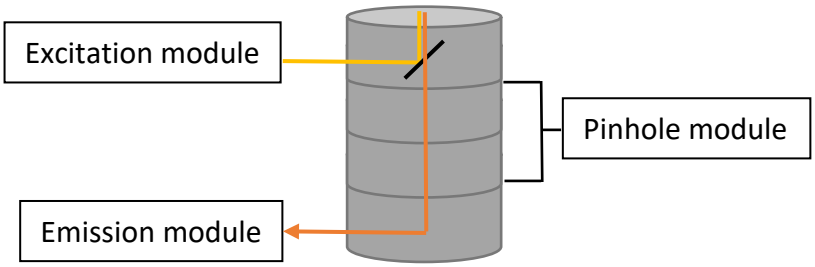

Figure 2.3. A simplistic schematic of the openFrame modules designed and the laser beam (yellow) and emission (orange) pathways.

2.3 Results and Discussion

2.3.1 Excitation Module

The first module that was designed was the excitation pathway. For reference the final version and components of this module are shown in Figure 2.4 and Table 2.1. A photograph of the manufactured excitation module is shown in Figure 2.5.

This module and design enabled a consistent, Gaussian laser beam into the openFrame. The main objective of this module was to align this laser beam onto the centre of the back aperture of the objective. This is important as it ensures only a single, small spot on the sample is illuminated. Any deviations from the centre would affect the back reflection of the sample coverslip imaged from a camera. Since this camera is used to determine the depth of the detection in the sample, this would hinder the ability of the microscope to determine the location of the observation volume. For example, we may not be able to determine if we were detecting above the coverslip (inside the sample) or below the coverslip (outside of the sample).

Part List			Part Description
Item	QTY	Part	
1	1	**30 MM Cage Cube -** (THL CM1-DCHM)	A component accommodating a dichroic filter in a fixed position
2	2	**Kinetic Mirror Mount** – (THL SM05 45Deg KCB05-M)	A component accommodating a mirror in at a right angle and in a fixed position
3	1	**Tube -** (THL SM1L10)	A component connecting the CMOS camera to the 30 MM Cage Cube
4	1	**Tube -** (THL SM1L15)	A component connecting the photodiode sensor to the angled tube.
5	1	**CMOS Camera** – (THL CS165MU)	An affordable CMOS camera
6	1	**Angled Tube –** (THL SM1L03T)	A component allowing the photodiode to be positioned at an angle
7	1	**Si Photodiode** – (THL DET10A2)	A photodiode sensor
8	1	**Tube adapter** – (THL SM1T2)	An adaptor connecting the CMOS camera to a tube
9	1	**Tube** – (SM05, machined)	A component connecting the 30 MM Cage Cube to the first alignment mirror
10	2	**Lens focal length 30 mm** – (THL AC254-030-A)	An achromatic lens at a focal length of 30 mm
11	1	**Cap Head** – (M4 X 16 MM)	Power meter cap head
12	1	**Tube** – (THL SM05L05)	A component connecting the 30 MM Cage Cube to the first alignment mirror
13	1	**Power sensor** – (THL S130C)	A power meter
14	1	**Iris** – (THL SM1D12C)	A variable iris
15	1	**Tube** – (THL SM05L20_OA_1)	A component connecting the second alignment mirror to the reflective collimator
16	1	**Power Sensor Mount A**	A custom-made mount to allow the power meter to slide in
17	1	**Power Sensor Mount B**	A custom-made mount to allow the power meter to slide in
18	4	**Rods** – (THL ER2)	Rods that attach to the power meter mounts
19	1	**Reflective Collimator** – (RC08APC-P01)	A collimator
20	2	**Interchangeable Filter Holders**	Custom-made filter holders

Table 2.1. A table comprising of all the parts used inside of the excitation module.

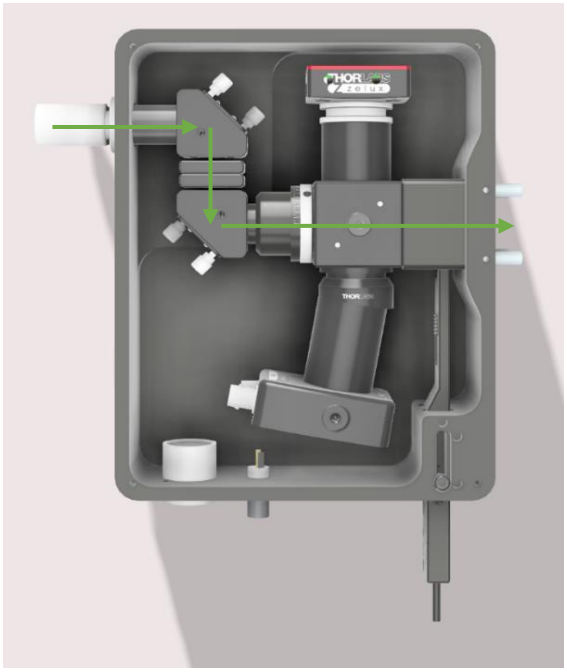

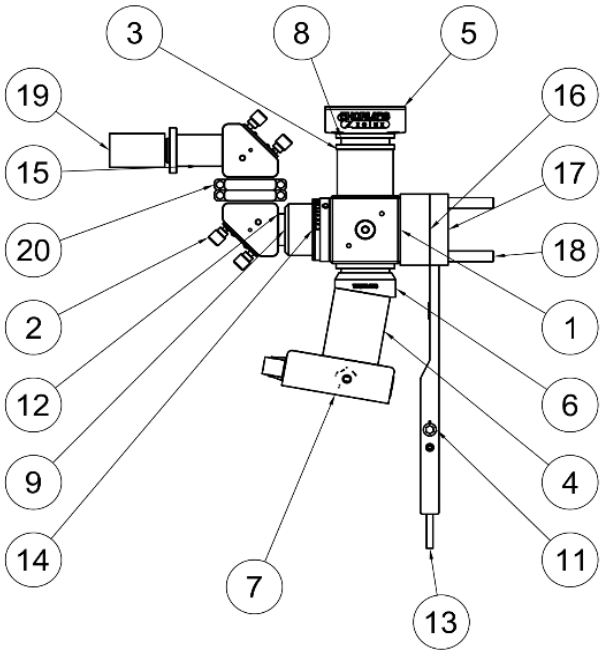

Figure 2.4. A diagram of the excitation module for the openFrame with all the optical components aligned inside the module labelled. The green arrow represents the laser beam path towards the openFrame and the sample.

In this module, the laser beam first entered the microscope through an optical fibre that was connected to a reflective collimator. This provided a uniform, collimated, Gaussian laser beam ideal for single-molecule experiments. The specific reflective collimator was chosen as it collimates the laser beam to a diameter of 8.2 mm. With the aim to achieve a small excitation spot, the diameter of the laser beam that entered the objective needed to match the diameter of the back aperture of the objective. This was based on the back aperture of the objective used, which was 8 mm. A beam diameter of 8.2 mm gave room to crop the beam with an iris to accommodate for this. The collimator could also be screwed into the outside of the box. This ensured that even if the fibre or collimator were to be replaced, the alignment of the laser beam would be in a similar position.

Once the collimator was attached, the laser beam was then reflected off two mirrors mounted on two kinematic mirror mounts. These could be manually changed to alter the direction and position of the laser beam. To guarantee that the laser beam could be steered to the centre of the objective lens, two mirrors were required. By adjusting two degrees of freedom (the tip and tilt mechanisms) of both kinematic mirrors more control was acquired, and a power reading of the laser beam could be taken at the sample. In addition, we designed an alignment tool that could be temporarily placed above the objective to allow easy alignment of the microscope. This consisted of a long aluminium tube containing two irises at approximately 40 cm away from each other, shown in Figure 2.5. In effect, this tube then replaced the objective lens. By ensuring the mirrors were aligned and both irises were in place, only the laser light that irradiated through the centre of the tube and parallel to the optical axis was allowed to be observed out of the end of the tube. This method and tool ensured the laser beam travelled

directly through the centre of the sample and in line with the confocal volume in the emission path.

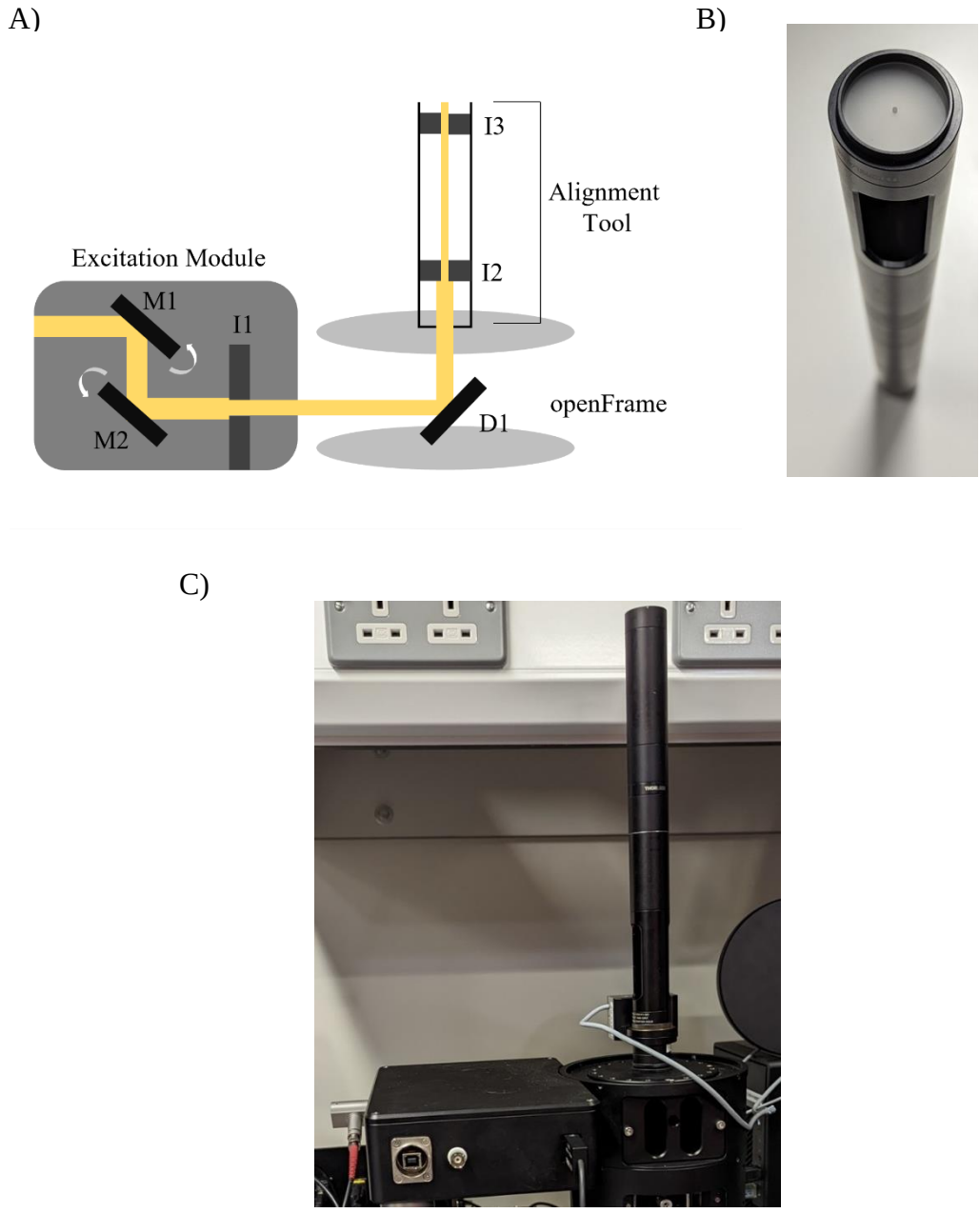

Figure 2.5. A) A simplistic schematic of the alignment tool in the perfect alignment on the openFrame. M1 and M2 represent mirrors. I1, I2 and I3 represent irises. D1 represents the dichroic mirror. The laser beam is represented by a yellow line. B) A photograph of the alignment tool. C) A picture of the alignment tool on the openFrame with the excitation module attached.

In addition to the alignment tool, the openFrame could be aligned by taking out the dichroic mirror (D1) inside the openFrame, shown in Figure 2.6. The laser beam then travelled directly through the openFrame top layer. This method checked that the laser beam travelled straight

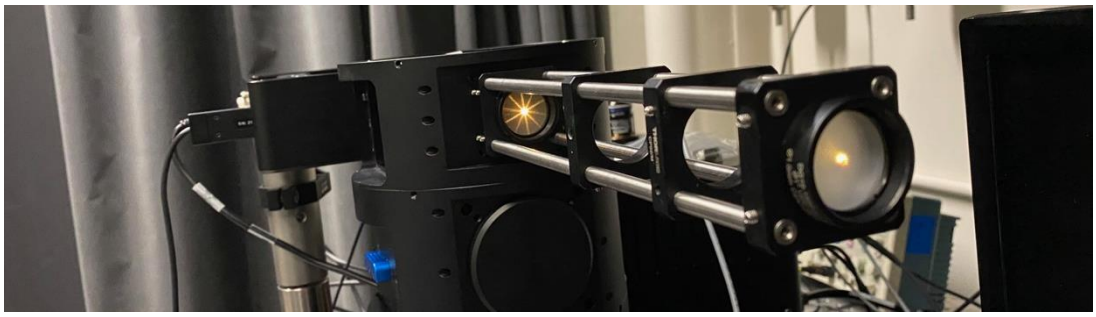

and through the centre of the entrance to the openFrame.

Figure 2.6. Alignment of the openFrame excitation pathway by taking out the dichroic mirror (D1). The laser beam travels directly through the openFrame and out the other end.

Continuing with the path of the laser beam, between these alignment mirrors, two interchangeable filters could be placed between the mirror mounts. These filters could be neutral density filters to decrease the power of the laser beam or filters for wavelength and polarity restriction depending on the required excitation properties.

The laser beam then travelled through an iris which precisely cropped the laser beam to the diameter of the back aperture of the objective lens. Here we opted for a variable iris due to the variation of back aperture diameters associated with using different objective lenses. The laser beam diameter was set to 5 mm to deliberately underfill the back aperture of the objective (8 mm). This meant that a bigger illumination spot would be observed at the sample. This made the microscope easier to align as the illumination volume was larger than the observation volume. The iris, mentioned previously, was placed before the detectors to avoid any unwanted back reflection.

The laser beam then travelled through a filter cube containing a 90:10 beam splitter. This reflected 10% of the laser beam onto a photodiode, used to monitor the power and stability of the laser. On the other side of the beam splitter cube is a CMOS camera which was used to monitor the back reflection of the coverslip. Once an image of the back reflection was formed, the z- position of the objective could be moved so that the confocal volume was inside the sample (above the coverslip). This essential step avoided the possible detection outside of the sample. A 45 degree angle on the photodiode was required to avoid reflection from the CMOS chip of the camera onto the photodiode. A lens before each detector was also required to focus the light onto the detector. These lenses were placed in lens tubes that allowed the distance between the detector and the lens to match the focal length of the lens. The focal length of these lenses had to be small (40 mm) to fit inside the case.

After the filter cube, a power meter was designed to be slotted into the module to provide a power reading in watts. This allowed for a quick and easy check of the power of the laser beam as it travelled towards the sample. This was important as a laser beam that was too low in power may not be able to excite the fluorophores in the sample. Conversely, a laser beam with too much power may increase the background noise of the experiment without adding much to the emission signal. A higher power can also lead to the photobleaching of dyes which may pose a problem for other single-molecule imaging applications not described here.

Finally, the laser beam is reflected off a dichroic mirror that was inserted into the openFrame layer and directed vertically upwards towards the sample. Here, the ability to steer the dichroic mirror was helpful. Although the two mirrors before should be sufficient to align the microscope alone, being able to use the dichroic mirror gave another option in case the previous method proved difficult. This was already part of the openFrame and the dichroic mount that was inserted into the top layer was not modified. Figure 2.7 and Figure 2.8 shows draft

excitation modules without the lid. In the draft version in Figure 2.7, it was clear that there was not enough room in the case to accommodate the two alignment mirrors, the collimator, and the cables for the detectors. The draft version in Figure 2.8 was enlarged however, we also concluded that the excitation module should be separate from the foundation of the openFrame. The two alignment mirrors were also positioned differently in the final version to make the system more compact.

Figure 2.7. The openFrame by Cairn Research with an early draft excitation module on the top layer. The excitation module was designed to input and easily align laser light into the microscope.

Figure 2.8. The openFrame by Cairn Research with an early draft excitation module on the top layer. The excitation module was designed to input and easily align laser light into the microscope.

After adjustments to the shape, length, and width of the draft versions along with adding the components mentioned earlier, we manufactured the first prototype of the excitation module shown in Figure 2.9.

Figure 2.9. A photograph of the excitation module for the openFrame with all the optical components aligned inside the module.

2.3.2 The Pinhole Module

For confocal single-molecule FRET measurements, a pinhole is required to block the out of focus light from other fluorophores in the sample. In confocal microscopy the pinhole is usually 0.25 – 1 Airy Units (AU) in size. This range of Airy Units has been found in conventional confocal microscopy to provide a good balance between resolution and emission strength. An Airy Unit is the distance between the peak of the signal and the first zero in the point spread function shown in Figure 2.10.

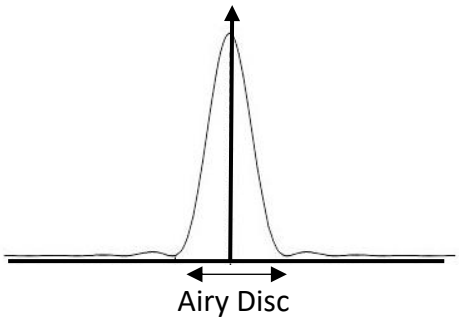

Figure 2.10. A diagram showing the intensity profile of the diffraction limit and the Airy Disc.

As the size of the pinhole decreases the resolution of the microscope increases. However, as the pinhole gets smaller less light is allowed through and so the emission signal decreases. The Airy Unit of this microscope can be calculated using Equation 2.1:

$$1 \text{ Airy Unit} = \frac{0.61\text{M}\lambda}{\text{NA}}. \tag{2.1}$$

Here, M denotes the magnification up to the pinhole (image plane), λ is the emission wavelength and NA is the numerical aperture of the objective lens. To find the total magnification up to the pinhole, Equation 2.2 can be used:

$$\text{Total Magnification}_{\text{ pinhole}} = \frac{\text{focal length of tube lens}}{\text{focal length of objective lens}}. \tag{2.2}$$

Unlike conventional confocal microscopy we designed this microscope to have a higher Airy number to give better emission signal. Based on the dimensions we selected and using these equations, an Airy unit of 3.6 was selected (based on the smfBox). To achieve this the same optical components as the smfBox were used. The focal length of the tube lens was 50.8 mm. The focal length of the objective lens (60x, NA 1.35) was 3 mm. Therefore, the total magnification up to the pinhole was (50.8 mm/3 mm) 16.9x. Therefore, 1 Airy Unit, using an emission wavelength of ATTO 550 (576 nm) a common single-molecule dye, was calculated to be 5.5 μm. To achieve an Airy unit of 3.6 AU, a 20 μm pinhole was used. However, it is important to remember that since the laser beam underfilled the back aperture of the objective lens, the effective NA of the objective lens would be lower than the value previously stated, and so this result would be an approximation. As mentioned previously the size of this pinole is more than 1 AU as we are interested in the emission signal instead of the spatial resolution. A lens before the pinhole was needed to focus the light emitted from the sample through the pinhole. Additionally, a lens placed after the pinhole was required to collimate the light rays parallel to the optical axis. Since the combined focal lengths of the lenses added to more than 100 mm, two openFrame layers were needed to sufficiently accommodate the space required for the setup shown in Figure 2.11.

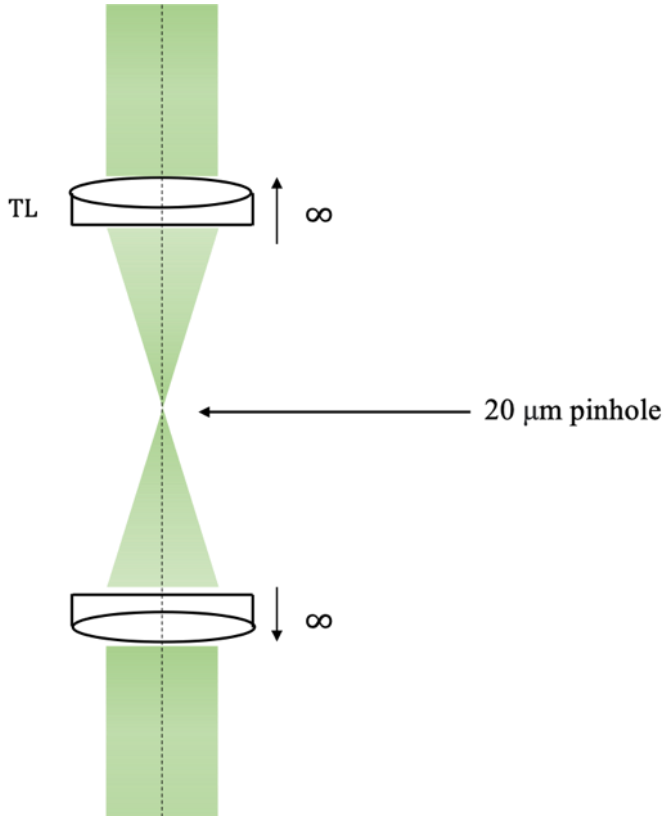

Figure 2.11. A diagram showing the pinhole module of the microscope. A tube lens (TL) focuses the light rays through the pinhole and the lens after directs the light rays parallel to the optical axis.

To allow emission from the sample to travel through the pinhole, the pinhole needed to be able to move laterally and axially. The axial direction allowed the focal length of the lens to match the distance away from the pinhole. The lateral direction allowed the focus of the lens to be aligned with the pinhole. Since the pinhole could move in both these directions, it was important to keep the lens before and after, static. This ensured that the emission light travels through the centre of both lenses.

The purpose of the pinhole module was to reduce the background and therefore increase the signal-to-noise ratio. This module contained an adapter and tube that attached to the inside of the openFrame. A cage system was placed vertically down the middle of the two layers containing both lenses and the pinhole. The lenses had the focal lengths 50.8 mm and 63.5 mm,

respectively. The zoom housing contained the pinhole and could be manually moved in the axial direction. Table 2.2 shows all the parts of the pinhole system and corresponds to the labelling in Figure 2.12. The pinhole setup was made from Thorlabs components and so could be easily assembled and plugged into openFrame via four cage rods.

Part List			Part Description
Item	Qty	Part	
1	1	**Cage Adapter Disc**	A component allowing attachment to the openFrame
2	4	**Rod** (THL, ER6)	Rods through all of the optical components
3	2	**Cage System** (THL, CXY1)	An optomechanical component allowing the lateral movement of the lenses and pinhole
4	2	**Zoom housing** (THL, SM1ZM)	A component allowing the movement of the pinhole in the axial axis
5	1	**Tube** (THL, SM1L03)	A component allowing for the accommodation of an objective lens

Table 2.2. The parts contained in the middle section of the microscope.

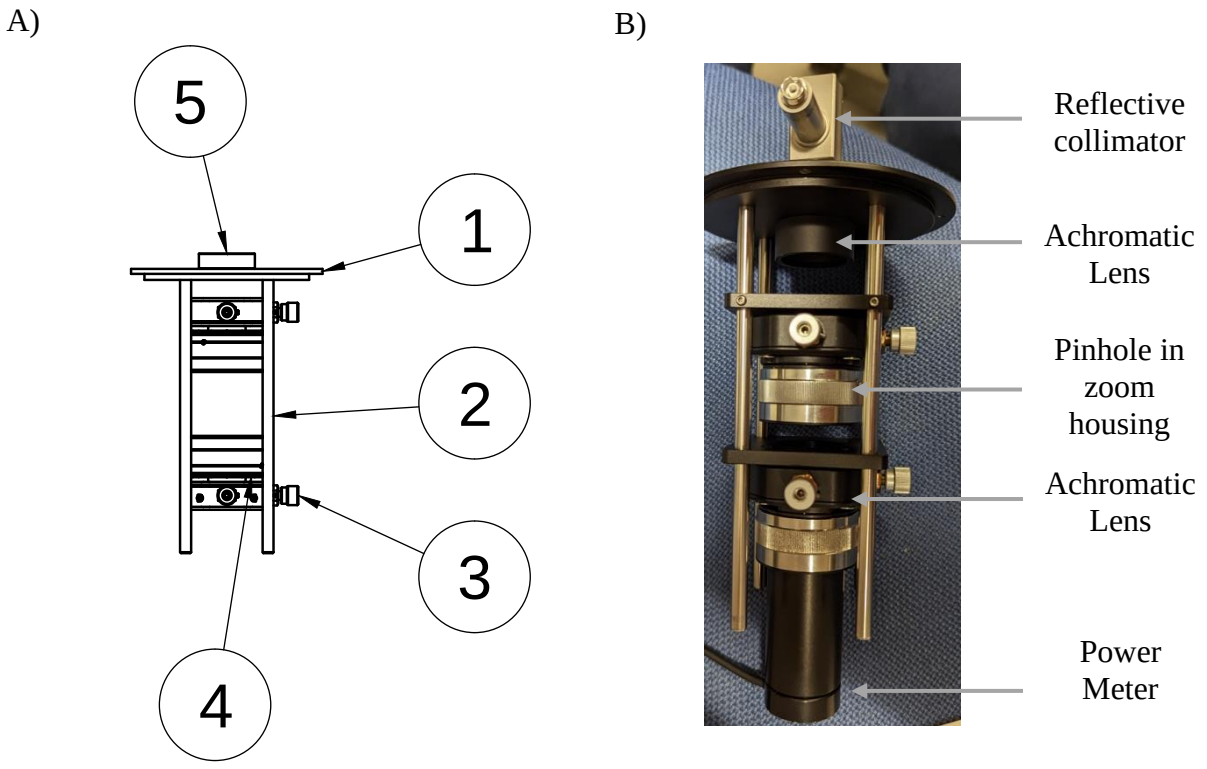

Figure 2.12. A) A schematic of the middle section of the microscope with the parts labelled. B) A photograph of the manufactured pinhole module with a collimator and power meter attached. This setup was used to align the pinhole module.

The pinhole module was aligned by using a collimated laser beam from a fibre and a reflective collimator shown in Figure 2.12. To ensure the laser beam was collimated to infinity space, the diameter of the beam close to the collimator was compared with the diameter of the laser beam as far away as possible. In this case, we measured the diameter approximately 15 m away. Two lenses were then placed in the module to check whether the laser beam travelled through the centre of the lenses. To check this, the lens furthest away from the pinhole was moved axially until the laser beam was collimated once again. This lens was then moved again in the axial position. If the laser beam moved laterally when the lens moved, this meant that the laser beam was not travelling through the centre of the lens. To fix this, the lens was moved in both the lateral directions until the laser beam no longer moved laterally. After this, the pinhole was placed into the module and a power meter was attached after the last lens. The next step was to maximise the power output after the pinhole (20 μm) to ensure the pinhole was in the correct position. The pinhole was first moved in the lateral directions to maximise the power displayed by the power meter. Then it was moved in the axial direction that increased this power reading. This process was repeated until the maximum amount of power possible travelled through the pinhole. Since the collimated laser beam for the openFrame was not perfectly collimated, this process could roughly put the optical components in the correct position. These components would need to be further adjusted very slightly when placed in the emission path.

2.3.3 Emission Module

To collect the emission from the sample, an emission module was required. A draft version of this module was designed and is shown in Figure 2.13. The curved edge of this draft was removed to accommodate a controller box for the avalanche photodiodes (APDs).

This module fitted onto to the bottom openFrame layer and split the sample emission between red and green light. Two avalanche photodiodes (APDs) were used to detect the emission of

each colour and were connected to a computer via a National Instruments data acquisition (NI DAQ) board.

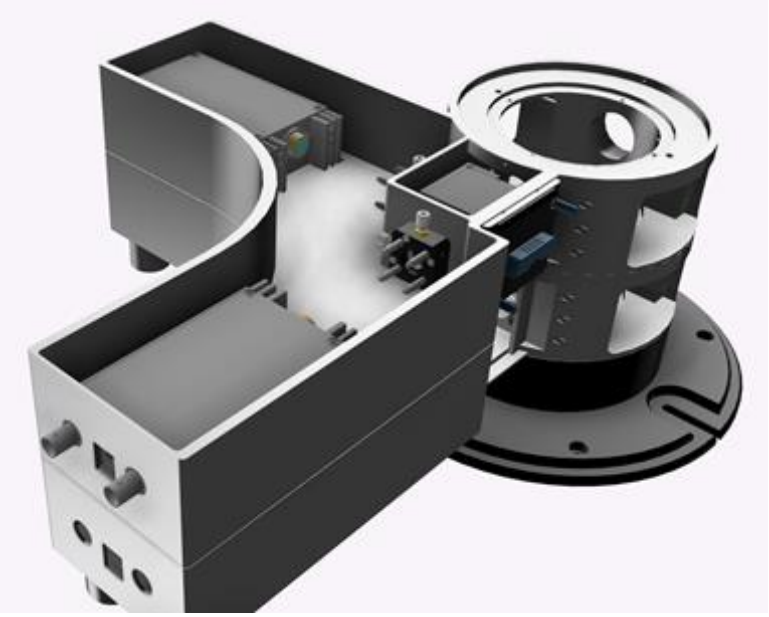

Figure 2.13. A draft version of two emission modules shown attached to the bottom two openFrame layers.

Table 2.3 and 2.4 show the components of the final version and Figure 2.14 shows the design of the final emission module.

Part List			Part Description
Item	Qty	Part	
1	1	**Combiner Cube**	A component holding a dichroic mirror in a fixed position
2	2	**Cube Adapter**	A component connecting the combiner cube to the photodiode module
3	2	**Si APD connector** (Excilitas)	A silicon avalanche photodiode
4	1	**Tube**	A component connecting the emission module to the avalanche photodiode

Tables 2.3. The parts contained in one APD box in the emission module of the microscope.

Part List			Part Description
Item	Qty	Part	
1	1	**Case**	A case for the emission module
2	1	**Si APD** (Excilitas)	A silicon avalanche photodiode
3	1	**Translation Mount** (THL, LM1XY)	An optomechanical component allowing the lateral movement of the lenses
5	4	**Cage rods** (THL, SR2)	Rods for the translation mounts

Tables 2.4. The parts contained in the full emission module of the microscope.

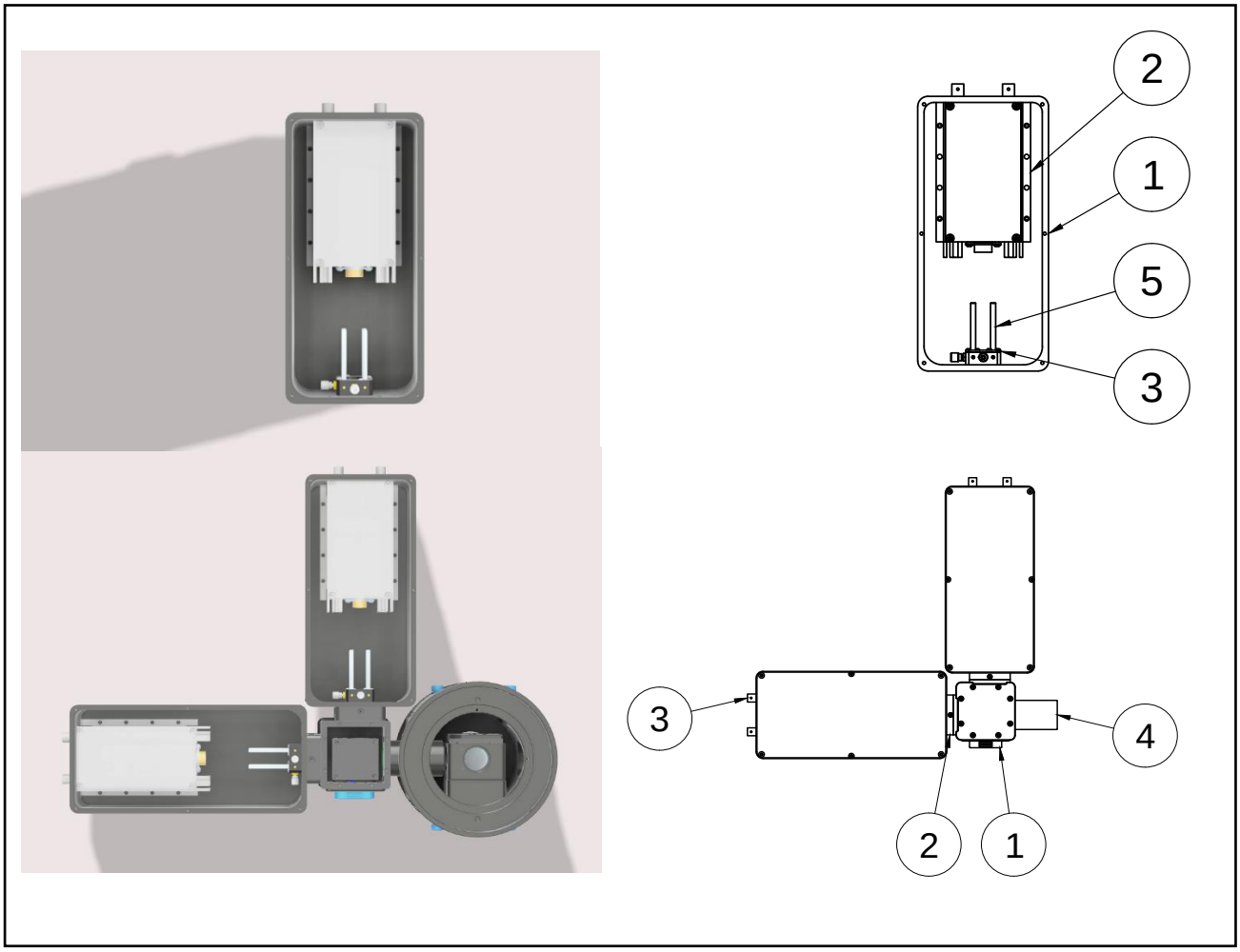

Figure 2.14. A diagram of the emission module for the openFrame with all the parts inside the module labelled.

The emission light from the sample was collimated by the static lens after the pinhole. It then travelled vertically down into the last layer. By inserting a mirror into this layer, the emission light was then steered towards the emission module. However, if a polarising filter was inserted and another layer with detection modules was fitted below with a mirror, then one detection module would detect polarised light and the other would be able to detect emission light perpendicular to the excitation polarisation (Figure 2.15). Polarisation studies are useful in capturing fast dynamics of biomolecules. [9] To carry out such studies a 50:50 beam splitter and picosecond electronics are required.

Figure 2.15. A diagram of the final two emission modules for the openFrame. This configuration can be used for polarisation studies.

For both cases, emission from the sample entered the detection module and was split by a dichroic mirror accommodated by a filter cube. This splits the light into green and red emission. This dichroic filter could be interchanged with a filter of choice allowing for different dyes to be observed.

The emission light from the sample was then focussed onto each of the two APDs via an achromatic lens shown in Figure 2.16.

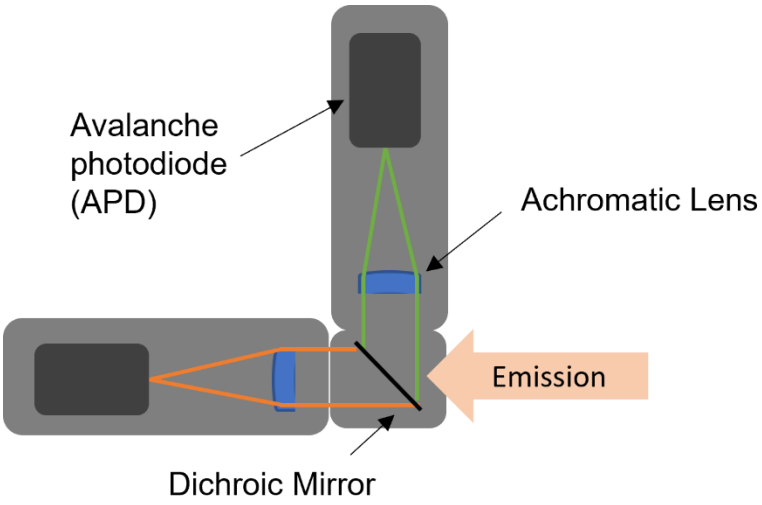

Figure 2.16. A schematic of the emission module showing the incoming emission from the openFrame, the two avalanche photodiodes, the dichroic mirror, and the achromatic lenses.

These lenses could be aligned onto the APDs as they were mounted on a translation mount that could move laterally. Since this mount was on cage rods, the lens could also move axially so that the focal length of the lens matched the distance between the lens and the detector. One of the APDs detected green emission (535 nm – 607 nm) from the sample and the other APD detected red emission (659 nm – 699 nm). This was ideal for single-molecule FRET where a sensitive detector and both the colours red and green need to be detected separately.

The final stage of the design provided solid support for the module by attaching post mounts below each detection module. Holes for the Bayonet Neill-Concelman (BNC) cables from the APDs and the lid for the module was also designed to keep the module light-tight. A gap between the two APDs was also left for a controller case which could control the microscope.

2.3.4 Sample Stage and Lid

The final part that required designing was the sample stage for accommodation of single-molecule samples. A light-tight lid was also designed to prevent the ambient light entering the

microscope. Many microscopy techniques are commonly used in combination with inverted microscopes. These microscopes use stages, shown in Figure 2.17, that are ideal for imaging where the sample can move around by manually moving the stage.

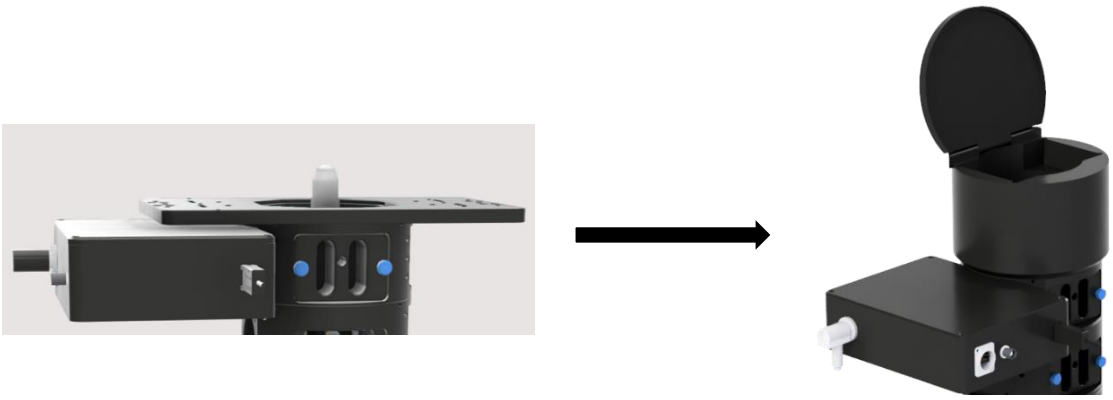

Figure 2.17. The sample stage (left) of the openFrame was replaced with a customised, light-tight lid (right).

Since we only need to detect fluorescence emission anywhere inside the sample, we opted for a design that had a specific sample placement layer that could be added onto the existing openFrame top layer. This layer needed to be bigger in size to accommodate a piezo z-stage which would allow the objective to move axially on the order of micrometres. Coarse adjustment of the objective was still allowed by a threaded tube attached below the piezo stage. This tube could then be locked with a nut to prevent large changes occurring when fine adjustments were being made. The lid was designed to sit back when open to allow for placement of the sample and when closed, was fully light-tight. Figure 2.18 shows the final design of the microscope showing all modules attached.

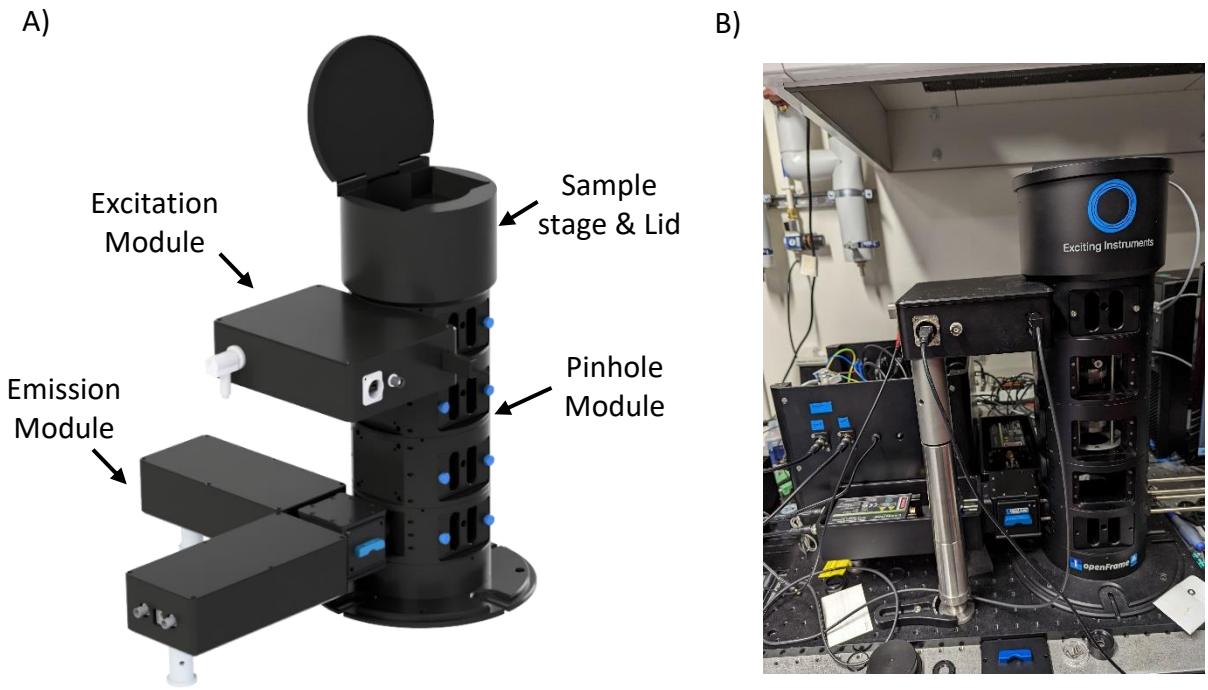

Figure 2.18. A) The fully designed openFrame with both detection and excitation modules attached B) A photograph of the CNC machined microscope with all the parts inside and modules attached.

2.3.5 Configurations

Due to the flexible nature of the openFrame, we imagine multiple configurations can be established besides the designed single-molecule FRET and FCS setup described above. For instance, a camera can be incorporated into the emission pathway to use for widefield microscopy (Figure 2.19). Widefield microscopy images the entire sample, although suffers from low signal to noise ratio. To use this technique the pinhole module would be removed, and a camera would be attached. Another particularly interesting setup would involve combining single-molecule FRET with a camera described in Chapter 6. This may allow for widefield or multiple smFRET experiments in the future. In addition, a three-colour single molecule emission module featuring three APDs instead of two would also be possible, allowing for three-colour smFRET experiments.

Figure 2.19. The openFrame design with a camera attachment used for super-resolution imaging and widefield microscopy.

This system can also be adapted for TIRF measurements. Here, one possibility would be to implement an objective micromirror design, after the excitation module. This would allow the excitation laser beam to be reflected off-centre at the back aperture of the objective lens, causing an evanescent wave at the surface of the coverslip. TIRF imaging would allow for samples to be immobilized onto the coverslip and observed with a camera. Super-resolution microscopy may also be implemented on the openFrame. Techniques such as Stochastic Optical Reconstruction Microscopy (STORM) or Photoactivated Localization Microscopy (PALM) and other single-molecule localisation experiments for live cell imaging should be possible on the current setup with minimal modifications. [10] Potentially in the future, modules catered for more complex techniques such as (Minimal Photon Fluxes) MINFLUX and structured illumination microscopy (SIM) may be developed allowing for vast improvements in spatial resolution. [11]

2.4 Conclusions & Further Design Suggestions

Here we present a design for an affordable, confocal single-molecule microscope. The openFrame system provides an excellent platform for flexible approaches to smFRET measurements and with some further development, could be made into a cost effect commercially available instrument. The flexibility of the three modules provides researchers with the starting blocks to measure single-molecule FRET and FCS experiments. We also expect researchers and the community to expand on the openFrame to make it applicable for many more techniques.

Since the production of these modules, there have been further modifications. The detectors in the excitation modules were too large, making the power switches located on the detectors, too difficult to reach. Here a larger excitation module may be the only option. Additionally, in the pinhole section, the cage rods were not fixed at both ends of the openFrame. This made it very difficult to align the pinhole and the corresponding lenses, due to the sensitive nature of both optical components. This has been temporarily fixed at both ends of the openFrame by adding a further cage rod and screwing it into the bottom layer of the openFrame. The openFrame focuses on ease of use, as all the light travels along the central axis, down through each of the layers, making the microscope easier to align. A more suitable alternative to an optical table is yet to be found, although we anticipate a vibration-free mountable breadboard might prove useful.

2.5 References

[1] T. Ha, T. Enderle, D. F. Ogletree, D. S. Chemla, P. R. Selvin, and S. Weiss, “Probing the interaction between two single molecules: Fluorescence resonance energy transfer between a single donor and a single acceptor,” *Proc. Natl. Acad. Sci. U. S. A.*, vol. 93,

no. 13, pp. 6264–6268, 1996

[2] A. N. Kapanidis, T. A. Laurence, K. L. Nam, E. Margeat, X. Kong, and S. Weiss, "Alternating-laser excitation of single molecules," *Acc. Chem. Res.*, 2005

[3] R. Strack, "The miCube open microscope," *Nat. Methods*, 2019

[4] A. Ingargiola, E. Lerner, S. Y. Chung, S. Weiss, and X. Michalet, "FRETBursts: An open source toolkit for analysis of freely-diffusing Single-molecule FRET," *PLoS One*, 2016

[5] P. R. Nicovich, J. Walsh, T. Böcking, and K. Gaus, "NicoLase - An open-source diode laser combiner, fiber launch, and sequencing controller for fluorescence microscopy," *PLoS One*, 2017

[6] P. G. Pitrone *et al.*, "OpenSPIM: An open-access light-sheet microscopy platform," *Nature Methods*. 2013

[7] J. T. Collins *et al.*, "Robotic microscopy for everyone: the OpenFlexure microscope," *Biomed. Opt. Express*, 2020

[8] B. Ambrose *et al.*, "The smfBox is an open-source platform for single-molecule FRET," *Nat. Commun.*, vol. 11, no. 1, p. 5641, 2020

[9] M. P. M. H. Benoit and H. Sosa, "Use of single molecule fluorescence polarization microscopy to study protein conformation and dynamics of kinesin–microtubule complexes," in *Methods in Molecular Biology*, vol. 1665, 2018, pp. 199–216.

[10] R. Henriques, C. Griffiths, E. H. Rego, and M. M. Mhlanga, "PALM and STORM: Unlocking live-cell super-resolution," *Biopolymers*, vol. 95, no. 5, pp. 322–331, 2011

[11] K. C. Gwosch *et al.*, "MINFLUX nanoscopy delivers 3D multicolor nanometer resolution in cells," *Nat. Methods*, vol. 17, no. 2, pp. 217–224, 2020

Chapter 3. An Open-source, Cost-Efficient Excitation Module for Single-molecule Microscopy

Publication accepted by Advanced Biology

An Open-source, Cost-Efficient Excitation Module for Single-molecule Microscopy

*Dylan R. George, Benjamin Ambrose, Ashley J. Cadby, Timothy D. Craggs**

The University of Sheffield, Western Bank, S10 2TN, United Kingdom

Keywords: Open-source, lasers, single-molecule microscopy, single-molecule FRET, FCS

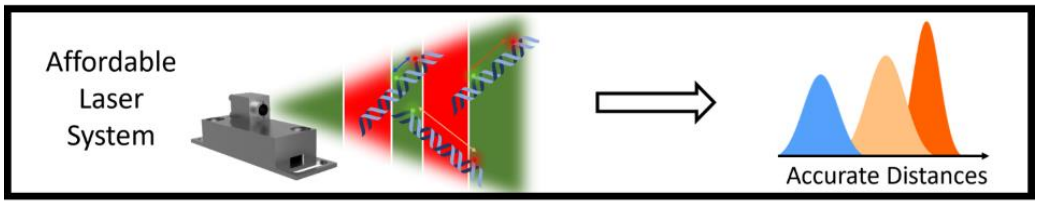

Contribution: DG wrote the manuscript and conducted construction of excitation module, performance tests, FCS and smFRET tests. BA helped analyse FCS data. AC and TC supervised the project and reviewed the manuscript.

Contents

3.	Abstract	73
3.1	Introduction	73
3.2	Hardware/ Methods	78
3.3	Results and Discussion	79
3.3.1	Power and power stability	79
3.3.2	Alternation rise and fall times for ALEX	81
3.3.3	Applications	82
3.3.3.1	smFRET	82
3.3.3.2	FCS	85
3.4	Discussion	86
3.5	Methods	88
3.5.1	Characterisation of the Laser diodes	88
3.5.2	Accurate smFRET Measurements	89
3.5.3	FCS measurements	90
3.6	References	90
3.7	Supplementary Material	93

3. Abstract

In fluorescence microscopy, scientific-grade laser diodes are key components and contribute a considerable expense to the total cost of the microscope setup. Existing open-source laser excitation modules are mainly designed for super-resolution imaging and have not been fully characterised to meet the standards of single-molecule spectroscopy measurements. In this paper we introduce an open-source, cost-efficient excitation module that can be used for confocal accurate single-molecule FRET, fluorescence correlation spectroscopy and low-power super-resolution techniques. The resulting excitation module delivers a 520 nm and 638 nm laser beam via a single-mode fibre that can be modulated on the microsecond timescale. By integrating this with easy-to-use software, we expect this will provide research groups with a way to address their single-molecule questions without incurring high costs.

3.1 Introduction

Fluorescence microscopy encompasses a range of biophysical imaging techniques such as epi-fluorescence, confocal and total internal reflection fluorescence (TIRF) microscopy. Fluorescent samples are excited by a high energy light source at specific wavelengths (typically a laser) and dichroic filters are used to separate the excitation light from the fluorescence emission to provide higher contrast than in conventional microscopy. Recently, some labs have provided a gateway into this area for non-specialists by publishing open-source microscopy platforms and software packages.[1] A range of fully open-source microscopy platforms are now currently available including: the miCube, capable of super-resolution microscopy, TIRF and LED brightfield microscopy;[2] the openSPIM, a light-sheet microscope; and the LifeHack microscope, which provides single-molecule localisation microscopy (SMLM) and live cell imaging.[3] Open-source projects also include common microscope components such as microfluidics systems, lasers and stages.[4–7] Open-source software for super-resolution

imaging has also been developed.[8–10] Previously, we introduced the smfBox, an open source single-molecule FRET microscopy platform to combat the high instrument costs and a lack of open-source hardware that has limited this technique's broad application by non-specialists.[11]

In general, the lasers for fluorescence microscopy applications incur a considerable expense. Since additional fluorophores with different spectra are often used to differentiate biological components, multiple lasers are employed to excite them. However, these laser setups, whether bought commercially or custom-made, often make up a large proportion of the overall cost of modern microscopes. Many fluorescence applications require different excitation specifications (in terms of laser powers and pulsed / alternation time periods) increasing the number of lasers needed. This makes it especially difficult to provide a universal excitation module that can be applied to all microscopy applications. Table 3.1 provides a short list of some of the most common fluorescence applications, their excitation requirements for normal operation and their key requirements.

Technique	Min. Number of Lasers	Approximate Power Range	Pulsed Time Period	Key Requirements
Confocal Single-molecule FRET with Alternating Laser Excitation (ALEX)	2	(Hundreds of) μW's	μs	Multiple Lasers
TIRF Single-molecule FRET with Alternating Laser Excitation (ALEX)	2	(Hundreds of) μW's	μs	Multiple Lasers
Fluorescence correlation spectroscopy (FCS)	1	(Hundreds of) μW- (Tens of) mW	CW	Stable power/ Fast modulation
Nano-second FCS (nsFCS)	1	(Hundreds of) μ W- (Tens of) mW	CW	Stable power/ Fast modulation
Fluorescence cross-correlation spectroscopy (FCCS)	2	(Hundreds of) μ W- (Tens of) mW	CW	Multiple Lasers
Single-molecule localization microscopy (SMLM)	1	(Ten's of) mW's - (Hundreds of) mW	CW	High laser power
Stimulated emission depletion (STED) microscopy	2	(Hundreds of) mW's	ps-fs	High laser power, multiple lasers
Light-sheet microscopy (LSM)	1	μW's	CW	Low laser power
Coherent raman scattering (CARS)	2	mW's	ps	Multiple lasers
Total internal reflection fluorescence (TIRF)	1	(Tens of) mW's	CW	Low laser power
Confocal	1	μW's-W's	CW	Low laser power
Structured illumination microscopy (SIM)	1	μW's-W's	CW	Low laser power
Widefield	1	μW's-W's	CW	Low laser power

Table 3.1. Common fluorescent applications, their excitation system requirements and primary expense.[12-15]

Over the last decade a few open source, affordable fluorescent laser systems have been developed (Table 3.2). However, these have mainly been targeted towards super-resolution imaging; For example, the low-cost, continuous wave Laser Engine (from Schroder et al.) which provides a homogeneous, scatter-free laser beam through a multi-mode fibre vital for single-molecule localisation microscopy.[5] The NicoLase (from Nico et al.) caters to a broader

range of applications with many different lasers in the visible spectrum and provides a full characterisation of the alternation of the lasers required for many single-molecule applications, albeit using higher-end laser diodes which may significantly add to the cost of the setup.[6]

Author	No. of Lasers	Wavelengths	Power	Modulation	Fibre	Key Application
Schroder *et al.*	3	405 nm, 488 nm, 638 nm (561 nm option)	(Hundreds of) mW	N/A	Multi-mode	Single-molecule localisation microscopy
Nico *et al.*	5	405 nm, 490 nm, 517 nm, 561 nm, 640 nm	(Hundreds of) mW's	Arduino Uno	Single-mode & Multi-mode	Fluorescence/super-resolution
This Work	2	520 nm, 638 nm	(Tens of) mW's	NI DAQ board	Single-mode	Single-molecule FRET, FCS

Table 3.2. A list of current open-source laser excitation modules; their properties and their primary application.[5-6]

While these open-source excitation modules are available, many researchers have not incorporated them into single-molecule spectroscopy methods as a full characterisation of their properties and suitability for this type of application has been lacking. This is particularly true for single-molecule FRET applications, in which precise modulation on the microsecond timescale and stable laser powers are crucial to achieve accurate FRET measurements. Here, we present, an open source, affordable and fully characterised excitation module capable of accurate single-molecule FRET and fluorescence correlation microscopy. This excitation module overcomes the cost of commercial pulsed laser systems whilst still offering high laser stability and precise modulation. This module reduces the cost of the smfBox by ~50%,

allowing more researchers to harness the power of single-molecule FRET in their research, whilst simultaneously reducing the cost and time taken to build an excitation system.

In single-molecule FRET, alternating laser excitation (ALEX) provides information about the presence of both donor and acceptor fluorophores.[16] In confocal smFRET, molecules freely diffuse through a near-diffraction limit spot formed by focussing expanded, collimated laser light through an objective lens. During the transit of this confocal volume, donor and acceptor fluorophores attached to an individual molecule are alternately excited by two lasers, leading to the emission of a burst of photons. These bursts can then be classified by their FRET efficiency and stoichiometry, an additional dimension, which defines the presence of the acceptor fluorophore (see methods). By using ALEX, donor only, acceptor only and dual labelled populations can be identified, and all the correction factors determined for generating accurate FRET efficiency values (see methods).[17, 18] Here we provide a full excitation module characterisation and explain in depth how to alternate these laser modules to achieve accurate single-molecule FRET (ALEX) and fluorescence correlation spectroscopy (FCS) measurements.

2. Hardware/ Methods

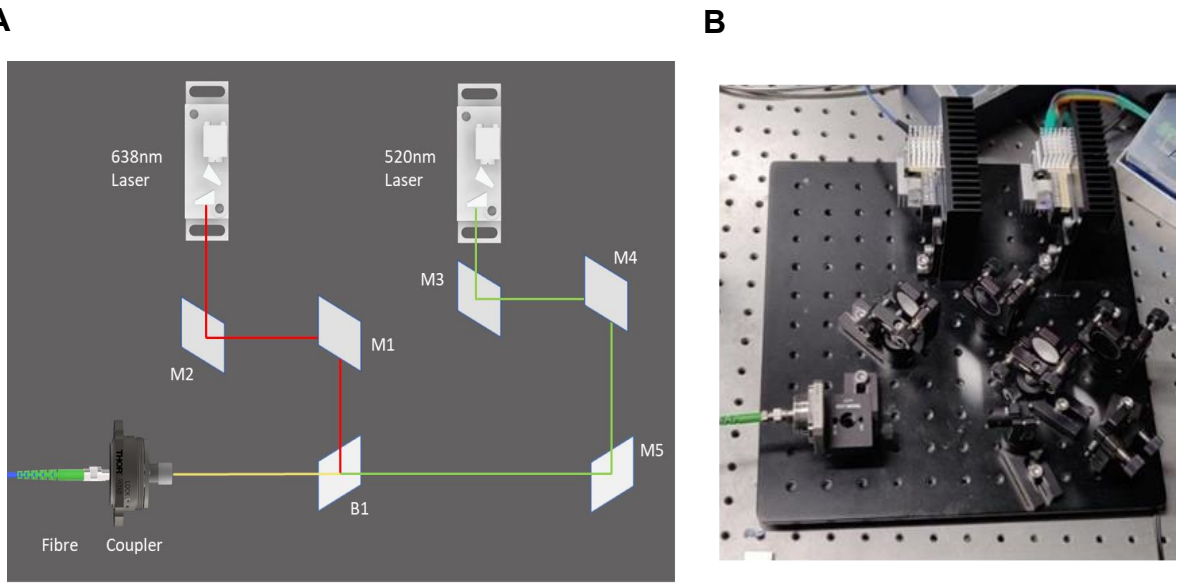

Figure 3.1. A) A schematic showing the excitation pathway of the module. Red and green line shows the path of the laser beams travelling towards the coupler. The mirrors (M1-M5) are used to align the laser beam. A dichroic beamsplitter (B1) reflects the red laser beam and allows the green laser beam to travel through. Both laser beams are then coupled into a fibre via a coupler. Further details (including part numbers) are found in supplementary information 1.1) B) A photograph of the finished excitation module showing the excitation in the same orientation as the schematic.

For single-molecule FRET (ALEX) the laser diodes need to be modulated at a frequency of 20 KHz at the wavelengths of 515 nm and 638 nm. Additionally, we require laser powers of around a few hundred microwatts at the objective lens. The system also needs to be coupled to a single-mode fibre to provide a single excitation spot. The single-mode fibre provides a Gaussian beam profile for forming a high-quality confocal excitation volume.

The chosen lasers (520 nm at 100 mW and 638 nm at 700 mW, Lasertack) met all these requirements and were chosen primarily for their low cost (< € 500). These wavelengths are popular for single-molecule FRET setups as they efficiently excite a range of commonly used donor (520 nm) and acceptor (638 nm) fluorophores. Although the power of the lasers is an order of magnitude higher than the requirements for single-molecule experiments, a single-mode fibre as previously mentioned, was required and so we anticipated a low coupling

efficiency. However, even with the achieved coupling efficiency of around 4 % (638 nm laser) and 25 % (515 nm laser) a power of 26 mW and 25 mW was delivered out of the fibre, higher than the requisite power.

The laser modules were mounted on aluminium heatsinks (100 mm x 100 mm x 30 mm, Fischer Electronik). These heatsinks were then mounted onto a 300 mm x 300 mm optical breadboard (MB3030/M, Thorlabs). The laser modules were aligned using two kinematic mirrors (KM05/M, Thorlabs) which steered the beam onto a dichroic mirror (DMLP567T, Thorlabs). The dichroic mirror combined the laser beams before a Fibreport (PAF2A-A15A, Thorlabs) coupled the beam into a single-mode fibre (P3-488PM-FC-10, Thorlabs).

To control the lasers, a modulation voltage of 5 V was delivered to the lasers at a frequency of 20 KHz. A National Instruments (NI) DAQ board was used to deliver the modulating voltage signal, controlled using the smOTTER software (available on GitHub, https://github.com/craggslab/smfBox). Alternatively, a simple LABVIEW program (supplied in the supplementary material) can be used.

3.3 Results and Discussion

3.3.1 Power and power stability

A full characterisation of the laser modules was required to check whether the excitation module was able to perform single-molecule experiments. To check whether the module needed excitation filters the wavelength spectrum of both the 520 nm and 638 nm laser modules was recorded (Figure 3.2). The wavelength of the green laser diode ranged from 512 nm – 526 nm and the spectrum of the red laser diode 630 nm – 644 nm (Figure 3.2). The resulting

spectrum from both lasers was within the range expected and was sufficiently tight for single-molecule experiments without any excitation filters.

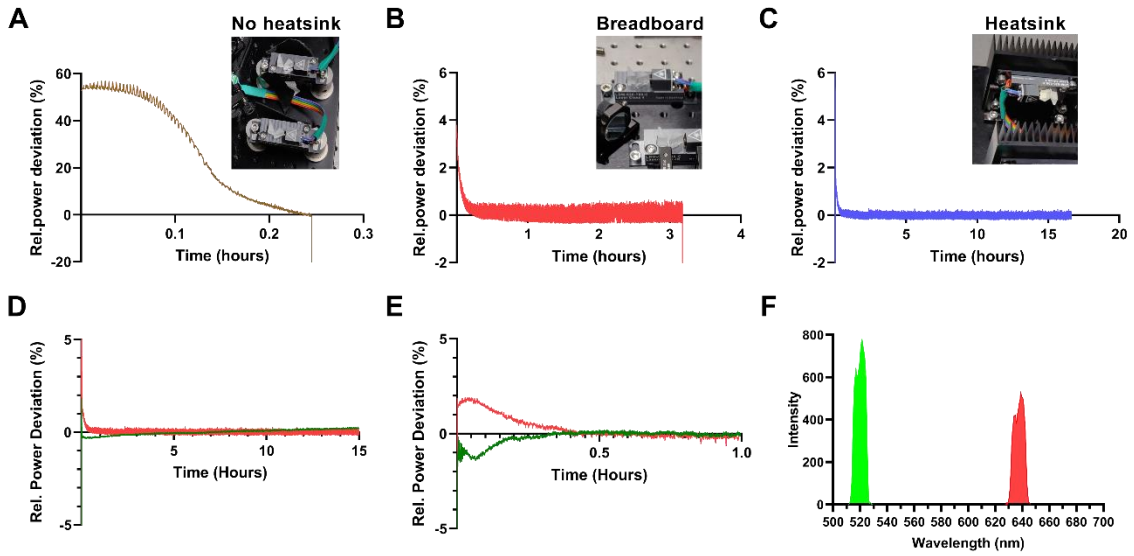

Figure 3.2. A-C) The power stability of the lasers with different heat dissipation mountings: posts alone (A), breadboard (B) and heatsinks (C) D) Relative power stability for green laser (green) and red laser (red) under continuous wave mode E) Relative power stability for both lasers under 20 kHz alternation F) The wavelength spectrum of the 520 nm 100 mW and the 638 nm 700 mW lasers.

Since single-molecule measurements are taken on short timescales (ms), inconsistencies in laser power on this timescale can give differences in fluorescent emission. This is particularly important in single-molecule FRET and FCS, where instabilities in laser power can affect the accuracy of results. In the initial design, the laser modules were placed on pedestal posts. A power stability assessment of the red laser module on these posts revealed that the laser power was particularly unstable. Additionally, the laser module switched off after less than 30 mins, below the acquisition period required for single-molecule FRET experiments. The laser modules were then mounted on an aluminium breadboard to improve heat dissipation. On the breadboard, the laser module had a mean relative stability percentage of 0.083 % with a standard deviation of 0.20 % and switched off after just over 3 hours. Finally, the laser modules were mounted on heatsinks. On the heatsinks, the laser module had a mean relative stability

percentage (M) of -0.03 % with a standard deviation (SD) of 0.10%. Furthermore, the laser beam remained stable and active for over 15 hours, well above the acquisition time required for single-molecule FRET experiments. The power stability test was repeated for the green laser (mounted on the heat sink) which showed a similar performance (M= 0.004 %, SD=0.14 %, Figure 3.2E). The laser modules were also alternated on and off for time periods of 45 μs on and 55 μs off using the single-molecule FRET acquisition software (smOTTER). After a 30 minute warm up time the laser modules showed high stability (Red - M = -0.08%, SD = 0.11 %, Green - M = 0.002 %, SD = 0.07 %), sufficient for single-molecule FRET measurements.

3.3.2 Alternation rise and fall times for ALEX

To achieve accurate FRET values, alternating the red and green lasers at a frequency of around 20 KHz was required. The lasers were alternated by the single-molecule FRET acquisition software (smOTTER). The output of the fibre was coupled to a photodiode, to measure the laser power with high (ns) time resolution. Initial results showed that the lasers in the excitation module could indeed be successfully modulated at the required microsecond timescales (Figure 3.3). We next investigated the rise and fall times of the lasers and compared them to the commercially available laser combining system currently used on the smfBox. Analysis fitting an exponential function to this data was conducted and the half-life of both laser systems was determined (supplementary material Table 3.6 and Table 3.7). We found that the half-life of the commercially available lasers (Omicron LightHUB) fall and rise times ranged from 0.89 μs to 0.96 μs. In contrast, we found the half-life for the excitation module rise and fall times ranged from 2.3 μs to 3.6 μs. While the rise and fall time of the excitation module performed slightly worse than the currently used lasers on the smfBox, crucially, these values were still within the acceptable range for obtaining high quality single-molecule FRET data.

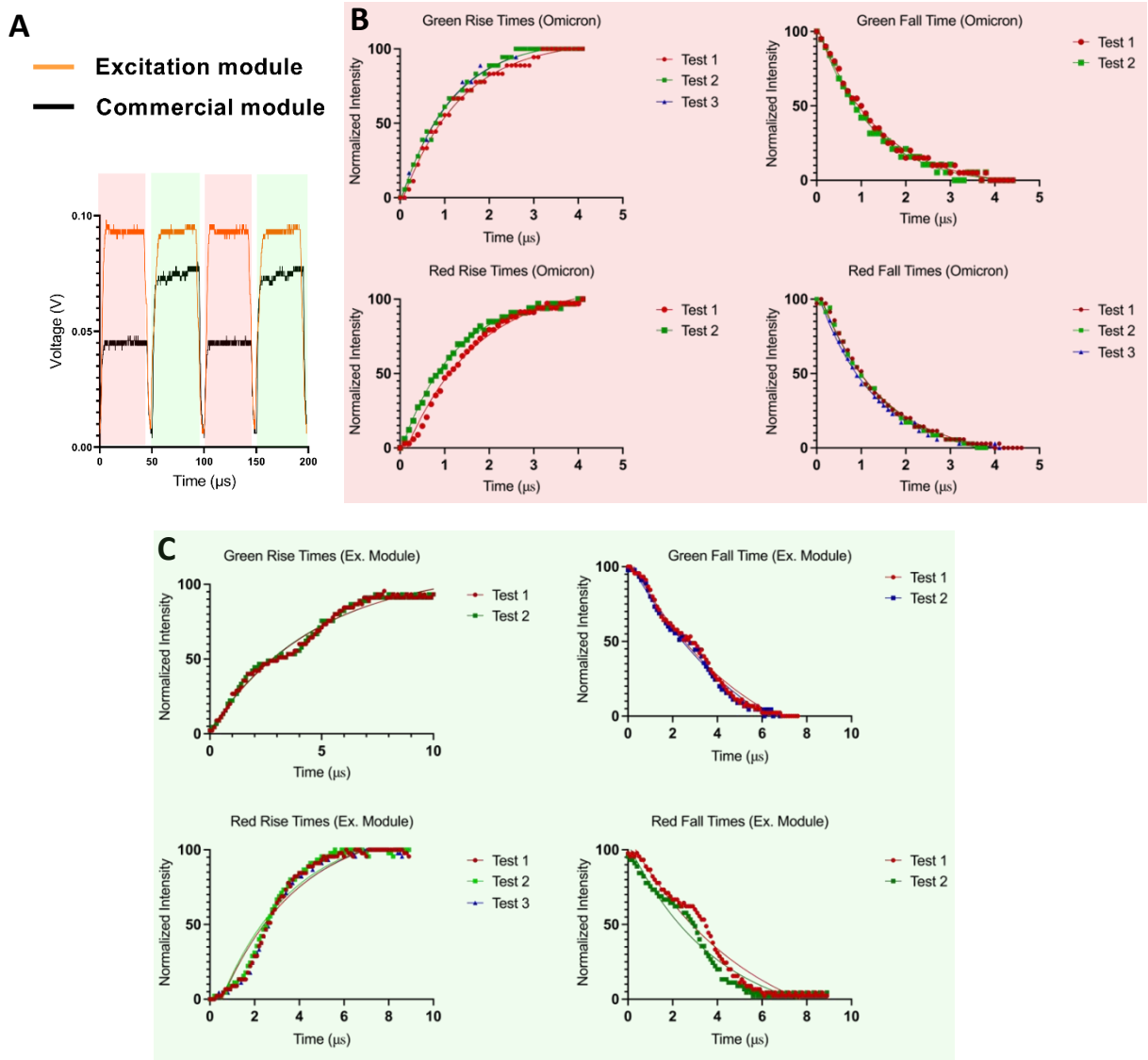

Figure 3.3. A) Time-resolved measurements of the laser power measured by a photodiode B) The rise and fall times of the green laser of both the commercially available laser (omicron laser system) and the excitation module. C) The rise and fall times of the red laser of both the commercially available laser and the excitation module. An exponential curve was fitted to the multiple tests conducted.

3.3.3 Applications

3.3.3.1 smFRET

Since the results of the characterisation of the laser modules were sufficient for single-molecule FRET measurements, the excitation module was used on the smfBox to take smFRET

measurements. Three double-stranded DNA samples were used, given their well characterised FRET values in the literature.[18] These samples are labelled with ATTO 550 (donor) and ATTO 647N (acceptor) with the donor dye positioned at 23bp, 15bp and 11bp away from the acceptor dye. These three DNA standards have reported FRET Efficiency values of 0.15±0.02, 0.56±0.03 and 0.76±0.015, respectively, as measured in a recent blind multi-lab study. [11, 18]

The procedure for determining accurate FRET efficiencies for absolute distance measurement is well documented in the literature. To yield accurate FRET efficiency values, both the uncorrected stoichiometry and the uncorrected FRET efficiency (proximity ratio) must be determined using alternating laser excitation (ALEX). The uncorrected stoichiometry provides a pathway for the identification of acceptor only and donor only populations. Both the stoichiometry and uncorrected FRET efficiency are calculated via Equation 3.1 and 3.2 where D_{ex} and D_{em} represent donor excitation and donor emission, respectively. Conversely, the symbols A_{ex} and A_{em} represent the acceptor excitation and acceptor emission. For instance, $D_{ex}A_{em}$ is the acceptor emission when under donor excitation.

$$S = \frac{D_{ex}D_{em}+D_{ex}A_{em}}{D_{ex}D_{em}+ D_{ex}A_{em} +A_{ex}A_{em}} \tag{3.1}$$

$$E^* = \frac{D_{ex}A_{em}}{D_{ex}D_{em}+ D_{ex}A_{em}} \tag{3.2}$$

To determine these parameters, Jupyter notebooks from the smfBox GitHub along with FRETBursts were used.[19] The correction factors used to find accurate FRET efficiency values were then determined. The first two correction factors α and δ are found to determine the donor fluorescence leakage into the acceptor channel and the direct excitation of the acceptor with the donor laser, respectively. Using the average values for both α and δ for all three samples,

the correction factors γ and β were determined. The correction factor γ describes the differences in the donor and acceptor detection efficiency and the fluorescence quantum yields. The correction factor β describes the excitation efficiency inequality of both dyes and considers the cross-sections of the fluorophores (see supplementary information).

To compare the results, Table 3.3 shows the FRET efficiency values of a benchmark study measuring these duplex DNA strands from 20 independent research groups (Hellenkamp et al., 2018). The table also contains the FRET values of these samples on the smfBox obtained using commercial lasers.[11] By implementing the excitation setup on the smfBox FRET efficiency values for the samples 1a, 1b and 1c were 0.198±0.02, 0.599±0.17 and 0.793±0.09, respectively (Figure 3.4). The results were consistent with the literature values of the 20 independent research groups, however, were not statistically significant compared to the literature values in Table 3.3. Overall, these results indicate that the excitation module can reproduce accurate FRET values.

	Hellenkamp et al., 2018	Ambrose et al., 2020	Excitation Module Data		Correction factors			
Sample	E	E	E	N bursts	α	δ	γ	β
1a	0.15 ±0.02	0.17 ±0.07	0.198 ±0.04	367	0.086	0.11	0.63	0.50
1b	0.56 ±0.03	0.57 ±0.10	0.599 ±0.04	471				
1c	0.76 ±0.015	0.77 ±0.07	0.793 ±0.006	450				

Table 3.3. Comparison of the excitation module to literature values.

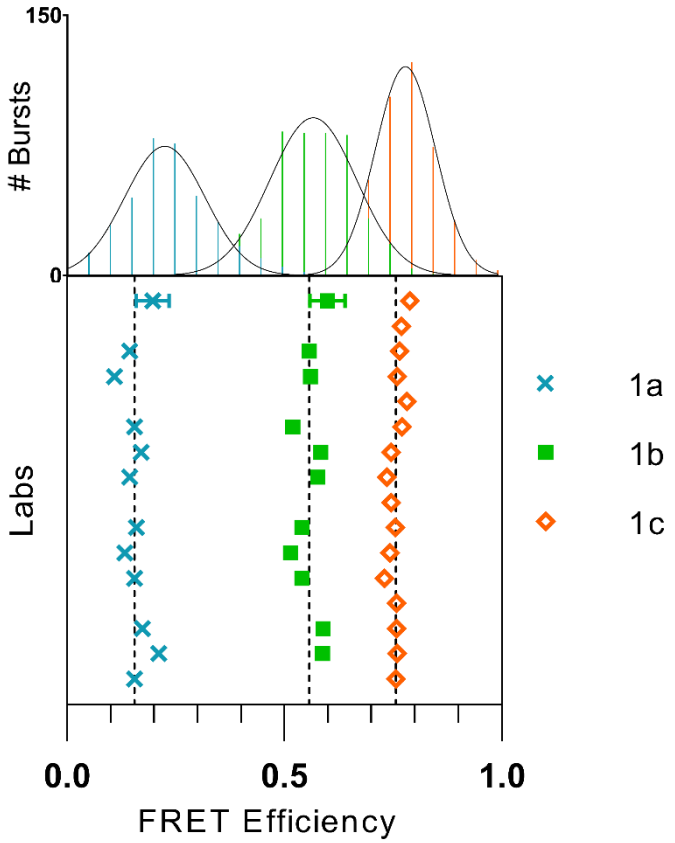

Figure 3.4. A graph showing the FRET efficiencies using the excitation module compared to the benchmark study.[18] The samples 1a, 1b and 1c represent low, medium and high FRET samples, respectively. The results from the excitation layer and the FRET histogram of the excitation module are also shown at the top of the figure. These data points have error bars calculated from the standard deviation of the repeats. The 1c sample has error bars that are too small to be seen in this graph. Compared with this is the data from different labs represented by the colours in the legend. The dashed line shows the mean FRET efficiency of the labs in the benchmark study.

3.3.3.2 FCS

Fluorescence correlation spectroscopy provides insights into the diffusion behaviour and absolute concentration of molecules by recording the fluctuation of fluorescence intensity in the observation volume. We previously measured the diffusion coefficient and molecular brightness for a duplex DNA sample on the smfBox using commercial lasers.[11] To check if the excitation module could reproduce similar results the same DNA duplex sample (1a) was placed on the smfBox. Figure 3.5 shows the autocorrelation curve of a Rhodamine 6G sample

which was used to determine the confocal volume and the diffusion coefficient of the duplex DNA sample.

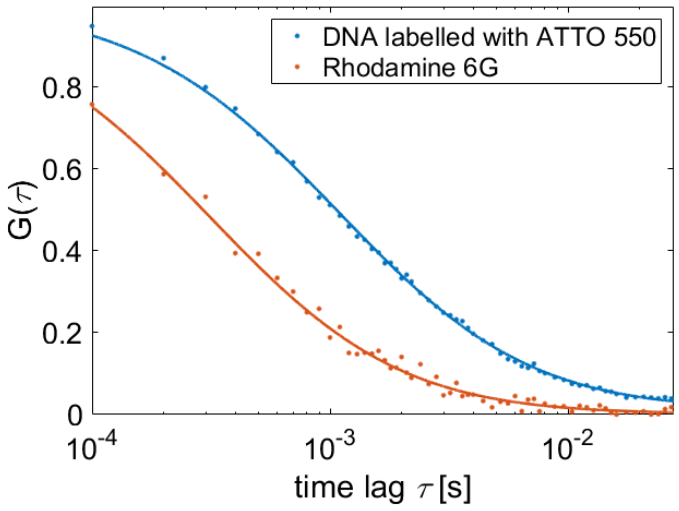

Figure 3.5. Fluorescence correlation spectroscopy measurements taken on Rhodamine 6G (orange) and a concentrated sample of ATTO 550 labelled DNA (blue) showing an autocorrelation curve.

The diffusion coefficient of the duplex DNA was measured as 118 $\mu m^2/s$. This was different by approximately 25% from the previous measurement on the smfBox, using the commercial lasers, of 88 $\mu m^2/s$.

3.4 Discussion

Here we present an affordable excitation module (costing > £ 2500) capable of fluorescence applications such single-molecule FRET and fluorescence correlation spectroscopy. This excitation module differs from existing modules, such as Schroder *et al.* and Nico *et al.* set out in the introduction, by using low-cost laser diodes inside a setup specifically designed for single–molecule spectroscopy measurements. Our data obtained using this excitation module shows that accurate FRET efficiencies and diffusion coefficients can be measured successfully. However, unlike the Nicolase and the Laser Engine, which can perform super-resolution imaging techniques, the power output of this module (~20 mW) likely falls short of the more

power-hungry super-resolution applications such as STED and single-molecule localization microscopy. We also believe that the system will not be able to achieve CARS due to much faster modulation requirements. Nevertheless, due to the power and alternation requirements of microscopy applications described in the introduction we do anticipate the system will be used for FCCS, light-sheet, TIRF, confocal, SIM and widefield microscopy.

For these lasers to work effectively over the timescales and stability needed for smFRET, a series of experiments stabilising the temperature and allowing faster heat dissipation was key. Here, we were successful by mounting these lasers on heatsinks, one issue we faced was the time the lasers needed to warm-up (~20 minutes), which still arose on the second time they were switched on in close succession. However, characterising these lasers in terms of the rise times, fall times and spectrum demonstrated they could function successfully for single-molecule measurements without further modifications such as excitation filters. A simple improvement could be made by implementing a variable neutral density filter in front of each laser. This will allow the power of the lasers to be controlled.

Since using a single-mode fibre to provide a Gaussian beam is required for confocal single-molecule measurements, a drawback of using this module was the difficulty of aligning both lasers for obtaining high coupling efficiency. Care is also needed to avoid disturbing the alignment due to the sensitivity of the setup. Although, we believe that this could be improved by ensuring the optics are well secured to the breadboard and stored in a solid container. This module also makes use of an expensive NI-DAQ board to drive the microsecond alternation of the lasers. In the future, it would be more economical to implement the software to run from an Arduino or alternative. However, whilst such a solution may provide the alternation

requirements, the single-photon counting electronics currently remains beyond such devices.

To conclude, this excitation module can be used for accurate single-molecule techniques at a very low-cost. This system performs well for FCS and smFRET experiments providing sufficient power and fast modulation of the lasers. We anticipate this simple to build, cost effective setup will be utilised in future single-molecule FRET and FCS setups.

3.5 Methods

3.5.1 Characterisation of the Laser diodes

Characterisation of the wavelength spectrum: The 520 nm and 638 nm lasers (Lasertack) on the setup were powered on and the fibre was connected to a lens tube (SM1S20, Thorlabs). A spectrometer (Ocean Optics) was then connected to the opposite side of the lens tube facing the fibre. A neutral density filter was placed in the lens tube to avoid saturation of the spectrometer. The resultant wavelength of each of the lasers was recorded separately.

Characterisation of the power stability: An optical power meter was placed in a lens tube (Thorlabs). The optical fibre from the excitation module was then placed in the lens tube facing the power meter. The 520 nm and 638 nm lasers (Lasertack) were then recorded separately in continuous mode and under alternation (45 μs on, 55 μs off) for 15 hours and 1 hour, respectively.

Characterisation of the modulation timescales: The 520 nm and 638 nm lasers (Lasertack) on the setup were powered on and the alternation script from smOTTER was then run. A photodiode (Thorlabs) was connected to a lens tube (Thorlabs) and the fibre was placed in the tube. The voltage of the photodiode was recorded on an oscilloscope (Tektronix 2014B).

3.5.2 Accurate smFRET Measurements

Three duplex DNA standards were labelled with ATTO 550 23bp, 15bp and 11bp away from the acceptor dye, ATTO 647N (supplementary information). The DNA duplex samples were diluted to approximately 25 pM with an observation buffer (20 mM $MgCl_2$, 5 mM NaCl, 5 mM Tris, pH 7.5). A volume of 10 μL was pipetted onto a coverslip enclosed in an airtight gasket and the data was recorded using the smfBox. Single-molecule analysis was performed using Anaconda with Jupyter Notebooks and using the FRETBursts python module. To account for the additional red laser power (0.6 mW) exceeding the commercial laser module power for common smFRET experiments, the alternation period for the red laser was reduced 15 μs / 100 μs cycles, whilst the green laser stayed on for 75 μs / 100 μs cycles. The background was corrected with a reduced threshold of L = 10 and F = 20, compared to previous studies to account for a lower laser power. The spectral cross-talk factors α and δ were determined by defining a donor only population >0.95 and an acceptor only population <0.2 (supplementary information). The stoichiometry and FRET efficiencies of the from all three DNA standards were plotted and fitted to obtain the last correction factors γ and β. The corrected FRET efficiencies were then determined using these four correction factors.

Name	Sequence
1a	5’ – GAG CTG AAA GTG TCG AGT TTG TTT GAG TGT TTG TCT GG – 3’ 3’ – CTC GAC TTT CAC AGC TCA AAC AAA CTC ACA AAC AGA CC – 5’ – biotin
1b	5’ – GAG CTG AAA GTG TCG AGT TTG TTT GAG TGT TTG TCT GG – 3’ 3’ – CTC GAC TTT CAC AGC TCA AAC AAA CTC ACA AAC AGA CC – 5’ – biotin
1c	5’ – GAG CTG AAA GTG TCG AGT TTG TTT GAG TGT TTG TCT GG – 3’ 3’ – CTC GAC TTT CAC AGC TCA AAC AAA CTC ACA AAC AGA CC – 5’ – biotin

Table 3.4. Accurate FRET standards used in the previous studies. Highlighted base pairs in red (acceptor) are labelled with ATTO 647N and the base pairs in green are labelled with ATTO

550. Biotin was also labelled for surface immobilisation for TIRF experiments, which were not used in this study.

3.5.3 FCS measurements

The green laser was turned on and the Rhodamine 6G solution was diluted with water until the smfBox measured ~25 KHz. A 2 minute acquisition period was recorded. A known diffusion coefficient of 414 $\mu m^2/s$ for Rhodamine 6G was then used as a standard to determine the confocal volume. A dilute doubly labelled DNA standard as previously described was placed on the smfBox using the same method and was recorded.

The diffusion coefficient and molecular brightness were then calculated in the MATLAB software package PAM.[20] First, the signal from the observation volume was recorded over time and used to calculate an autocorrelation curve (Figure 3.6) using Equation 3.3:

$$G(\tau) = \frac{<I_0(t).I_0(t+\tau)>}{<I_0(t^2)>} - 1 \,. \tag{3.3}$$

The decay of the autocorrelation curve depends on the rate of diffusion of the sample. A 3D diffusion model shown in Equation 3.4 was then used to fit this curve:

$$G(\tau) = \frac{1}{N_p}\left(1 + \frac{\tau}{\tau_D}\right)^{-1} \frac{1}{\sqrt{1+\frac{w_0^2\,\tau}{z_0^2\,\tau_D}}} \,. \tag{3.4}$$

3.6 References

[1] G. E. Fantner and A. C. Oates, “Instruments of change for academic tool development,” *Nature Physics*, vol. 17, no. 4. pp. 421–424, 2021

[2] R. Strack, “The miCube open microscope,” *Nat. Methods*, 2019

[3] P. G. Pitrone *et al.*, “OpenSPIM: An open-access light-sheet microscopy platform,” *Nature Methods*. 2013

[4] P. Almada *et al.*, “Automating multimodal microscopy with NanoJ-Fluidics,” *Nat. Commun.*, 2019

[5] D. Schröder, J. Deschamps, A. Dasgupta, U. Matti, and J. Ries, “Cost-efficient open source laser engine for microscopy,” *Biomed. Opt. Express*, 2020

[6] P. R. Nicovich, J. Walsh, T. Böcking, and K. Gaus, “NicoLase - An open-source diode laser combiner, fiber launch, and sequencing controller for fluorescence microscopy,” *PLoS One*, 2017

[7] J. T. Collins *et al.*, “Robotic microscopy for everyone: the OpenFlexure microscope,” *Biomed. Opt. Express*, 2020

[8] M. Ovesný, P. Křížek, J. Borkovec, Z. Švindrych, and G. M. Hagen, “ThunderSTORM: A comprehensive ImageJ plug-in for PALM and STORM data analysis and super-resolution imaging,” *Bioinformatics*, 2014

[9] M. Müller, V. Mönkemöller, S. Hennig, W. Hübner, and T. Huser, “Open-source image reconstruction of super-resolution structured illumination microscopy data in ImageJ,” *Nat. Commun.*, 2016

[10] S. Culley *et al.*, “Quantitative mapping and minimization of super-resolution optical imaging artifacts,” *Nat. Methods*, 2018,

[11] B. Ambrose *et al.*, “The smfBox is an open-source platform for single-molecule FRET,” *Nat. Commun.*, vol. 11, no. 1, p. 5641, 2020,

[12] A. N. Kapanidis, T. A. Laurence, K. L. Nam, E. Margeat, X. Kong, and S. Weiss, "Alternating-laser excitation of single molecules," *Acc. Chem. Res.*, 2005

[13] O. Krichevsky and G. Bonnet, "Fluorescence correlation spectroscopy: The technique and its applications," *Reports Prog. Phys.*, vol. 65, no. 2, pp. 251–297, 2002

[14] P. Kask, P. Piksarv, and U. Mets, "Fluorescence correlation spectroscopy in the nanosecond time range: Photon antibunching in dye fluorescence," *Eur. Biophys. J.*, vol. 12, no. 3, pp. 163–166, 1985

[15] M. Bates, S. A. Jones, and X. Zhuang, "Stochastic optical reconstruction microscopy (STORM): A method for superresolution fluorescence imaging," *Cold Spring Harb. Protoc.*, vol. 8, no. 6, pp. 498–520, 2013

[16] N. K. Lee *et al.*, "Accurate FRET measurements within single diffusing biomolecules using alternating-laser excitation," *Biophys. J.*, 2005

[17] J. Hohlbein, T. D. Craggs, and T. Cordes, "Alternating-laser excitation: Single-molecule FRET and beyond," *Chemical Society Reviews*, vol. 43, no. 4. pp. 1156–1171, 2014,

[18] B. Hellenkamp *et al.*, "Precision and accuracy of single-molecule FRET measurements—a multi-laboratory benchmark study," *Nat. Methods*, 2018,

[19] A. Ingargiola, E. Lerner, S. Y. Chung, S. Weiss, and X. Michalet, "FRETBursts: An open source toolkit for analysis of freely-diffusing Single-molecule FRET," *PLoS One*, 2016,

[20] W. Schrimpf, A. Barth, J. Hendrix, and D. C. Lamb, "PAM: A Framework for Integrated Analysis of Imaging, Single-Molecule, and Ensemble Fluorescence Data," *Biophys. J.*, 2018

3.7 Supplementary Material

3.7.1 Excitation module parts

Part	Product information	Part	Product information
2x Lasertack Laser Diode	638 nm, (700 mW), 520 nm, (100 mW)	45 deg Mirror Mount	H45A
4x Table Clamp	CL5	Dichroic Mirror	DMLP567T
2x LED Heatsink (Fischer Elektronik)	SK 508 100 SA	FibrePort	PAF2A-A15A
7x Universal Pole Holder	UPH1	Post Mounting Bracket	HCP
7x Optical Posts	TR30/M-P5	Patch Cable, PM, 488 nm	P3-488PM-FC-2
6x Kinematic Mirror Mount	KM05/M	M6 Cap Screws	SH6MS16V
5x Mirrors	PF05-03-G01	Breadboard	MB3030/M

Table 3.5. List of all the parts (all from Thorlabs unless stated otherwise).

	Commercially available red rise time	Commercially available green rise	Commercially available red fall time	Commercially available green fall time
Half-life	0.96 μs	0.89 μs	0.93 μs	0.89 μs
R^2	0.99	0.99	0.99	0.99

Table 3.6. A table showing the mean half-life and R squared values of the commercially available (Omicron laser system) rise and fall times for both the green and red laser. These values were determined by using the mean of multiple test runs.

	Excitation module red rise time	Excitation module green rise	Excitation module red fall	Excitation module green fall
Half-life	2.3 μs	3.3 μs	3.1 μs	3.6 μs
R^2	0.95	0.98	0.96	0.98

Table 3.7. A table showing the mean half-life and R squared values of the excitation module rise and fall times for both the green and red laser. These values were determined by using the mean of multiple test runs.

3.7.3 FRET Efficiency Data

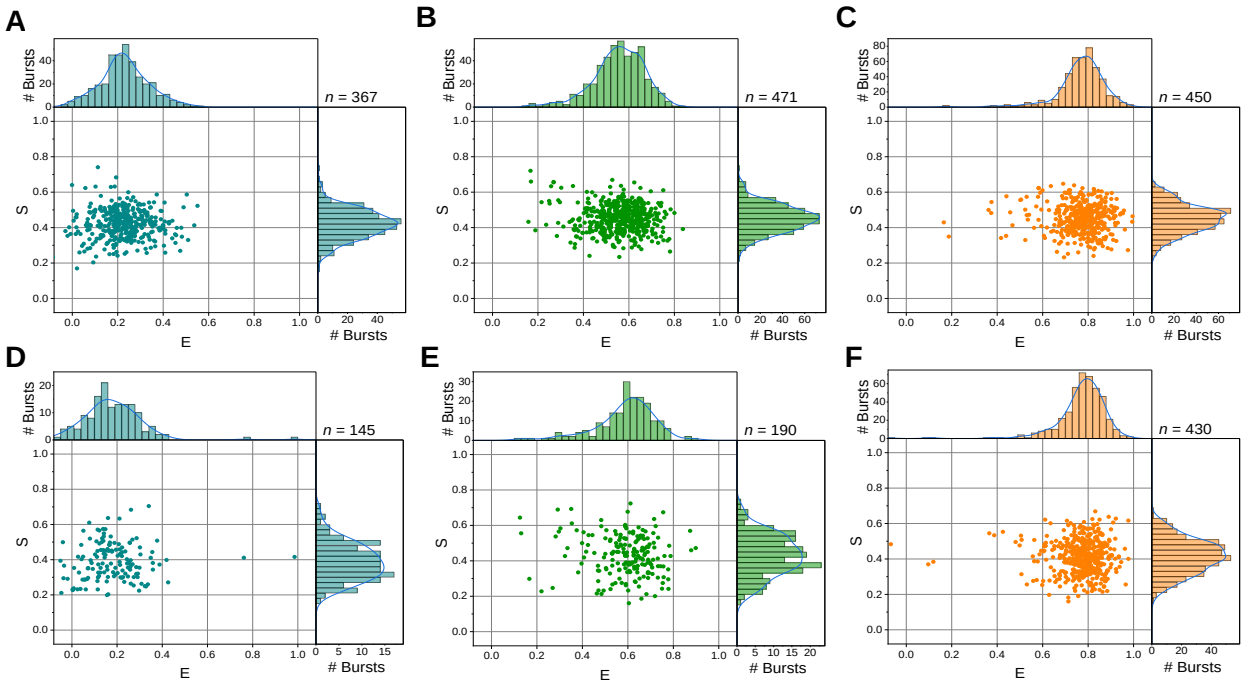

Figure 3.6. E-S histograms for the samples 1a, 1b and 1c. A-C) 1a-1c E-S histograms D-F) 1a-1c repeat experiment E-S histograms.

1a	1b	1c
0.225	0.570	0.784
0.171	0.628	0.793

Table 3.8. FRET Efficiency values for the samples; 1a, 1b and 1c.

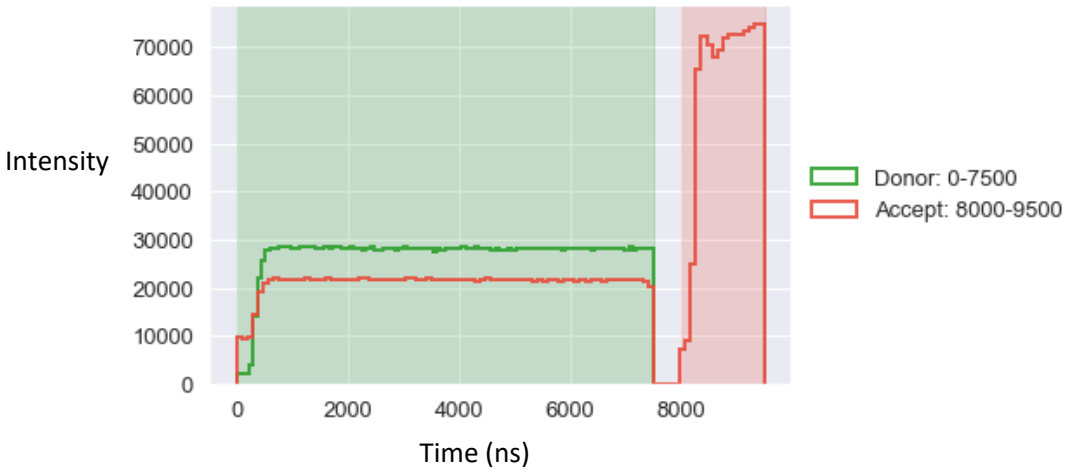

Figure 3.7. Alternation cycle of the laser diodes.

3.7.4 Finding α and δ Correction factor

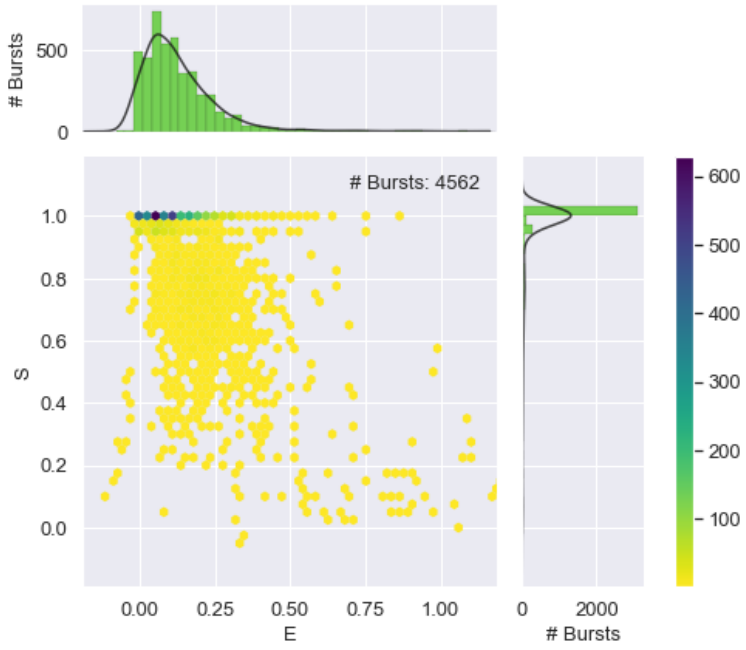

Figure 3.8. Uncorrected E-S histogram for sample 1a, used to determine bursts in the donor only and acceptor only region.

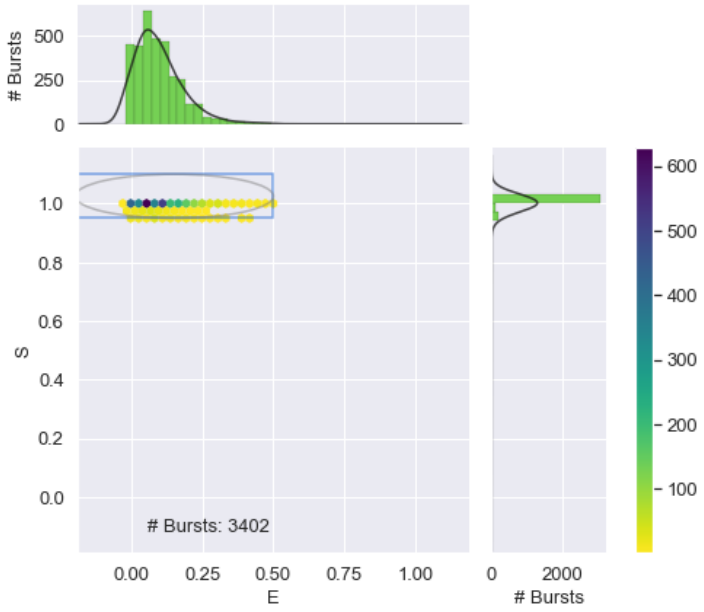

Figure 3.9. Uncorrected E-S histogram for sample 1a, highlighting the donor only region (S >0.95).

The donor only single-molecule events are used to calculate α (the photons emitted by donor detected by the acceptor detector) by Equation 3.5:

$$\alpha = \frac{E_{donor\ only}}{(1 - E_{donor\ only})} \tag{3.5}$$

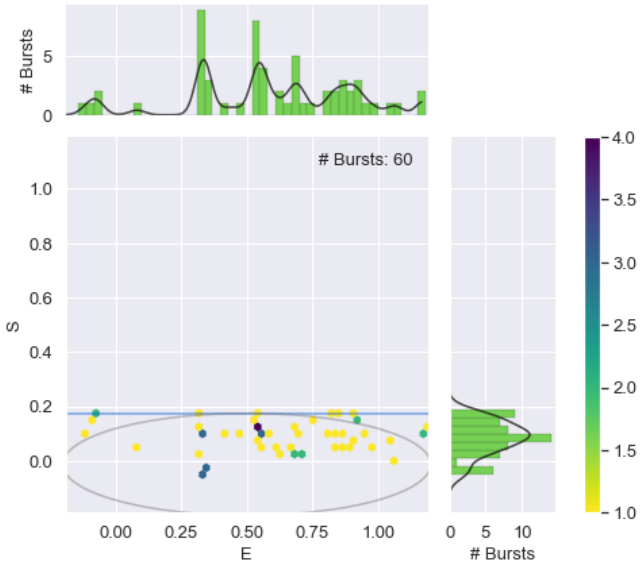

Figure 3.10. Uncorrected E-S histogram for sample 1a, showing the acceptor only region (S < 0.2).

The acceptor only single-molecule events are used to calculate δ (the direct excitation factor) via Equation 3.6:

$$\delta = \frac{S_{acceptor\ only}}{(1 - S_{acceptor\ only})} \tag{3.6}$$

3.7.5 Finding γ + β correction factor

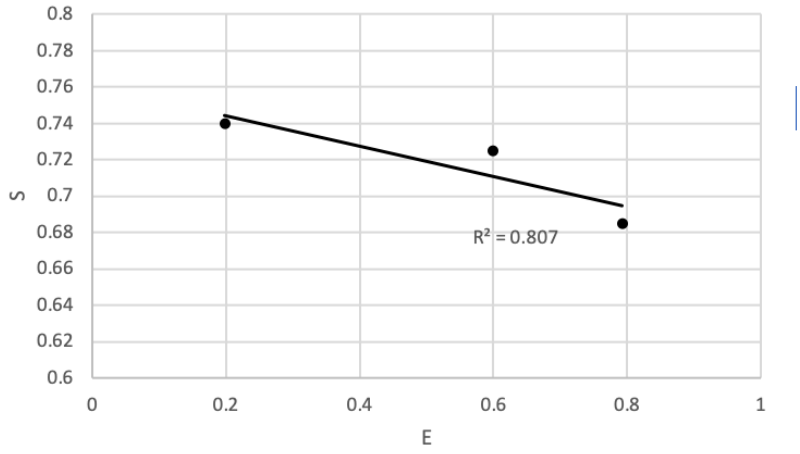

Figure 3.11. A) graph showing the extracted E and S positions of all three duplex DNA standards. B) The same graph zoomed in on the y-axis and showing the R^2 value.

Both γ and β correction factors can be determined by fitting the data to the Equation 3.7:

$$S = \frac{1}{1 + \beta\,\gamma + (1 - \gamma).\beta\,.E} \tag{3.7}$$

3.7.6 FCS

Sample	Counts [KHz]	Brightness [KHz]	N	D [μm^2/s]	w_r[μm]	w_D[μm]
Rhodamine 6G	58.2	5.94	9.80	118.6	0.73	2.11
Duplex DNA (1a)	5.04	2.32	2.17	414	0.73	2.11

Table 3.9. FCS data acquired from the MATLAB package PAM

Chapter 4. Performance of Modern Cameras for Single-Molecule Detection

Contents

4.1	Introduction	101
4.1.1	Types of noise in modern cameras	102
4.1.2	The signal-to-noise ratio (SNR)	105
4.1.3	Photon Transfer Curve	106
4.2	Methods	108
4.3	Results	109
4.3.1	Photon Transfer Curves Comparison	109
4.3.2	SNR of Fluorescent Molecules	112
4.3.3	DNA Paint Comparison	113
4.4	Conclusion	118
4.5	References	119

4.1 Introduction

Single-molecules are well characterized as having a low photon count rate (around 10^5 photons/s^{-1}). [1] For multiple single-molecules to be measured simultaneously a detector that can separate the emission observed from each molecule is required. Therefore, finding sensitive detectors with a large field of view (in this case cameras) is a particularly important aspect to the design of a single-molecule optical system. To image the dynamics of single-molecules, the system needs to be able to image at high frame rates, preferably 800 frames per second and above. This is due to the rapid dynamic behaviour of biological molecules. Although some shorter disordered peptides display conformational dynamics on the order of nanoseconds, in this study we would start to look at biomolecules displaying dynamics on the millisecond timescale. Secondly, the detector needs to generate the highest signal-to-noise ratio (SNR) possible from the experimental system. Typically, this is a contradiction to the first requirement of achieving highest frame rate, as increasing the speed of acquisition of the detector decreases the SNR. Therefore, here we aim to drive the system to the lowest possible noise. Since single molecules irradiate a very low number of photons per second, it is essential to look at the 'read noise' of the detector (described below). As such, this will be investigated in the next segment under the description of photon transfer curves. We will test a variety of available cameras on single-molecule data to see if the lowest read noise provides the greatest SNR.

Hence our aim in this chapter is to investigate and select the best camera performance for a multi-spot confocal microscope that will be used in the following chapters. We aim to find the best camera for this microscope by performing noise characterizations tests on each of the cameras available.

4.1.1 Types of noise in modern cameras

In general, detectors have a single process of quantifying light from a sample and displaying it as a time trace or an image on a computer. Photons are converted to electrons within the detector via the photoelectric effect. Consequently, charge is then accumulated and the voltage due to the charge is measured. This voltage is then converted to a digital signal by an amplified digital converter (ADC) as shown in Figures 4.1 and Figure 4.2.

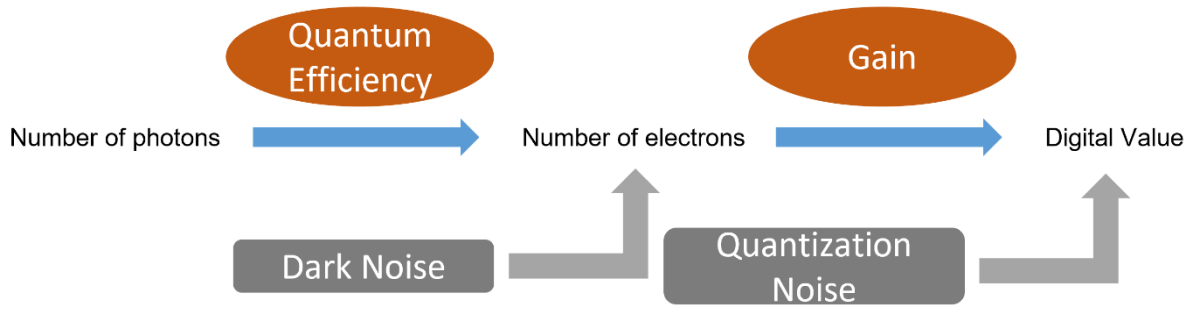

Figure 4.1. A general schematic of how digital values are obtained in detectors, including the factors; quantum efficiency, gain, dark noise and quantization noise.

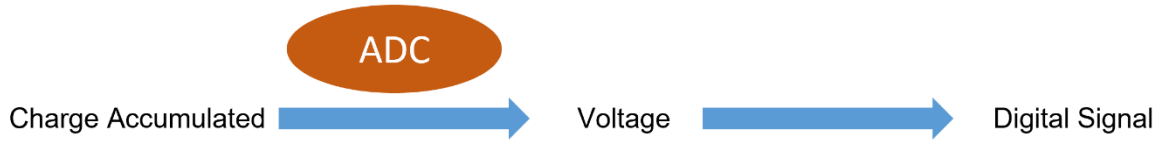

Figure 4.2. A schematic of the process of converting the charge generated by electrons to obtaining a digital value.

There are many factors to consider when deciding which camera to use for a specific application. The EMVA1288 is a document that provides a standard for characterization of image sensors and cameras. This section reviews its fundamentals and principles to help understand the concepts behind noise measurements. [2][3]

One of the main characteristics of a camera is its spectral sensitivity, known as the quantum efficiency. This is the percentage of photons that hit the detector from the sample that are converted to electrons. For example, if the sample irradiates 50 photons per millisecond and the detector has a quantum efficiency of 50%, the maximum number of electrons that will be converted by the detector will be 25 electrons per millisecond. The other 25 photons would not be converted and lost, decreasing the signal. The quantum efficiency of a detector varies with wavelength. It is also important to note that quantum efficiency takes account of the area of the detector that is photoreceptive. Micro lenses, which focus the photo irradiance on only the photo receptive areas of the detector will therefore increase the quantum efficiency. An example of this is the SPAD array which, at present, has a relatively low fill factor ~44% without micro lenses. This means that only 44% of the area of the detector is photo receptive, this lowers the quantum efficiency and therefore increases the number of photons lost in the system. For a standard optical detector, the instantaneous photoelectron conversion rate $\alpha\ (t)$ is proportional to the instantaneous incident power $\Phi(t)$ and the quantum efficiency $\eta\ (v)$ as defined in Equation 4.1.

$$\alpha\ (t)\ =\ \frac{\eta\ (v)}{hv}\Phi(t) \tag{4.1}$$

Here, h represents the Planck constant (h = 6.63 x 10^{-34} J s) and α is expressed in the units of photoelectrons/s. [3]

Image noise is the random variation of brightness observed in images and is expressed as a variance. One type of noise in a camera is “dark noise”. This is the noise when no light is currently hitting the detector. This is made up of dark current, which is the statistical variance in electrons induced thermally within a pixel. This noise increases linearly with exposure time and exponentially with temperature. However, its contribution tends to be negligible compared with the other types of noise within sCMOS cameras and so will no longer be considered.

There are three more important contributing noise factors. The first, which dominates at lower photo irradiance is the “read noise” or “quantization noise”. This is the noise generated from converting the electrons to a digital signal. This type of noise occurs even without photons. Converting an analogue signal to a digital signal requires an analogue to digital converter (ADC). This noise is constant for a pixel but may vary between pixels in the camera (fixed pattern noise).

The second noise factor to consider is “photon shot noise”. This type of noise becomes increasingly dominant at higher levels of photo irradiance. This arises as upon the detection of light, only discrete particle-like units called photons can be recorded. These fluctuations are characterised by Poisson statistics. Even under stable light, the measurement of the number of photoelectron conversions that occur within an arbitrary detection integration time, appear noisy.

The final noise factor, called “spatial nonuniformity”, is founded on the knowledge that pixels have different noise to each other and are not uniform. This type of noise is detectable at high photon irradiance, which will not be attained by single molecules and as such this will not be covered in depth.

The total noise, ${\sigma_y}^2$, can be characterized by Equation 4.2:

$$ {\sigma_y}^2 = K^2({\sigma_d}^2+{\sigma_e}^2) + {\sigma_q}^2. \tag{4.2} $$

Here, K^2 represents the gain of the system (how much the digital signal has been amplified), ${\sigma_d}^2$ represents the dark noise, ${\sigma_e}^2$ represents the shot noise and ${\sigma_q}^2$ is the quantization noise. This can also be written as shown in Equation 4.3:

$$ {\sigma_y}^2 = (K^2{\sigma_d}^2 + {\sigma_q}^2) + K(\mu_y - \mu_{dark}). \tag{4.3} $$

Here, μ_y is the mean digital signal and μ_{dark} is the mean digital signal in the dark. From this equation, we can see that the variance (total noise) increases with the digital signal. By plotting variance against mean digital signal minus the dark signal, we can obtain the gain of the system from the slope and the dark noise variance. This will be used to find the gain of the camera later in the chapter.

4.1.2 The signal-to-noise ratio (SNR)

As highlighted in the introduction the SNR is a very important factor to consider, along with the noise reduction. The SNR provides the combined information on the signal from the sample compared to the noise of the detector and the noise of the background and is defined by Equation 4.4.

$$ \mathrm{SNR} = \frac{\mu_y - \mu_{y.dark}}{\sigma_y} \tag{4.4} $$

This can also be written in terms of factors of the quantum efficiency and noise factors stated in Equation 4.5.

$$ SNR\ (\mu_p) = \frac{\eta\mu_p}{\sqrt{{\sigma^2}_d + {\sigma^2}_q/K^2 + \eta\mu_p}} \tag{4.5} $$

Interestingly, the SNR can be approximated to two different equations under two different photon intensity ranges: high photon range and the low photon range.

$$\text{SNR} \approx \sqrt{\eta\mu_p} \quad \text{for high photon range, where } \eta\mu_p \gg {\sigma_d}^2 + \frac{{\sigma_q}^2}{K^2} \tag{4.6}$$

$$\text{SNR} \approx \frac{\eta\mu_p}{\sqrt{{\sigma_d}^2 + \frac{{\sigma_q}^2}{K^2}}} \text{ for low photon range, where } \eta\mu_p \ll {\sigma_d}^2 + \frac{{\sigma_q}^2}{K^2} \tag{4.7}$$

Hence, the typical SNR curve changes from a square root increase at low irradiance to a linear increase at high irradiance. This is often plotted against the ideal SNR curve shown in Equation 4.8:

$$SNR_{ideal} = \sqrt{\mu_p}\,. \tag{4.8}$$

This ideal sensor has a quantum efficiency of 1 and negligible quantization noise. An important measure is the minimum detectable sensitivity. This is the mean number of photons required to measure a SNR value of 1. Equation 4.9 shows the number of photons needed to obtain a specific SNR and Equation 4.10 shows the number of photons needed to achieve a SNR of 1:

$$\mu_p(SNR) = \frac{SNR^2}{2\eta}\left(1 + \sqrt{\frac{1+4\left({\sigma_d}^2 + \frac{{\sigma_q}^2}{K^2}\right)}{SNR^2}}\right). \tag{4.9}$$

$$\mu_p(SNR = 1) = \frac{1}{\eta}\left(\frac{\sigma_{y.dark}}{K} + \frac{1}{2}\right). \tag{4.10}$$

4.1.3 Photon Transfer Curve

Photon transfer curves capture the above information to give a detailed characterization of the noise of cameras as the intensity of the signal is varied. This is particularly useful, as it will guide the decision of which camera to use for a required intensity range and gives an indication of the source of the noise. Photon transfer curves are commonly measured by varying the intensity of the light detected and measuring the variance of the images. This can be obtained by varying the exposure time of the camera or from increasing the intensity of the illumination source. In this chapter we will use the latter technique.

We first consider the read noise, which is the dominating factor at low light levels. Read noise is the noise for zero illumination at zero accumulation time. Read noise is a constant for every exposure time and pixel for each camera. Photon shot noise becomes dominant over the read noise from low to medium amount of intensity. Photon shot noise follows a Poisson distribution and is caused by the discrete nature of electrical charge. Photon shot noise, σ_p , increases by the square root of the average number of events, N, shown in Equation 4.11:

$$\sigma_p = \sqrt{\mathrm{N}}. \tag{4.11}$$

The third type of noise, obtained from photon transfer curves, is the Fixed Pattern Noise (FPN). This arises due to pixels on the detector having different individual read noise. This dominates over the photon shot noise at high intensities. These three noise types combined give the photon transfer curve shown in Figure 4.3.

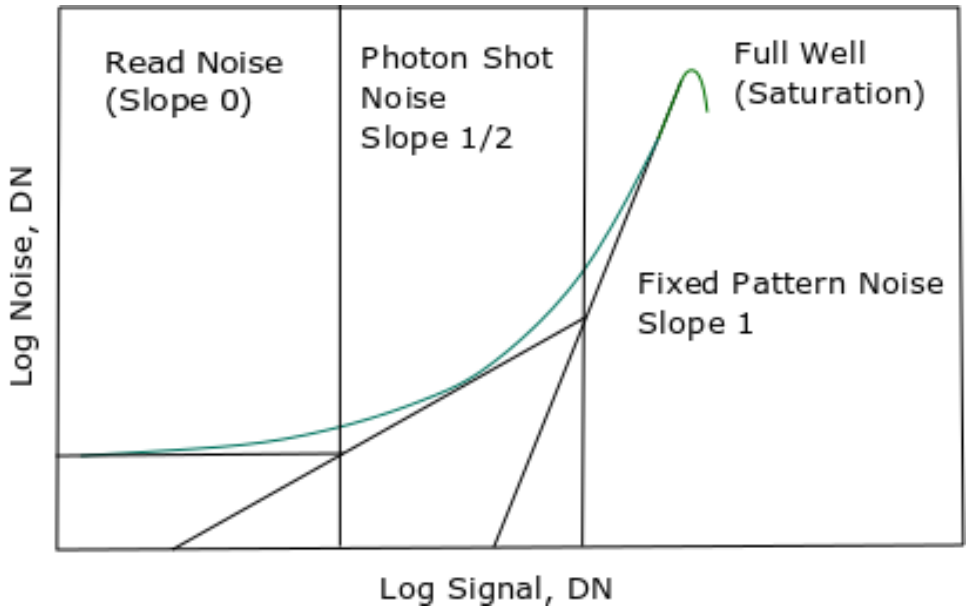

Figure 4.3. A typical Photon Transfer Curve indicating three parts of the curve; the read noise, the photon shot noise and the fixed pattern noise (FPN). The unit DN stands for the digital number and represents the brightness value of the pixel. The green line shows the sum of the contributions of each of the types of noise.

4.2 Methods

Determining Photon Transfer Curves; Photon transfer curves were taken for three sCMOS cameras; the Hamamatsu Fusion, the Hamamatsu Flash V4.0 and the Photometrics 95B. The method involved varying the voltage of an LED to change its intensity. The light was directed through a tube containing lenses and neutral density filters to provide uniform light across all the pixels of the camera (shown in Figure 4.17). Data were collected when the LED was off up until the LED had saturated the camera. MATLAB was used to analyse the data, and to plot the mean grey values of the pixels in the camera against the mean variance of the pixels.

DNA PAINT on three different cameras and generating a maximum z-stack; DNA Paint (Gattaquant) was placed on the Cairnfocal setup. A 640 nm laser illuminated the sample. DNA paint was observed with three different cameras. These included two sCMOS cameras

(Hamamatsu Flash 4.0 and Photometrics Prime 95B) and one EM-CCD camera (Andor iXon). For each experiment the sample was imaged in the same conditions.

Cairnfocal optical setup; An LDI laser setup (405, 445, 470, 520, 520, 528, 555, 640 nm) illuminated the digital micromirror chip (Texas Instruments DLP7000) controlled by a ViALUX controller board using MATLAB. These micromirrors allow the light incident to be reflected +12° or -12°. An inverted microscope (Nikon Ti-E) housed a Nikon 60x ApoTIRF oil objective lens (NA 1.49) which focused the laser onto the sample.

4.3 Results

4.3.1 Photon Transfer Curves Comparison

Photon transfer curves were taken for three of the latest sCMOS cameras; the Hamamatsu Fusion, the Hamamatsu Flash 4.0 and the Photometrics 95B. By changing the intensity of the illumination source of a light emitting diode shown in Figure 4.4, the mean signal on the camera was varied and the variability of the signal was quantified.

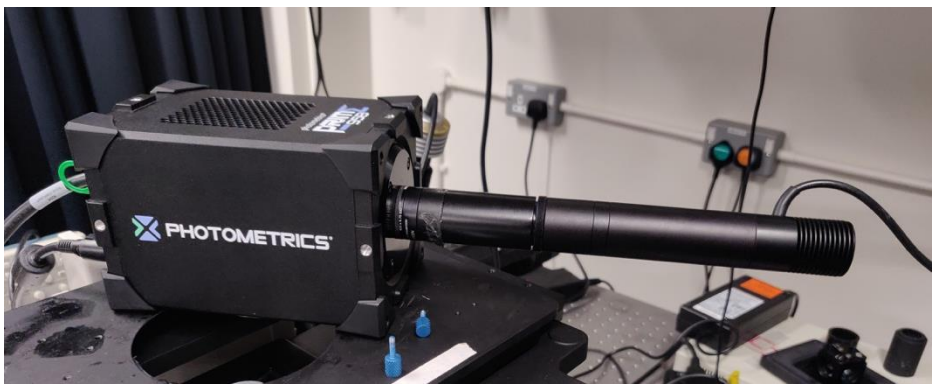

Figure 4.4. The method taken for generating photon transfer curves on the Photometrics Prime 95B.

MATLAB was used to analyse the data, and to plot the mean grey values of the pixels in the camera against the mean variance of the pixels. The grey value represents the brightness of the pixel. An example of such a plot is displayed below in Figure 4.5.

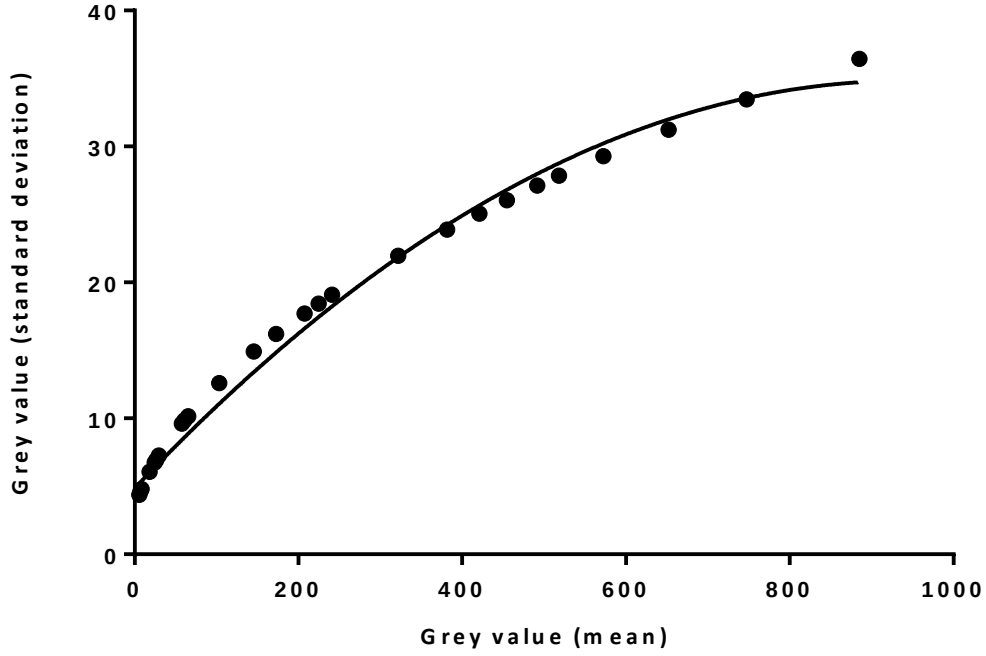

Figure 4.5. A graph showing the standard deviation in grey values against the mean signal in grey values for the Photometrics Prime 95B.

To calculate the gain of the camera Equation 4.12 was used. A quadratic function was fitted to this graph to determine the gain of the camera. Using Equation 4.13 below, the signal in grey values was then converted into electrons:

$$\text{Gain} = \frac{\text{Mean grey values of image}}{\text{Variance of the image}} \tag{4.12}$$

$$\text{Signal (electrons)} = \frac{\text{signal (grey values)}}{\text{gain}} \tag{4.13}$$

The uniformity of the light hitting the camera was also an important factor to consider. If the light was not uniformly illuminating the camera some pixels would have different signal and variance from each other. By measuring a line plot of the image, we could check whether this was the case. The results from this measurement showed that the light was still not uniform, especially near the edges. To counter this, only a small area of around 100 pixels^2 in the centre of the camera was taken for analysis. The line plot measurement shown in Figure 4.6 was then shown to be similar across this number of pixels.

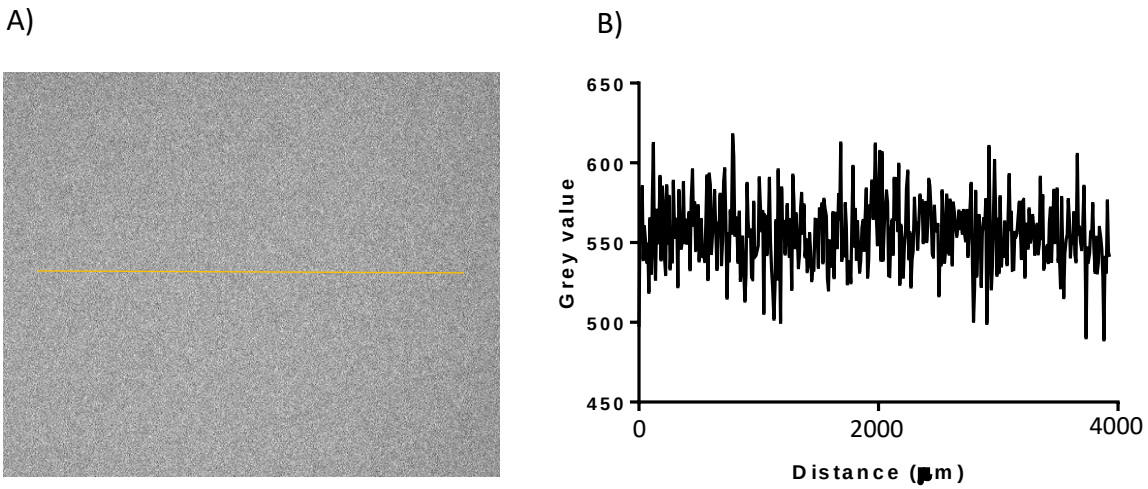

Figure 4.6. A) A cross section of the illumination pattern of pixels on the detector B) The grey values across this cross-section of the illumination pattern.

The photon transfer curve was obtained using the log(signal) and log(standard deviation) of the entire image. From this graph, the read noise was obtained as the data point with the lowest signal, where it crossed the y-axis. From the resultant signal in units of electrons (Equation 4.13) a plot of the photon transfer for each of the cameras was compared and is shown in Figure 4.7. Figure 4.7 showed that the Hamamatsu Fusion had the lowest read noise (0.8 e-), followed by the Hamamatsu Flash v4.0 (1.1 e-) and finally the Photometrics Prime 95B (2.4 e-). This data showed similarities to the read noise in the datasheets for each of these cameras.

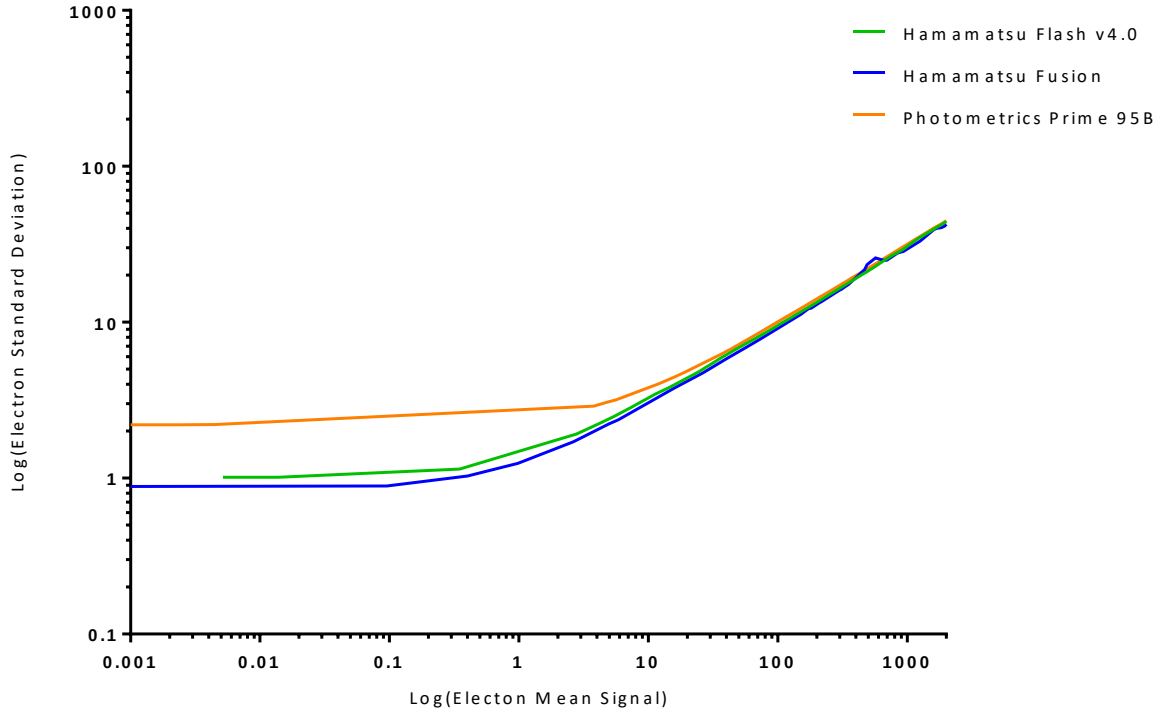

Figure 4.7. A photon transfer curves for the Hamamatsu Flash v4.0, Hamamatsu Fusion and Photometrics Prime 95B.

4.3.2 SNR of Fluorescent Molecules

In order to characterize the SNR of these modern cameras, the cameras were attached to a current super-resolution microscope (Cairnfocal) described in the methods section. Fluorescent beads were used to first test if they could be seen. If successful, less bright single-molecules would then be used with all the cameras for comparison. Here, we expected the cameras with the lowest read noise to achieve the highest SNR. Unfortunately, the Hamamatsu Fusion was unavailable for these experiments and was replaced with an EM-CCD camera (Andor iXon).

The sCMOS camera Prime 95B (Teledyne Photometrics) was first employed to detect the fluorescent beads sample. Once these were detected, the frame rate of the camera was increased to check to see if the sample was still visible. The resulting graph (Figure 4.8), shows the

maximum signal of the fluorescent beads at a specific frame rate and shows the expected decline in signal strength with increasing frame rate approaching the magnitude of the background around 500 frames/s. It was clear that this camera could detect these fluorescent beads at lower frame rates. However, above 300 frames/s the signal could not be separated from the noise. In this experiment the background of the camera (120 grey counts) was much higher than the offset of the camera (100 grey counts). This may have affected the performance of detecting these fluorescent beads as there was already a significant background signal originating from the microscope.

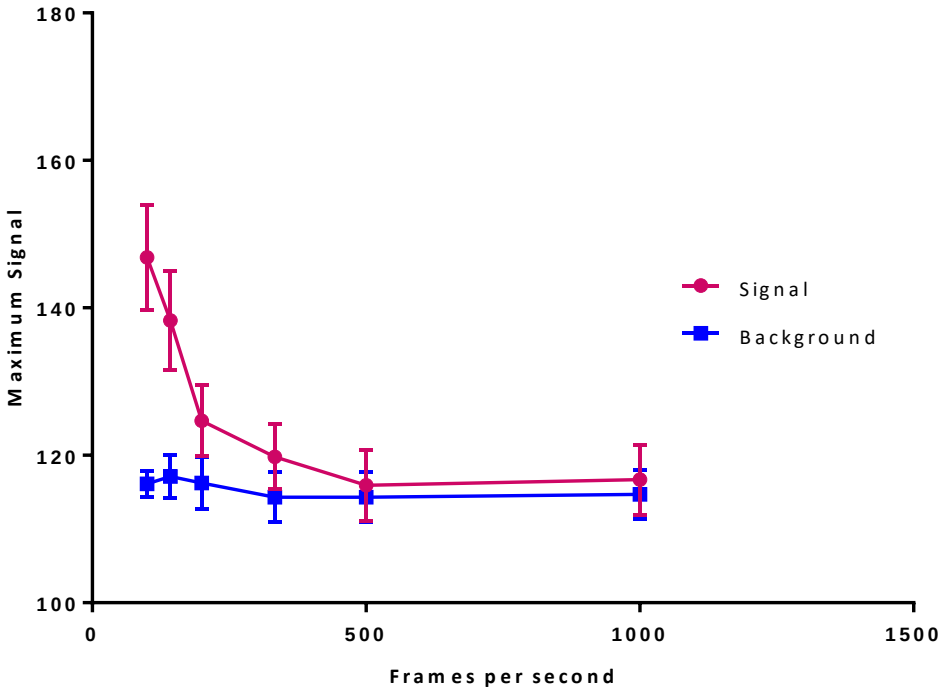

Figure 4.8. The signal on an sCMOS camera (Photometrics 95B) at a range of camera speeds. A background count of 120 grey counts was recognized as the main contribution to not observing fluorescent beads (0.1 μm) at high frame rates.

4.3.3 DNA Paint Comparison

To examine which camera was optimal for detecting single-molecules, smaller molecules were investigated. DNA paint was chosen as it was at the relevant single-molecule level and contains the dye ATTO 647N, which would be needed in future smFRET experiments. Here, it was

immobilized on a glass slide which made it easier to test for these experiments. In addition, DNA Paint was chosen as it 'blinks' on and off representing when the dye was conjugated to the DNA. This makes DNA Paint easier to visualize against the background and resembles dynamic molecules that diffuse through the observation volume.

DNA paint was observed with three different cameras. These included two sCMOS cameras (Hamamatsu Flash 4.0 and Photometrics Prime 95B) and one EM-CCD camera (Andor iXon). The resultant maximum intensity projection of all the frames is shown for each of the cameras in Figures 4.9-4.11. The maximum intensity projection of all the images was found to identify the brightest molecules and to investigate whether the camera could initially detect the sample.

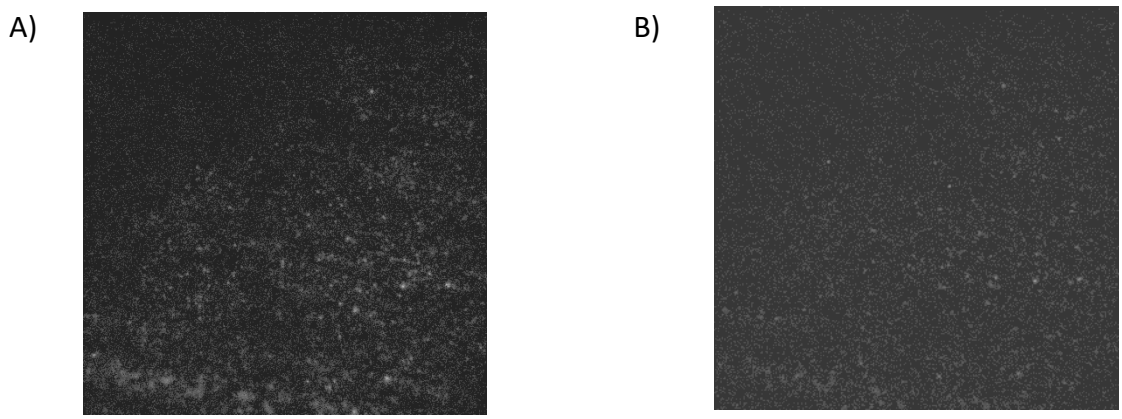

Figure 4.9. A maximum intensity projection of DNA paint detected on an EM-CCD camera (Andor iXon) at A) 17 frames per second B) 100 frames per second.

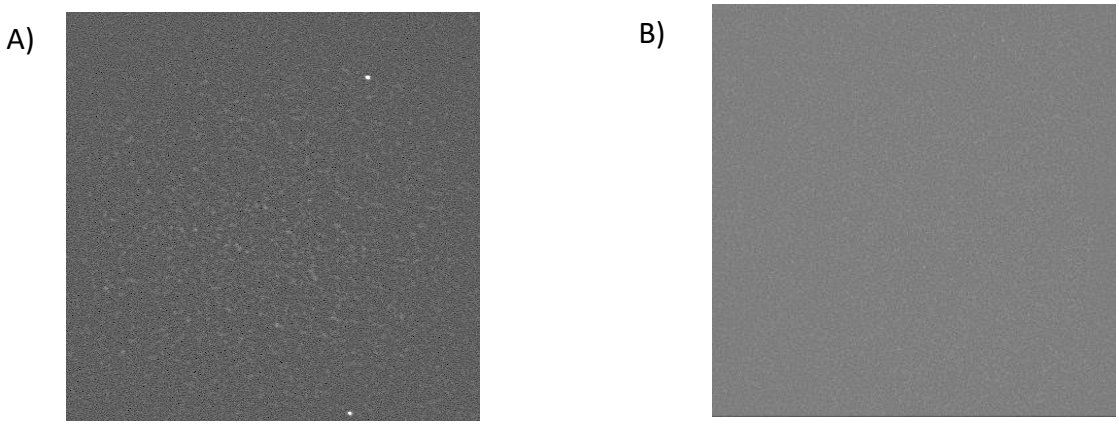

Figure 4.10: A maximum intensity projection of DNA paint detected on an sCMOS camera (Photometrics Prime 95B) at A) 17 frames per second B) 100 frames per second.

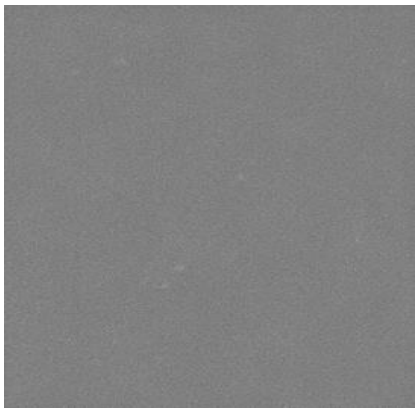

Figure 4.11. A maximum intensity projection of DNA paint detected on an sCMOS camera (Hamamatsu Flash 4.0) at 17 frames per second.

The images in these figures, by visual inspection, showed that the Andor iXon could detect the DNA Paint better than the Photometrics Prime 95B and the Hamamatsu Flash 4.0. By calculating the net signal of the maximum intensity projections shown in Figures 4.9-4.11 for each camera, we confirmed that the EM-CCD, Andor iXon, showed the highest net signal followed by the Prime 95B and then the Hamamatsu Flash 4.0. On this sample, the EM-CCD (Andor iXon) camera was first analysed to investigate whether a high SNR could be maintained at high frame rates and is shown in Figure 4.12. On this camera, to achieve these high frame rates, the field of view was reduced to 50 pixels x 50 pixels and a 2 pixel x 2 pixel binning was required.

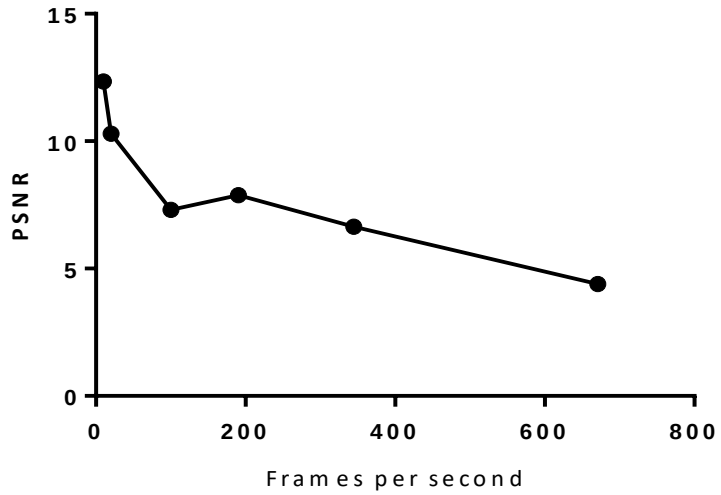

Figure 4.12. A graph representing the Peak SNR (PSNR) of DNA Paint against the frame rates for the EM-CCD camera (Andor iXon). The PSNR was calculated by taking the maximum value of an averaged 4 pixel x 4 pixel area and dividing this value by the standard deviation of the same 4 pixel x 4 pixel area.

The EM-CCD camera performed well with a SNR of 5 above 600 frames per second. However, the camera could not image faster than around 700 frames per second. This limits its application to single-molecule FRET measurements, as we would not be able to image the faster dynamics of biomolecules. To compare this to a sCMOS camera, the Prime 95B was attached with the same sample and conditions (Figure 4.13).

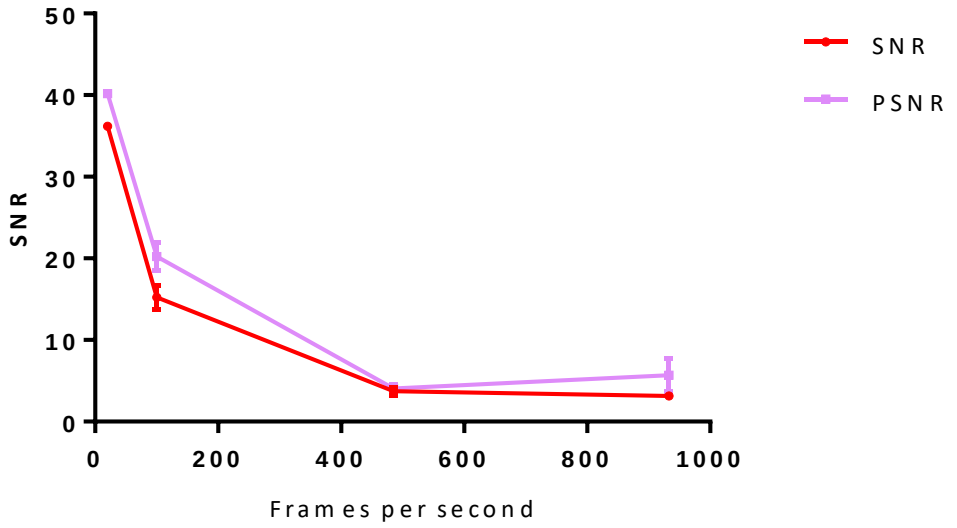

Figure 4.13. A graph representing the Peak SNR (PSNR) and the SNR of DNA Paint against the frame rates for the Photometrics Prime 95B. The PSNR was calculated by taking the maximum value of an averaged 4 pixel x 4 pixel area and dividing this value by the standard deviation of the same averaged 4 pixel x 4 pixel area of a background sample of water. The SNR was taken by the same method but by taking the mean of the 4 pixel x 4 pixel area instead of the maximum.

Experiments testing the Photometrics Prime 95B showed that the camera had an SNR of 3.16 with an error of 0.18 at 933 frames per second. Even at low frame rates, the sCMOS camera outperformed the EM-CCD camera. This might have been due to the low brightness of the sample. The EM-CCD cameras have a higher overall read noise which makes them better for brighter samples where read noise is not the limiting factor. Finally, data on the Hamamatsu Flash 4.0 was taken, however, because the SNR was below two for all measurements with this camera, it was left out of this comparison. This was surprising as this camera displayed the lowest read noise. However, a possibility for this could be the small pixel size of the Hamamatsu camera (6.5 μm) compared to the EM-CCD (13 μm) and the Photometrics 95 B (11 μm). Since all these experiments were performed at the same magnification, the read noise for the Hamamatsu camera would be approximately four times higher, reducing the resulting SNR.

4.4 Conclusion

To conclude, in this section we characterized the latest modern cameras and compared the read noise and SNR on single-molecules. The photon transfer curves for all the cameras showed that the Hamamatsu Fusion had the lowest read noise. This result was encouraging, as it closely resembled the value stated by Hamamatsu. The Hamamatsu Flash 4.0 had the second lowest read noise and lastly the Photometrics with the highest read noise.

Since the Hamamatsu Fusion was too costly for this project, the Hamamatsu Flash 4.0 was chosen for the confocal system used in studies described in later chapters. This decision was mainly due to its comparatively low read noise. It had a read noise of more than 2-fold less than the Photometrics 95B. Although the quantum efficiency of the Hamamatsu was lower than the Photometrics camera (based on the supplier's datasheet), the reduction in quantum efficiency was small and so we believed that this would not make up for the high read noise. Therefore, we expected that by using Hamamatsu Flash 4.0 it would give us around a two-fold increase in SNR in comparison to the Photometrics 95B.

In addition, this study showed DNA Paint was detected using the Photometrics Prime 95B at a peak SNR of 6.8 at 1000 frames per second. More data needs to be collected on smaller, dynamic molecules to understand if the Photometrics 95B would work with this optical system. The EM-CCD camera (Andor iXon) performed well maintaining a SNR of 4.4 at around 670 frames per second. However, this would not be able to capture the fast dynamics of single-molecules. Further, the low field of view to collected at this speed (50 pixel x 50 pixel image) would not be sufficient for a high-throughput smFRET system. For example, a projected 2 pixel x 2 pixel multi-spot pattern within a 50 pixel x 50 pixel field of view, would only fit a

maximum of 64 spots. This would only deliver a 64-fold increase in speed compared to traditional smFRET microscopes.

To summarise, in this chapter, sCMOS cameras showed promise at imaging fluorescent molecules at fast speeds. The information gathered also indicated that the Hamamatsu Flash 4.0 would be the best camera for single-molecule imaging and was taken forward for the subsequent chapters.

4.5 References

[1] G. T. Dempsey, J. C. Vaughan, K. H. Chen, M. Bates, and X. Zhuang, "Evaluation of fluorophores for optimal performance in localization-based super-resolution imaging," *Nat. Methods*, vol. 8, no. 12, pp. 1027–1040, 2011

[2] "EMVA Standard 1288 Standard for Characterization of Image Sensors and Cameras," 2010. Accessed: May 21, 2019

[3] J. Mertz, *Introduction to Optical Microscopy*. 2019.

Chapter 5. Identifying Single-Molecules with a Camera at High Speeds using a Digital Micromirror Device

Contents

5.1 Introduction 122

5.1.1 Developing a multi-spot confocal microscope 122

5.1.2 Integrating single-molecule analysis for multi-point detection 128

5.2 Methods 131

5.3 Results and Discussion 131

5.3.1 Preliminary Fluorescent Time Traces 131

5.3.2 Identifying Individual Spots containing Fluorescence Emission 133

5.3.3 Changing the spot size 138

5.3.4 Measuring the Diffusion Coefficient of Fluorescent Beads 139

5.3.5 An APD detector in combination with the digital micromirror device 145

5.4 Conclusion 149

5.5 References 150

5.1 Introduction

5.1.1 Developing a multi-spot confocal microscope

A single confocal spot microscope has been well characterized for single-molecule FRET and FCS experiments .[1]–[3] These instruments are based around a single pinhole in the emission path which is then aligned onto an avalanche photodiode to detect single-molecule events. Since only one pinhole spatially confines the detection volume, at low concentrations, only one single-molecule can be observed at a time. To build a statistically relevant dataset, hundreds of FRET events in single molecules need to be observed. [4] Since only one molecule is observed on average per second and only a fraction of these undergo FRET, experiments typically last 30 minutes to 1 hour. [2]

Although single-molecule FRET can determine binding constants to determine potential drug candidates through distance measurements, its application has been limited in the pharmaceutical industry due to long experimental times. Here, reducing the time of single-molecule FRET measurements by a factor of over 50-fold could resolve this issue and open the door to a high-throughput drug screening with the added advantages of using a single-molecule technique. Single-molecule methods provide the only way to identify the heterogeneity of samples. Previously, this has not been possible in drug discovery, with ensemble methods such as surface plasmon resonance. In this regard, the ability to screen hundreds to thousands of candidate molecules every hour via a single-molecule FRET instrument, would clearly spur innovation in the pharmaceutical industry.

A high-throughput single-molecule FRET instrument requires multiple single-molecules to be observed in different areas of the sample simultaneously. Traditionally to detect single-

molecules, avalanche photodiodes have been used because of their high sensitivity. However, these detectors can only provide one intensity value per unit time. A camera, on the other hand, has thousands of pixels from which it can provide multiple intensity values.

In optical microscopy there are many methods that allow improvements of the signal-to-noise ratio (SNR) for single-molecule imaging. Structured illumination microscopy (SIM) is a common super-resolution technique that illuminates the sample with a known spatially structured pattern of light. [5] In this chapter we will use this technique to project a multi-spot pattern on to the sample. Digital micromirrors have been used in the past for multifocal Raman hyperspectral imaging, but to the best of our knowledge, have not been used for high-throughput single-molecule imaging or FRET. [6] This method will allow the illumination of multiple small volumes in the sample defined by the size of the micromirrors projecting the laser onto the sample. Furthermore, the fluorescent emission will only be detected from these spots, as the emission will only be directed to a detector by micromirrors at a certain angle. In this method the resolution of the single-molecules will be enhanced as the full width half maximum (FWHM), a measure of spatial resolution, of the point spread function laterally and axially will be reduced. Moreover, the SNR of the experiment will be increased.

To create the multi-spot pattern, a digital micromirror (DMD) was used. We chose this spatial modulator as it can be easily operated and can quickly change the pattern projected on the sample and the micromirrors act as a physical pinhole. The DMD is located inside the Cairnfocal, a multi-modal microscope capable of Image Scanning Microscopy (ISM) and Confocal techniques. [7] The image generated, the optical setup and a photograph of the setup, respectively, is shown in Figure 5.1, Figure 5.2 and Figure 5.3 below. To observe the multi-spot pattern on the detector, selected micromirrors reflect the laser beam on to the sample. A

multi-spot pattern is a series of spots defined in shape and size by the DMD to segregate the image. Figure 5.1 shows an image on a sCMOS camera of the multi-spot pattern. Areas on the DMD that are switched to the 'on' position are seen on the 'on' detector as spots. Only molecules that pass through these spots can be observed. The dark areas outside of these spots are from the micromirrors that are not reflecting towards the detector. These 'off' mirrors can be used in combination with another detector. Molecules that pass through these areas on the 'on' detector are not visible but are on the 'off' detector. The emission path with the micromirrors in the 'on' position is shown in Figure 5.2. In this chapter the 'off' camera was not used. Additionally, since the micromirrors in the 'on' position reflect emitted light from the sample, signal can only be observed in each of the spots.

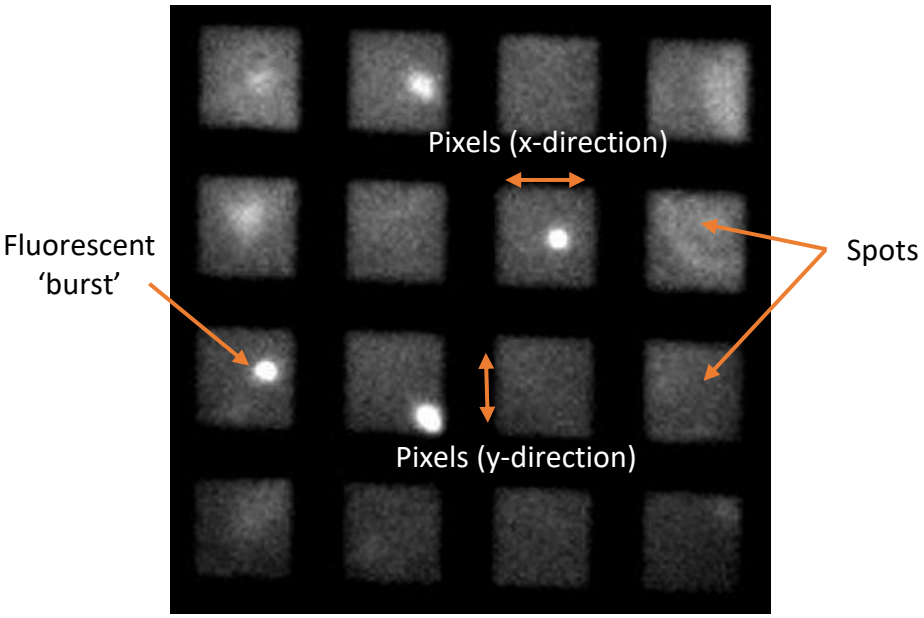

Figure 5.1. An example of a multi-spot pattern formed by the DMD and projected on a sCMOS camera where each spot is measured by a number of 'x' pixels in the x direction and a number of 'y' pixels in the y direction. The micromirrors are small enough to act as pinholes. A sample of fluorescent beads was used.

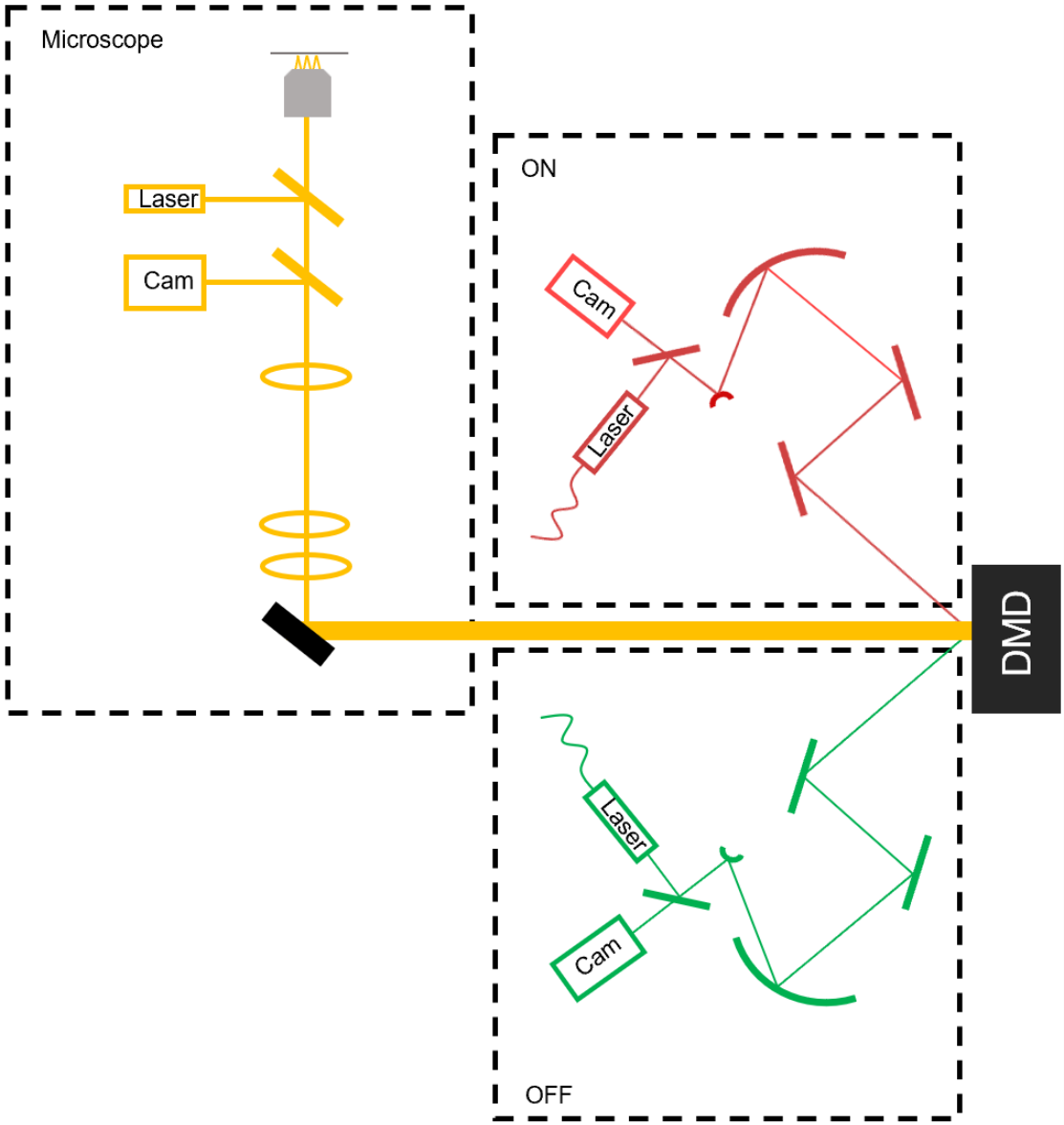

Figure 5.2. A schematic showing the setup of the Cairnfocal. The digital micromirror device reflects both in the 'on' and 'off' direction. If a multi-spot pattern is generated on the DMD the resultant multifocal structured illumination is produced.[7]

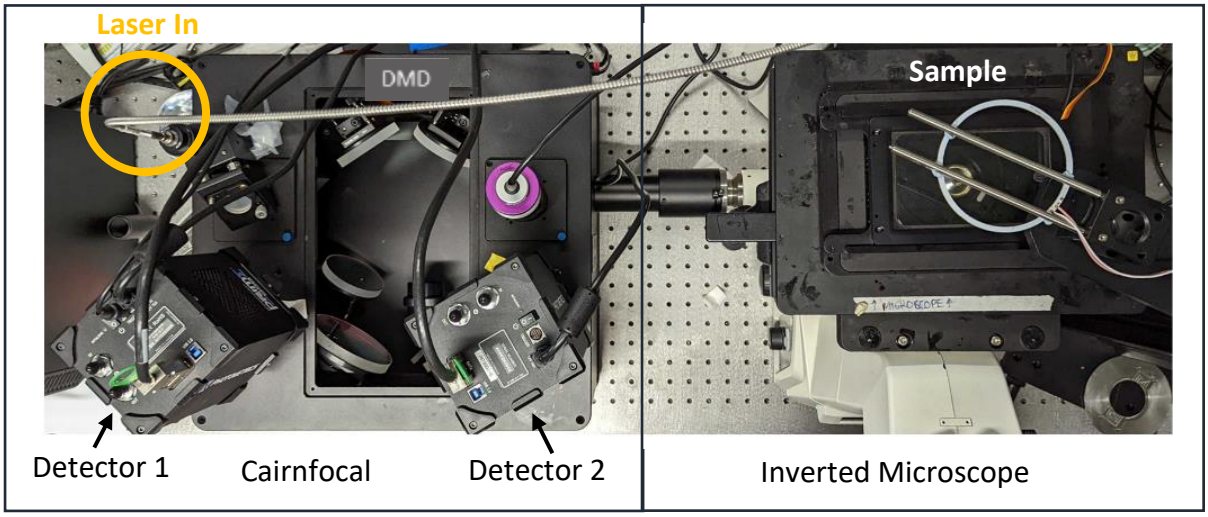

Figure 5.3. A) A photograph showing the emission path of the Cairnfocal. The emission is directed towards detector 1. The micromirrors angle can be changed so that detector 2 observes emission too. The orange circle shows where the laser enters via an optical fibre. The laser follows the same path as the emission path to the sample.

The Cairnfocal confocal microscope, which houses the DMD is similar to a spinning disk confocal microscope. Spinning disk confocal microscopy has hundreds of pinholes on a disk. This disk then rotates allowing for fast image acquisition. In the Cairnfocal the micromirrors in the DMD act as pinholes. In this method, an image of these pinholes or micromirrors is demagnified onto the sample. Each illumination area on the sample is smaller than the diffraction limit. Therefore, multiple illumination volumes would be observed, all as a three-dimensional point spread function as depicted in Figure 5.4.

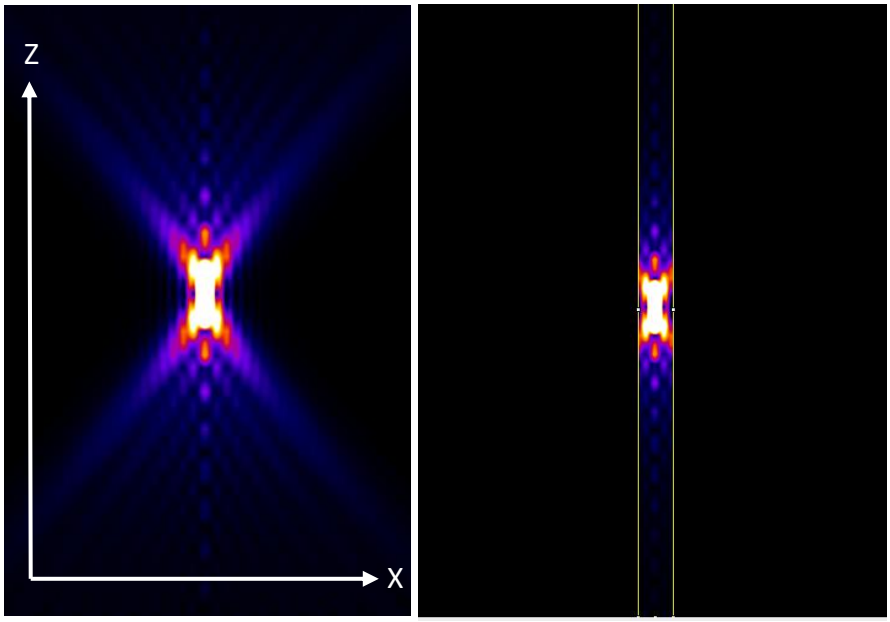

Figure 5.4. A) Three-dimensional point spread function observed by both the illumination and emission of the Cairnfocal B) The 'tube effect' created by placing the pinhole in the emission path. Simulated 3-D Point Spread Function generated by PSFGenerator. [8]–[12]

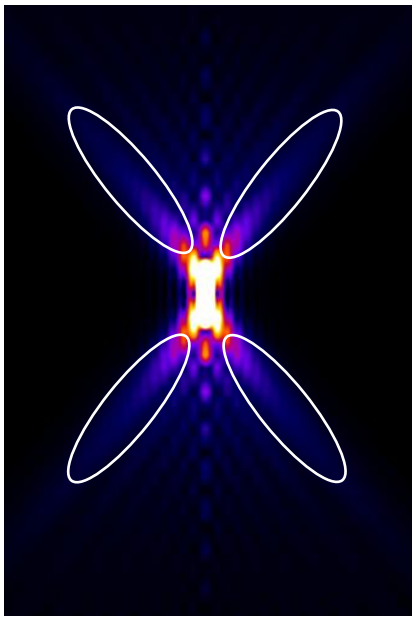

Figure 5.5. The lobes highlighted in white that contain most of the background signal to be rejected. Simulated 3-D Point Spread Function generated by PSFGenerator. [8]–[12]

Consequently, when a fluorophore within that volume emits fluorescence, the emission would then be observed as a three-dimensional point spread function. If a pinhole (or micromirror) is placed in this emission path, the contributions that fall outside of this "tube" in the emission

point spread function shown also in Figure 5.4 would be rejected. Since the majority of the signal falls outside of this and within the white lobes shown in Figure 5.5, most of the out of focus light is rejected. For the Cairnfocal confocal to work, both the structure of the pinhole needs to be illuminated onto the sample and the emission needs to go through the pinholes in the emission path. A visualization of the fluorophores in the sample, the illumination paths and the observation volumes are shown in Figure 5.6. [13]

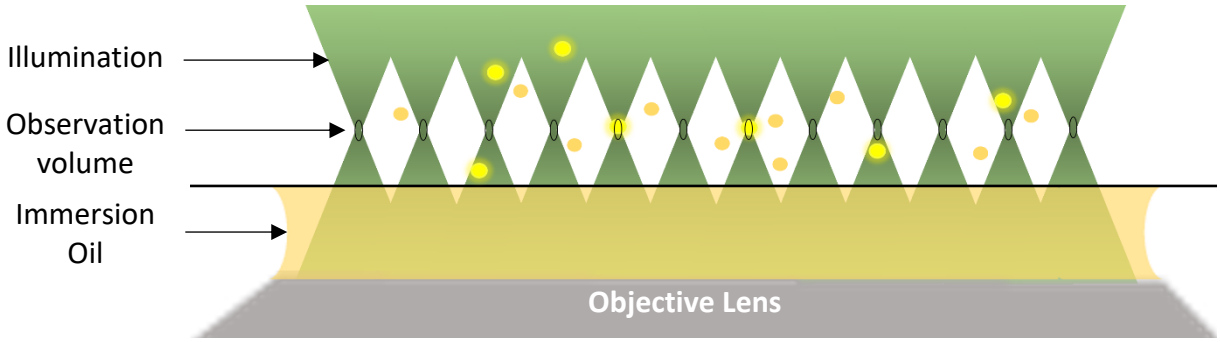

Figure 5.6. A schematic showing the illumination from a multi-spot pattern of the microscope and the observation (confocal) volumes. Fluorophores that are illuminated are shown in yellow and fluorophores that are not illuminated are shown in orange.

To summarize, with this technique shown in Figure 5.6, the out of focus fluorophores are illuminated but cannot be detected as they are outside of the observation volume. However, if the pinholes are not sufficiently spaced out, the light emitted by out of focus fluorophores illuminated by one pinhole might end up passing through an adjacent pinhole instead of being rejected. If the pinholes are sufficiently far apart then the amount of light that passes through the wrong pinholes should be minimal and so greatly reducing the background signal.

5.1.2 Integrating single-molecule analysis for multi-point detection

To realize the full potential of a high-throughput single molecule FRET instrument, fluorescent signal from single-molecules needs to be analysed and FRET values need to be determined

without manual intervention. Since hundreds to thousands of single-molecule events may occur per second, automation of this process is vital to achieve a system that improves the throughput of experiments. The multi-spot pattern provides a method of spatially resolving single-molecules within each of their respective spots. This is important as it prevents the detection of more than one molecule in a spot. It also allows for easy identification of molecules as we know their location if they can emit fluorescence.

To obtain FRET values within each of the spots, the total emission of green and red emission inside each spot in the multi-spot pattern, requires analysing. The process of analysing the data within these spots should achieve the following goals;

1. *To find spots that only contain signal emitted from the sample.*

We aim to achieve this goal by implementing a threshold of intensity or SNR. We can also remove the background of the acquisition, providing a net emission signal. If single-molecule events are proving difficult to identify, binning of the image may also be implemented. This process sums the intensity of the pixels in a selected area. While the background is also added, if the signal is spread out over several pixels on the camera, this process should make it easier to identify.

2. To identify more than one single-molecule within a single spot. To count the number of these occurrences and to discard them for single-molecule measurements.

Since there is a possibility that more than one single-molecule could pass through a spot at any given time, an upper limit of signal threshold should be implemented. To achieve this, the

multi-spot pattern needs to put the single-molecules in focus. The photons arriving at the camera for the single-molecules should be consistent with multiple events. Since two single-molecules would emit double the photon count, single-molecule events detected that have emission intensities around 1.5-1.75x more than the average single-molecule event may be deemed more than one single-molecule and can be excluded. To limit this occurring a concentration test at the start of the experiment should be carried out. Based on past experimental single-molecule FRET data, the observation of one single molecule burst per second should be used as a rough guideline before single molecule FRET experiments are carried out. As previously mentioned in chapter 3, this single molecule FRET data showed similar FRET efficiency values when directly compared with 20 single-molecule FRET labs from around the world. Here, we decrease the throughput of the method but ensure that there is a low probability of two molecules entering the confocal volume simultaneously during the experiment. In summary, this would limit the error of the FRET efficiency value while still allowing an acceptable experimental length.

3. To obtain FRET efficiency values within each of the spots.

To achieve this goal, the intensity of both the donor and acceptor signal needs to be measured within each spot. To image these, two colours are therefore needed, requiring an image splitter. An image splitter splits the emission light into two, the emission from the green spectrum would be observed on one half of the camera. The other half would observe fluorescence from the red spectrum. To observe both intensity values in the same spot, these two halves need to positionally match.

Throughout Chapters 5 and 6, we aim to explore the analysis of single-molecule datasets and find an optimal method for obtaining FRET efficiency values from a multi-spot system. By

analysing multiple spots with multiple single-molecule datasets in combination with experimental procedure, we also aim to provide reliable results that can influence experimental decisions.

5.2 Methods

Cairnfocal optical setup; An LDI laser setup (405, 445, 470, 520, 520, 528, 555, 640 nm) illuminated the digital micromirror chip (Texas Instruments DLP7000) controlled by a ViALUX controller board using MATLAB. These 13.6 µm micromirrors allow the incident light to be reflected +12° or -12°. An inverted microscope (Nikon Ti-E) housed a Nikon 60x ApoTIRF oil objective lens (NA 1.49) which focused the laser onto the sample. The sCMOS camera (Andor Zyla) was used to detect the fluorescence emission. Samples used in this chapter include; FluoSpheres™ Sulfate Microspheres, 4.0 µm (580/605 nm) from ThermoFisher, FluoSpheres™ Carboxylate-Modified Microspheres, 0.1 µm (625/645 nm) from ThermoFisher, 36bp dsDNA with ATTO 550 and ATTO 647N attached 11bp apart.

Switching DMD on in sequence and recording data with the APD and camera; The DMD was switched on and off sequentially by MATLAB code. For the avalanche photodiode (Excilitas, Si-APD) to detect counts over a millisecond timescale, it was connected to a NI-DAQ board and LABVIEW code enabled the counts to be detected per millisecond. The Andor Zyla camera was controlled with micromanager. [14]

5.3 Results and Discussion

5.3.1 Preliminary Fluorescent Time Traces

To test the concept of the digital micromirror device, an experiment was designed to measure a signal change when a fluorescent object passed through one of the spots in the multi-spot pattern. Initially to make the detection easier, a less diffusive and bright fluorescent object was

used to observe these changes. A sample of fluorescent beads (4 μm) were chosen for their slow diffusion coefficient and high brightness. Furthermore, experiments varying the concentration of the fluorescent beads and varying pixel sizes were conducted to determine the optimal spot size for the system. A larger spot would be expected to increase the signal as more micromirrors would direct the emission towards the sample. However, it would also increase the background as the confocal volume will be less confined axially, letting in the emission of fluorophores in the background.

Fluorescent signal was measured within the spots by projecting a spot pattern down on the digital micromirror device and imaging at an exposure time of 100 ms. To find the percentage of spots that contained fluorescence emission from the fluorescent beads the maximum intensity values of each of the pixels were calculated. The resultant ‘z-stack image’ displayed in Figure 5.7 shows that 35% of the spots within the illumination beam contained emission. This was calculated by finding the percentage of spots in a circular area in the centre of the image. By using an SNR threshold of three, we can check whether there are any outliers in the data, since 99.7% of values are within 3 standard deviations of the mean.

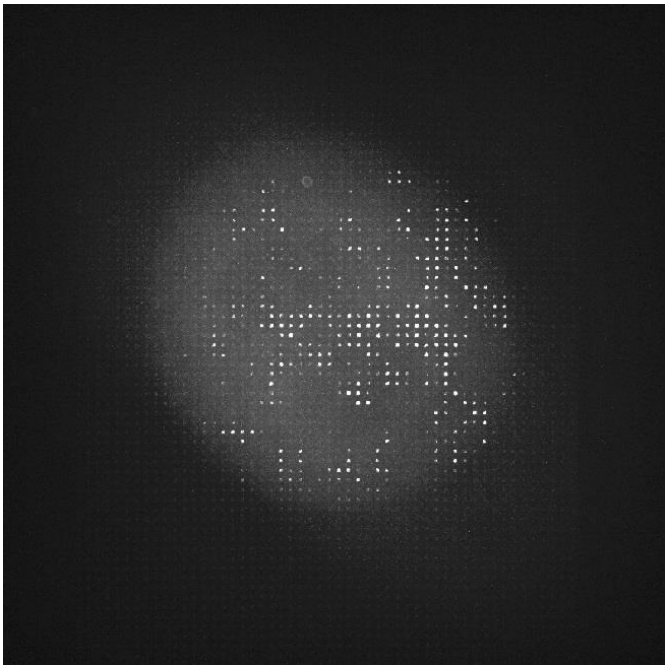

Figure 5.7. An image of the resultant z-stack showing the maximum signal of each pixel for all 255 frames at an exposure of 100 ms. A highly concentrated sample of fluorescent beads (4 μm) were imaged. The spots in this image are 10 pixels x 10 pixels in size. The spots which show fluorescent activity (a fluorescent bead has passed through them) result in white squares.

5.3.2 Identifying Individual Spots containing Fluorescence Emission

Initially, we manually picked a 3 pixel x 3 pixel spot that visually showed fluorescent activity from this analysis, a time frame was then analysed and displayed as a time trace in Figure 5.8 using ImageJ. [15] This time trace showed that fluorescent beads entered and exited this selected spot and showed that single bursts were observed.

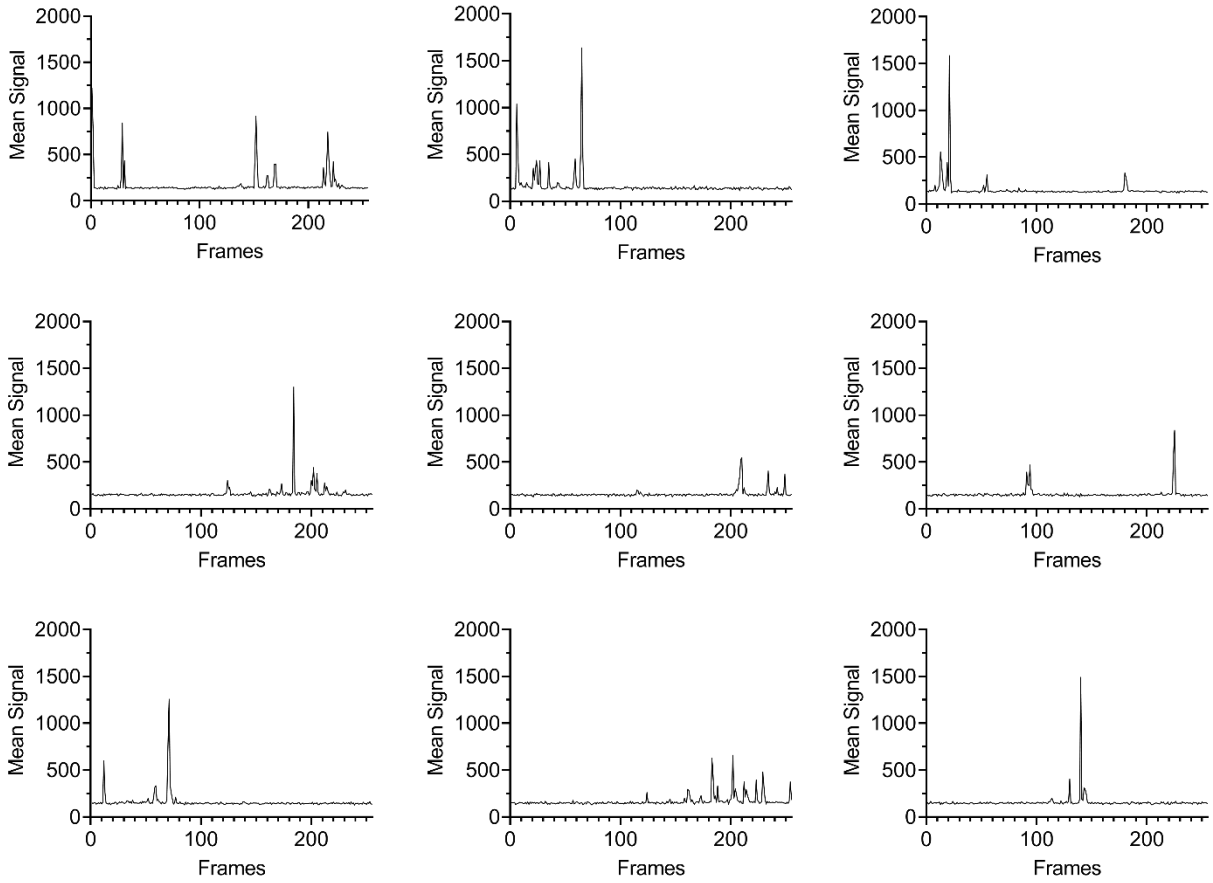

Figure 5.8. Multiple graphs showing the mean fluorescent signal of 4 μm fluorescent beads inside a 2 x 2 pixel area within 10 pixel x 10 pixel spots. This pattern was projected onto the DMD and recorded by a camera at an exposure time of 100 ms.

The time trace shows that the signal rose and fell over short time periods (~ 2 seconds). When the beads were absent, only the offset of the camera and the background was observed within the spot. The maximum fluorescent signal was over 1000 grey counts on the camera compared to a mean background of ~150 grey counts. Within one of these spots, the SNR was calculated by taking the net signal of these bursts (1153 grey counts) and dividing this by the standard deviation of the background. This gave a maximum single-molecule burst in this data of 18. To calculate the time the beads spent in the spot, a threshold of three was taken for the SNR. This would guarantee that any fluorescent beads observed had sufficient emission compared to the noise. Over the 255 frames analysed in this experiment, the average number of frames a

fluorescent bead spent in the spot was 1.6. As the camera detected at 10 ms exposure time per frame this was equal to a time of around 160 ms on average.

The above method worked very well for a single spot, however, if we have multiple spots, we require analysis that can investigate single-molecule bursts in multiple spots. Here, we explore a method of identifying and locating fluorescence emission within the spots in the multi-spot pattern. This analysis investigated single-molecule bursts by using a SNR threshold. As mentioned earlier, the SNR used here, was the net signal from the sample divided by the background standard deviation. This provides a confidence level of the single-molecule fluorescence emission. Figure 5.9 shows an example of this from a simulated single-molecule data set (described in Chapter 6). Here the orange centroids are plotted on the time trace on any data point in one spot greater than a SNR of 5.

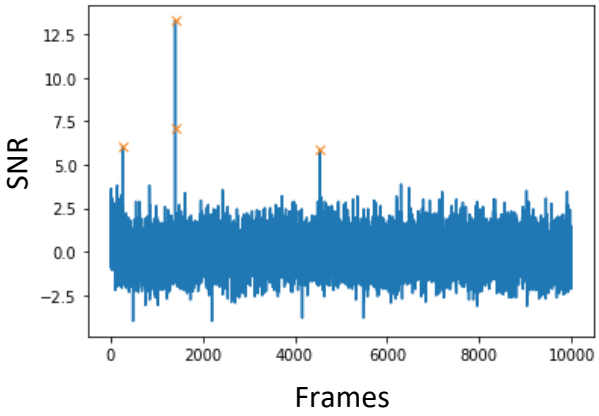

Figure 5.9. A simulated time trace showing centroids plotted on burst greater than a SNR of 5.

A challenge with SNR as an identification method is that it relies on the background signal and variation being constant throughout the experiment. If the background was to vary during the experiment, then we might expect a negative net signal in some time periods, as the background in some parts of the experiment may be greater than the signal of a single-molecule burst in other parts. This is particularly true with a changing laser power throughout an experiment.

Laser power can decrease during an experiment due to the temperature as shown in Chapter 3. However, this can be solved by taking multiple average backgrounds over shorter time periods.

Basing the SNR from the signal inside the spot and the background outside of the spot is acceptable if the background outside the spot represents the background in the spot. To check this the mean and standard deviation of the background within the spot and outside the spot on this optical system was compared and shown in Figure 5.10.

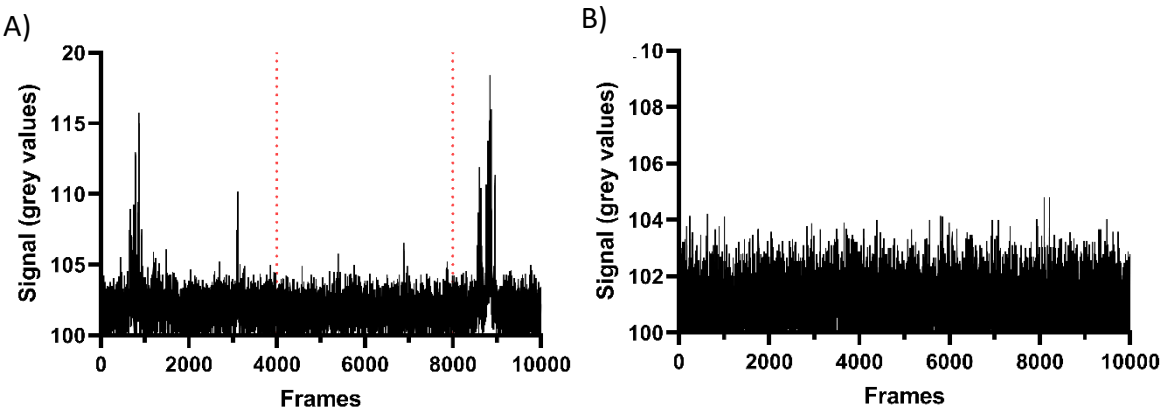

Figure 5.10. Time traces of 0.1 µm fluorescent beads in a 10 x 10 pixel spot. A) Inside the spot. The background was taken between the red dashed lines where no burst was visually observed. B) Outside the spot the background was taken of all this data. The y-axis scale is different on this graph to highlight that no bursts were observed in this graph.

Inside the spot, the mean of the whole data set was 102.0 grey values, and the standard deviation was 1.49. Within the red dashed lines where no fluorescence emission was visibly observed the mean was 101.8 and the standard deviation was 0.99. This compared with a mean of 101.0 and standard deviation of 0.93 outside the spot. We can conclude that the background values outside the spot are within experimental error of the background values inside the spot when no fluorescence emission is observed. Therefore, the resultant SNR values calculated by comparing the signal inside the spot to the background outside provides us with a good approximation of background. To ensure the confocal volumes generated by the digital

micromirror had the same dimensions, FCS analysis could be performed with a sample that has a well-documented diffusion coefficient.

Using this SNR approach on a digital micromirror (DMD), analysis in MATLAB generated a maximum intensity projection from a fluorescent bead (4 μm) sample over 200 frames. (Figure 5.11). The net signal is calculated as the signal subtracted by the average background over the whole time trace. This net signal is then divided by the background standard deviation. To ensure the background was representative of the experiment, for each data set, a gap to the right of the fluorescent activity (outside of the spot) was left and then the mean and standard deviation of the same size region of interest was calculated. The gap between the signal region of interest and the background region of interest meant that no signal from the spot entered the background datasets.

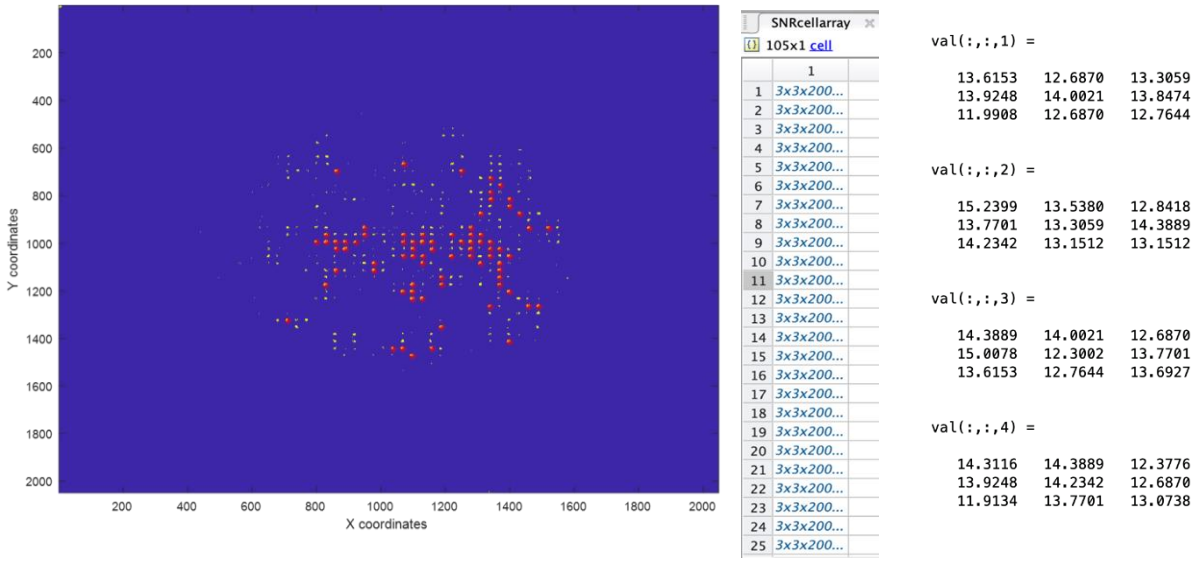

Figure 5.11. A figure generated from MATLAB code showing the maximum z-stack signal of the image on the detector with centroids marked on areas of intensity greater than 3 pixels^2. The intensity below a grey count of 130 is coloured in purple.

This figure shows a multi-spot pattern with centroids fitted to spots with a signal threshold of over 130 grey counts and an area above 3 pixels^2. An area, manually selected as one quarter of the size of the spot, was also used as a minimum threshold to discard fluorescent beads that did not spend long in the spot. To begin with, since the background was constant in this experiment, we were able to determine fluorescence emission from the beads by a signal threshold. However, further MATLAB code was prepared to generate SNR values for each pixel within spots that contained fluorescence emission. In doing so, a 4-D matrix containing time traces of all the spots was accessible. In each spot there are 9 values representing each pixel in a 3 pixel x 3 pixel area. From here a maximum signal in each frame can be made and plotted as a time series for each spot. While simple, this approach proved effective in identifying the location of fluorescent activity in these spots. This method was also adaptable to different spot sizes by changing the area that identified the signal. This made it easier to implement after running experiments with varied spot sizes.

5.3.3 Changing the spot size

Increasing the spot sizes in the pattern projected on the sample would provide two pieces of information. Firstly, since increasing the spot sizes would decrease the diameter distance of the micromirrors acting as pinholes, it would provide a measurement of the background signal and so the optimal spot size for maximising the SNR. Secondly, since this spot pattern was well defined, it may also be possible to obtain diffusion coefficients, similar to fluorescent correlation spectroscopy (FCS) measurements. Multiple experiments increasing the spot size and investigating the resultant signal of fluorescent beads was therefore conducted. By reflecting the emission and illumination light using more micromirrors the spot size was increased. A comparison of the SNR values obtained in doing this are shown in Figure 5.12.

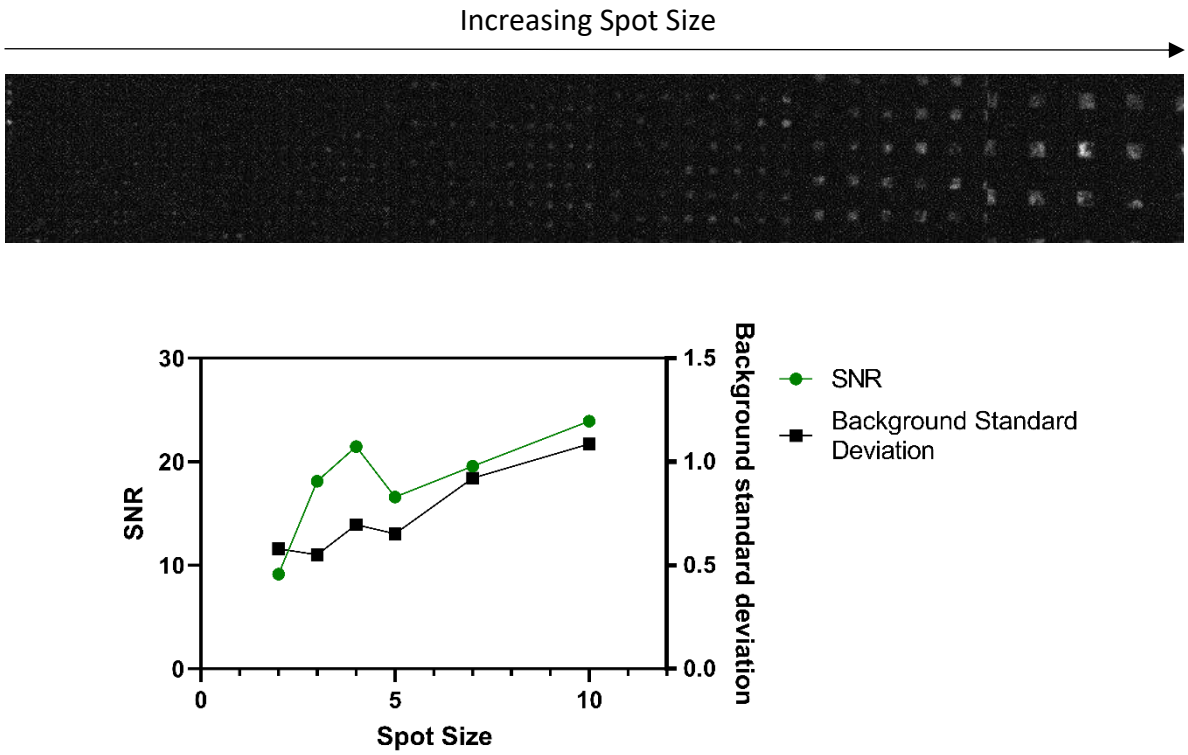

Figure 5.12. This graph shows the SNR and background standard deviation with different size spots (in pixels) and a sample of 0.1 µm fluorescent beads. The SNR was calculated from the signal of the fluorescent emission inside and the background inside the spot without fluorescence emission. Spot Size represents the length of the spot in pixels.

As the spot size was increased from 2 pixels to 10 pixels on the detector, the signal increased. As expected, this indicated that as more micromirrors were 'on', more fluorescent emission was reflected towards the detector. Furthermore, since a larger spot size would illuminate a greater volume of the sample, out of focus fluorophores would also emit fluorescence. This was shown by the increasing background standard deviation as the spot size was increased. However, since the background did not increase significantly for larger spots, the SNR also increased as the spot size increased. One reason for the background increasing only marginally was linked to the concentration of the sample. In this case the concentration was so low that there was a low chance of out of focus fluorophores being detected and causing an increase in background. Increasing the spot size does increase the SNR, but also decreases the throughput

of the experiment and the probability of observing single-molecules. This experiment will help determine the optimal spot size based on whether single-molecules can be observed at lower spot sizes.

5.3.4 Measuring the Diffusion Coefficient of Fluorescent Beads

An experiment to determine if the size of the spots was limiting the time the fluorescent beads spent in multiple spots was conducted and analysed in MATLAB for all the spots. Here we showed that as spot size increased, the maximum and average number of consecutive active frames increased, shown in Figure 5.13. The maximum number of active frames appeared to increase by the power of two and the average number of frames increased linearly.

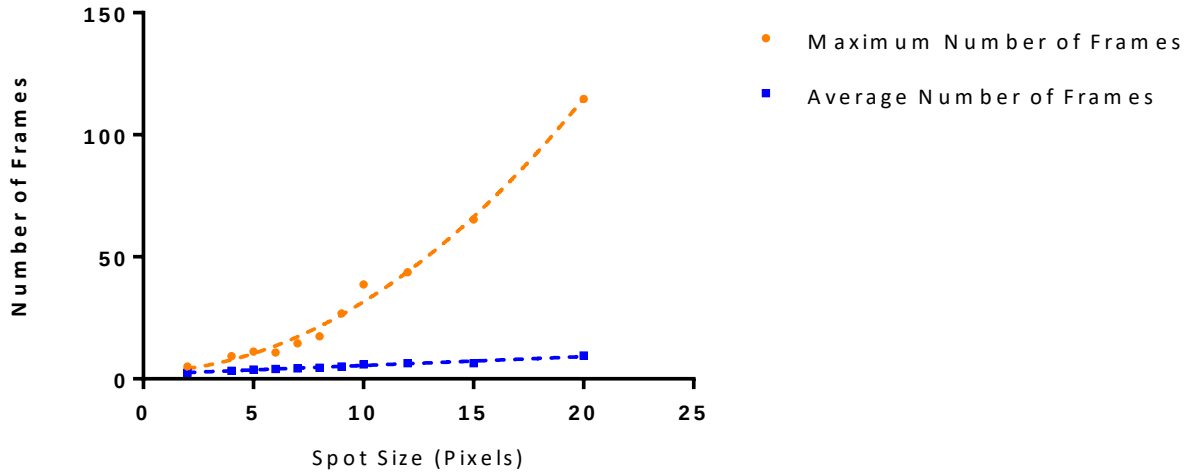

Figure 5.13. A graph showing the spot size against the number of consecutive frames the fluorescent beads stayed in the spot. The exposure time of the camera was 100 ms. A linear dotted line was fit to the average number of frames and a second order polynomial was fit to the maximum number of frames.

Logically, the fluorescent beads were observed for a longer period when more micromirrors were switched in the ‘on’ position. This trend from this graph confirmed this hypothesis.

To image single-molecules, we progressively moved towards less intense samples. In general, the smaller the size of the fluorescent bead, the less bright the sample will be. An sCMOS camera (Andor Zyla 5.5) was used to image 0.1 µm fluorescent beads in a solution of 50 % glycerol. While determining if these fluorescent beads could be observed, the diffusion coefficient of the beads was also investigated. By comparing the diffusion coefficient of fluorescent beads observed from this microscope with the diffusion coefficient cited in the literature, we would understand if the setup performed as we expected. The diffusion coefficient is related to the time spent in each spot by Equation 5.1:

$$D = \frac{\sigma^2}{4t} \tag{5.1}$$

Here, D represents the diffusion coefficient, σ is the spot size and t is the dwell time. The time each of fluorescent beads spent in a spot was calculated by tracking the beads using TrackMate, shown in Figure 5.14. This tool provided data quantifying the number of frames the beads spent within multiple spots.

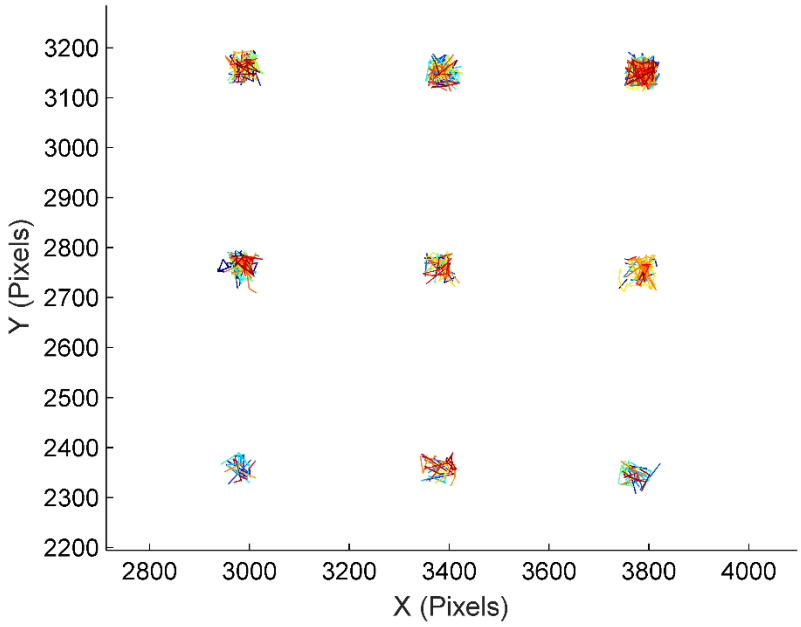

Figure 5.14. A graph displaying the region of a 100 pixel x 100 pixel multi-spot pattern on the camera. The tracking of 0.1 µm fluorescent beads is shown in multicolour lines by TrackMate.

Approximately 30 tracks were recorded at a 10 ms exposure time using the Photometrics 95B. [16]

Once the bead exited the individual spot of the multi-spot pattern, it could no longer be observed, and the tracking stopped. This tool provided a way to analyse multiple trajectories in a single acquisition, important for making the results reliable. A mean squared displacement graph was then plotted against the delay time providing an indication of how far the beads have moved in time. Figure 15 show the resultant mean squared displacement graphs from three experiments where the spot size was increased from a 100 pixel x 100 pixel spot pattern to 10 pixel x 10 pixel spot pattern, and finally to a 5 pixel x 5 pixel spot pattern.

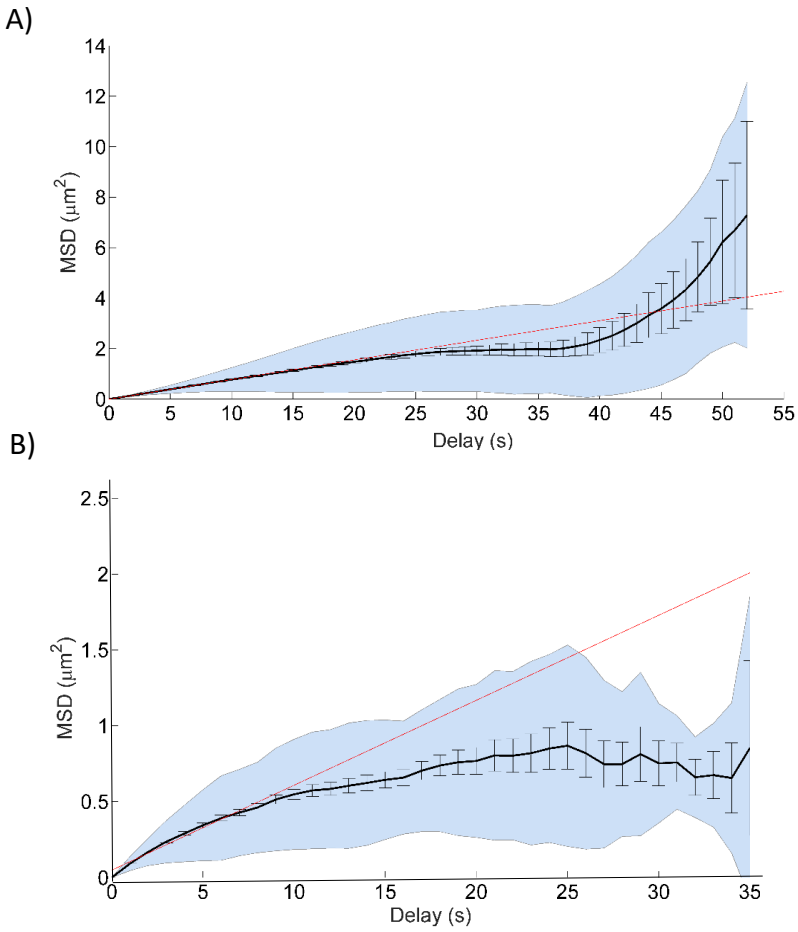

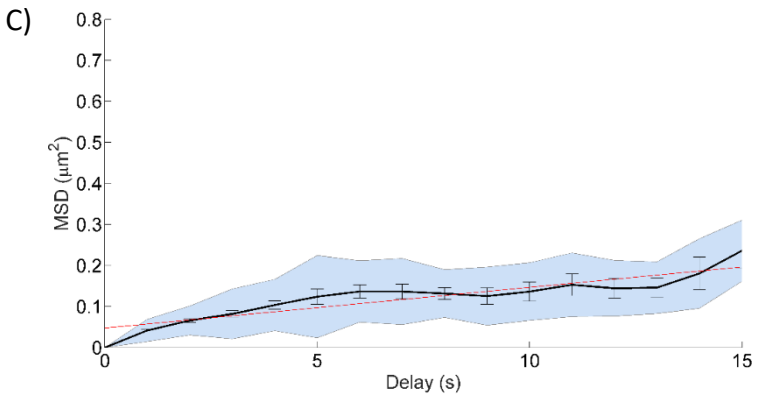

Figure 5.15. A mean squared displacement graph using a; A) 100 pixel x 100 pixel spot pattern B) 10 pixel x 10 pixel spot pattern C) 5 pixel x 5 pixel spot pattern. [17] A line of best fit (red) was added to the first 25% of data points. The black error bars represent the standard deviation, and the blue area represents the weighted standard deviation over all the MSD curves.

For all the graphs shown in Figure 5.15, the first set of data points were approximately linear. The 10 pixel x 10 pixel spot deviated from this trend after a short delay time. This may have been due to the virtual containment by the spot. Only the beads that stayed in the spot were measured. Therefore, the number of beads that spent a prolonged period in the spot, would only have the available maximum displacement of the width of the spot. This would mean at longer delay times the mean displacement would reach a limit, meaning only molecules observed would have the same or lower displacement than the size of the spot, this would mean at longer delay times the mean displacement graph would deviate from a linear trend. The 5 pixel x 5 pixel spot pattern does not fit the linear trend as the beads exited the spot too quickly. For all these experiments, the diffusion coefficient was calculated by taking the gradient of the first 25% of the slope using Equation 5.2:

$$\mathrm{MSD} = 2\,\mathrm{d}\,\mathrm{D}\,\mathrm{t} \tag{5.2}$$

Here, d is the dimensionality of the problem (2 for 2-D), D represents the diffusion coefficient and the time. Only the first part of the MSD graph was taken into consideration as higher delay times meant fewer beads were measured and so the variance increased substantially. The diffusion coefficient was determined to be $2.82 \times 10^{-14}\mathrm{m}^2/\mathrm{s}$ for the 100 pixel x 100 pixel

spot pattern, $2.02 \times 10^{-14}\mathrm{m}^2/\mathrm{s}$ for the 10 pixel x 10 pixel spot pattern and $6.75 \times 10^{-15}\mathrm{m}^2/\mathrm{s}$ for 5 pixel x 5 pixel spots. These diffusion coefficients were substantially smaller than the diffusion coefficient calculated for these fluorescent beads (0.1 μm) in 50% glycerol ($5.37 \times 10^{-13}\mathrm{m}^2/\mathrm{s}$). This was calculated using the Stokes Einstein equation, shown in Equation 5.3:

$$D = \frac{k_B T}{6\pi\mu R_0} \tag{5.3}$$

Here, D represents the Diffusion Coefficient, k_B is the Boltzmann's constant, T is the temperature, μ is the solvent viscosity and R_0 is the solute radius. Longer acquisition lengths to measure more molecules may be required to achieve approximate diffusion coefficients for this method. Another approach was therefore taken to see whether the diffusion coefficient could be better approximated. Here, we simulated the number of frames and hence the time the beads spent in the spots based on the Stokes Einstein equation (Equation 5.3). We anticipated that by using the maximum number of frames the fluorescent beads took to diffuse within the spots, an accurate width of the spot could be used to calculate the diffusion coefficient. Since the same conditions as the previous experiment were used, the calculated diffusion coefficient ($5.37 \times 10^{-13}\mathrm{m}^2/\mathrm{s}$), the radius of the beads (0.05 μm), the temperature (294.15 K) and the dynamic viscosity at 50:50 glycerol to water (0.0080289 Nsm^{-2}), was used. We then used Equation 5.1 to calculate the expected number of frames for a given spot size based on the pixel size of the camera (11 μm) and magnification of the microscope (60x). Comparing these values with the maximum experimental times observed at different spot sizes, we found the values between the simulation and experiment were similar (Figure 5.16). A nonlinear fit was applied for both datasets with R squared values of 0.99 and 1 for the simulated and experimental variables, respectively. The correlation was calculated between the simulated and experimental variables, and the coefficient of determination (r^2) was 0.99. Here, we found a very strong positive correlation and we can therefore conclude that, with this method, the DMD

can approximate diffusion coefficients of fluorescent beads using the maximum observed times in the spot.

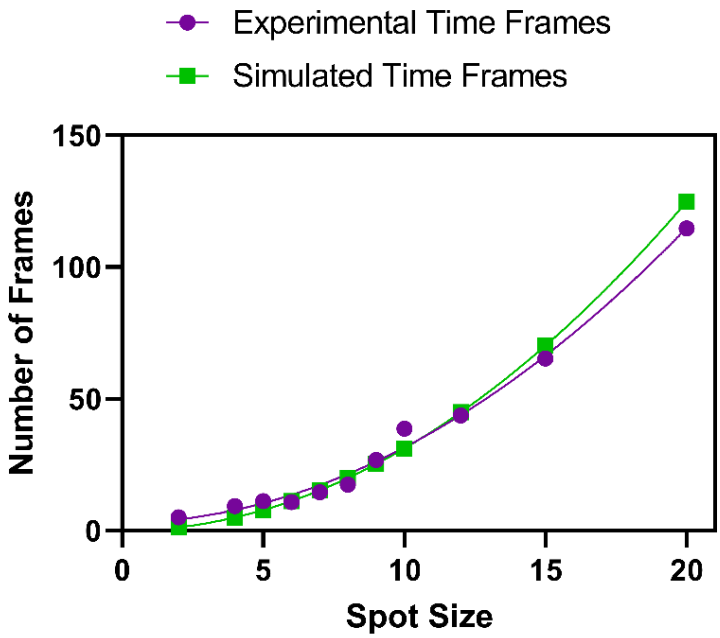

Figure 5.16. A graph showing the maximum number of frames fluorescent beads were inside the spot against the size of the spot. Simulated time frames are based upon the Stokes-Einstein equation.

3.5 An APD detector in combination with the digital micromirror device

To determine if single-molecules could be observed with a camera on the Cairnfocal setup, dsDNA labelled with ATTO 647N and ATTO 550 were prepared in a solution of imaging buffer (Tris pH 7.5 1M, BSA 20 mg/ml, NaCl 1mM, $MgCl_2$ 1M). A laser (640 nm) illuminated this sample and the sCMOS camera (Photometrics 95B) detected red emission. Single-molecule concentration (20 pM) was used for the low FRET sample used in Chapter 2. The results (Figure 5.17) showed that at a high exposure time (100 ms), the fluorescent emission could be observed from the dsDNA. However only a very small peak observed visually could

be seen at a low exposure time (2 ms) with 2-fold binning of the camera. Binning of the camera allows multiple pixels to be summed up as a single pixel. This sums the fluorescence signal, but also adds the background and the offset of the camera.

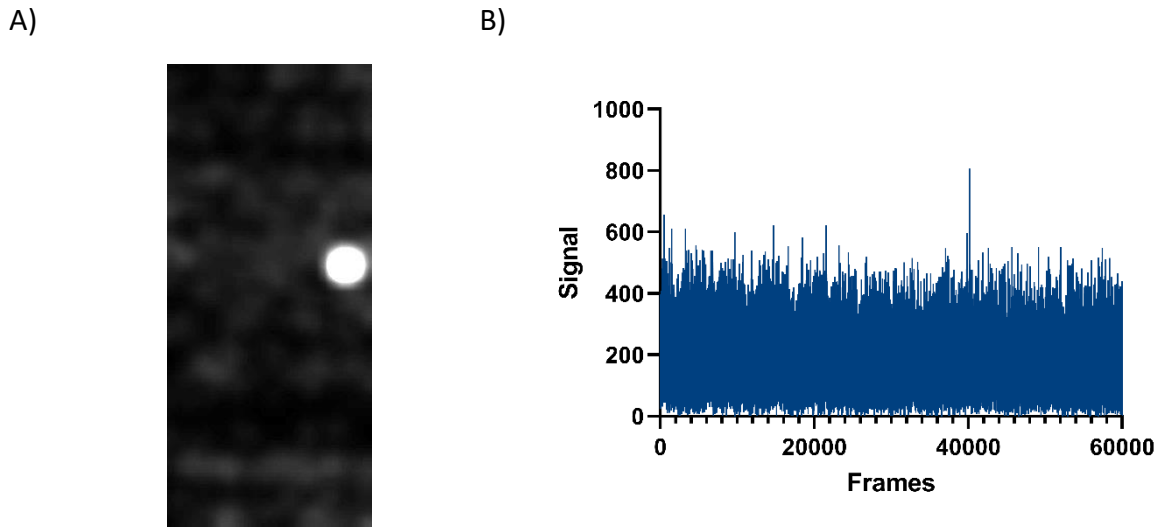

Figure 5.17. A) A picture of the red emission of dsDNA attached with ATTO 647N and ATTO 550 at an exposure of 100 ms. B) A time trace of the dsDNA with two-fold binning of pixels at an exposure of 2 ms.

As the camera could not detect single-molecules at high frame rates with sufficient signal, an avalanche photodiode (APD) was employed to investigate the background of the microscope. In this experiment an APD replaced the camera. Since the camera had a large field of view and the APD has only a small detection area, the micromirrors were switched 'on' in sequence to find which micromirror corresponded to an emission signal on the APD. Once aligned and the emission signal was detected on the APD, the experiment was repeated but with a series of dilutions from 10 nM to 0.125 nM, was conducted. The results, shown in Figure 5.18, indicated that as the concentration of the sample decreased by 2-fold each dilution, the signal on the APD decreased by around 2-fold, as expected. This showed that the emission detected on the APD was from the dsDNA sample and not from other sources such as dust or buffer.

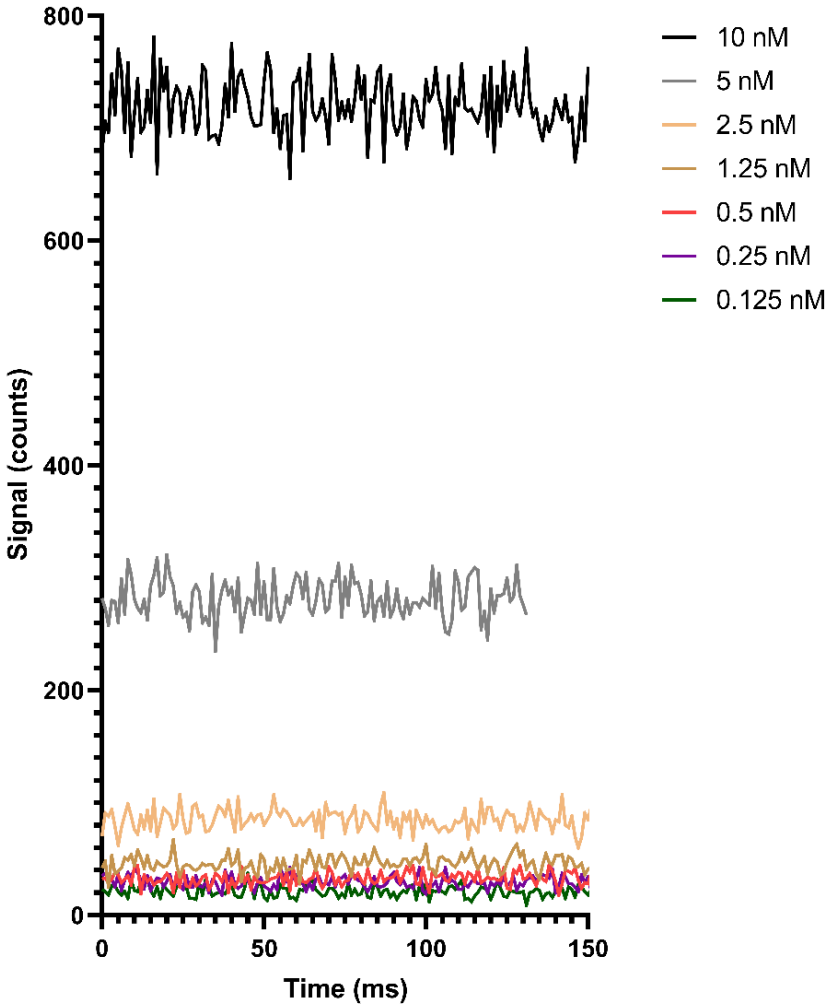

Figure 5.18. A graph showing the signal from an avalanche photodiode at various concentrations of dsDNA with ATTO 550 and ATTO 647N attached.

When the single-molecule solution was diluted further to picomolar concentrations, that have been shown to produce single-molecule burst on the smfBox, no single bursts were recorded, and the background remained the same as the background of the 0.125nM solution. To investigate this, a sample of ATTO 647N on its own was placed on the microscope with a sample of Milli-Q water to compare. Figure 5.19 shows that the emission from the dye on the APD was found by switching the micromirrors 'on' and 'off' in sequence. At nanomolar concentration of ATTO 647N, the SNR of the detection, when the subsequent area of the DMD

that reflected light to the SPAD was turned on, was 28.5. Although the SNR was high, the background count was also high (~3000 counts per 10 ms). When water was placed on the microscope the signal of the selected DMD disappeared, but the high background remained constant.

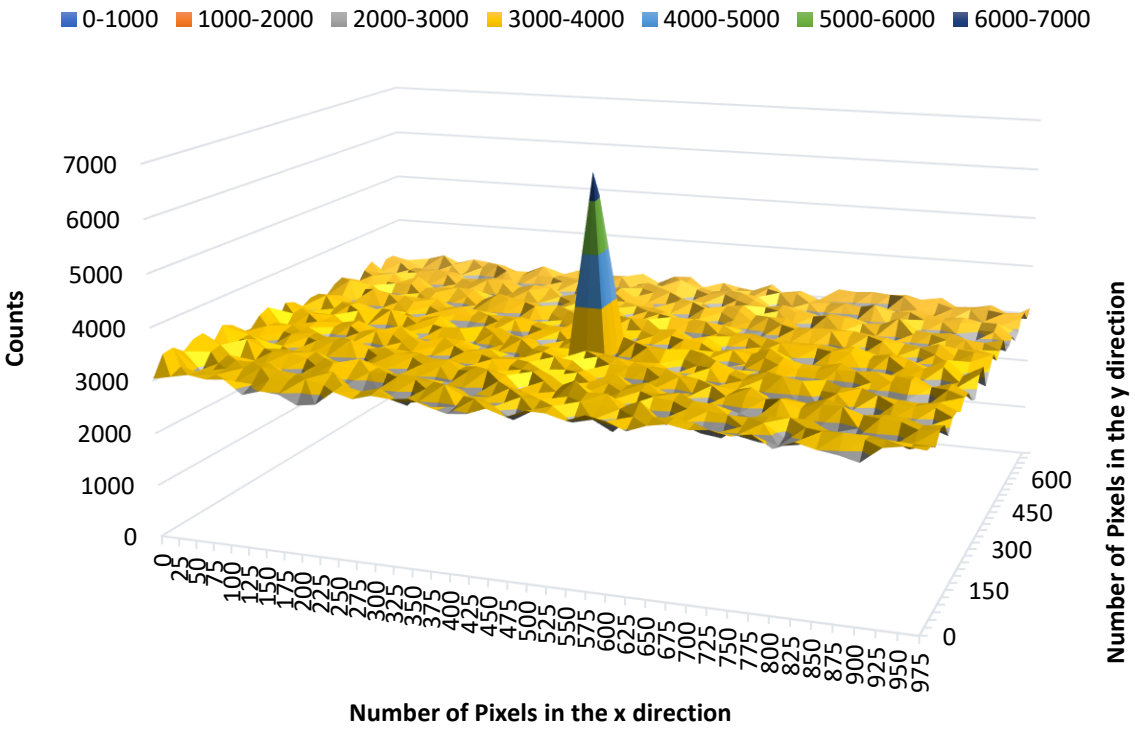

Figure 5.19. The counts/10 ms of the whole DMD turned 'on' in sequence. Data was acquired by switching a 5 pixels^2 area on and off sequentially until the whole DMD had been on once.

On the smfBox, the same dsDNA sample resulted in single bursts of 30 counts/ms with a low background of 0-2 counts/ms. The background in this experiment on the Cairnfocal was 300 counts/ms. Looking forward, we suspect the background is a result of the high laser power needed to irradiate the sample. A high laser power is needed for the digital micromirror device to send enough laser power to the sample and some of laser power is lost as it is not reflected. Here, this laser power may be reflected in the optical system back towards the detector and have passed through the emission filter. The light tightness of the microscope also needs to be

addressed. In this system, the Cairnfocal is attached to an inverted microscope that is not designed to be light tight.

Before detection of single-molecules on a camera are observed, the background needs to be reduced and single-molecules need to be detected on the APD first. Since this was not a failure of the multi-spot approach but rather due to the intrinsic light tightness and optical components of the instrument, in the next chapter we continue the progress made here by using the same technique but with a custom-built single-molecule microscope.

5.4 Conclusion

In this chapter we have implemented a multi-spot pattern with a digital micromirror device. This technique could observe large fluorescent beads in multiple spots and can approximate diffusion coefficients of these beads.

The goal of achieving single-molecule bursts to calculate FRET efficiencies, however, was not achieved. By decreasing the concentration of dsDNA to a single-molecule concentration and analysing water as a sample, it became apparent that the high background of the system was a major factor in not observing single-molecules with an avalanche photodiode. This background was evident when implementing an APD onto the Cairnfocal in the place of a camera. Here a background count rate of 3000 counts per 10 ms was recorded. Since single-molecule bursts are commonly recorded at 30-60 counts per ms on the smfBox, this was the main challenge of this project. These spots were also characterized with fluorescent beads and showed that increasing the spot size, increases the emission signal on the detector. This agreed with our hypothesis. However, unexpectedly, the background within the spots did not increase as

significantly, leading to a higher SNR of the larger spots. Since resolution was not the key challenge here, larger spots were used for higher signal.

By analysing fluorescent beads diffusing inside spot, we could measure approximate diffusion coefficients using the maximum number of frames the beads remained in the spot. We found that this method for determination of diffusion was better than tracking of individual beads, which did not closely resemble the diffusion coefficients calculated for the size and viscosity of the fluorescent bead sample. We also found that introducing a spot pattern virtually confines the molecules when tracking them.

5.5 References

[1] A. N. Kapanidis, T. A. Laurence, K. L. Nam, E. Margeat, X. Kong, and S. Weiss, "Alternating-laser excitation of single molecules," *Acc. Chem. Res.*, 2005

[2] B. Ambrose *et al.*, "The smfBox is an open-source platform for single-molecule FRET," *Nat. Commun.*, vol. 11, no. 1, p. 5641, 2020

[3] R. Roy, S. Hohng, and T. Ha, "A practical guide to single-molecule FRET.," *Nat. Methods*, vol. 5, no. 6, pp. 507–16, 2008

[4] A. Ingargiola *et al.*, "8-spot smFRET analysis using two 8-pixel SPAD arrays," in *Single Molecule Spectroscopy and Superresolution Imaging VI*, 2013

[5] M. Lachetta, H. Sandmeyer, A. Sandmeyer, J. S. A. Esch, T. Huser, and M. MÃller, "Simulating digital micromirror devices for patterning coherent excitation light in structured illumination microscopy," *Philos. Trans. R. Soc. A Math. Phys. Eng. Sci.*, vol. 379, no. 2199, 2021

[6] F. Sinjab, Z. Liao, and I. Notingher, "Applications of Spatial Light Modulators in Raman Spectroscopy," *Applied Spectroscopy*, vol. 73, no. 7. pp. 727–746, 2019

[7] L. Valiya Peedikakkal, V. Steventon, A. Furley, and A. J. Cadby, “Development of targeted STORM for super resolution imaging of biological samples using digital micro-mirror device,” *Opt. Commun.*, vol. 404, pp. 18–22, 2017

[8] H. Kirshner, F. Aguet, D. Sage, and M. Unser, “3-D PSF fitting for fluorescence microscopy: Implementation and localization application,” *J. Microsc.*, vol. 249, no. 1, pp. 13–25, 2013

[9] A. Griffa, N. Garin, and D. Sage, “Comparison of Deconvolution Software in 3D Microscopy: A User Point of View—Part 1,” *G.I.T. Imaging Microsc.*, vol. 12, no. 1, pp. 43–45, 2010

[10] D. Sage *et al.*, “DeconvolutionLab2: An open-source software for deconvolution microscopy,” *Methods*, vol. 115. pp. 28–41, 2017

[11] D. Sage *et al.*, “Quantitative evaluation of software packages for single-molecule localization microscopy,” *Nat. Methods*, vol. 12, no. 8, pp. 717–724, 2015

[12] D. Sage *et al.*, “Super-resolution fight club: assessment of 2D and 3D single-molecule localization microscopy software,” *Nat. Methods*, vol. 16, no. 5, pp. 387–395, 2019

[13] I. Khaw, B. Croop, J. Tang, A. Möhl, U. Fuchs, and K. Y. Han, “Flat-field illumination for quantitative fluorescence imaging,” *Opt. Express*, vol. 26, no. 12, p. 15276, 2018

[14] A. D. Edelstein, M. A. Tsuchida, N. Amodaj, H. Pinkard, R. D. Vale, and N. Stuurman, “Advanced methods of microscope control using μManager software,” *J. Biol. Methods*, vol. 1, no. 2, p. e10, 2014

[15] T. J. Collins, “ImageJ for microscopy,” *Biotechniques*, vol. 43, no. 1S, pp. S25–S30, 2007

[16] J. Y. Tinevez *et al.*, “TrackMate: An open and extensible platform for single-particle tracking,” *Methods*, vol. 115, pp. 80–90, 2017

[17] N. Tarantino *et al.*, “Tnf and il-1 exhibit distinct ubiquitin requirements for inducing NEMO-IKK supramolecular structures,” *J. Cell Biol.*, vol. 204, no. 2, pp. 231–245, 2014

Chapter 6. Developing a Single-Molecule Multipoint Detection System using Multiple Static Pinholes

All work in this chapter was conducted by Dylan George, except at the end of the chapter, the low, medium and high FRET dsDNA samples were measured on the smfBox by Mahmoud Abdelhamid, Sophie Fountain and Jessica Crummack.

Contents

6.1 Introduction 155

6.2 Methods 156

6.2.1 Optical Setup 156

6.3 Results and Discussion 158

6.3.1 Performance Measurements 158

6.3.2 Single-molecule (dye) measurements 164

6.3.3 Improve In-Focus Molecular Detection 166

6.3.4 Simultaneous imaging of single-molecules with an APD and a sCMOS camera 168

6.3.5 Using a TEM Grid as a multiple pinhole array 171

6.3.6 Characterizing the TEM Grid 174

6.3.7 Z-drift Measurements 179

6.3.8 Concentration Measurements 180

6.3.9 Dual Colour Measurements 182

6.3.10 Analysis of FRET Efficiencies using an image splitter 184

6.4. Future work analysing single-molecule bursts 190

6.4.1 Identifying single-molecule bursts 190

6.4.2 Location of single-molecule bursts 191

6.5 Conclusion 197

6.6 References 198

6.1 Introduction

In this chapter, we aim to continue the development of a novel single molecule microscope with high-throughput capability. We previously explored whether multiple single molecule measurements could be observed simultaneously but found the high background of the Cairnfocal was the limiting factor. Here, we focus on reducing the high background signal when attempting single-molecule detection in multiple observation volumes. This new method introduces the use of a transmission electron microscopy (TEM) grid as an array of pinholes that closely resembles the technique of the digital micromirror used in the previous section. In this method, we illuminate and project the structure of the array of pinholes (the TEM grid) onto the sample. This grid is an array of round holes, acting as pinholes, that are 35 μm in diameter, shown in Figure 6.1.

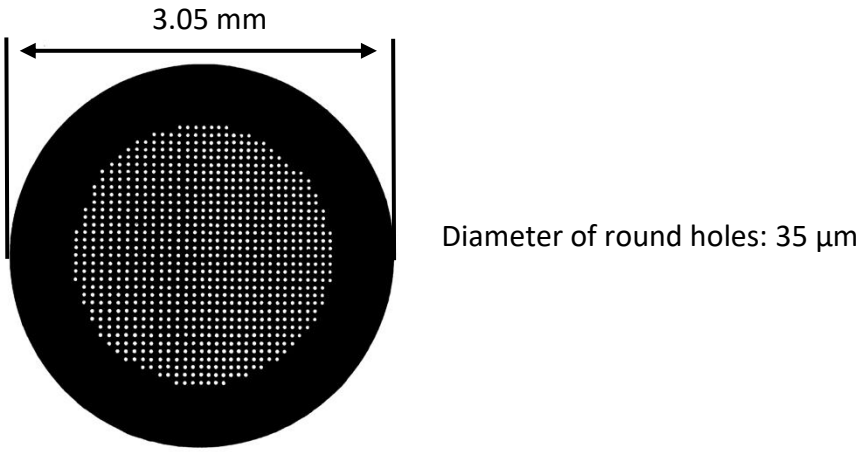

Figure 6.1. A copper, round hole TEM grid. The diameter of the grid is 3.05 mm and the diameter of each hole is 35 μm.

The fluorescence emission from the sample then returns through this pinhole array. Our hypothesis is that this will optically section the sample, rejecting emission from out of focus fluorophores and increasing the signal-to-noise ratio (SNR). This also results in the single molecules being spatially separated on a camera.

Since the method developed in this chapter, to our best knowledge has not been constructed before, the first experiments were designed to test the performance of this approach. For example, testing the background of the setup. We then assessed whether double stranded DNA labelled with red and green dyes (required for FRET) could be observed at low exposure times in both green and red emission channels on the camera.

6.2 Methods

The hardware of the optical setup

In this setup a 647 nm laser was used in combination with an excitation filter (Semrock, FF02-628/40) and a dichroic mirror (Semrock, FF662-FDi01). An objective lens (Olympus, UPLANFLN 100x) attached to the inverted microscope (Nikon Eclipse Ti2) focused the laser beam onto the sample. The emission filter (Semrock, FF02-685/40) was used to filter the fluorescence before detection with a camera (Hamamatsu Flash 4.0) and an avalanche photodiode (Excilitas, Si-APD). To record counts on the APD, a NI-DAQ board connected to the computer was used. Additionally, achromatic lenses (Thorlabs) and kinematic mirrors (Thorlabs) were used.

6.2.1 Optical Setup

This new microscope was assembled with a pinhole in the illumination and the emission path, shown in Figure 6.2. Initially, the setup used a single pinhole prior to testing multiple pinholes. In this setup, the laser is directed by a dichroic mirror through the pinhole. This illuminated the sample with one confocal spot based on the structure of the pinhole. Since the setup has epifluorescence geometry, meaning the illumination and emission paths are in the same place although travelling in different directions, the fluorescence emission from the sample travelled back through the same pinhole. This results in the detection volume being in the same location

as the illuminated spot in the sample. As described in detail in the previous chapter, this effectively rejects out of focus light reducing the background. Here we anticipated that the multiple pinhole array would increase the SNR sufficiently to detect FRET emission within multiple spots generated on the camera.

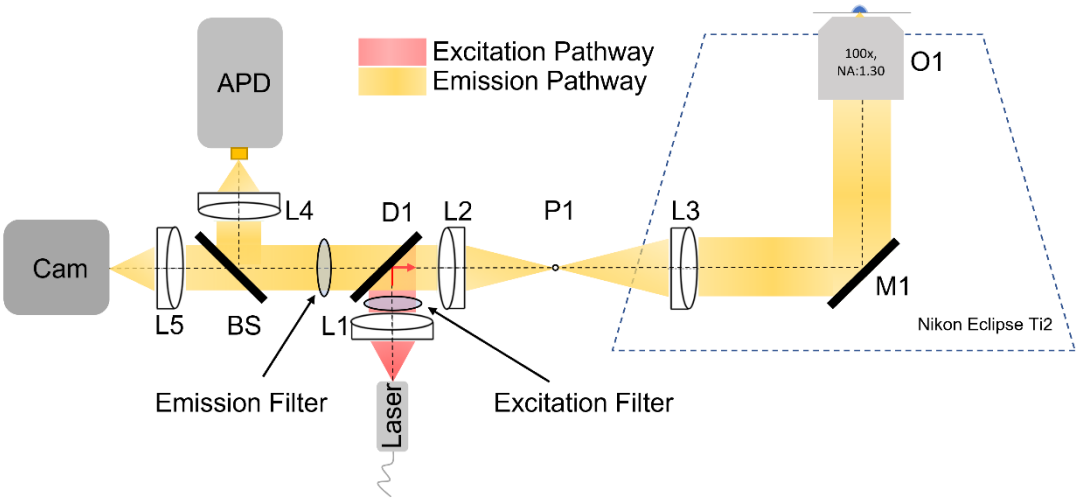

Figure 6.2. A reflective, confocal microscope design for single-molecule fluorescence measurements. The illumination light (red) from a 647 nm laser travels through an excitation filter and the pinhole to the sample via an inverted microscope (Nikon Eclipse Ti2). The fluorescent emission (orange) travels back through the same pinhole to the detectors. A 50:50 beam splitter (BS) is placed in the emission path to direct half the emission towards an avalanche photodiode and half to the camera (Hamamatsu Flash 4.0).

In this microscope, the objective lens (O1) that focused the illumination to a small spot on the sample was an Olympus UPLANFLN 100x with a numerical aperture (NA) of 1.30. This was chosen primarily for the high NA value, which improves the SNR, and provides minimal chromatic aberrations. The tube lens (L3) had a focal length of 180 mm, common for Olympus objective lenses. Based on Equation 2.1 and 2.2 outlined in Chapter 2, a pinhole of 100 μm in size was used to maximize the signal instead of the spatial resolution. This pinhole would confine the confocal detection volume to the same extent as the openFrame module providing the microscope with a high signal. [1] The lens before the pinhole (L2) and the collector lenses

(L4 and L5) had focal lengths of 45 mm and 75 mm, respectively. The lens before the camera ensured the total magnification to the detector remained high enough (41.6x) to detect fluorescent molecules across multiple pixels. A 647 nm laser, collimated through a collimation lens (L1), was also selected as its wavelength was well matched to the excitation of the ATTO 647N dye which we used on its own and attached to dsDNA (38 base pairs long, supplied by ATDBio). Initially, a 50:50 beam splitter (BS) was used to separate the signal between the camera and the APD, although this was taken out in several experiments to maximize the signal on the camera.

6.3 Results and Discussion

6.3.1 Performance Measurements

Initially, to test this setup, a Chroma autofluorescent plastic slide was used to observe if fluorescence emission could be detected on the camera. These diagnostic slides are intended to determine the consistency and evenness of illumination. When illuminated with the 647 nm laser, the slide emitted fluorescence which helped align the avalanche photodiode (APD) and the camera onto the sample. A laser with a power of 11 mW, measured before the objective lens, was used to illuminate the slide and the camera and APD were aligned without the pinhole in place. This measurement was then compared with a non-fluorescent imaging buffer on the avalanche photodiode, shown in Figure 6.3.

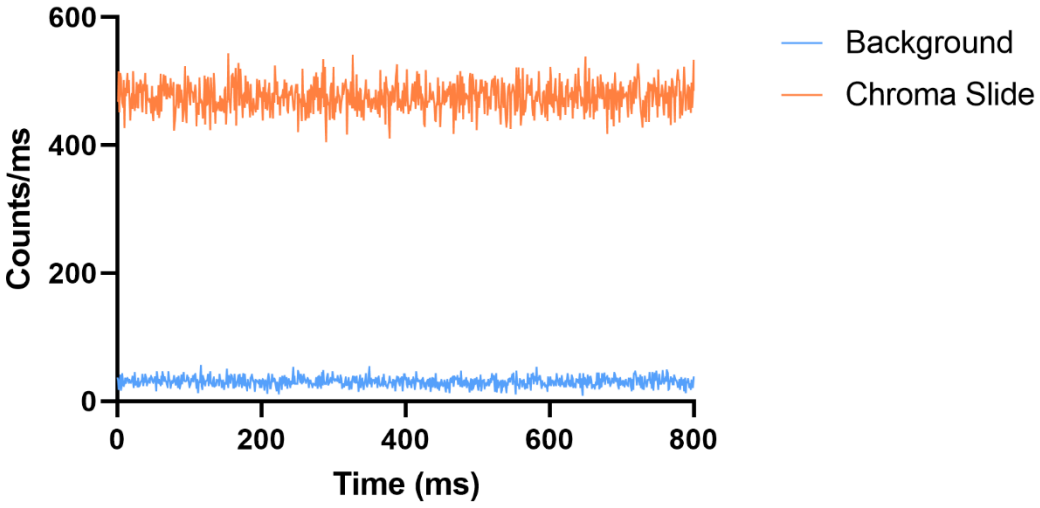

Figure 6.3. A preliminary test of a bright chroma slide (Orange) against a non-fluorescent imaging buffer (Blue) on the avalanche photodiode. The avalanche photodiode binned the signal every millisecond.

As expected, the Chroma autofluorescent slide emitted a high mean count of 455 ms^{-1} and helped align both detectors. This experiment showed that the avalanche photodiode was aligned onto the sample. The non-fluorescent imaging buffer generated a mean count of 20 ms^{-1}. The count rate for the imaging buffer was higher than expected. Here, we expected a minimal background count rate of 0-2 ms^{-1}.

To determine the origin of the background arising from the imaging buffer, a fluorescent sample of ATTO 647N attached to dsDNA was placed on the microscope and compared to a sample of Milli-Q water. Here, we expected to observe fluorescence emission for the dsDNA sample and no emission for the Milli-Q water sample. This experiment was conducted in dark conditions, meaning that all the lights were switched off, so the background from ambient light would not affect the results. For both measurements the shutter (an iris after the pinhole), which allowed the laser beam to travel to the sample, was set to either open or closed. To ensure that no laser light entered the sample when the shutter was closed, a power meter replaced the

position of the objective lens, and a power recording confirmed no laser light was recorded. Figure 6.4 shows a graph combining these experiments with an increasing laser power.

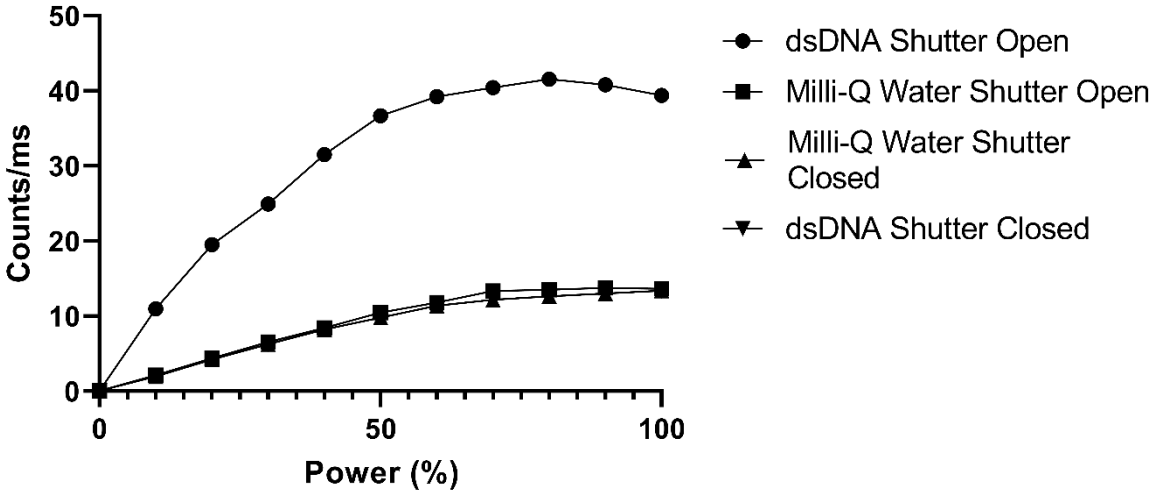

Figure 6.4. A background experiment showing the signal on an avalanche photodiode with the red laser on at different power percentages. The dsDNA sample with shutter open is represented with circle symbols. The Milli-Q water sample with shutter open is represented with square symbols. Below this are both the dsDNA sample and the Milli-Q water with the shutter closed sharing the same values. Both are visible beyond 50 % compared with the shutter open experiments.

This experiment showed that the signal from both the dsDNA sample and Milli-Q water sample increased with increasing laser power. A substantial change in signal was observed with the dsDNA with the shutter open compared to the water with the shutter open, demonstrating that the detector was sensitive to the increased fluorescence emission from the labelled sample, as expected. When the shutter was closed, both the dsDNA sample and Milli-Q water sample showed identical count rates for all power intensities and were indistinguishable. Interestingly, the difference between the Milli-Q water sample with the shutter open and the shutter closed only became apparent at a laser power percentage greater than around 40%. One possible reason for this could be the small fluorescence emission of Milli-Q water if it has been contaminated. More surprisingly, the signal of the Milli-Q water sample increased even with the shutter closed. This shows that the background light was emerging from before the shutter.

This could indicate that an optical component, such as the emission filter before the shutter, may be causing the background to increase. If this was the case, we would expect the background to increase as the laser power increases, matching the observation in this experiment. To rectify this, a measurement of the spectral properties of the dichroic mirror was performed and compared with the expected specifications from the suppliers, alongside those for the excitation and emission filters shown in Figure 6.5 and 6.6.

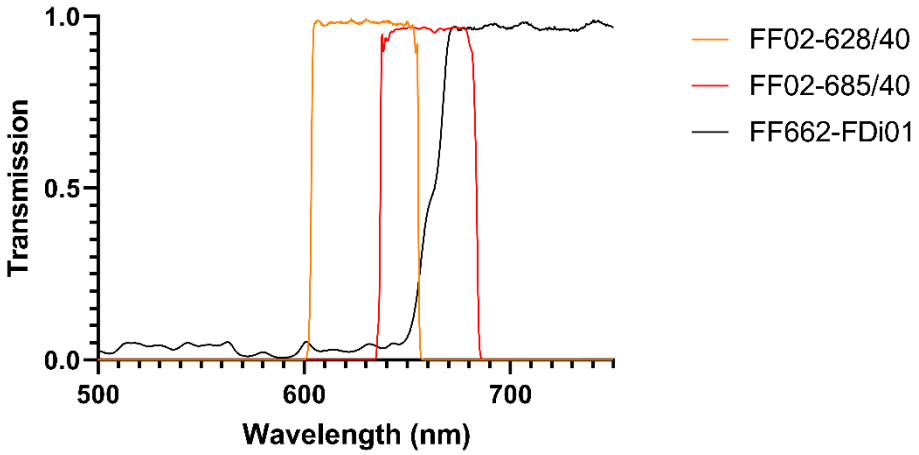

Figure 6.5. Filters in the microscope, values retrieved from the suppliers. FF02-628/40 is the excitation filter, FF02-685/40 is the emission filter and FF662-FDi01 is the dichroic mirror.

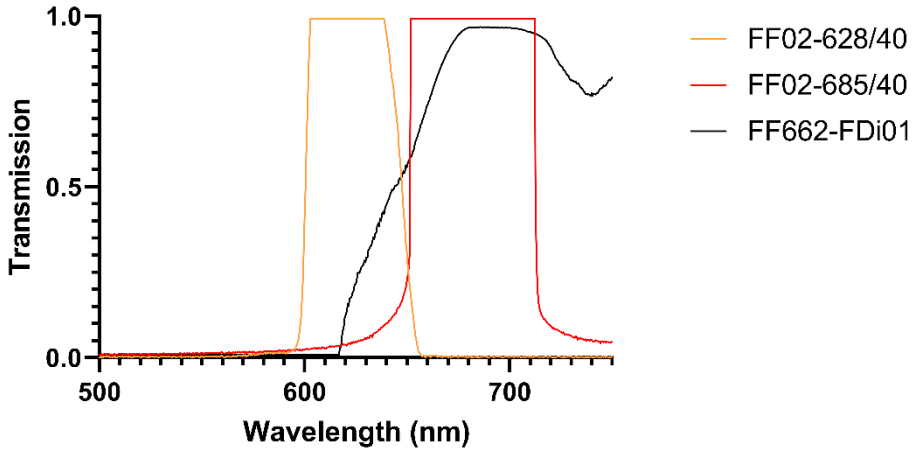

Figure 6.6. Experimental values of the filters in the microscope. FF02-628/40 is the excitation filter, FF02-685/40 is the emission filter and FF662-FDi01 is the dichroic mirror. Values measured by illuminating with a white laser. The resultant intensity after passing through the filters was recorded with a spectrometer (Ocean Optics).

It was found that the emission filter and the excitation filter overlapped, and the emission filter transmitted a broader spectrum than the values obtained from the supplier. The dichroic mirror was also found to be transmissive at a lower wavelength than expected. We also showed that the laser emitted a broad red spectrum of 620 nm – 670 nm and the intensity of the laser could be observed with the excitation filter and dichroic mirror in place (Figure 6.7).

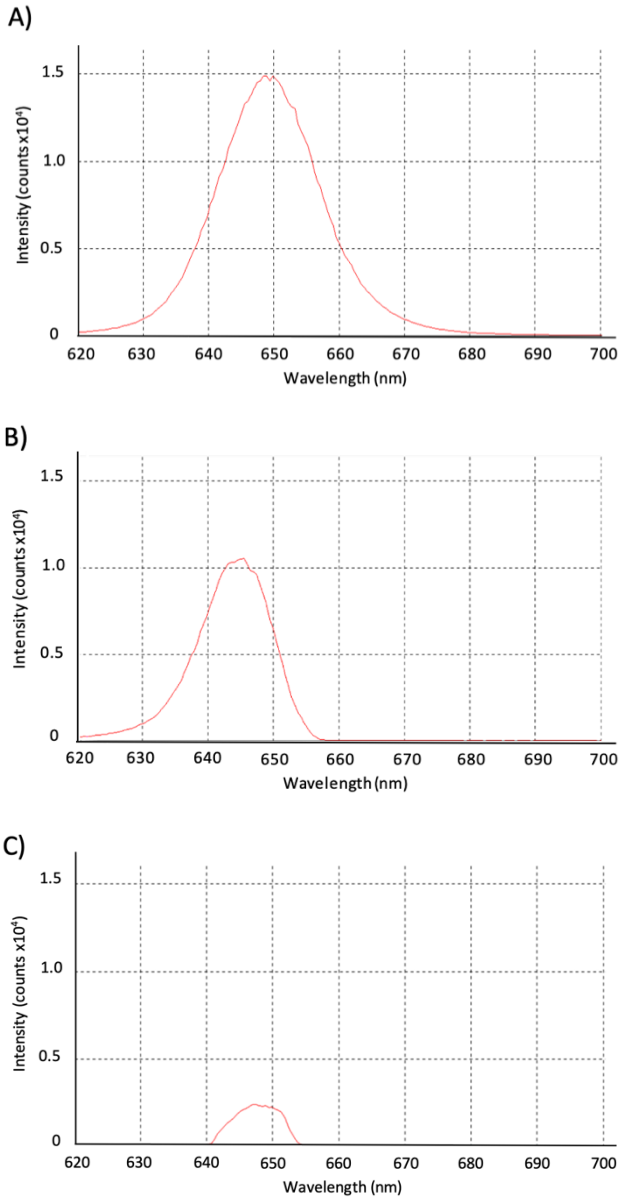

Figure 6.7. A) The 647 nm laser wavelength, measured by a spectrometer (Ocean Optics) B) The 647 nm laser wavelength, with an excitation filter in front. C) The 647 nm laser wavelength with an excitation and dichroic mirror in front.

This would mean that a percentage of the excitation laser light could also pass through the current emission filter. To solve this, a new excitation filter (to cut out the lower wavelengths of the laser) was put in place and combined with a new dichroic filter that had a lower cut-on wavelength at 650 nm (Semrock FF545/650-Di01). After these implementations, to further ensure that the system had a reduced background, a final measurement was taken of the setup in dark conditions with a fluorescent sample (ATTO 647N) and a non-fluorescent sample (Milli-Q water), shown in Figure 6.8 and 6.9.

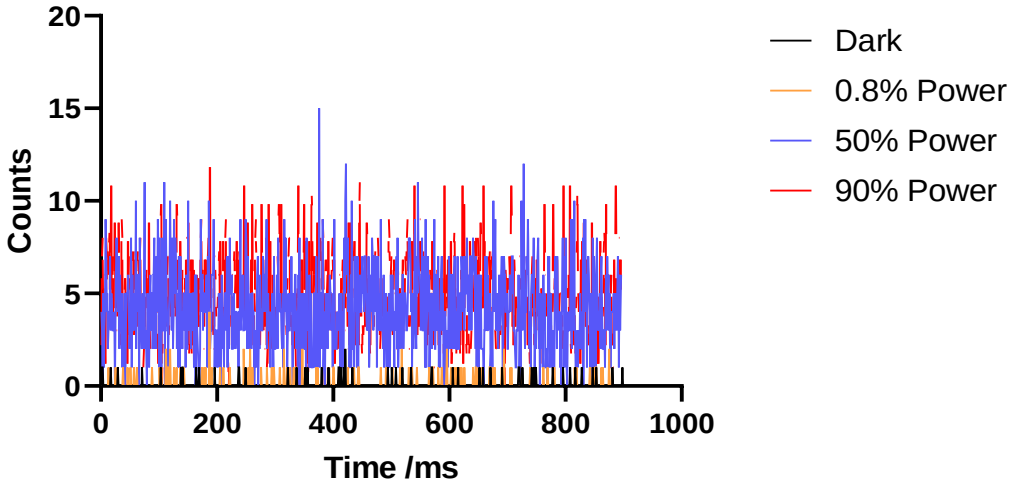

Figure 6.8. Signal on the APD with Milli-Q water in dark conditions with varying laser power. The laser was off in the dark measurement.

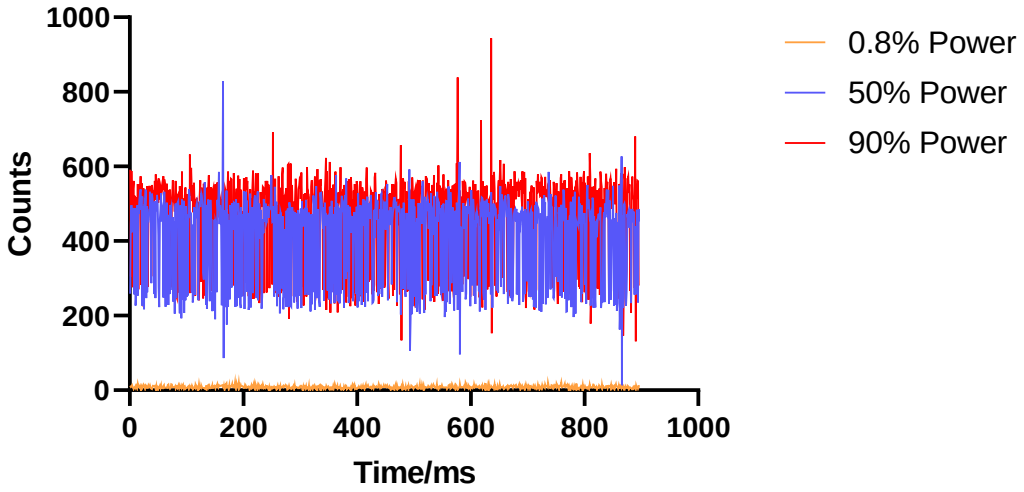

Figure 6.9. Signal on the APD with ATTO 647N dye in dark conditions with varying laser power.

These graphs show that at high laser power the mean counts of a concentrated sample (nanomolar) of ATTO 647N was around 450 ms^{-1} compared to around 5 ms^{-1} for the Milli-Q water. It also showed that counts when the laser was off were extremely low (0-1 ms^{-1}). From this experiment we can deduce that the laser power continued to be the source of the background but was much lower than the previous experiment. We expected that the background would reduce further with a lower laser power. To test this, the laser power at the sample was recorded (11 mW) at 20% of the maximum achievable laser power. After a 50 μm pinhole was installed, the laser power dropped to 2 mW at the sample. By reducing the size of the pinhole to 10 μm, the laser power was reduced further to 500 μW. After these results, we put in place neutral density filters, with an optical density based on the size of the pinhole, to further reduce the laser power at the sample to a similar power on the smfBox (~150 μW).

6.3.2 Single-molecule (dye) measurements

Following these background measurements and setup optimisations, the next step was to determine if single bursts could be seen from ATTO 647N dye at low concentrations (100 pM) (Figure 6.10). For these experiments a 100 μm pinhole was used. If this sample could be

observed, then the concentration would be lowered to single molecule concentrations (tens of picomolar).

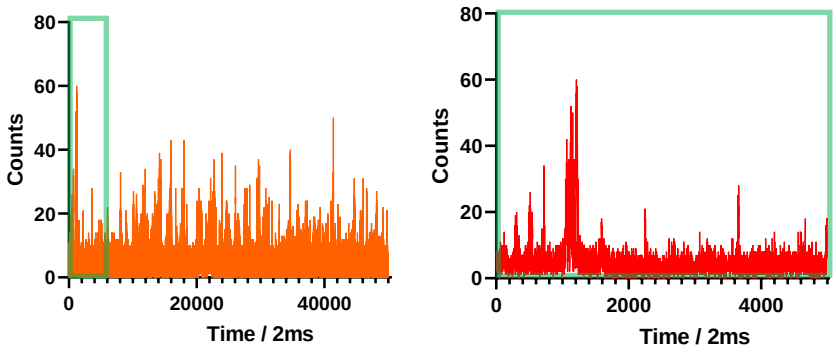

Figure 6.10. A time trace from an ATTO 647N sample at a concentration of hundreds of picomolar measured on the avalanche photodiode over a 100 second period (right) and a zoomed in time trace of a 10 second period at the start of the experiment.

Figure 6.10 shows the signal of concentrated dye using the avalanche photodiode. At an exposure time of 2 ms, many bursts could be seen throughout the acquisition. Other experiments were carried out at exposure times of 1ms, 5ms and 10ms. In all of these experiments, single bursts could be seen. However, once the concentration was lowered (1-15 pM), single bursts were not seen at these exposure times. This implies that bursts observed may not be due to individual molecules.

This was probably due to sub optimal z direction positioning of the fixed tube lens within the commercial inverted microscope. This would decrease the SNR measured on the detectors as the single-molecules would not be in focus. Since the position of the fixed tube lens was unknown, this made it increasingly difficult to arrange the other flexible optical components to retrieve the emission from the inverted microscope. To conclude, these experiments have shown that this optical setup was limited to imaging the dye ATTO 647N at high picomolar concentrations and could achieve single bursts, by visual observation, at a count rate of 60 ms^{-1}.

6.3.3 Improve In-Focus Molecular Detection

To focus the emitted light more precisely on the pinhole, the Nikon Eclipse Ti2 inverted microscope was replaced with an achromatic lens (L4), a right angle mirror (M1) and a stage holder (Figure 6.11). We also anticipated that this would make the optical system light-tight and significantly less expensive.

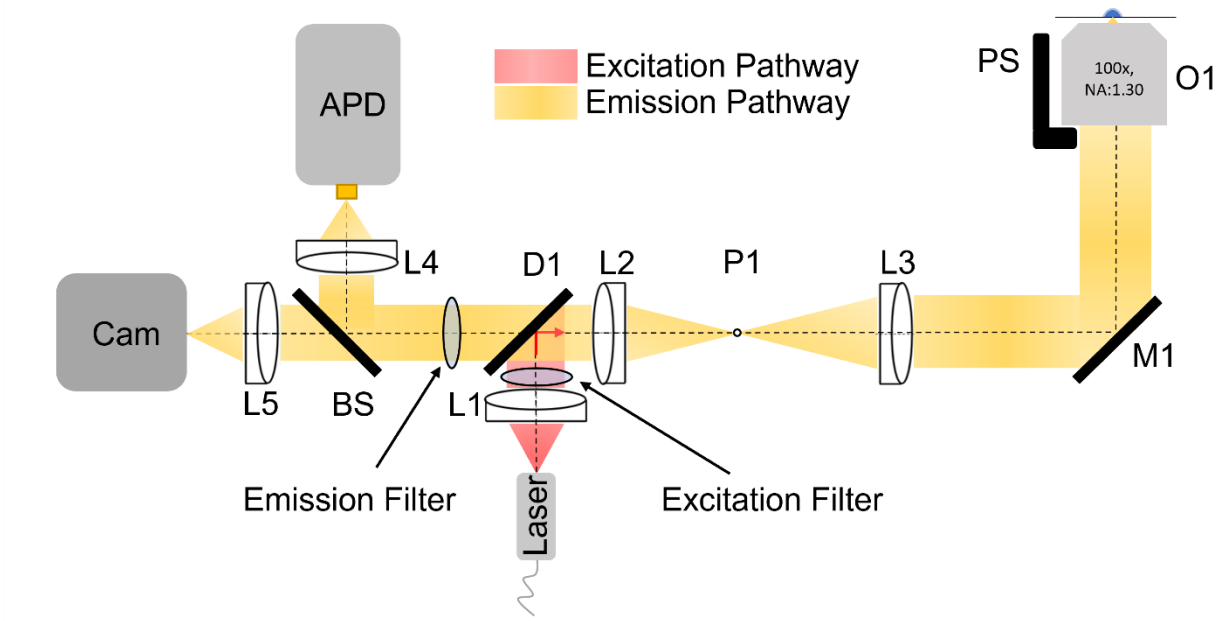

Figure 6.11. The schematic of the optical pathway of the single-molecule fluorescence microscope having removed the Nikon Eclipse Ti2 and added a z-stage piezo scanner (PS). The tube lens (L3) was changed to a focal length of 150 mm.

A z-stage piezo scanner (PS) was also employed to position the objective lens to micrometre precision. Since the setup had been changed, the fluorescence emission passing through the pinhole needed to be aligned onto the detectors again. In addition, an experiment confirming that the signal from a concentrated dye sample could be observed, was conducted. In this experiment a dilute sample of dye (ATTO 647N) was placed on the microscope and detected using a camera (Hamamatsu Flash 4.0). Time traces of two areas on the image were compared. One area was selected where single-molecules were observed inside the pinhole spot, where

emission was expected (Figure 6.12). The other area was outside the pinhole spot, where emission was expected to be absent (Figure 6.13).

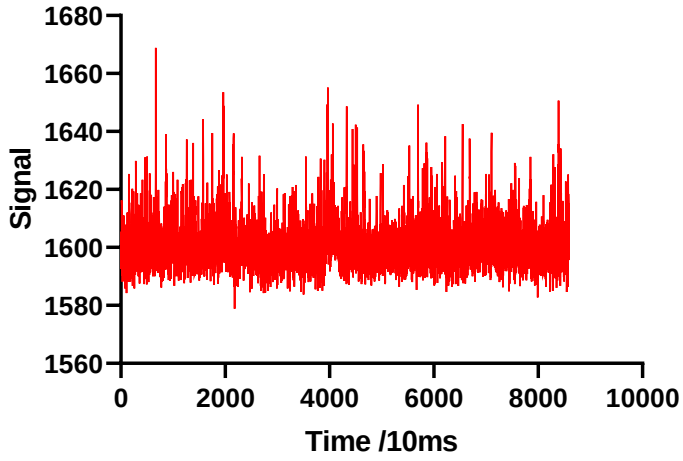

Figure 6.12. The signal from a picomolar concentration (150 pM) of dye (ATTO 647N) sample inside the pinhole spot on the Hamamatsu Flash 4.0 camera with an exposure time of 10ms and binned over 4 x 4 pixels.

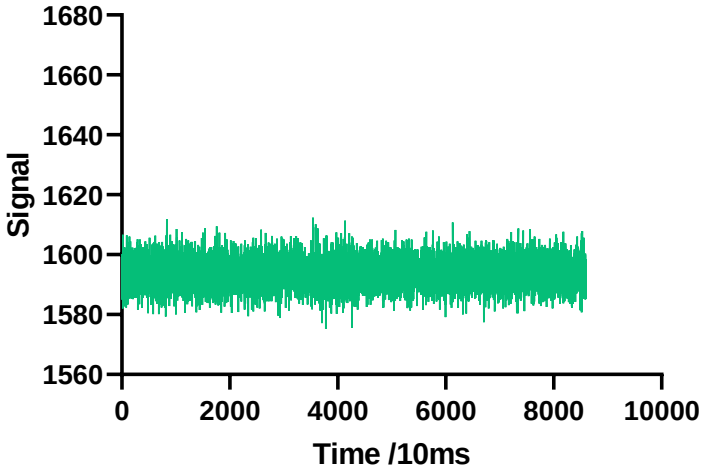

Figure 6.13. The signal from a picomolar concentration (150 pM) of dye (ATTO 647N) sample outside the pinhole spot on the Hamamatsu Flash 4.0 camera with an exposure time of 10ms and binned over 4 x 4 pixels.

In this experiment the dye sample was detected at an exposure time of 10 ms. These results showed clearly that the dye sample could be observed on the camera at picomolar concentrations when using the pinhole.

6.3.4 Simultaneous imaging of single-molecules with an APD and a sCMOS camera

The next step was to determine if single-molecule bursts could be observed with a camera at single-molecule concentrations. If this was successful, we could then test whether single-molecules could be detected with a camera at the lower exposure times required to reveal fast conformational dynamics of biomolecules.

To investigate this, we explored if single molecules could be seen by both the APD and camera simultaneously at single-molecule concentrations. This was an important comparison, as the camera is less sensitive than the APD, and so if single-molecules could not be seen on the camera but were seen on the APD, we could conclude that the camera does not have sufficient sensitivity to capture single-molecules at low exposure times.

To detect fluorescence emission on both the avalanche photodiode and the camera simultaneously, a 50:50 beam splitter was placed in front of the APD and the camera. If aligned correctly, we would expect both detectors to observe fluorescence emission in the same observation volume in the sample. A 100 μm pinhole was used in conjunction with a 647 nm laser to illuminate the sample. Initially, to ensure both detectors could observe the same fluorescent emission, the detectors recorded at an exposure time of 100 ms. To validate the sample, a solution of ATTO 647N was diluted in Milli-Q water to a concentration of 10 pM (single-molecule level) before being placed on the smfBox, a well calibrated and high standard single molecule FRET microscope [1] Once it was confirmed by the smfBox that single bursts of FRET were detectable at these concentrations, the sample was then placed on the custom-

built microscope and measured using a camera (Hamamatsu Flash 4.0) and an APD simultaneously (Figure 6.14).

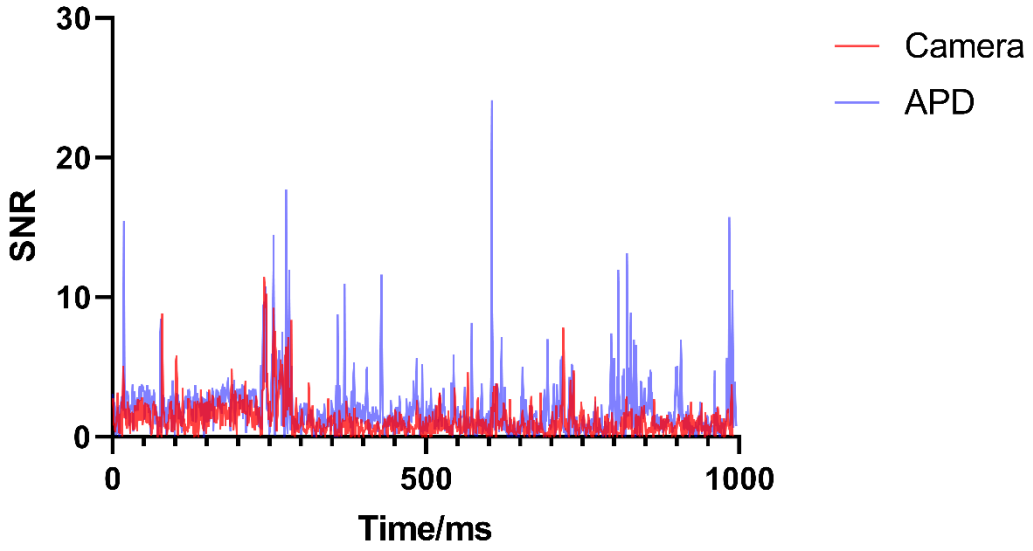

Figure 6.14. The SNR of a dilute sample of Atto647N (10pM) detected at an exposure time of 100 ms with; A) Avalanche Photodiode B) sCMOS Camera (Hamamatsu Flash 4.0).

Figure 6.14 shows that single molecules bursts were seen with both the camera and the APD at a high exposure time of 100 ms. Furthermore, these bursts occurred at almost the same time on both detectors. This result was encouraging as it showed that the APD was measuring the same fluorescence emission as the camera. It also meant that the APD was correctly aligned and so we could proceed to taking data at faster speeds (lower exposure times).

The next experiment used the same sample, but the detectors recorded at a much lower exposure time of 1 ms (Figure 6.15). As mentioned previously this was important to capture the fast dynamics of these single molecules.

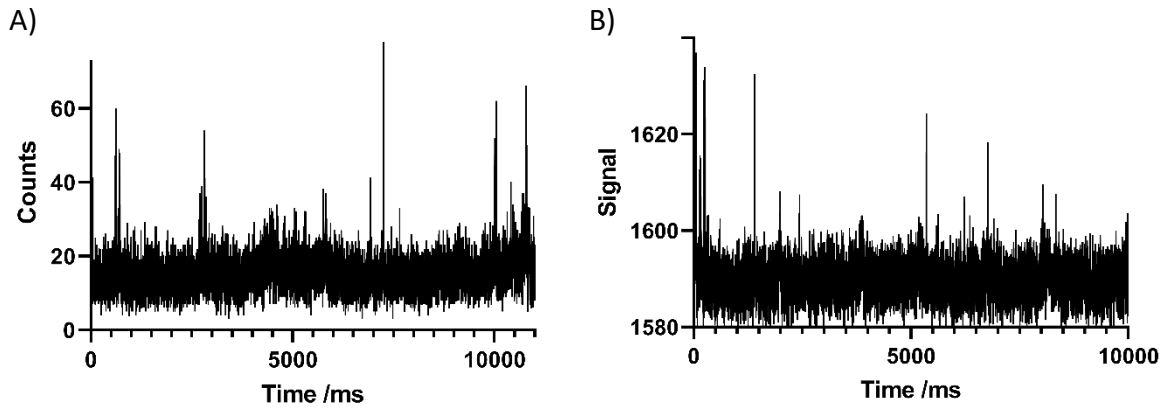

Figure 6.15. A dilute sample of ATTO 647N (10pM) detected at an exposure time of 1 ms (without the 50:50 beam splitter in place) with; A) Avalanche Photodiode B) sCMOS Camera (Hamamatsu Flash 4.0)**.**

These graphs show that single bursts were detected on both the APD and the camera at a low exposure time of 1 ms. However, for this experiment the beam splitter was taken out, as single molecules could not be observed on the camera with it in place. Therefore, these two detectors were not imaging at the same time. Nevertheless, it was promising that the camera detected bursts shortly after the APD. A repeat of the same experiment using the camera was performed to ensure it was a reliable measurement (Figure 6.16). The repeat also proved that single molecules were detected on the camera at 1000 frames per second.

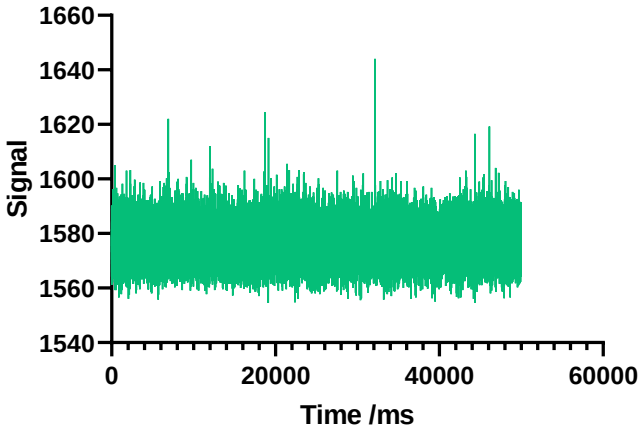

Figure 6.16. A repeat of a 1000 frames per second. A dilute sample of ATTO 647N (10pM) detected at an exposure time of 1 ms (without the 50:50 beam splitter in place) with an sCMOS Camera (Hamamatsu Flash 4.0)**.**

Here, we demonstrated that single bursts could be detected with an sCMOS camera at single-molecule concentration and the low exposure time (1 ms) required for single-molecule FRET experiments.

6.3.5 Using a TEM Grid as a multiple pinhole array

Having demonstrated that the camera could detect single bursts at single-molecule concentration and low exposure times (1 ms), the next step was to simultaneously image single molecules in multiple confocal volumes.

Previously, this was conducted in Chapter 5 using the digital micromirror device (DMD) on the Cairnfocal. In this experiment the TEM grid supplied by Agar Scientific had approximately 850 round holes with a 35 μm diameter and a bar width, which separates the pinholes, of 40 μm. The TEM grid would use the same method by demagnifying the structure of the pinhole array onto the sample and further collecting the emission from the sample through the same pinhole array. This static pinhole method would be simpler than the Cairnfocal digital micromirror device and this optical system contains fewer optical components and is light-tight. Unlike the DMD approach, however, in which the pattern of the mirrors could be changed to facilitate larger pinholes, the round holes in the TEM grid are fixed. Therefore, if the pinhole needed to be bigger or smaller, a new grid with different sized holes would have to replace the current one. Figure 6.17 shows the new microscope setup without the avalanche photodiode and a green laser (520 nm) to illuminate the sample. A change of laser was needed to excite the ATTO 550 dye attached to the dsDNA. We also went a step further than Chapter 5 by adding in an image splitter. The image splitter was required to split the FRET emission of the ATTO 647N dye from the emission of the ATTO 550 dye.

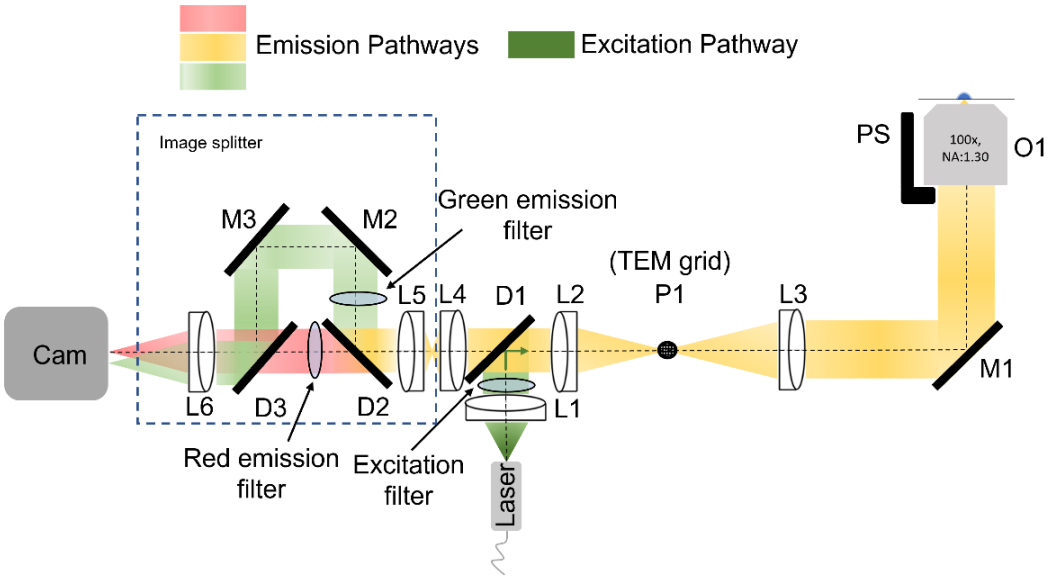

Figure 6.17. The schematic of the multi-confocal setup with the multiple pinholes (P1 - TEM grid) and the image splitter before the camera. The focal lengths of the lenses: L1- collimator, L2- 45 mm, L3- 150 mm, L4- 75 mm, L5 & L6 – inside image splitter. PS - piezo stage, M1, M2, M3 – mirrors, O1 – objective lens, D1 – dichroic mirror.

In this setup, new filters were also needed to restrict the wavelength of the laser. Emission filters for the green fluorescence emission were also used. All the filters used in this setup are characterised in Figure 6.18. By using an image splitter, the green emission arm and the red emission arm follow different optical paths to reach the detector. Here, the green emission is reflected by two additional mirrors before reaching the detector compared with the red emission path. Since the mirrors only reflect this emission independent of its wavelength, we would not expect to observe any losses resulting from these additional mirrors. This is critical as any loss in one of the emission arms would not be corrected for in the analysis of the FRET efficiencies. This can be compared to the absorption and emission spectrum of the dyes used shown in Figure 6.19. The optical components in each emission path are important as any losses would be taken into account when determining the FRET efficiency.

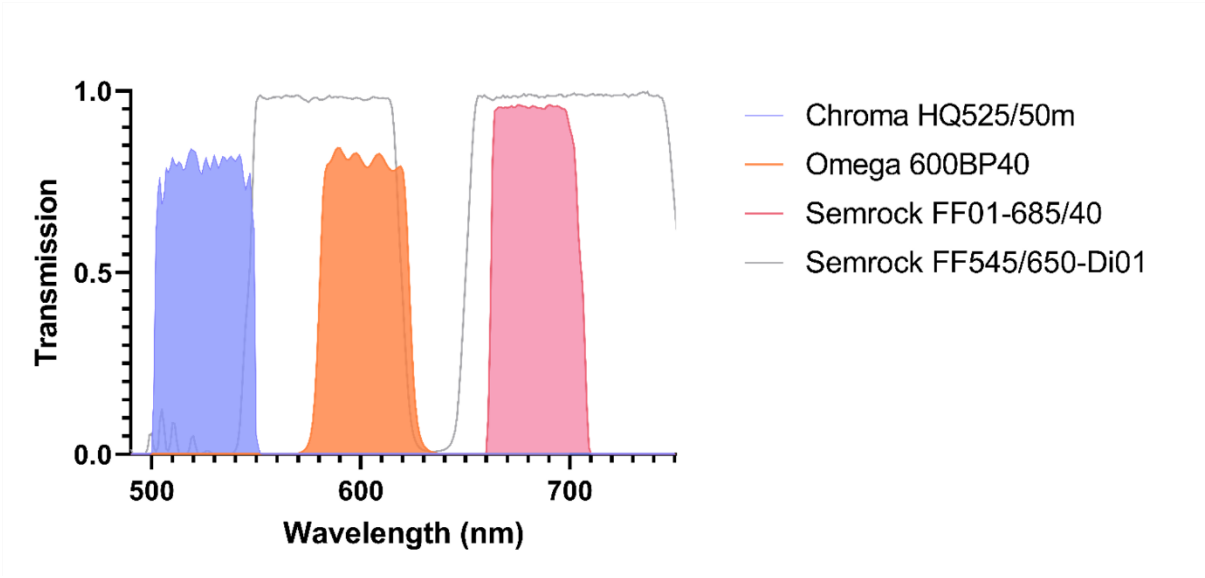

Figure 6.18. Filters in the single-molecule microscope. Excitation filter – Chroma HQ525/50m, green emission filter – Omega 600BP40, red emission filter – Semrock FF01-685/40, dichroic mirror (D1) – Semrock FF545/650. Values from FPBase.

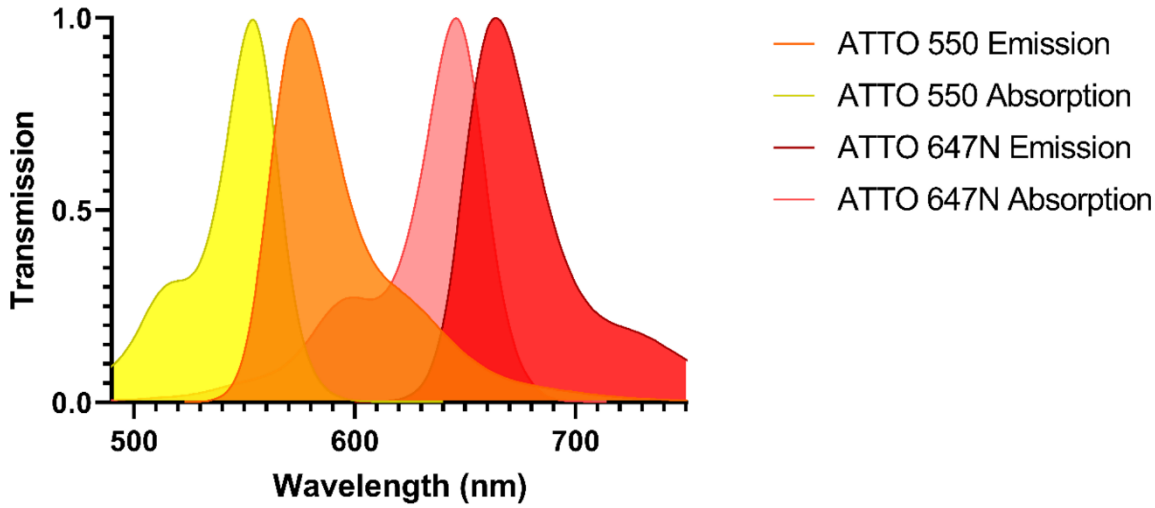

Figure 6.19. The absorption and emission spectrum of the dyes ATTO 550 and ATTO 647N. Values from FPBase.

6.3.6 Characterizing the TEM Grid

To investigate whether the TEM grid could be used as multiple pinholes for single-molecule imaging, a full characterization of the grid was performed.

Here, the TEM grid was installed in the microscope at the focal length of the tube lens. A sample of dsDNA (500 pM) labelled with both ATTO 550 and ATTO 647N in a solution of imaging buffer was placed on the microscope. Since only a green laser (520 nm) initially illuminated the sample, only the ATTO 550 fluorescent emission was observed. Fluorescence emission was observed through the pinholes and more importantly, not between the pinholes. To check that this originated from the sample, a buffer solution was placed on the sample stage. In this experiment no signal was recorded through the pinholes. The surface of the coverslip was also found as the z-position where single-molecules were brightest and static, shown in Figure 6.20. This was important as we could the determine if we were imaging in the sample (above the coverslip) or at the surface of the coverslip. Since we could determine the surface of the sample, in the next experiments, we imaged above the coverslip in the solution.

A) B)

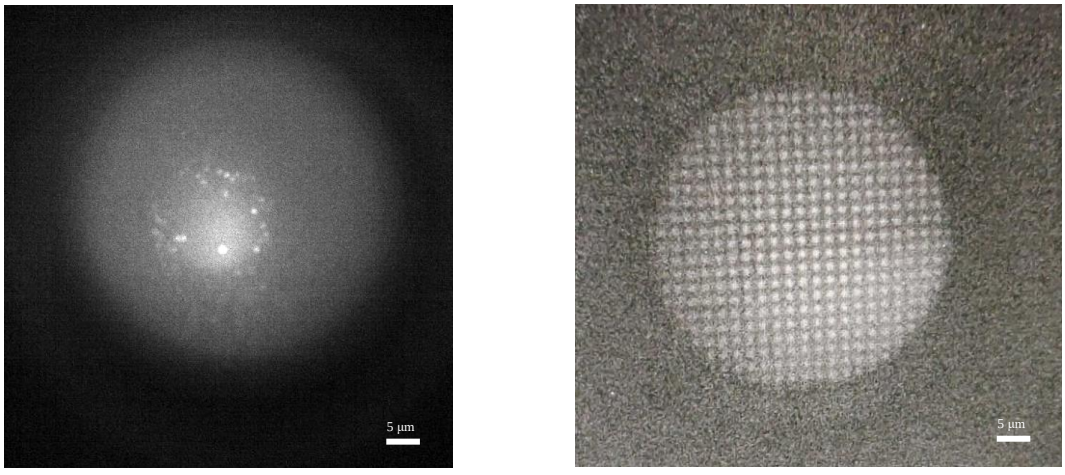

Figure 6.20. A) The surface of the coverslip showing static bright molecules B) The surface of the coverslip observed with the TEM grid placed at the focal length of the tube lens.

To determine if the array of pinholes was increasing the SNR, a sample of 0.1 μm TetraSpeck Microspheres (ThermoFisher) was placed on the microscope. Time traces of a spot on the camera with and without the TEM grid were recorded at an exposure time of 10 ms and shown in Figure 6.21.

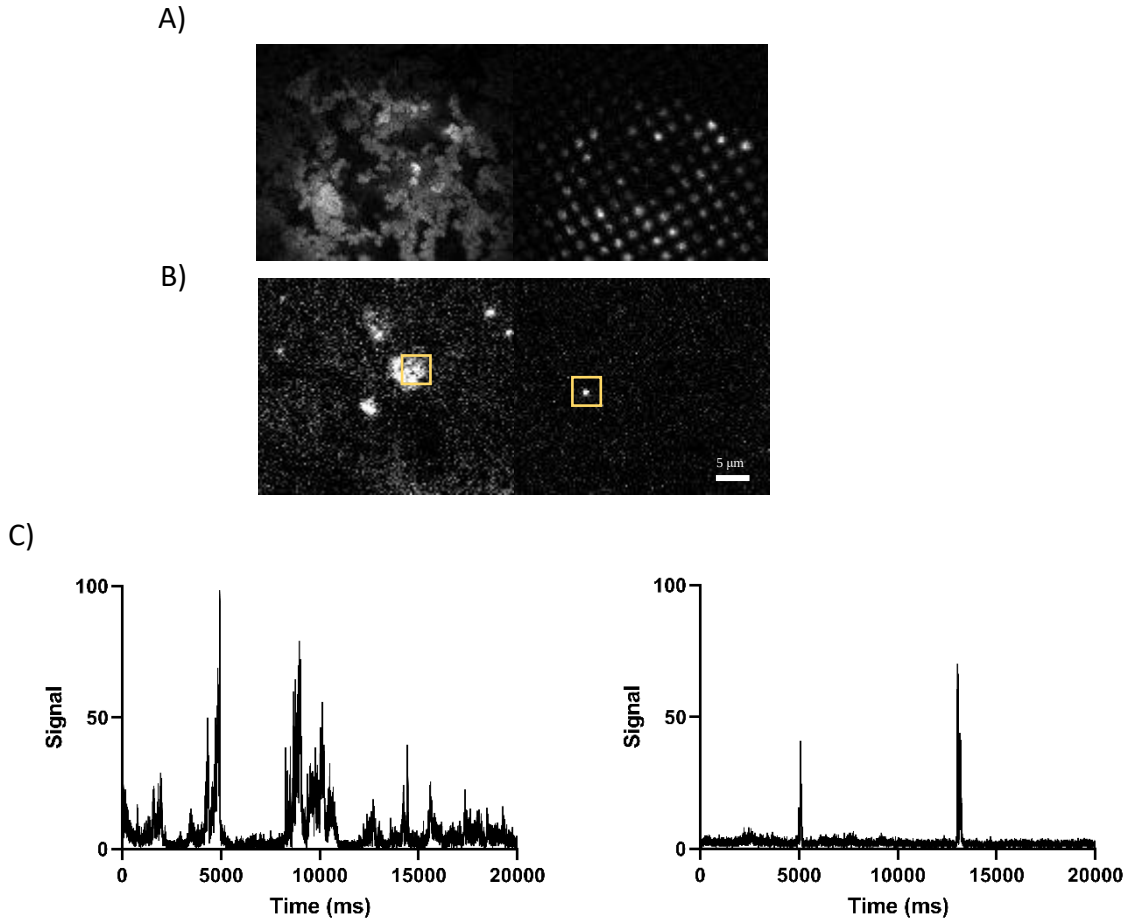

Figure 6.21. Time traces of a sample of 0.1 μm TetraSpeck Microspheres (ThermoFisher) recorded with the Hamamatsu Flash 4.0 at an exposure time of 10 ms A) Max z-stack images of fluorescent beads without the TEM grid (left) with the TEM grid (right) B) An image at a peak signal at 5000 ms into the image without the TEM grid (left) and with the TEM grid (right) C) Time traces of an average of 5 x 5 pixels shown in the yellow boxes without the TEM grid (left) and with the TEM grid (right).

The signal and background without the TEM grid in comparison with the TEM grid was greater, as expected. The TEM grid also eliminates the out of focus single-molecules, reducing the number of bursts, but improving the quality of the burst. The SNR increased 1.34x with the

TEM grid due to a lower standard deviation of the background. The background for these calculations were taken on both images where emission was not present.

Since we found we could use these TEM grids to improve single-molecule imaging, the next step was to use the image splitter in the emission path to split the fluorescence emission from ATTO 550 and ATTO 647N. Fluorescence emission in the green channel would be observed on one half of the camera and the red emission would be observed on the other half of the camera. The same three duplex DNA standards, labelled with ATTO 550 23bp, 15bp and 11bp away from the acceptor dye ATTO 647N, as in Chapter 2 were used. These were prepared with observation buffer (20 mM $MgCl_2$, 5 mM NaCl, 5 mM Tris, pH 7.5). Since these dyes were in proximity (1-10 nm), we anticipated some red emission would occur upon green excitation, due to FRET.

Since the TEM grid is in both the illumination pathway and the emission path, the pattern of the grid could be observed in both coloured emission channels. The first experiment tested whether the multiple pinhole configuration generated by the TEM grid could be observed in the green channel. The results shown in Figure 6.22 show fluorescent emission could be seen in the green channel with and without the grid. The exposure time of the camera was reduced to 1 ms to check whether a low FRET dsDNA sample (10pM) could be observed. In this channel single-molecule bursts were observed at the low exposure time of 1 ms.

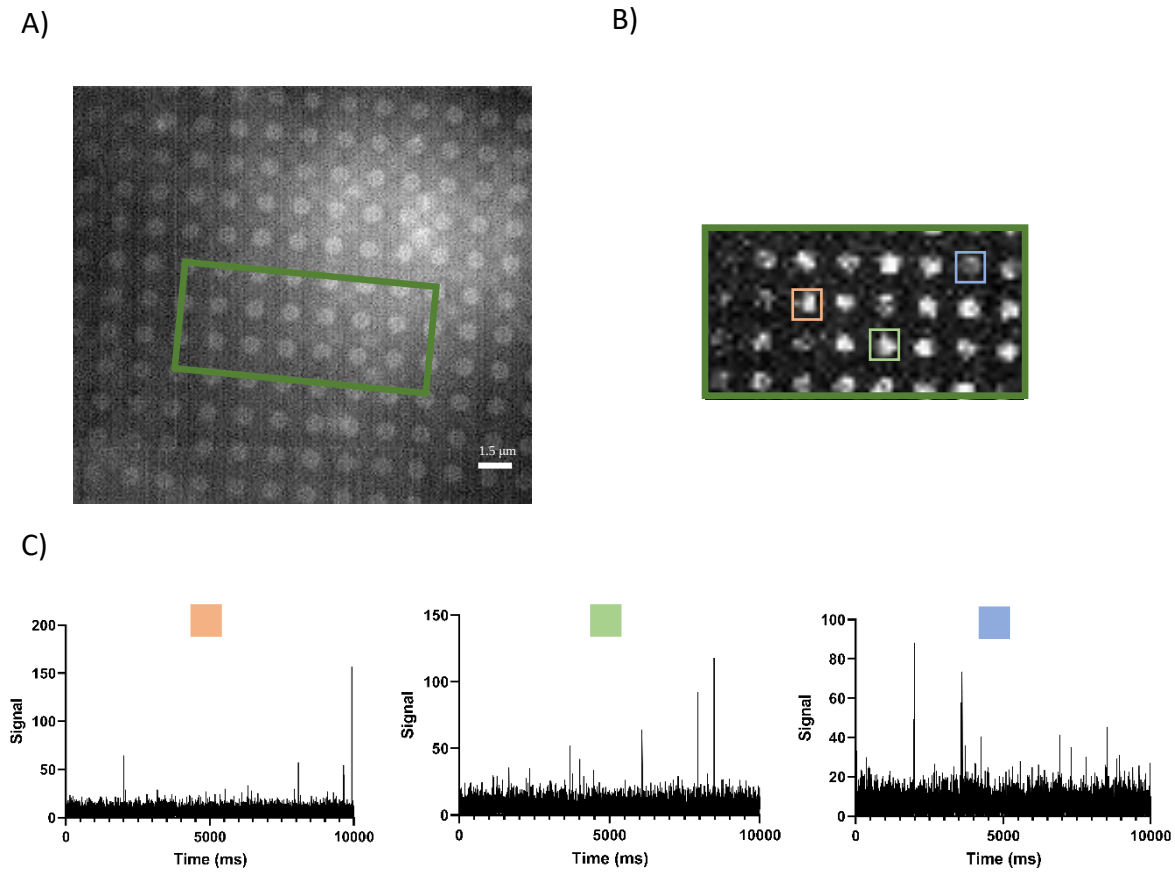

Figure 6.22. A) An image of the mask (TEM Grid) in the green channel of the camera B) A max z-stack of the acquisition of a low FRET dsDNA sample (10 pM) taken with the Hamamatsu Flash 4.0 and the TEM grid in place at an exposure time of 1ms C) Three time traces of the corresponding colour coded boxes (3 x 3 pixels average) at a camera exposure time of 1 ms.

The next experiment was designed to test if emission could be also observed in the red emission channel on the camera. A high FRET dsDNA sample with the dyes attached described above, was placed on the microscope. In this scenario, we hypothesised that the signal in the red channel would be associated with FRET. Figure 6.23 shows that we observed signals from these single-molecules in both the green and red channel without the TEM grid. However, when we changed the z-position of the objective, the single-molecules in the green channel were in focus and the single-molecules in the red channel were out of focus.

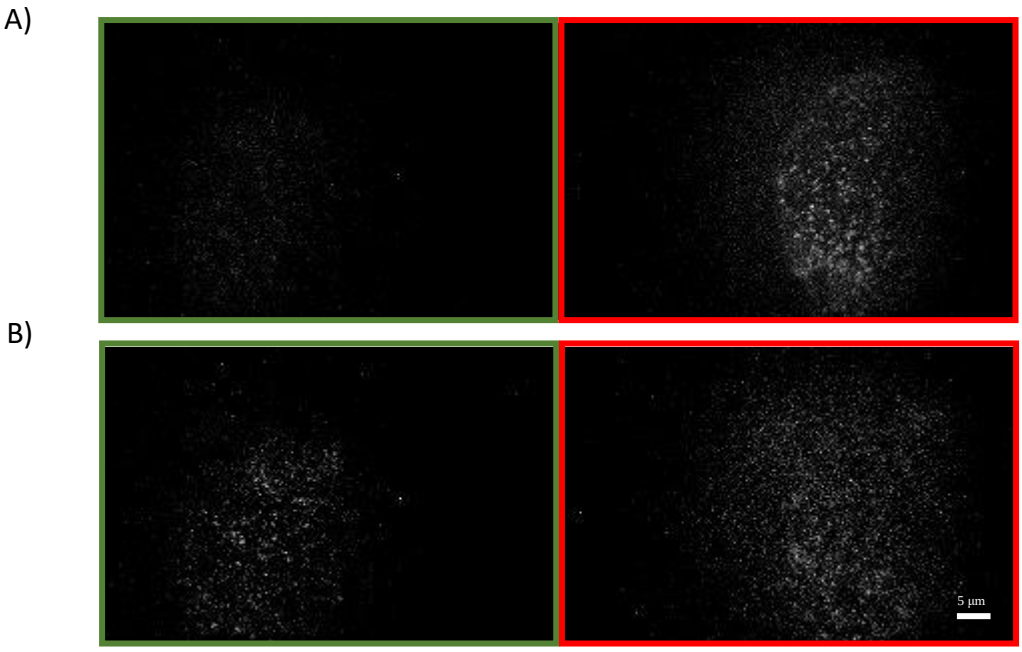

Figure 6.23. A maximum intensity projection (z-stack) of the fluorescent emission in the green (left) and red (right) emission channel at different stages of the acquisition. During the acquisition the axial position of the objective was increased to focus on the red emission and then the green emission. The fluorescence emission in the green channel is from the dye ATTO 550 and the fluorescence emission on the right from the ATTO 647N dye (FRET). A) the axial position of the objective focusing on the red emission at the start of the acquisition. B) the axial position of the objective focusing on the green emission at the end of the acquisition.

This observation revealed that the focal point of the image on the camera was different in the two channels. This was probably due to the absence of an additional lens in the red channel, given the additional distance the green emission light must travel to reach the camera. This additional lens, shown in Figure 6.24, would optimize the image splitter by correcting the z-focus in the red channel ensuring both channels would be in focus simultaneously.

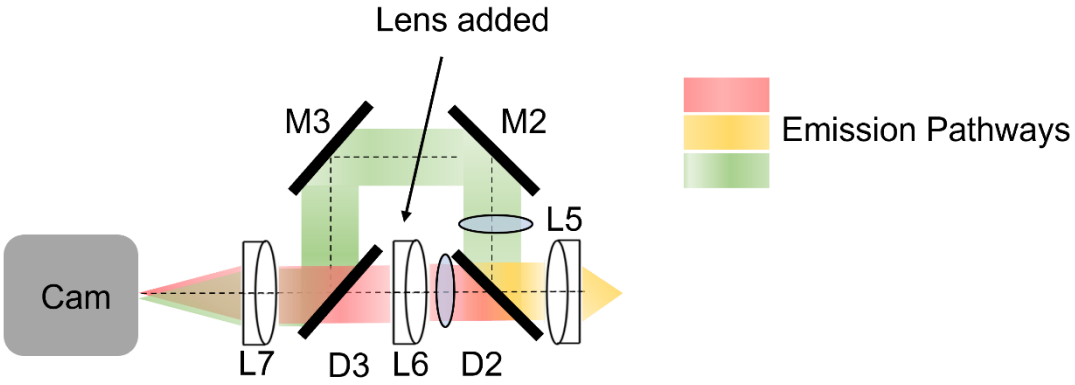

Figure 6.24. The optimized image splitter showing an additional achromatic lens (focal length 10,000 mm) added.

6.3.7 Z-drift Measurements

Due to issues with the z-focus, a full characterization of the z-focus of the microscope without the TEM grid was conducted. In this experiment single-molecules were placed on a sample stage. They were then focused with the objective lens and the camera recorded for 8 minutes. Here, the aim was to record the length of time it took for the single-molecules to become unfocused. We measured the maximum signal of every frame, assuming that when the maximum signal of the whole image was decreasing, the single-molecules were becoming out of focus. To determine whether this was due to the focus of the molecules and not from other external variables the sample was then refocused to see if the signal of the sample emission returned to its original signal at the start of the experiment. The results of this experiment are shown in Figure 6.25.

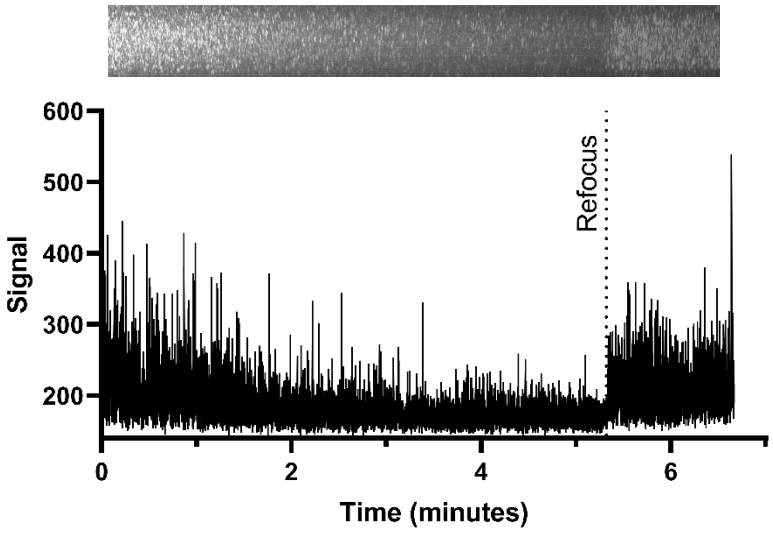

Figure 6.25. A graph representing the z-drift of the microscope in the green channel. The maximum signal of the whole image was recorded and left untouched. The dashed line shows the time at which the microscope was refocused. A z-stack image above the graph shows the molecules that were observed consistent with the time of the graph.

These results showed that the single-molecules drifted out of focus over a period of around 5 minutes. When the microscope was refocused the detected emission signal for the single-molecules returned close to the signal at the start of the experiment. This issue could have been due to the objective lens moving over time. Alternatively, this could have been the natural drift of the sample after it was pipetted onto the microscope. To ensure the former did not occur, the mirror (M1) before the objective lens, was secured with optical posts to prevent any movement of the objective lens. This did not stop the drift and so measured samples were also left to settle on the microscope for ~2 minutes before acquisitions were taken.

6.3.8 Concentration Measurements

To determine if single-molecules were imaged, an experiment was conducted to determine the effect of concentration of a fluorescently labelled dsDNA sample on the developed microscope signal response. Here, we expect to observe an inconsistent fluorescent emission at a high picomolar concentration resulting from multiple fluorophores. At a lower concentration, we

would expect a low background and distinguishable single-molecule bursts resulting from single fluorophores. To establish this, a dsDNA sample at a concentration of 5000 pM and then 50 pM was dispensed. The results in Figure 6.26 showed that single-molecule bursts were observed at 50 pM (blue) while no clear single-molecule bursts were observed at a higher concentration of 5000 pM (orange). This shows that single-molecules the fluorescence emission depended upon the concentration of the sample indicating that single-molecules were observed.

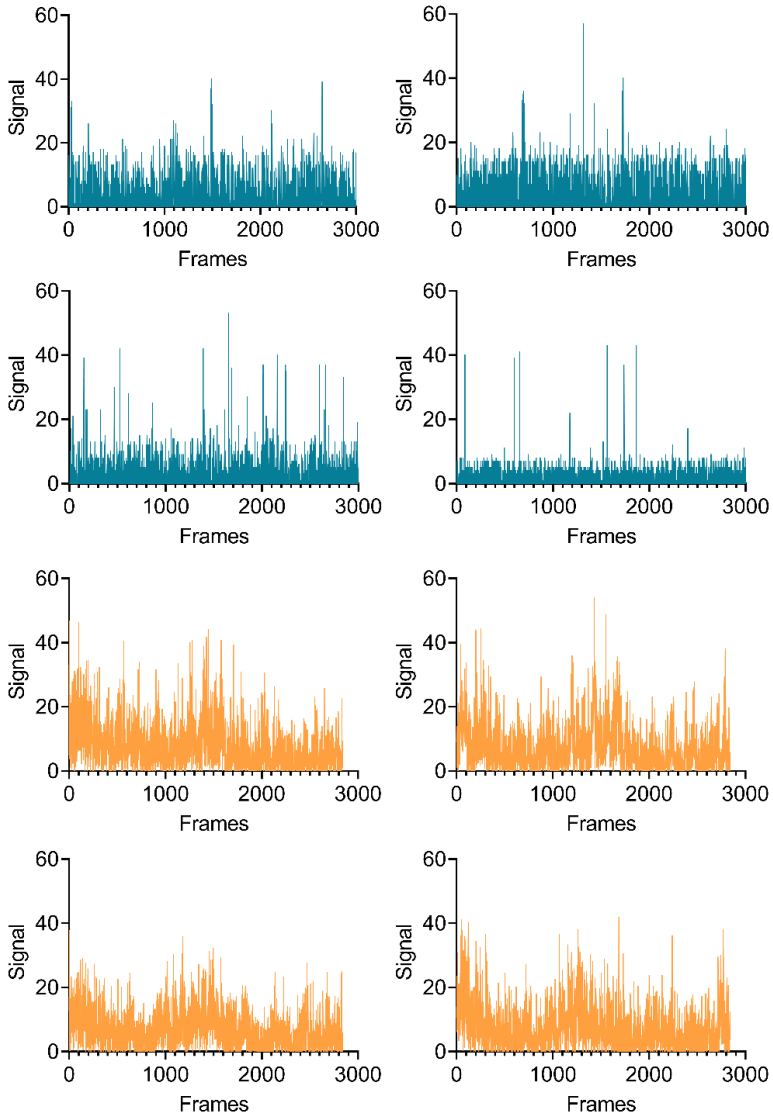

Figure 6.26. Multiple time traces of fluorescent emission in the green channel at 50pM (blue) and at 5000 pM (beige). A 3 x 3 pixel average was selected for single-molecules present in both acquisitions and conditions were the same except for the concentration.

6.3.9 Dual Colour Measurements

After implementing an additional lens in the red emission path, an experiment to determine whether single-molecules could be observed simultaneously with the image splitter in both the green and red channel, was conducted. For this experiment a high FRET dsDNA sample described above was placed on the microscope. Here, fluorescence emission could be detected in multiple spots in both the red and green emission channels shown in Figure 6.27.

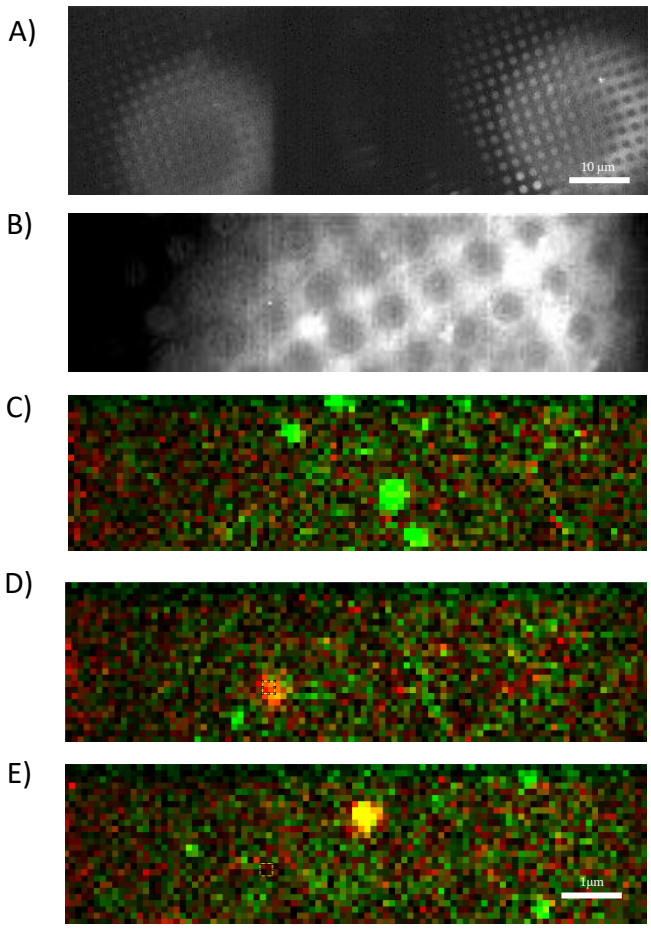

Figure 6.27. A) An average z-stack of the TEM grids in both the green emission channel (left) and red emission channel (right) used to subtract as the background. B) The area of the TEM grid imaged for the following acquisitions so that low exposure times could be taken. C-E) Acquisitions were taken at 30 ms with the Hamamatsu Flash 4.0 and a high FRET dsDNA sample concentration of 50 pM. The background of the TEM grid was subtracted so cannot be seen. C) Combined green and red emission channel showing green single-molecules observed. D) Combined green and red emission channel showing red (FRET) single-molecules observed. E) Combined green and red emission channel showing FRET signal (yellow) observed when there is an overlap of red and green emission.

While single-molecules could be observed in the same spots in both channels simultaneously, the camera speed of this acquisition was slow (exposure time of 30 ms). One spot of this acquisition is shown as a time trace in Figure 6.28.

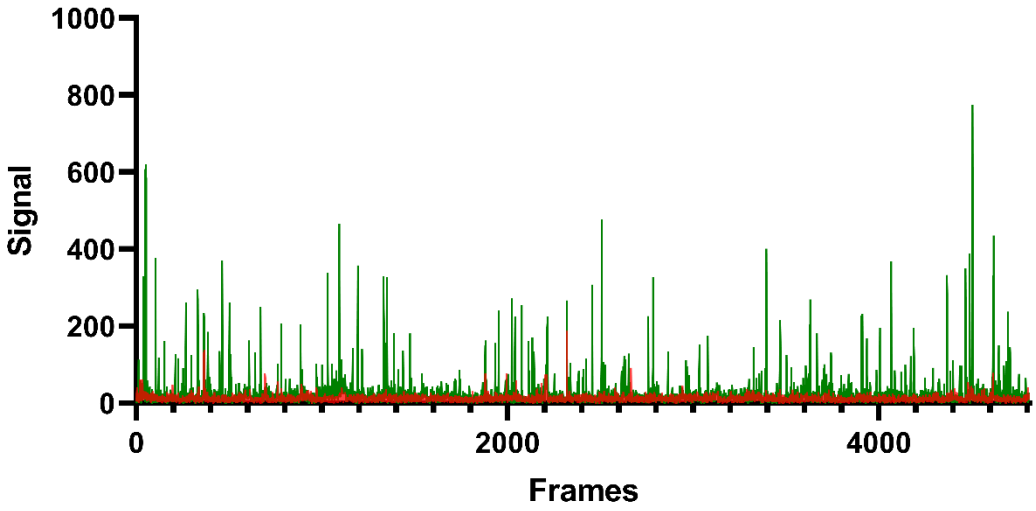

Figure 6.28. A time trace of both the green and red molecules in a single 'spot' at an exposure time of 30 ms.

In this time trace the frequency of the green emission was around one burst per second on average. This was expected and compared closely with a comparable concentration of this sample commonly taken on the smfBox. However, we expected the red (FRET) emission to be more frequent than was observed. In this case, we also expected to observe FRET signal at around one burst per second. Since the sample used here was the same sample used in Chapter 3, one possible reason for this was that the sample had degraded over time and may have less acceptor molecules attached to dsDNA or the sample buffer may be contaminated. Both cases would result in less FRET emission.

We could also rule out that this was the result of the green emission passing through the red emission filter. If this was the case, red emission would be detected as a proportion of the strength of the green emission. Here, we can see that when the green emission was strong, sometimes the resultant red emission was not observed. To obtain FRET efficiency histograms

single-molecules on both channels were aligned so that the TEM grid was matching in both colours and a FRET efficiency graph using the software iSMS was generated and discussed below.

6.3.10 Analysis of FRET Efficiencies using an image splitter

To achieve single-molecule FRET efficiency histograms, analysis of the multi-spot pattern in both colours was done in the iSMS software. [2] This software, commonly used for immobilized molecules in TIRF smFRET, allows the alignment of two images on a camera in two colours. Figure 6.29 shows the TEM grid spots that can be matched on both areas of the camera with a region of interest box. The resultant image, deliberately unmatched for demonstration, shows the red and green spots can be combined on a single image.

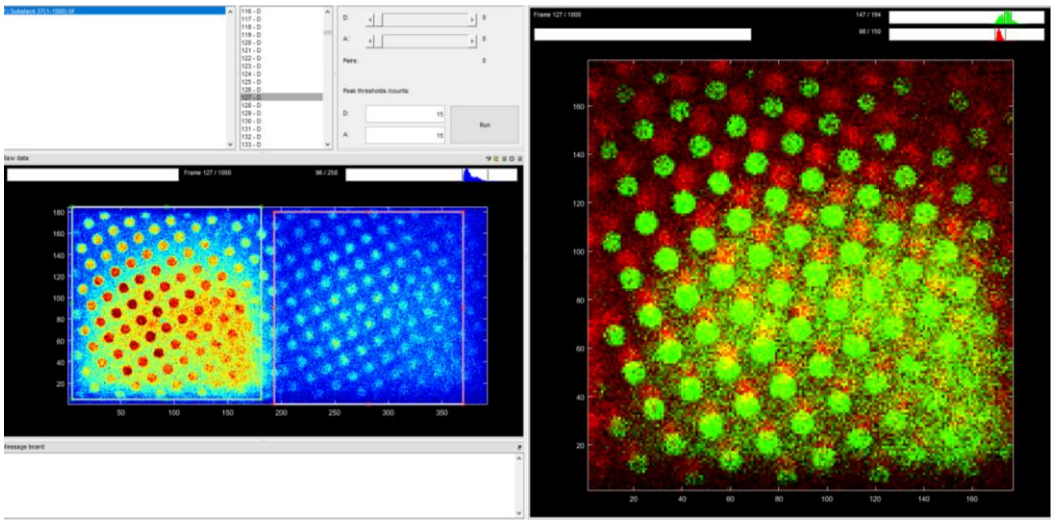

Figure 6.29. A picture of the multi-spot pattern out of alignment using the iSMS software. These spots were put into alignment by matching the two regions of interest (left). The combined fluorescent emission was combined, and the spots were matched (right). Here we show the spots unmatched for demonstration. [2]

These spots were then analysed, and single-molecule events in all the spots were manually selected such as the two single-molecule bursts highlighted in boxes shown in Figure 6.30. The software subtracts the background by using the local pixels around the molecule. A FRET

efficiency histogram was then created for this high FRET dsDNA sample and compared with the measurement of this sample on the smfBox (Figure 6.31).

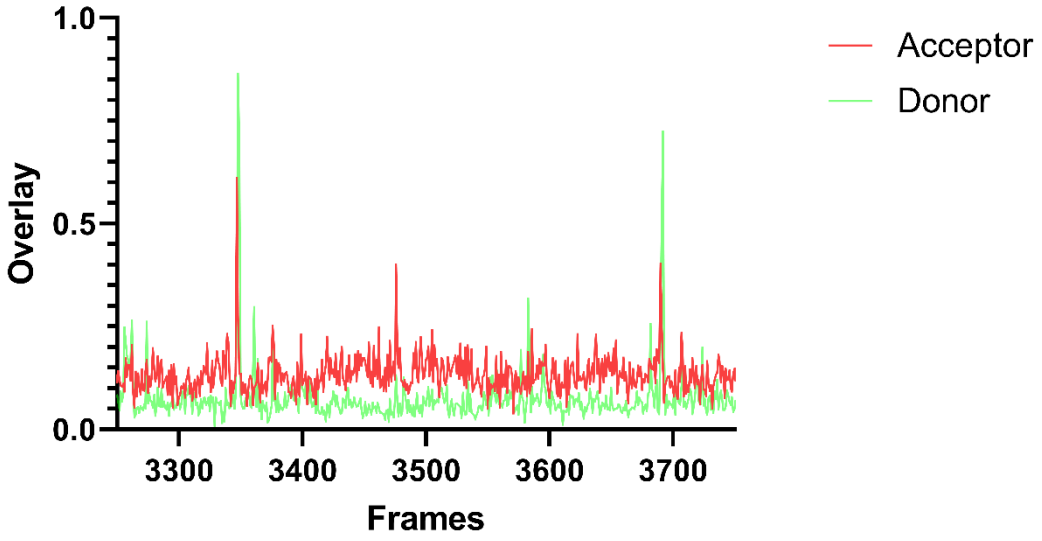

Figure 6.30. A time trace of one of the spots in the multi-spot pattern using the iSMS software at a camera exposure time of 30 ms [2]

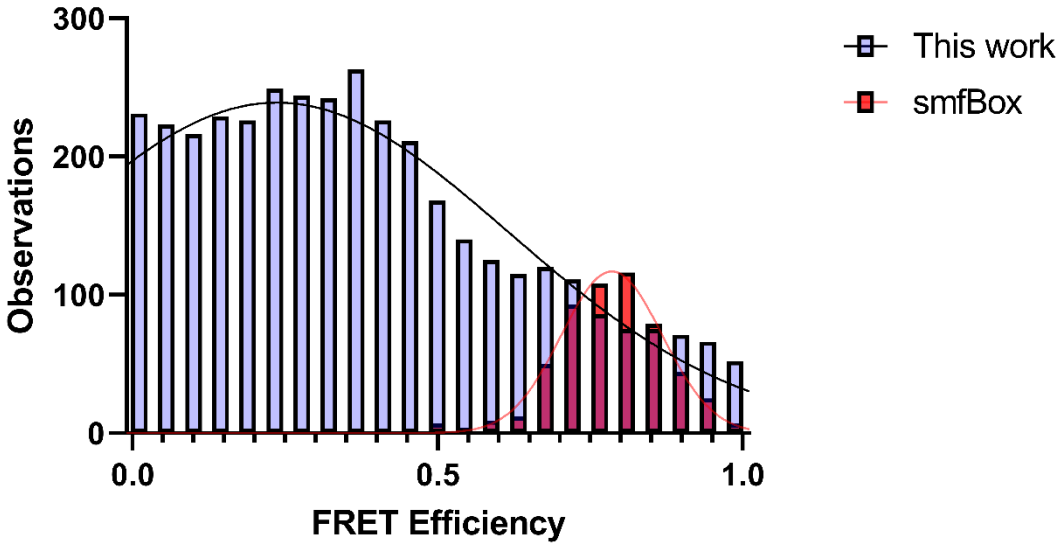

Figure 6.31. A FRET Histogram showing the FRET efficiency when a high FRET sample of ds DNA was placed on the microscope and analysed with iSMS. [2] This was recorded at an exposure time of 30 ms for a time of 2.5 minutes on 25 spots. In comparison to the excitation module on the smfBox with the same sample recording for 1 hour.

In these experiments we expected the FRET efficiency for this sample to peak at 0.79 as shown by the FRET efficiency histogram for this sample on the smfBox. The results show that this sample did not exhibit the high FRET efficiency by using this optical setup. A repeat experiment, shown in Figure 6.32, on both the low FRET and the high FRET samples at an exposure time of 1 ms was completed to investigate whether a different FRET efficiency value was observed and if FRET could be observed at this high speed.

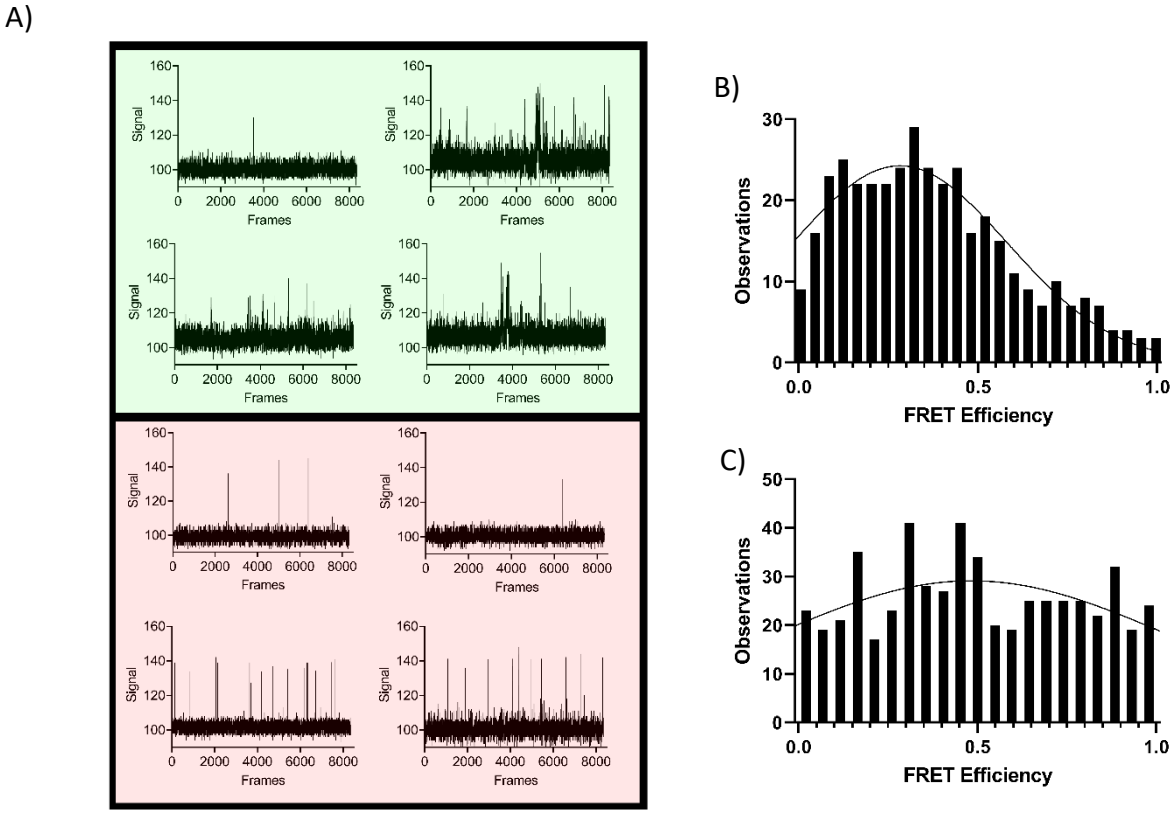

Figure 6.32. Time traces for the low FRET sample inside four spots at an exposure time of 1 ms in the green emission channel (green, top) and the red emission channel (red, bottom). B) A FRET Efficiency histogram of the low FRET sample recorded at an exposure time of 1 ms and measured for 10 seconds inside 25 spots C) A FRET Efficiency histogram of the high FRET sample recorded at an exposure time of 1 ms and measured for 20 seconds inside 25 spots.

In these repeat experiments single-molecule bursts of green emission and FRET emission could be observed at a low exposure time of 1 ms. However, the low FRET sample showed a broad

peak higher than the expected value (0.17) and the high FRET sample also did not show the expected result (0.79).

To ensure the filters did not cause problems in the emission paths, we tested both the red and green emission channels separately with TetraSpeck™ Microspheres (0.1 µm) and high red emission and green emission was observed (Figure 6.33) when illumined with red and green lasers, respectively. Therefore, the filters or the microscope optical setup were not the origin of the problem.

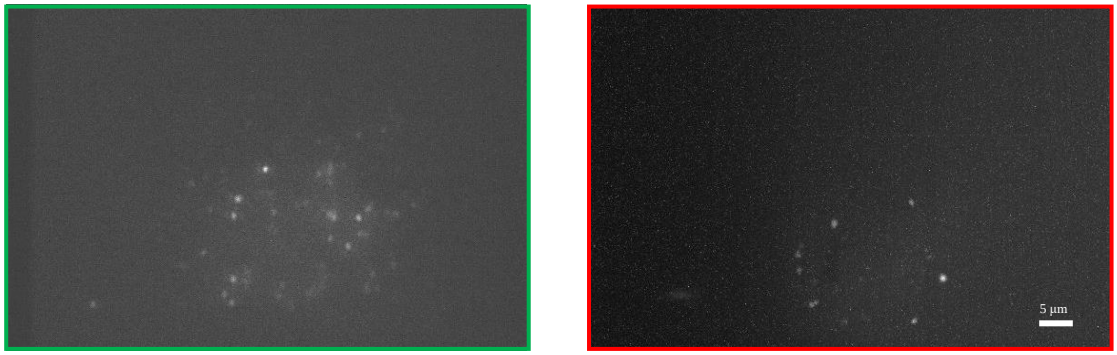

Figure 6.33. Images of TetraSpeck™ Microspheres (0.1 µm) taken separately without the TEM grid in place. In the green box, an image of this sample in the green emission channel with green laser illumination. In the red box an image of this sample in the red emission channel with red laser illumination.

We believe these the reason for these incorrect FRET efficiencies was due to the mismatch in the background intensity for both red and green emission when using the iSMS software. This is shown clearly in Figure 6.30, where the background of the green emission channel is lower than the background of the red emission channel. This can be explained by the method that the iSMS software calculated the background intensity. Here, the background intensity of both emission channels was calculated locally, around the molecule. However, the background pixels chosen for the software were selected on the TEM grid bar instead of inside the spot. The background between the spots on the TEM grid was different in both emission channels

shown in Figure 6.29. Since the TEM grid bar generated a different background in each emission channel compared to the background intensity inside the spot, this would provide an inaccurate ratio of the intensity values between red and green emission. Furthermore, when single-molecule events were manually selected using the software, it was difficult to select single-molecule bursts without the inclusion of the background around the peak, further contributing to the problem.

One contributing factor could be sample degradation and contamination. To test this, the same low FRET, medium FRET, and high FRET sample was placed on the smfBox. After a 1 hour acquisition each, the results show (Figure 6.34) that the smfBox was able to detect a change in FRET efficiencies, however, the number of observations of FRET was too low to determine accurate FRET efficiency values. This could have been due to a lack of acceptor dye molecules in the sample or contamination of the buffer. However, since smfBox detected a change in FRET efficiency for these samples, we believe that this microscope should have been capable of measuring this sample.

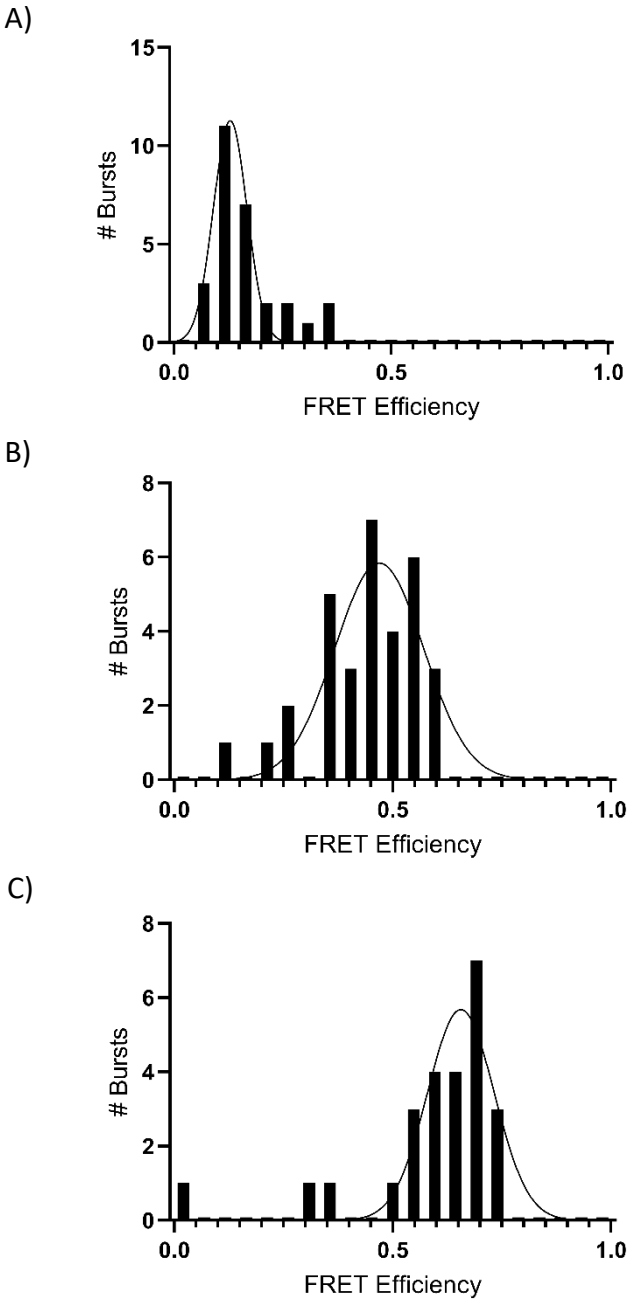

Figure 6.34. The FRET efficiency histograms of dsDNA samples used in this chapter recorded on the smfBox. A) Low FRET dsDNA sample B) Medium FRET dsDNA sample C) High FRET dsDNA sample.

In this section we have shown that this high-throughput single-molecule microscope can detect FRET emission at 1000 frames per second in multiple spots (25) with the TEM grid. In this work the smFRET experiments were not performed at the magic angle. However, the excitation and emission arms are designed in such a way that polarizers can be inserted if required for

downstream experiments. The only limiting factor for expanding the number of spots used was the field of view of the camera at an exposure time of 1 ms. However, we have not yet demonstrated that this microscope can accurately determine FRET efficiency values.

6.4 Future work analysing single-molecule bursts

6.4.1 Identifying single-molecule bursts

Since the iSMS software was difficult to apply to multi-spot smFRET analysis and indeed may have been the source of error in measuring FRET efficiencies, different analysis methods were explored to accurately select FRET bursts automatically.

The first analysis method we investigated was the use of "Change Point Analysis". This approach has been used in a wide number of sectors such as the financial markets. [3]–[6] The approach determines the number of changes in the dataset and provides a time and a confidence interval for an estimated change point. Here, we aim to identify single-molecule events based on the method described in the article from Truong et al. [7] Using a binary segmentation search method, a single change point method is applied to the data to see if a split exists. If a split is detected, the sequence is divided into two and both sections are further investigated. A penalty or computational cost of O (n log n) where n is the number of data points is also used. Change Point Analysis (GitHub: Change-Point-Analysis-Single-Molecules) was performed on a low FRET dsDNA sample time series obtained from this instrument at a single-molecule concentration of 10 pM and at an exposure time of 1 ms shown in Figure 6.35. [7]

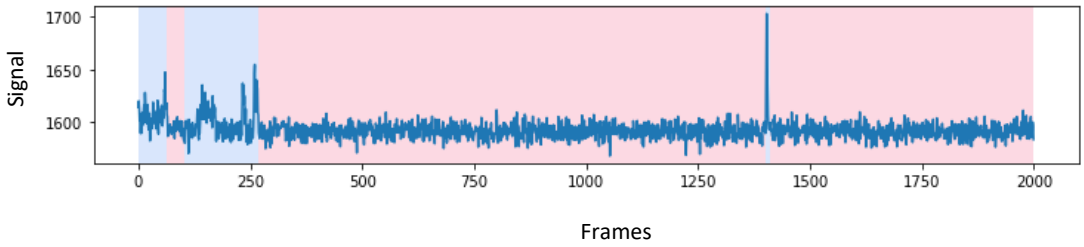

Figure 6.35. Initial change point analysis performed on a single-molecule dataset. The blue areas show detected events, and the red area shows areas where the analysis revealed no significant changes. This time trace was recorded with the Hamamtsu Flash 4.0 at an exposure time of 1 ms with a 100 μm pinhole in place.

As shown in Figure 6.35, the initial analysis using the default penalty suggested in the literature, identified all the events in the dataset. However, in the first 260 frames the blue areas covered a wide range of the dataset which included data that does not show single-molecule events. Since we are only interested in the peaks of the data, as the FRET efficiency can be calculated from this, the conditions of the algorithm were changed. By increasing the penalty of the algorithm to detect events with progressively higher confidence levels, we eventually managed to generate a more rigorous analysis that only identified the peaks associated with single-molecule events in the dataset (Figure 6.36).

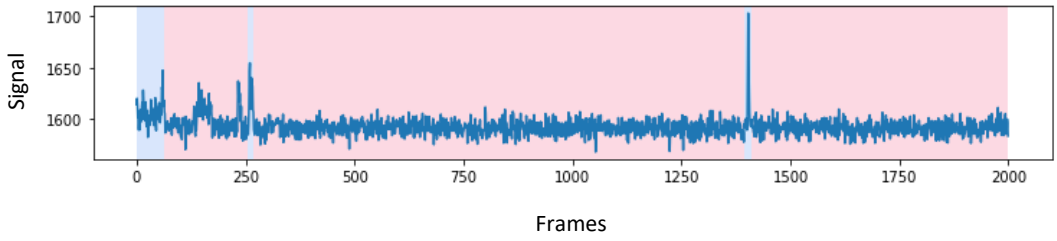

Figure 6.36. The change point analysis performed after increasing the penalty on a single-molecule dataset. The blue area shows detected events, and the red area shows areas where the analysis revealed no significant changes. This time trace was recorded with the Hamamatsu Flash 4.0 at an exposure time of 1 ms with a 100 μm pinhole in place.

This analysis method could be used in conjunction with the high FRET data shown earlier, to automatically identify all the peaks in the FRET emission time traces.

6.4.2 Location of single-molecule bursts

The second data analysis method used was Principal Component Analysis (PCA). This statistical data analysis method can also be used to identify clusters within datasets with common features and has been shown to identify outliers in sample detection in RNA-Seq data. [8] PCA could be valuable for finding clusters of interest in our acquisitions that we should investigate further, for example FRET emission peaks within spots.

To apply this analysis, first a time trace of a fluorescent molecule was required. Initially, we simulated a time trace of multiple molecules diffusing by Brownian motion. These molecules were assigned physical properties such as the diffusion coefficient and brightness and allowed to diffuse within a constrained volume (a 3D array). A 3D detectable area was defined within this array and if molecules diffused inside this array, a time trace was recorded. Initially, these molecules were made to start at a random location in the 3D array and exhibit a point spread function (PSF), which required the wavelength of the fluorescent emission and the numerical aperture of the objective lens. In addition, these molecules were given an arbitrary brightness of 1 and the detection region considered the offset of the Hamamatsu Flash 4.0 camera (100 grey values).

The simulation in Figure 6.37, shows the tracking of these molecules and the detectable array at the centre. It also shows the resultant time trace when molecules entered the array. As shown, some of the simulations contained molecules that did not enter the array, and so to counter this more molecules were added.

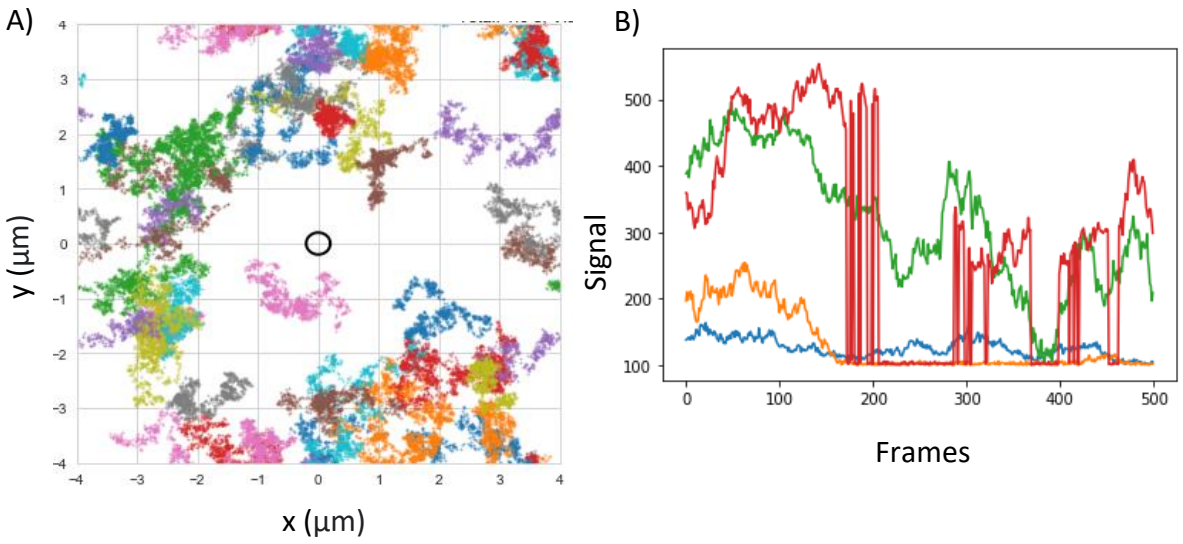

Figure 6.37. A) A simulation of single-molecule trajectories. Each track represents the location of the molecule in time from a starting point at the centre. The circle represents the detection volume, showing that in this acquisition no molecules entered. B) Simulation of time traces of four single-molecules that entered the 3D array in the central circle of the 3D array.

Here, we tested four different single-molecule event time traces against background measurements to test whether PCA could identify single-molecule events. To analyse these time traces, PCA.fit() was called from scikitlearn.decomposition. [9] This enables PCA in Python and computes vectors, reducing the dimensions of our data. Time traces that contained intensity values for these four molecules, and four additional datasets where only the background was observed (the offset of the camera), were used. Since each row in these datasets is two dimensional, each of the vectors will be two dimensional. We then call PCA.transform() to project each row of our data into the vector space that was learnt when PCA.fit() was called. The result reduces the number of columns of our data, while preserving as much information as possible. Figure 6.38 shows PCA of these 8 datasets, four datasets representing the diffusion of four molecules (blue), and four data sets containing only background (red).

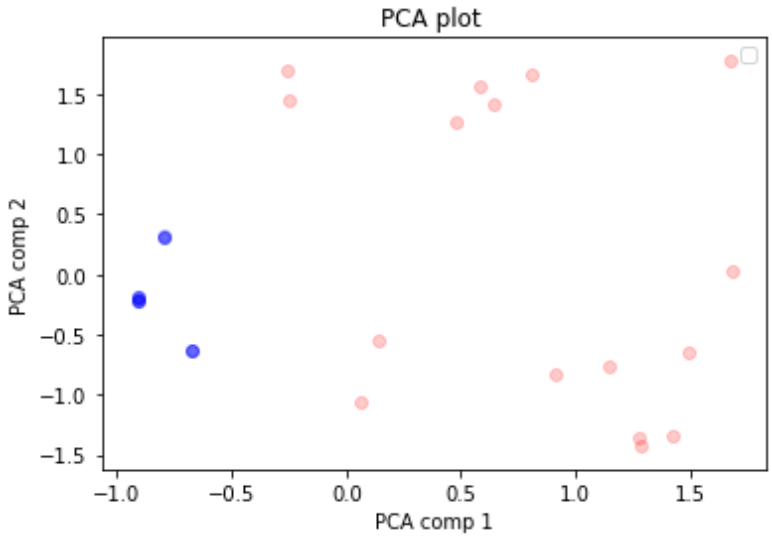

Figure 6.38. Principal Component Analysis of a simulation of four molecules diffusing in a 3D array (blue) compared to four background only datasets (red).

This PCA showed that these molecules could be identified in clusters away from the background. However, these were not representative of fast diffusing single-molecules we have observed with the optical imaging system in this chapter. To replicate this, we simulated fluorescence emission (https://github.com/DylanRhysGeorge12/simulate-single-molecules-on-a-camera.git) based on the microscope used in this chapter. The resultant time trace of a single pixel on the camera is shown in Figure 6.39. This simulation involved building a 2D array of data involving random 3D diffusion described above. A Ground Truth array, using the fluorescence emission from ATTO 647N (photons per second), was generated. We then convolved both the PSF and the Ground Truth arrays. A camera array was created, by using the properties of the optical system. With a 60x objective lens and a 6.5 μm pixel size (Hamamatsu Flash 4.0), we expected each pixel to observe 108 nm in the sample. We then combined these two arrays and added read noise, photon shot noise and fixed pattern noise to the image, based on the information gathered in Chapter 4. We then decreased the area of detection so that single bursts were observed. PCA was used on the resulting simulation to assess which time traces contained single bursts (Figure 6.39 and Figure 6.40).

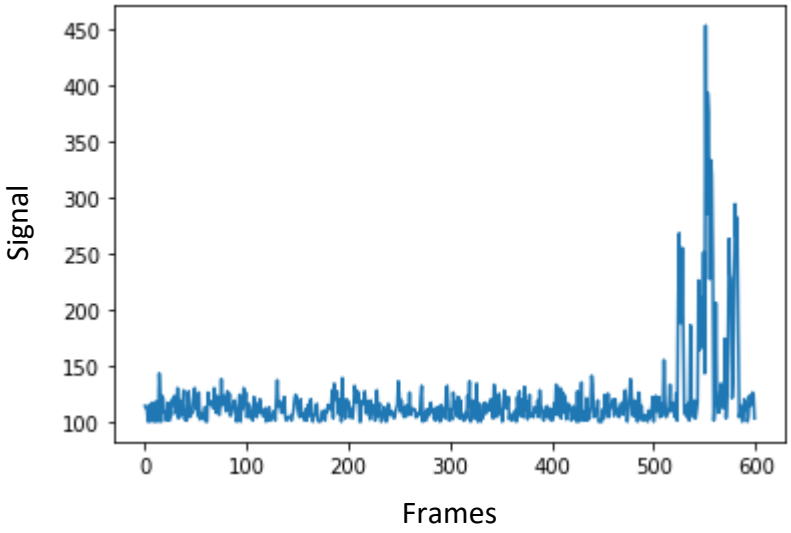

Figure 6.39. Simulation of time traces of single-molecules with a decreased detection area and a read noise and photon shot noise based on an sCMOS camera (Hamamatsu Flash 4.0).

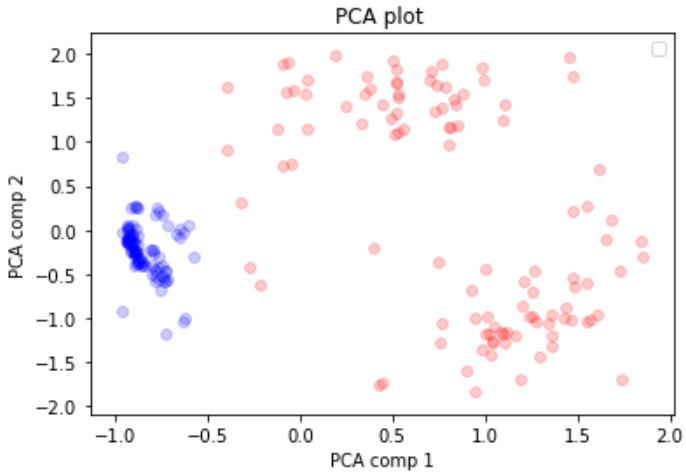

Figure 6.40. A PCA plot on multiple images of simulated single-molecule data based off the optical system in this chapter. Time traces containing single-molecule events (blue) and time traces containing only background (red) are shown.

Here we showed, that PCA could identify simulated time traces containing single bursts compared to background datasets. The next step was to explore whether PCA could identify time traces containing single bursts on the data collected in this project.

To test this, we analysed a raw data containing background noise against a dataset which contained events. A time series from a low FRET dsDNA sample obtained from this instrument

at a single-molecule concentration of 10 pM and recorded at an exposure time of 1 ms, was used. Figure 6.41 shows the time traces of and PCA plots for both measurements. In the datasets containing both background measurements no clear cluster was found. However, in the dataset containing one event measurement and one background measurement, two separate clusters were clearly differentiated by the PCA plot.

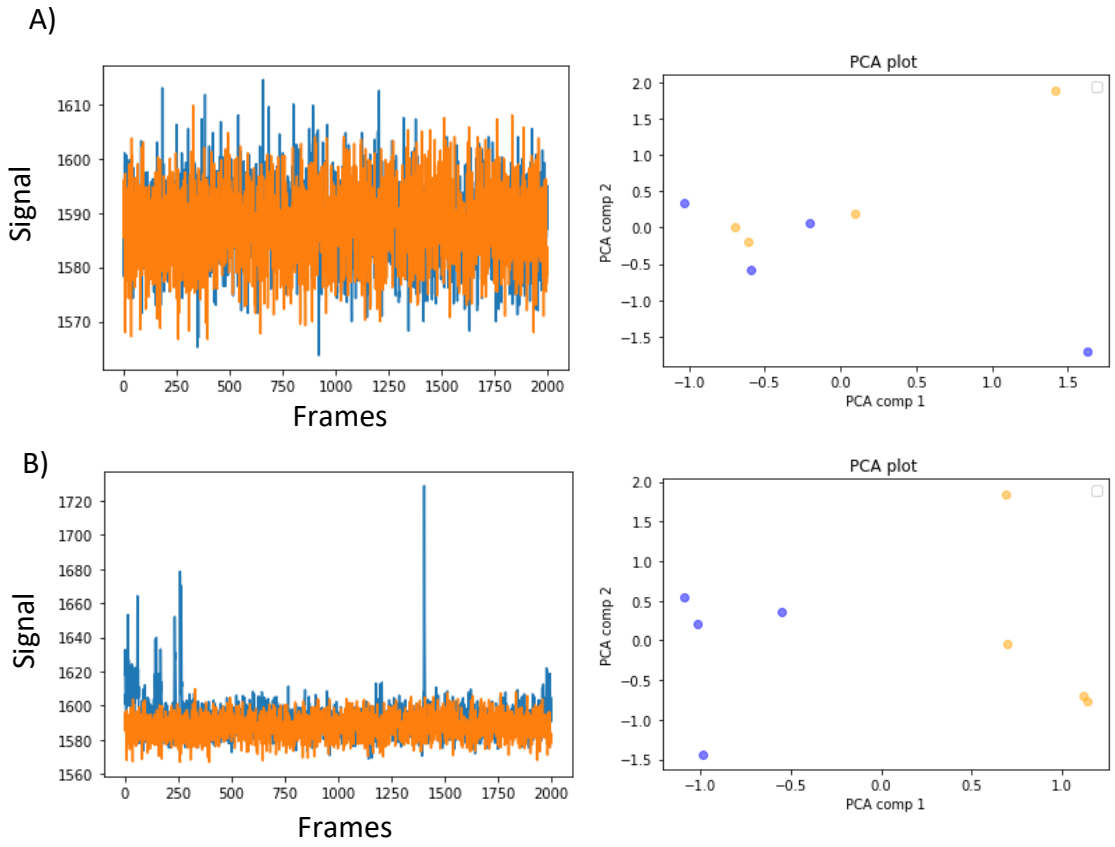

Figure 6.41. Experimental time traces of single-molecule data and principal component analysis plots A) time traces of two background measurements B) Time traces of one background measurement and one measurement containing single-molecule events. The sample was a low FRET dsDNA sample (10 pM) recorded at an exposure time of 1 ms with the Hamamatsu Flash 4.0.

Here, we found both PCA and change point analysis can be used to identify time traces where single bursts are observed. Both these methods can be used with the single-molecule microscope in this chapter to identify FRET bursts. Change point analysis would be more useful for measuring FRET efficiency values as it can determine the start and end time of FRET

emission. This can prevent background values entering the analysis and altering FRET efficiency values.

6.5 Conclusion

Through sequential optimisation of the microscope, we were able to observe single-molecule FRET at 1000 frames per second at a low background. This shows that we can capture the fast dynamics of biological molecules. FRET emission can be observed within each of the multiple spots provided by the TEM grid opening-up simultaneous measurements and studies of molecular populations. This was achieved through systematic experimentation summarized in Figure 6.42.

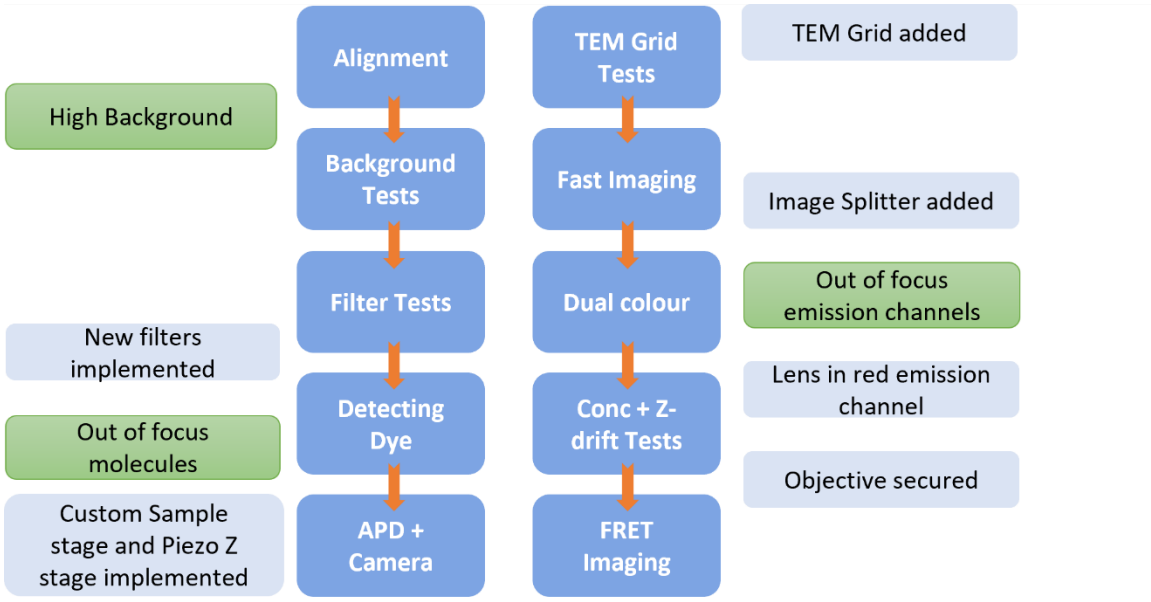

Figure 6.42. Timeline of the experiments (dark blue), problems (green) and components (light blue) added to the setup.

Precise determination of the FRET efficiency, however, remains an important goal. Whilst we struggled to align FRET efficiency to the expected values for dsDNA labelled molecules within the timeline of the project and availability of equipment, we believe that with improved analysis methods this is achievable. We explored methods for improving the collection and

analysis of data derived from these measurements with several approaches showing promise for this new way of collecting FRET data. We expect, with further testing on highly validated samples and improvements in data handling methods shown at the end of this chapter, this new method can be used for high-throughput single-molecule measurements in the future.

6.6 References

[1] B. Ambrose *et al.*, "The smfBox is an open-source platform for single-molecule FRET," *Nat. Commun.*, vol. 11, no. 1, p. 5641, 2020

[2] S. Preus, S. L. Noer, L. L. Hildebrandt, D. Gudnason, and V. Birkedal, "ISMS: Single-molecule FRET microscopy software," *Nature Methods*, vol. 12, no. 7. pp. 593–594, 2015

[3] S. N. A. M. Arif, M. F. M. Mohsin, A. A. Bakar, A. R. Hamdan, and S. M. S. Abdullah, "Change point analysis: A statistical approach to detect potential abrupt change," *J. Teknol.*, vol. 79, no. 5, pp. 147–159, 2017

[4] S. H. You *et al.*, "Change point analysis for detecting vaccine safety signals," *Vaccines*, vol. 9, no. 3, pp. 1–10, 2021

[5] C. Malesios, N. Jones, and A. Jones, "A change-point analysis of food price shocks," *Clim. Risk Manag.*, vol. 27, 2020

[6] D. Ballová, "Global and local trend analysis and change-point analysis of selected financial and market indices," *J. Autom. Mob. Robot. Intell. Syst.*, vol. 13, no. 3, pp. 56–63, 2019

[7] C. Truong, L. Oudre, and N. Vayatis, "Selective review of offline change point detection methods," *Signal Processing*, vol. 167. 2020

[8] X. Chen, B. Zhang, T. Wang, T. Wang, A. Bonni, and G. Zhao, "Robust principal component analysis for accurate outlier sample detection in RNA-Seq data," *BMC*

Bioinformatics, vol. 21, no. 1, 2020

[9] F. Pedregosa *et al.*, “Scikit-learn: Machine learning in Python,” *J. Mach. Learn. Res.*, vol. 12, pp. 2825–2830, 2011.

Chapter 7. Conclusion and Future Work

Contents

7.1 Summary and Future work 202

7.2 Impact of this work 205

7.3 References 206

7.1 Summary and Future work

In Chapter 2, we revealed an affordable single-molecule FRET commercial microscope, designed around the openFrame by Cairn Research. In this chapter, we iterated draft modules of an excitation, pinhole and emission module to identify the best instrumentation and hardware for single-molecule fluorescence applications at low-cost. Here, we constructed the final designs with Cairn Research and tested the instrument on a known high FRET sample to show the instrument could detect single-molecule events. At present the openFrame allows for a multitude of different techniques. In the future more experimental techniques may also be added such as continuously controlled spectral-resolution (CoCoS) microscopy. [1] This technique uses two amici prisms to split the fluorescence emission so that the camera can visualize all the colours at the same time. This increases the throughput and sensitivity of the collected emission. By utilizing coverslip TIRF or prism TIRF, a high signal to noise ratio of single-molecule could be detected in combination with a camera. The openFrame also has the potential to be applicable for super-resolution applications. In the long term, we expect researchers will adopt this microscope instead of using traditional inverted microscopes because of the customizability of the openFrame and its ease of use.

In the third chapter, an affordable excitation module for single-molecule microscopy was designed. This module has the potential to provide multiple colour laser beams for a multitude of super-resolution and single-molecule methods in academic and industrial research. In the short-term, researchers can improve the design by implementing a pinhole system after the collimator. This would create a Gaussian intensity laser beam that may improve the collimation efficiency. In doing so, more power hungry techniques such as STED microscopy may be feasible. In the long term, illumination in single-molecule methods could benefit from a compact single module combining multiple laser beams into a single fibre that can be

introduced by reducing the size of the optical components and machining custom parts instead of Thorlabs parts.

In Chapter 4, analysis of the performance of the latest sCMOS cameras was performed. Here we revealed the sCMOS camera with the best performance at low-light levels. In this chapter we also explored the parameters that we need to consider for single-molecule imaging. This entailed weighing up the quantum efficiency with the read noise of cameras. Also, whether the camera could image at fast speeds and if this decreased the field of view significantly. In the short term, this photon transfer method could be automated. Before using a camera, a simple plug-in module combined with a computer program to measure the noise profile of the camera could be implemented. This would inform the user of the best camera to use for their imaging applications, based on the cameras read noise, quantum yield, pixel size and the expected photon rate from the sample.

In Chapter 5, we demonstrated the use of a digital micromirror device for single-molecule imaging. This instrument could approximate diffusion coefficients inside multiple spots and had the flexibility of changing the size of the spot. While this method was not able to image single-molecules at a low exposure rate, due to high backgrounds in the optical system, in the future there are a few things that could be implemented to improve the system. Since we only required the micromirrors in the ‘on’ position, most of the optics inside the Cairnfocal confocal system were unnecessary. A new setup using the digital micromirror, without the ‘off’ optical components and the inverted microscope, could be built and made light-tight.

In the final chapter. a multi-spot pattern was projected by a TEM grid. This method was able to improve the signal to noise ratio of the single-molecules 1.34x. We could also image single-

molecules at 1000 frames per second and achieve FRET in multiple spots. In addition, we show that iSMS could not be used in conjunction with the multi-spot pattern due to different background in both the emission channels. In the short term, FRET efficiencies should be calculated in conjunction with Change Point Analysis and Principal Component Analysis. These methods avoid manual selection of the single-molecule events and succeeded in locating and identifying all the single bursts in simulated and experimental time traces. This should allow FRET efficiency values to be identified within multiple spots with ease in the future. Further, new samples should be validated on the smfBox to ensure a high frequency of FRET bursts from the dsDNA samples. In the mid-term, a way to decrease the read noise further would be to use a 'Non-Destructive Readout' (NDR) camera. [2] This camera measures the accumulation of charge in each pixel without the pixel being read out. The signal collected within each pixel increases until the pixel is emptied, this means that the new measurement or image is the value of the previous pixel plus the noise and any newly collected photons. Previously, this camera has been found to increase the signal to noise ratio and increase the number of detected single-molecule events. [2] The signal to noise ratio increases because the read noise of the camera is reduced. We expect by using this camera, single-molecule FRET measurements in combination with solving the low red emission frequency will make multiple FRET measurements possible. In the long-term, we expect the Abel trap to be used in conjunction with single-molecule experiments. [3] This electrostatic trap confines single-molecules physically in space so they can be measured in real time. One possible challenge of this method may be the photobleaching of the single-molecules due to the length of time the molecule spends in the illumination volume. However, a multitude of single-molecule FRET data can be collected, even if the molecule lasts in the trap for a few seconds. This has the potential to increase the throughput of single-molecule FRET substantially.

7.2 Impact of this work

In this work, novel commercial and open-source instrumentation for the traditional, single-spot, confocal single-molecule FRET technique was explored. The excitation module has reduced the cost of a single-molecule FRET microscope 2-fold, increasing the techniques accessibility to more researchers. Since the design of the openFrame single-molecule FRET modules and the alignment, a university start-up 'Exciting Instruments' has been founded. This instrumentation provides affordable single-molecule FRET access without requiring specialist expertise in optics or an optical lab. We anticipate the results from both these projects will increase the uptake of single-molecule FRET to the wider research community.

In addition, by analysing the performance of modern sCMOS cameras at low-light levels, this project has established the optimal optical set up for single-molecule imaging. Finally, a multi-spot single-molecule FRET microscope was also investigated for improving the throughput of single-molecule FRET. This was first explored with a digital micromirror device which could image fluorescent beads in multiple spots and determine diffusion coefficients. We then explored a second multi-spot approach through an array of pinholes generated with a transmission electron microscopy grid (TEM grid). This novel method enhanced the signal to noise ratio enabling imaging and FRET emission of high and low FRET dsDNA sample at 1000 frames per second in multiple (25) pinholes. A camera with an improved field of view, could measure single-molecules simultaneously in up to approximately 800 spots, reducing the length of smFRET experiments to 2 seconds per sample. Furthermore, improved methods including signal to noise ratio thresholds, Principal Component Analysis and Change Point Analysis were used to identify single-molecule bursts were explored. These analysis methods will be used in the future in conjunction with this high-throughput single-molecule FRET

microscope for high throughput studies of multiple molecules and identify populations of biological molecules at relevant time scales and an enhanced speed of measurement.

7.3 References

[1] J. Jeffet *et al.*, "Multi-modal Single-molecule Imaging with Continuously Controlled Spectral-resolution (CoCoS) Microscopy," *bioRxiv*, p. 2020.10.13.330910, Jan. 2020,

[2] S. F. H. Barnett, M. Snape, C. N. Hunter, M. A. Juárez, and A. J. Cadby, "A Novel Application of Non-Destructive Readout Technology to Localisation Microscopy," *Sci. Rep.*, vol. 7, 2017

[3] A. E. Cohen and W. E. Moemer, "Method for trapping and manipulating nanoscale objects in solution," *Appl. Phys. Lett.*, vol. 86, no. 9, pp. 1–3, 2005